UNIVERSITÀ
DEGLI STUDI
FIRENZE

Università degli Studi di Firenze
European Laboratory for Non-linear Spectroscopy (LENS)
Corso di Dottorato in International Doctorate in Atomic and Molecular Photonics

Cavity-enhanced measurement for the generation of spin squeezed states in strontium atom interferometry

Candidate
Enlong Wang

Supervisor
Prof. Guglielmo M. Tino

Co-Supervisor
Dr. Leonardo Salvi

PhD Coordinator
Prof. Francesco S. Cataliotti

ciclo xxxiii, 2017-2020

Università degli Studi di Firenze, European Laboratory for Non-linear Spectroscopy (LENS).

Thesis submitted in partial fulfillment of the requirements for the degree of Doctor of Philosophy in International Doctorate in Atomic and Molecular Photonics.

Acknowledgments

Pursuing a PhD degree far away from home has never been an easy journey for me. By finishing this thesis and accomplishing the PhD courses in success, I want to say thanks to a lot of people.

First of all, I would like to express the utmost gratitude to my supervisor, Prof. Guglielmo M. Tino. I still remember four years ago when I first met Guglielmo in a skype interview, his kindness and hospitality confirmed my determination to pursue a PhD degree in his group in Florence. Prof. Tino is THE expert of atom interferometry and a pioneer in the field of atom, molecular physics and photonics. The past three years in his group were abundant to me, during which I could work vigorously in the lab and occasionally meet visiting scientist from all over the world. Guglielmo is not only a perfect group leader but also a good friend in life. He has always been supportive and friendly to me and his encouragement for me to study the Italian language proved to be super beneficial both in the research work and in daily life.

All the work of this thesis was done together with Dr. Leonardo Salvi, the person who actually proposed the spin squeezing project on strontium atoms. Working with Leonardo is both pedagogical and recreational. He has always been patient and ready to give a whole lecture just to answer one of my simple questions, which indeed helped a lot during the period when I started working on the squeezing experiment. Besides being an expert in electronics, optics and numerical simulations and so on, Leonardo is also a master of making jokes and laughter both in and outside of the lab. I have no idea how lucky I am to have this fantastic person to work with during my whole PhD years. Thank you Leo.

I would also like to thank Dr. Liang Hu, who is the first person I met in this group and the first person I worked with on an experiment. We spent eight months together searching for the single-photon interferometer both on the bosonic ^{88}Sr and the fermionic ^{87}Sr atoms. Liang is the most hard-working man I have ever worked with, he has formed deeply in my mind a role model that, being physicists or engineers, in order to solve a problem, we can study anything, try every possibility and shall never give up. I really appreciate the time we spent together.

The Florence group is not too big that I got the chance to know every group member very well. I would like to thank Dr. Gunjan Verma for working together in the squeezing experiment. I would also like to say thanks to Prof. Nicola Poli and Dr. Jonathan N. Tinsley, with whom we worked closely and shared a lot of instruments and experiences. Particularly, I am grateful to Nicola for his helpful cooperation not only in the field of ultra-cold strontium, but also in the field of soccer balls, we are the Champions all the time! I am also grateful to

the MAGIA group members Gabriele Rosi and Manan Jain. Gabriele has always been a resourceful person to whom I can ask questions whenever I am stuck by a problem, and he has never disappointed me. I thank Giovanni Gangale and Mauro Chiarotti, who did their Bachelor's thesis with us and continued the study in our group. Especially, I want to say thanks to Giovanni and his girlfriend Sabrina for offering me numerous free meals both in the canteen and at home, and for teaching me the recipe for the amazing *Pasta allo scoglio*. Their typically Italian-style generosity and hospitality make me fall in love with this country and the people here. I would also like to say thanks to the new group members Joep Assendelft, Giuseppe Vilinni, and Shamaila Manzoor, Satvika Bandarupally from the Poli group, for the wonderful moments we spent together. Thank you all.

LENS is a wonderful place for research with a group of wonderful people. I do not remember how many times I have knocked the door of the LENS Electronic Workshop and the Mechanical Workshop, asking for help in electronics or manufacturing small parts. They have always been friendly and helpful. I will remember these names for my whole life, Mauro Giuntini, Alessio Montori and Roberto Concas from the EW, and Riccardo Ballerini, Ahmed Hajeb from the MW. I am especially grateful to Riccardo for his interest in learning the Chinese language, and for the short communication in Chinese every time we met. Thanks good men! I am also grateful to the LENS administration staffs for organizing wonderful courses and seminars, and dealing with the administrative work related to my PhD courses. Special acknowledgment goes to my PhD coordinator Prof. Francesco S. Cataliotti and the LENS secretary Gaudia Mantelli.

I am very lucky to have some wonderful friends apart from my lab members, Maja Colauttti, Nicola Biagi, Natalia Bruno, Nicola Dalla Pozza, Ludovica Donati, Tecla Gabbrielli, Ivana Mastroserio, Marco Seminara, Riccardo Tani, Ilaria Vagniluca, Paolo Vezio and Xiaojuan Mo. We spent the precious time together during the lunch and enjoyed some wonderful trips in the holidays. Friendship is something natural and priceless, it is really an honor to have your friendship. I love you guys.

Most importantly, I would like to thank all my family members. My father Wang Chengwei and mother Sun Yuzhen have been working hard to raise me and my sisters up, which has drained their energy and life, but they have never stopped marching. My father taught me the responsibility to family and my mother taught me to love. I am also grateful to my sisters who take care of my parents as they are growing old and weak, while I am absent. You have always been my backbone. Father and mother and sisters I love you.

Finally, I would like to extend my acknowledgment to the China Scholarship Council (CSC) for the financial support during my whole PhD fellowship.

Abstract

Over the last three decades, atom interferometry has been developed rapidly and has become an important tool in quantum metrology. It has been widely applied both in the test of fundamental physics and in the precise measurement of gravity and gravity gradients.

Atom interferometers based on the alkaline-earth (like) atoms such as strontium (Sr) and ytterbium (Yb) have attracted increasing attention due to the existence of narrow intercombination transitions and ultra-narrow clock transitions. The bosonic ^{88}Sr is a good candidate for transportable and space-borne atom interferometers due to the immunity to stray magnetic fields in its electronic ground state, long coherence time and low collision rate. It can therefore be used in space projects for precision measurement of gravity and gravity gradients. However, there is a fundamental limit to the precision in a phase shift measurement with atom interferometers, which is set by the number of atoms involved $\delta\Phi_{SQL} = 1/\sqrt{N}$. This limit is known as the standard quantum limit. It is possible to surpass this limit by introducing correlations in the atomic ensembles thus reducing the phase uncertainty at the expense of an increase in the population uncertainty. In this case the spin-squeezed states are generated and can be used to improve the phase resolution of atom interferometers.

In this thesis, a method to generate spin squeezed states in ^{88}Sr momentum states for atom interferometry is considered and the necessary technology that allows its implementation will be presented. Spin squeezing is achieved by resolving the Doppler effect due to momentum state superposition via cavity-enhanced nondestructive measurement. An optical ring cavity is designed and constructed for quantum nondestructive measurements. However, one major obstacle that blocks the way to spin squeezing via cavity-enhanced measurement arises from cavity length fluctuations, which can totally mask the atomic signal if no appropriate scheme is adopted. Therefore, a method to cancel the cavity length fluctuations in measuring the atom-induced phase shift is proposed and close to 30 dB reduction of the cavity noise down to the noise floor has been demonstrated.

We further apply the demonstrated noise-reduced measurement scheme in the simulated squeezing experiment, where we mimic the atom-induced cavity phase shift by varying the frequency of one of the two circulating beams. The noise cancellation scheme demonstrates an improvement of a factor of 40 in phase sensitivity with a phase resolution of 0.7 mrad. With this improvement we estimate that the cavity noise will no longer play an important role in a real spin squeezing measurement.

Contents

List of Figures

List of Tables

Chapter 1

Introduction

Atom interferometry (AI) [1], since the first experimental realization some 30 years ago [2], has been developed rapidly and finds applications in various fields [3]. It has stimulated a new generation of quantum sensors with unprecedented precision, in measuring gravity acceleration [4, 5], gravity gradients [6, 7], gravity curvature [8] and rotations [9, 10]. It provides also an excellent tool for testing fundamental physics by measuring the Newtonian gravity constant G [11, 12, 13], the fine-structure constant α [14, 15] and for testing the equivalence principle [16, 17, 18, 19]. Furthermore, it paves the way for the search of new physics beyond the Standard Model, with heralded potential in the detection of gravitational waves [20] and dark matter [21].

Atom interferometers with ultra-cold alkaline-earth (-like) atoms such as Sr and Yb have attracted more attention in the last decade due to their exotic atomic properties and promising advantages in quantum metrology. Ultra-cold bosonic ^{88}Sr, for example, has zero nuclear spin in the ground state which makes it immune to ambient magnetic field fluctuations. With this advantage it becomes a prominent candidate for transportable [22] or space-borne sensors [23] since no magnetic shield is needed. The extremely long coherence time of Sr in an optical lattice [24, 25] has enabled the quantum sensor to reach a sensitivity unprecedented by its alkaline counterparts like Rb and Cs. The large-momentum-transfer technology based on Bragg diffraction [26, 27] also demonstrates, in some cases, superior performance compared to the traditional AI with two-photon Raman transition. Moreover, the famous *clock transition* existing in alkaline-earth (-like) atoms like Sr and Yb with a sub-Hz narrow linewidth, which has already been explored intensively and matured in the optical lattice clock and frequency standard community [28, 29], has triggered the so-called single-photon interferometer [30, 31, 32] which is by nature insensitive to the laser phase noise and has a potential in the detection of mid to low frequency gravitational waves [33, 34].

1.1 Atom interferometer beyond the SQL

The ultimate aim for an atom interferometer is the estimation of a phase shift [35]. In fact, an atom interferometer is a device that converts the phase information into a measurable atom population, where the quantity of interest (gravity acceleration, gradient, etc.) is embedded in this accumulated phase. However, there is a fundamental limit to the sensitivity of phase estimation which is set by the number of atoms involved,

$$\delta\Phi_{SQL} = \frac{1}{\sqrt{N}}, \tag{1.1}$$

where N is the number of atoms. This limit is known as the standard quantum limit (SQL) [36]. Here the N uncorrelated atoms are assumed to be in the coherent spin state (CSS) [37]. However, if correlation is introduced among the atoms and thus entanglement forms, it is possible to create the so-called spin squeezed state (SSS) [38, 39], which has a reduction in the phase uncertainty at the expense of an increase in the atom number uncertainty. With SSS it is possible to achieve a phase resolution beyond the SQL and ultimately approach the Heisenberg limit (HL) [40],

$$\delta\Phi_{HL} = \frac{1}{N}. \tag{1.2}$$

There are several methods to generate spin squeezed states useful for quantum metrology, which can be categorized into atom-light interactions and atom-atom collisions [37]. Atom-light interactions, of which the effect can be significantly enlarged by optical resonators, currently represents one of the most successful methods for producing large amounts of squeezing and entanglement in atomic ensembles [35]. This method relies on the non-destructive measurement of the collective atomic states instead of the single atomic state, while essentially preserving the coherence of the atomic ensemble. The optical resonators, through which the light interacts with the atomic ensemble multiple times and amplify the accumulated phase shift, can reach a metrological gain given by the collective cooperativity [41] $N\eta$, where N is the number of atoms and η is the single-atom cooperativity, which is proportional to the finesse of the cavity.

The direct consequence of using spin squeezing in atomic sensors is the metrological enhancement, which is given by the Wineland parameter [39].

$$\xi_R^2 = \frac{(\Delta\phi)^2}{(\Delta\phi)^2_{CSS}}, \tag{1.3}$$

where $\Delta\phi_{CSS} = 1/\sqrt{N}$ is the phase resolution of the CSS (standard quantum limit). Experiments have demonstrated metrologically useful spin squeezing through quantum non-demolition (QND) measurements with alkaline atoms

Cs [42, 43] in free space and Rb [44, 45, 46] with the aid of an optical cavtiy. Metrological gain up to 20 dB with respect to the standard quantum limit is achieved [45]. Recently, experiments in alkaline earth (-like) atoms Yb [47, 48] and Sr [49, 50] have reported prominent results with large spin squeezing in the operation as an optical clock.

This thesis is focused on the design, construction and commissioning of a new experimental apparatus for the realization of a Sr atom interferometer with a phase resolution beyond the SQL with spin squeezed states [51, 52]. The aim is to generate SSSs for a Bragg diffraction-based Sr atom interferometer by resolving the collective population difference between two momentum states through the Doppler effect. To this end, an optical ring cavity is built to perform non-destructive measurement for the generation of spin squeezed states. An optical ring cavity in this case, provides a versatile tool since it allows for the manipulation of both the atomic external states, as well as the internal states. Moreover, this cavity scheme allows for the presence of two counter-propagating beams that function as probe and reference, thus allowing the implementation of a differential scheme where the common-mode cavity noise can be canceled.

One important obstacle in obtaining highly spin-squeezed states with cavity-aided non-demolition measurement is the cavity length fluctuations. Since the measurement of the atomic state can be enclosed into the measurement of a cavity resonance phase shift, the cavity length-induced phase shift can completely mask the atom-induced phase shift, in which case no valuable information can be gained. In this thesis, a new method is proposed to cancel the effect of cavity-length fluctuations by using two counter-propagating beams that function as probe and reference, in this differential scheme the common-mode cavity length fluctuations can be canceled. Experiments have demonstrated close to 30 dB reduction in the cavity length fluctuations down to the noise floor and a factor of 40 improvement in the phase resolution. With this improvement one important barrier against obtaining highly spin squeezed states is removed [53].

1.2 Contribution to the single-photon Sr atom interferometer

Apart from the spin squeezing activity presented in this thesis, I have also worked on the single-photon Sr atom interferometer project together with Dr. Liang Hu during the first part of the PhD fellowship and contributed to the publication [31]. My personal contribution focused on the update and optimization of the experimental apparatus and the exploration of the single-photon atom interferometer

based on fermionic ^{87}Sr atoms. For consistency, this part of work is not presented in the main text of this thesis, but is briefly introduced here.

Most previous light-pulse atom interferometers have relied on multi-photon transitions to generate the superposition of momentum states required for sensitivity to inertial forces. These transitions, driven by Raman or Bragg beams, involve stimulated emission and absorption processes from two counter-propagating laser beams, which imprint their relative phase difference on the interacting atoms [1]. Due to the finite speed of light, however, atoms at different spatial positions will interact with light emitted from the interferometric lasers at different times, meaning that any laser phase fluctuations on this timescale will be transferred to the interferometer and will not cancel even in a gradiometeric scheme [33, 54]. For laboratory scale experiments the resultant phase error is negligibly small, but for proposed long-baseline experiments, this noise term could begin to dominate [34, 54]. One potential application which would be affected by this noise is gravitational wave detection, where in order to attain the necessary instrument sensitivity, long baselines are usually employed, as for example in the LISA detector which is designed for a 2.5×10^6 km arm length [55].

Nevertheless, atom interferometers based on multi-photon transitions have been proposed as a means of detecting gravitational waves, both in space-based and in ground-based applications [34, 56, 55, 57], although they will be severely affected by this noise at large scales. In our work, in contrast, we study a novel atom interferometer based on the single-photon clock transition of atomic strontium (^{1}S$_0$-^{3}P$_0$), where this problem is absent. As the phase of the interacting photon is set at the point of emission from the laser, and does not acquire noise in the vacuum path between the two sensors, the common laser phase noise does not appear at the output of a single-photon gradiometer [34, 54].

In this work, we characterize the performance of a gravimeter and a gravity gradiometer based on the ^{1}S$_0$-^{3}P$_0$ clock transition of strontium atoms. We use this new quantum sensor to measure the gravitational acceleration with a relative sensitivity of 1.7×10^{-5} after 150 s of integration time, representing the first realisation of an atomic interferometry gravimeter based on a single-photon transition. Various noise contributions to the gravimeter are measured and characterized, with the current primary limitation to sensitivity seen to be the intrinsic noise of the interferometry laser itself. In a gravity gradiometer configuration, a differential phase sensitivity of 1.53 rad/$\sqrt{\text{Hz}}$ was achieved at an artificially introduced differential phase of $\pi/2$ rad. We experimentally investigated the effects of the contrast and visibility based on various parameters and achieved a total interferometry time of 30 ms, which is longer than previously reported for such interferometers. The characterization and determined limitations

of the present apparatus employing ^{88}Sr atoms provides a guidance for the future development of large-scale clock-transition gravimeters and gravity gradiometers with alkali-earth and alkali-earth-like atoms (e.g. ^{87}Sr, Ca, Yb, Cd).

1.3 Organization of thesis

The rest of the thesis is organized as follows.

Chapter 2 presents the theoretical background of quantum metrology with spin squeezed states. The Bloch sphere representation is utilized to visualize collective spin states and the noise distributions of coherent spin states and spin squeezed states. The phase resolution of Ramsey interferometers with coherent spin states and spin squeezed states are derived and the relationship between spin squeezing and entanglement is explored. Finally, various approaches for the generation of spin squeezed states are reviewed and the main experimental achievements are cited.

Chapter 3 focuses on the proposal of squeezing on the momentum states in Sr atom interferometry. The basic properties and laser cooling and trapping of Sr atoms are introduced. The working principle of atom interferometry is studied and the derivation of the phase shift for different types of atom interferometers are presented. Finally the theoretical proposal for using spin squeezed states in Sr atom interferometer to surpass the SQL is discussed, which lies the foundation of this thesis.

Chapter 4 presents in detail the procedures of building an optical ring cavity. The considerations for cavity design are reviewed and the basic properties of optical cavities are introduced. Then the procedures and the first-hand experience in cavity construction are recorded, including cavity mirror manipulation, ring cavity alignment, cavity components epoxying, etc. This chapter provides a tutorial-like reference for people who want to build an optical cavity for general experimental purpose.

Chapter 5 presents the experimental apparatus for laser cooling and squeezing detection. The vacuum systems for Sr cooling and trapping and the science chamber which holds the experimental ring cavity are presented. Then various laser systems used in the experiments are discussed and a homemade optical shutter is built. Finally, a detection system developed specifically for the detection of light in the spin squeezing experiment is presented, which features a high gain and low noise.

Chapter 6 presents a novel cavity noise cancellation scheme for precise phase shift measurement and spin squeezing. The theoretical model for canceling the cavity-length fluctuations in measuring a cavity phase shift is developed. Two

laser beams with a frequency difference of one cavity free spectral range are simultaneous resonant with the cavity, demonstrating noise correlation in the Pound-Drever-Hall error signal due to the common-mode cavity-length fluctuations. Experimental results show that the scheme reduces the cavity-length fluctuations by 30 dB down to the noise floor. The scheme is further applied onto a simulated spin squeezing experiment which shows an improvement in phase resolution by a factor of 40. The proposed scheme removes one important barrier against attaining highly spin-squeezed states.

Chapter 7 concludes the contents of this thesis and presents some prospects for future work.

Chapter 2

Quantum metrology with spin squeezed states

In this chapter, the theoretical background of spin squeezing in atom interferometry is discussed. An atom interferometer is a device that converts the accumulated relative phase into an atomic population difference, the phase resolution with uncorrelated atoms has a lower bound given by the standard quantum limit, which is imposed by the number of atoms involved. However, by introducing correlation or entanglement among the atoms thus producing the spin squeezed states, it is possible to surpass the SQL and reach a phase sensitivity approaching the Heisenberg limit. Various approaches have been proposed and used to generate the SSSs, among them the quantum non-demolition measurement is one of the most successful. QND measurements enhanced by optical cavities have demonstrated so far the largest amount of spin squeezing in atomic ensembles.

2.1 Description of collective spin systems

In this first section the tools and methods to describe collective spin systems are introduced [35, 58]. An atom or an atomic ensemble can be modeled as two-level systems, which can be represented by a single spin or collective spins on a Bloch sphere. The evolution of the atomic states under interaction with external electromagnetic radiations can be described by a rotation of the spin states on the Bloch sphere.

2.1.1 Single spin

When the two-level approximation holds for an atom, the two levels can be associated with spin down $|\downarrow\rangle$ and spin up $|\uparrow\rangle$ states. The two modes can either be the

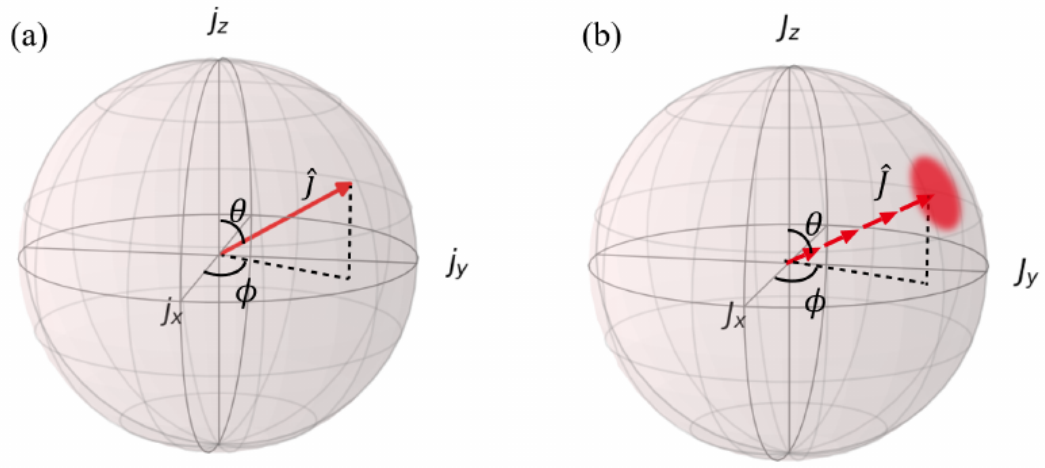

Figure 2.1: Bloch sphere representation of an atomic state. The Bloch vector (red arrows) can be fully parameterized by the polar and azimuthal angles θ and ϕ. (a) Single spin with radius of 1/2; (b) collective spins with N spin-1/2 particles pointed at the same direction, the shade area shows the uncertainty region.

atomic internal electronic energy levels ($|g\rangle$ for ground state and $|e\rangle$ for excited state), or the external momentum states. In the Bloch sphere representation, a single atom is a spin-1/2 particle, which is an arrow of radius 1/2 and with the tip on the surface of the sphere. This arrow is also called the Bloch vector.

More generally, any pure state on the Bloch sphere can be written as,

$$|\theta, \phi\rangle = \cos\left(\frac{\theta}{2}\right)|\uparrow\rangle + e^{i\phi}\sin\left(\frac{\theta}{2}\right)|\downarrow\rangle\,, \tag{2.1}$$

with $0 \leq \theta \leq \pi$ and $0 \leq \phi \leq 2\pi$ the polar and azimuthal angle, respectively, as shown in Fig. 2.1 (a). The physical significance of θ and ϕ are related to the amplitude probability and the relative phase between $|\uparrow\rangle$ and $|\downarrow\rangle$, respectively.

The Bloch vector can also be parameterized by,

$$\hat{\mathbf{j}} = j_x\hat{x} + j_y\hat{y} + j_z\hat{z}, \tag{2.2}$$

with $j_i \equiv \langle\hat{j}_i\rangle,\ i \in \{x, y, z\}$, where $\langle\ \rangle$ denotes the expectation value. $\hat{j}_i$ is the spin operator which is directly proportional to the Pauli spin operators as $\hat{j}_i = \hat{\sigma}_i/2$, where,

$$\hat{\sigma}_x = \begin{pmatrix} 0 & 1 \\ 1 & 0 \end{pmatrix},\quad \hat{\sigma}_y = \begin{pmatrix} 0 & -i \\ i & 0 \end{pmatrix},\quad \hat{\sigma}_z = \begin{pmatrix} 1 & 0 \\ 0 & -1 \end{pmatrix}. \tag{2.3}$$

We can also define the mean spin vector,

$$\vec{n} = \langle\hat{\sigma}\rangle = \{\sin\theta\cos\phi, \sin\theta\sin\phi, \cos\theta\} \tag{2.4}$$

with $|\vec{n}| = 1$. By these definitions the Bloch sphere is normalized and the z component of the Bloch vector $j_z = (P_\uparrow - P_\downarrow)/2$ is equal to the difference of probability amplitude between the two states.

2.1.2 Collective spins

In a real experiment, usually an atomic ensemble of 10^4-10^6 atoms is used. Therefore, we consider the collective spin states with N indistinguishable spin-1/2 particles. We introduce the collective spin vector,

$$\hat{\mathbf{J}} = \{\hat{J}_x, \hat{J}_y, \hat{J}_z\}, \tag{2.5}$$

where,

$$\hat{J}_x = \frac{1}{2}\sum_{l=1}^{N}\hat{\sigma}_x^{(l)}, \quad \hat{J}_y = \frac{1}{2}\sum_{l=1}^{N}\hat{\sigma}_y^{(l)}, \quad \hat{J}_z = \frac{1}{2}\sum_{l=1}^{N}\hat{\sigma}_z^{(l)}, \tag{2.6}$$

and $\hat{\sigma}_i^{(l)}$ is the Pauli vector of the lth particle.

In the Hilbert space, the collective spin operator Eq. (2.6) has a dimension of 2^N, where each individual spin can have an independent orientation. One possible choice of the basis of the 2^N dimension Hilbert space is the symmetric Dicke basis $|J, m\rangle$ [59, 60], which are the eigenstates of both $\hat{J}_z$ and $\hat{\mathbf{J}}^2$,

$$\hat{\mathbf{J}}^2 |J, m\rangle = J(J+1) |J, m\rangle , \tag{2.7a}$$

$$\hat{J}_z |J, m\rangle = m |J, m\rangle , \tag{2.7b}$$

with $J \in \{N/2, N/2-1, ...\}$ the pseudo-spin vector length which is proportional to the atom number, and $m \in \{-J, -J+1, ..., +J\}$ is related to the number of excitations.

One often assumed simplification is exchange symmetry among all the atoms [58], which is physically motivated since in many experiments all operations done with the atomic ensemble affect each spin in the same way. Under exchange symmetry the dimension of the Hilbert space is reduced to $N+1$, which will linearly increase with the number of the atoms. Also in this case, the maximum total spin length $J = N/2$ is obtained. In the following, unless otherwise stated, we will assume that the maximal spin system is considered.

There are some important features of the collective spin operators Eq. (2.6). First, since the Pauli matrix $\hat{\sigma}_z^{(l)}$ is given by $|\uparrow_l\rangle\langle\uparrow_l| - |\downarrow_l\rangle\langle\downarrow_l|$, the collective spin operator $\hat{J}_z$ can also be expressed as the population difference as,

$$\hat{J}_z = \frac{\hat{N}_\uparrow - \hat{N}_\downarrow}{2}, \tag{2.8}$$

where $\hat{N}_\uparrow = \sum_{l=1}^{N} |\uparrow_l\rangle \langle\uparrow_l|$ and $\hat{N}_\downarrow = \sum_{l=1}^{N} |\downarrow_l\rangle \langle\downarrow_l|$ are the collective atomic population operators for spin up and spin down, respectively, and can be easily measured via fluorescence detection or other methods.

Second, the collective spin operators obey the angular momentum commutation relations,

$$[\hat{J}_x, \hat{J}_y] = i\hat{J}_z, \quad [\hat{J}_z, \hat{J}_x] = i\hat{J}_y, \quad [\hat{J}_y, \hat{J}_z] = i\hat{J}_x, \tag{2.9}$$

which lead to a Heisenberg uncertainty relationship between ΔJ_z and ΔJ_y given by,

$$\Delta J_z \Delta J_y \geq |J_x|/2, \tag{2.10}$$

where $(\Delta J_z)^2 = \langle \hat{J}_z^{\,2} \rangle - \langle \hat{J}_z \rangle^2$ is the variance of the measurement outcomes of the spin projection J_z for many identical preparations and measurements of the same collective spin state. This uncertainty in J_z can also be interpreted as the randomness of projection when each atom is measured, as depicted by the shade area in Fig. 2.1 (b). To be noticed, the uncertainty relationship like Eq. (2.10) is completely general and does not rely on any assumption of the orientation of the collective spin.

2.1.3 Collective rotations and phase estimation

Any unitary transformation of a single spin is a rotation $e^{-i(\theta/2)\hat{\sigma}_\mathbf{n}}$ on the Bloch sphere, where $\mathbf{n}$ is an arbitary spin direction and the rotation axis and θ is the rotation angle, respectively. With N spins, each locally rotated about the same axis $\mathbf{n}$ and angle θ, the transformation is $\bigotimes_{l=1}^{N} e^{-i(\theta/2)\hat{\sigma}_\mathbf{n}^{(l)}} = e^{-i\theta\hat{J}_\mathbf{n}}$ [35]. This collective rotation is the idealized model of most of the interferometric transformations discussed in this chapter. In the collective spin language, a balanced beam splitter is described by $e^{-i(\pi/2)\hat{J}_x}$ and a relative phase shift by $e^{-i\theta\hat{J}_z}$. Combining the three transformations,

$$e^{-i(\pi/2)\hat{J}_x} e^{-i\theta\hat{J}_z} e^{-i(\pi/2)\hat{J}_x} = e^{-i\theta\hat{J}_y}, \tag{2.11}$$

the whole interferometer sequence (Mach-Zehnder or Ramsey) is equivalent to a collective rotation around the y axis on the generalized Bloch sphere of maximum radius $N/2$.

When an interferometric measurement is performed with a single particle, the phase estimation is limited by the quantum projection noise (QPN). To see how this arises, we recall that in the interferometer one can arrange a situation where the phase shift is measured through the relation $\Delta\phi \simeq P_\downarrow - P_\uparrow \propto \langle \hat{J}_z \rangle$. The uncertainty of this measurement is therefore given by the variance of the

operator, $(\Delta\hat{J}_z)^2$. The phase resolution in the presence of quantum projection noise can be computed as,

$$\delta(\Delta\phi) = \frac{\Delta J_z}{|\frac{\partial\langle J_z\rangle}{\partial\Delta\phi}|}. \tag{2.12}$$

This expression is important in determining the limit of phase estimation in the following sections.

2.2 Coherent spin states and the standard quantum limit

Coherent spin states are the most classical-like quantum states of a symmetric ensemble of N spin-1/2 particles. In this section the definition of CSS is given and the representations both in the Bloch states $|\theta,\phi\rangle$ and the Dicke states $|J,m\rangle$ are discussed. The probability distribution of CSS is shown on the Bloch sphere and the limit of phase resolution with CSS is derived, which is known as the standard quantum limit.

2.2.1 Coherent spin state

A CSS is made up of N identical but independent spin-1/2 particles with no quantum correlations or entanglement among the particles. Mathematically, a CSS can be written as the product of many single spin-1/2 particles (Eq. (2.1)),

$$|\theta,\phi\rangle = \prod_{l=1}^{N}\left(\cos\frac{\theta}{2}|\uparrow_l\rangle + e^{i\phi}\sin\frac{\theta}{2}|\downarrow_l\rangle\right). \tag{2.13}$$

The physical significance of θ and ϕ is that the mean spin vector $\mathbf{J} = \langle\hat{\mathbf{J}}\rangle = \langle\theta,\phi|\,\hat{\mathbf{J}}\,|\theta,\phi\rangle$ points in the direction given by the spherical coordinates (θ,ϕ), the same as in Eq. (2.1). The tip of the Bloch vector resides on the surface of the sphere with a radius of $J = N/2$. Without considering fluctuations or noise in the spin projections, the vector will behave classically.

In order to develop a more detailed understanding of the coherent spin state and its fluctuations we start with the discussion of a special case where each particle is in a 50/50 superposition of the two modes with 0 relative phase, i.e., each spin points in σ_x direction and its quantum state is,

$$|x\rangle = \left(|1/2,-1/2\rangle + |1/2,+1/2\rangle\right)/\sqrt{2}, \tag{2.14}$$

where we have chosen the Dicke states in σ_z direction as the basis states. The probability to observe each individual elementary spin in state up or down is

equal to,

$$|\langle 1/2, \pm 1/2|x\rangle|^2 = 1/2. \tag{2.15}$$

The N atom coherent spin state is a collection of these independent elementary spins,

$$|X\rangle = \left[\left(|1/2,-1/2\rangle + |1/2,+1/2\rangle\right)/\sqrt{2}\right]^{\otimes N} \tag{2.16}$$

and therefore the measurement of the J_z spin component is equivalent to N measurements on a single spin. The probability distribution over the Dicke states is therefore binomial. We could have chosen equally the Dicke states in J_y direction to describe the spin state which shows again that the spin fluctuations in the directions perpendicular to J_x, i.e., the mean spin direction, are isotropic.

A general coherent spin state $|\theta,\phi\rangle$ can therefore be described as a binomial sum of Dicke states $|J,m\rangle$:

$$|\theta,\phi\rangle = \sum_{m=-J}^{J} |J,m\rangle \langle J,m|\theta,\phi\rangle\,, \tag{2.17}$$

where,

$$\langle J,m|\theta,\phi\rangle = \left(\begin{array}{c} 2J \\ J+m \end{array}\right)^{1/2} \cos(\theta/2)^{J-m} \sin(\theta/2)^{J+m} e^{-i(J+m)\phi}. \tag{2.18}$$

The CSS is one of the most common states used in atom interferometry, mainly because it is readily obtained by the interaction with the laser fields. Indeed, starting with all the atoms pumped in the ground $|\downarrow\rangle$ state, corresponding to $|\theta=\pi,\phi\rangle$, the state is rotated into any state $|\theta,\phi\rangle$ by the interaction with the electromagnetic radiations.

2.2.2 The standard quantum limit

Assuming that a particular coherent spin state $|\theta,0\rangle$ is the output of an atom interferometer. Because of the mapping of phase shift $\Delta\phi$ into population difference, we have $\theta = \Delta\phi + \pi/2$. In order to compute the spin mean value and the variance, we note that the expression Eq. (2.18) corresponds to the binomial distribution with probability,

$$|\langle J,m|\theta,\phi\rangle|^2 = \left(\begin{array}{c} 2J \\ J+m \end{array}\right) \cos(\theta/2)^{2(J-m)} \sin(\theta/2)^{2(J+m)}. \tag{2.19}$$

The average is therefore $\langle \hat{J}_z\rangle = -\frac{1}{2}N\sin\Delta\phi$ and the variance is,

$$(\Delta J_z)^2 = N\cos^2(\theta/2)\sin^2(\theta/2) = \frac{1}{4}N\cos^2\Delta\phi. \tag{2.20}$$

With these information the interferometer phase resolution Eq. (2.12) can be calculated as,

$$\delta(\Delta\phi) = \frac{1}{\sqrt{N}}. \tag{2.21}$$

This phase resolution limit is known as the Standard Quantum Limit and the corresponding phase noise is known as the shot noise.

We next consider the case where the interferometric measurement is repeated m times with a single particle and assume that the various repetitions are uncorrelated, i.e., the outcome of one measurement does not affect the outcomes of the following measurements [61]. In this case we will consider the random variable J_z to be the sum of the random variables corresponding to each measurement trial $k, (J_z)_k$. If the independent trials are indistiguishable, by making use of the error propagation formula, in the previous results we therefore make the replacements,

$$\langle J_z\rangle \to \sum_{k=1}^{m}\langle (J_z)_k\rangle = m\langle J_z\rangle, \tag{2.22}$$

$$(\Delta J_z)^2 \to \sum_{k=1}^{m}(\Delta J_z)_k^2 = m(\Delta J_z)^2, \tag{2.23}$$

and the phase resolution is given by,

$$\delta(\Delta\phi) = \frac{1}{\sqrt{m}}. \tag{2.24}$$

The phase measurement can also be performed with more than one atom. If the atomic states of different atoms are uncorrelated, then this measurement is equivalent to the repetition of a measurement with a single atom. This follows from the fact that the interactions in the interferometer, namely the interaction with the laser field and the phase shift, are local operations. This means that the interferometer does not create correlations between particles. Therefore, with m trials of the experiment, each with N atoms, the phase resolution is given by,

$$\delta(\Delta\phi) = \frac{1}{\sqrt{Nm}}. \tag{2.25}$$

2.2.3 Visualizing CSSs using the Q representation

Employing the Husimi Q-representation [62], spin states can be conveniently visualized on a generalized Bloch sphere with radius J. In order to describe the most general spin state, i.e., pure states and statistical mixtures, the density matrix formalism is used [63]. The density operator $\hat{\rho}$ in coherent spin state basis is

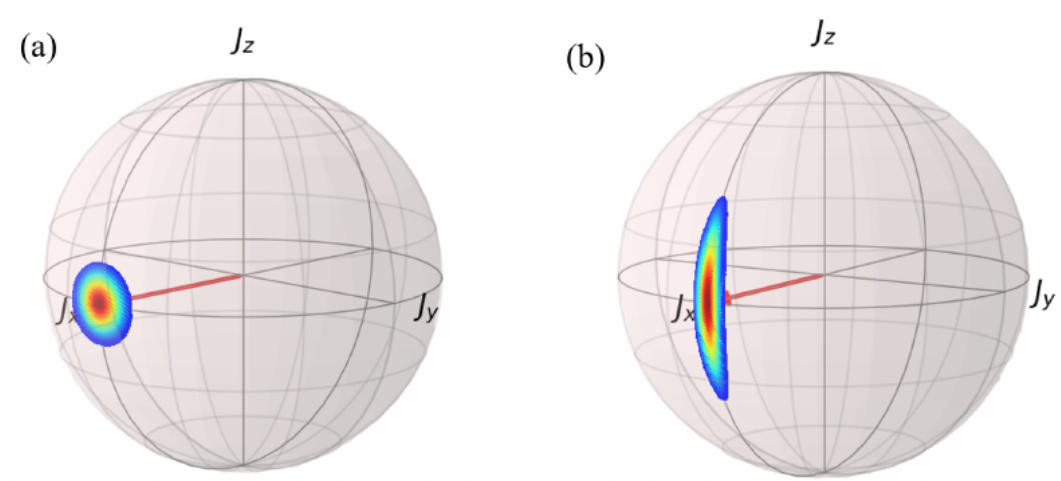

Figure 2.2: Husimi Q representation of the coherent spin state (a) and the spin squeezed state (b). The probability distribution of CSS is a disk on the surface of the the Bloch sphere, while that of the SSS has a reduced spin noise distribution in one direction, at the expense of an increased noise in the orthogonal spin direction. Python scripts for the plot at the courtesy of Dr. Leonardo Salvi [52].

given by,

$$\hat{\rho} = \int P(\theta, \phi) \, |\theta, \phi\rangle \, \langle \theta, \phi| \, d\Omega, \tag{2.26}$$

where the integral covers the full solid angle and $d\Omega = \sin(\theta) d\theta d\phi$. The probability distribution $P(\theta, \phi)$ is normalized to one. The Q-representation uses the diagonal elements of the density operator to represent the quantum state,

$$Q(\theta, \phi) = \frac{2J+1}{4\pi} \, \langle \theta, \phi| \, \rho \, |\theta, \phi\rangle \, . \tag{2.27}$$

The Husimi Q function can then be written as,

$$\begin{aligned} Q(\theta, \phi) &= \frac{2J+1}{4\pi} \int \sin\theta' d\theta' d\phi' P(\theta', \phi') | \, \langle \theta, \phi | \theta', \phi' \rangle \, |^2 \\ &= \frac{2J+1}{4\pi} \int \sin\theta' d\theta' d\phi' P(\theta', \phi') (\cos\Theta/2)^{4J}, \end{aligned} \tag{2.28}$$

where Θ is the angle between the directions of the coherent spin states $|\theta, \phi\rangle$ and $|\theta', \phi'\rangle$ and is given by,

$$\cos\Theta = \cos\theta \cos\theta' + \sin\theta \sin\theta' \cos(\phi - \phi'). \tag{2.29}$$

In the limit of large atom numbers, $J \gg 1$, this expression can be approximated

by,

$$Q(\theta,\phi) \simeq \frac{J}{2\pi}\int \sin\theta' d\theta' d\phi' P(\theta',\phi') \exp\left[-\frac{J}{2}(\theta-\theta')^2 - \frac{J}{2}(\phi-\phi')^2\sin^2\theta'\right]. \tag{2.30}$$

If we consider the CSS $\rho = |\theta_0,\phi_0\rangle\langle\theta_0,\phi_0|$, then $P(\theta',\phi') = \delta(\theta'-\theta_0)\delta(\sin\theta'(\phi-\phi_0))$ and the Q function is expressed by a Gaussian distribution,

$$Q(\theta,\phi) = \frac{J}{2\pi}\exp\left[-\frac{J}{2}(\theta-\theta_0)^2 - \frac{J}{2}(\phi-\phi_0)^2\sin^2\theta_0\right]. \tag{2.31}$$

This function is represented in Fig. 2.2 (a) for a CSS pointing in the direction $(\theta=\pi/2,\phi=0)$.

2.3 Spin squeezing and entanglement

The Heisenberg uncertainty relations for the collective spin operators Eq. (2.10) set a lower bound to the product of spin variances. However, the spin variance of one spin component can be reduced, at the expense of an increase in the variance of the other. The result of spin variance reduction is the metrological enhancement in quantum metrology, which drives the intuition of spin squeezed states. In this section, we introduce the mainstream definitions of SSSs and the relationship between spin squeezing and multiparticle entanglement. In the next section we will show the metrological enhancement with SSSs in a Ramsey interferometer.

2.3.1 Spin squeezed states

Spin squeezed states are a class of states having squeezed spin variance along a certain direction, at the cost of an anti-squeezed variance along an orthogonal direction. Spin squeezing is one of the most successful approaches to witness large-scale quantum entanglement beating the standard quantum limit in interferometry [35, 37].

There are various definitions of spin squeezing depending on its applications [37]. Among them the most popular ones are the squeezing parameter given by Kitagawa and Ueda [38] in terms of squeezing reduction and that given by Wineland et. al [39, 64] in the application of spectroscopy enhancement.

Kitagawa criterion We first introduce the squeezing parameter ξ_S^2 given by Kitagawa and Ueda [38]. For a CSS the variance of spin operators depends on

the mean spin vector $\vec{n}$ and there exists a prior direction: the mean-spin direction (MSD),

$$\vec{n}_0 = \frac{\langle \vec{J} \rangle}{|\langle \vec{J} \rangle|} = \frac{\langle \vec{\sigma}_1 \rangle}{|\langle \vec{\sigma}_1 \rangle|}, \tag{2.32}$$

where the second equation results from the exchange symmetry.

Below, we use $\vec{n}_\perp$ to denote the direction perpendicular to the MSD. For a CSS, we have $(\Delta J_{\vec{n}_\perp})^2 = j/2$, thus a state is spin squeezed if the variance of $J_{\vec{n}_\perp}$ is less that $j/2$. We define the spin-squeezing parameter,

$$\xi_S^2 = \frac{\min(\Delta J_{\vec{n}_\perp}^2)}{j/2} = \frac{4\min(\Delta J_{\vec{n}_\perp}^2)}{N}, \tag{2.33}$$

where $j = N/2$, and $\vec{n}_\perp$ refers to an axis perpendicular to the MSD and the minimization is over all directions $\vec{n}_\perp$.

It is a fact that the spin-squeezing parameter ξ_S^2 is equal to 1 for the CSS. Thus, if there are certain quantum correlations among the elementary spins, we may have $\xi_S^2 < 1$, i.e., the fluctuation in one direction is reduced, as shown in Fig. 2.2 (b). Therefore, the squeezing parameter ξ_S^2 has natural connections with quantum correlations (entanglement).

Wineland criterion We then discuss the spin-squeezing parameter proposed by Wineland et al. [39, 64] in the study of Ramsey spectroscopy. The squeezing parameter proposed by Wineland et al. is defined as,

$$\xi_R^2 = \frac{(\Delta\phi)^2}{(\Delta\phi)_{CSS}^2} = \frac{N(\Delta J_{\vec{n}_\perp})^2}{|\langle \vec{J} \rangle|^2}. \tag{2.34}$$

This is the ratio of the phase sensitivity of a general state versus the CSS. Here, we choose the direction $\vec{n}_\perp$ where $\Delta J_{\vec{n}_\perp}$ is minimized. The CSS here acts as a noise-reference state. According to Eq. (2.12), the phase sensitivity can be written as,

$$\Delta\phi = \frac{\xi_R}{\sqrt{N}}. \tag{2.35}$$

If $\xi_R^2 < 1$, $\Delta\phi < (\Delta\phi)_{CSS}$ beats the quantum projection noise, which is also known as the shot-noise limit. In contrast with ξ_S^2, which is the analogue of bosonic squeezing [65], the parameter ξ_R^2 is substantially connected to the improvement of the sensitivity of angular-momentum states to rotations, and thus is attractive for interferometric experiments.

This Wineland parameter ξ_R^2 is related to ξ_S^2 via,

$$\xi_R^2 = (\frac{j}{|\langle \vec{J} \rangle|})^2 \xi_S^2. \tag{2.36}$$

Since $j = N/2 \geq |\langle \vec{J} \rangle|$, we have,

$$\xi_S^2 \leq \xi_R^2. \tag{2.37}$$

Even though these two parameters are similar (when $j = |\langle \vec{J} \rangle|$, $\xi_R^2 = \xi_S^2$), their physical meanings are different. In other words, metrological spin squeezing $\xi_R^2 < 1$ implies spin squeezing $\xi_S^2 < 1$ according to the definition of Kitagawa and Ueda. The converse is not true: there is no direct relation between $\xi_S^2 < 1$ and the improvement of metrological sensitivity.

The lower bound of the phase sensitivity is given by the Heisenberg uncertainty relation,

$$(\Delta J_{\vec{n}_\perp})^2 (\Delta J_{\vec{n'}_\perp})^2 \geq \frac{1}{4} |\langle J_{\vec{n}} \rangle|^2, \tag{2.38}$$

from which we have,

$$\xi_R^2 \frac{4(\Delta J_{\vec{n'}_\perp})^2}{N} \geq 1. \tag{2.39}$$

Using the relations $N^2/4 = j^2 \geq \langle J_{\vec{n}}^2 \rangle \geq (\Delta J_{\vec{n}})^2$ and the fact that the largest eigenvalue of $J_{\vec{n}}^2$ is j^2, we obtain,

$$\xi_R^2 \geq \frac{1}{N}. \tag{2.40}$$

By using Eq. (2.35), we further have,

$$\Delta\phi \geq (\Delta\phi)_{\mathrm{HL}} = \frac{1}{N}, \tag{2.41}$$

where $(\Delta\phi)_{\mathrm{HL}}$ is the Heisenberg limit [40].

2.3.2 Squeezing and entanglement

It has been shown that spin squeezing can be used to surpass the standard quantum limit in quantum phase estimation. In this subsection we exploit the relationship between squeezing and entanglement.

Multi-particle entanglement A state of N particles in two modes is separable (non-entangled) when it can be written as [66],

$$\hat{\rho}_{sep} = \sum_k p_k \hat{\rho}_k^{(1)} \otimes \hat{\rho}_k^{(2)} \otimes \ldots \otimes \hat{\rho}_k^{(N)}, \tag{2.42}$$

where $p_k > 0$, $\sum_k p_k = 1$, $\hat{\rho}_k^{(i)}$ is the density matrix for the ith particle. Multi-particle entanglement is quantified by the number of particles in the largest non-separable subset. A mixed state is k-separable if it can be written as a mixture

of k separable pure states [67],

$$\hat{\rho}_{k\ sep} = \sum_{q} |\Psi_{k\ sep,q}\rangle \langle \Psi_{k\ sep,q}| . \tag{2.43}$$

A state that is k-separable but not $(k-1)$-separable is called k-particle entangled, it contains at least one state of k particles that does not factorize. In other words, it has an entanglement depth large than $k-1$ [68].

According to [69], particles are entangled if the state satisfies,

$$\xi^2 \equiv \frac{N(\Delta \hat{J}_{\vec{n}_3})^2}{\langle \hat{J}_{\vec{n}_1} \rangle^2 + \langle \hat{J}_{\vec{n}_2} \rangle^2} < 1, \tag{2.44}$$

also it is spin-squeezed along the direction $\vec{n}_3$. This criterion is consistent with the Kitagawa or Wineland definition of spin squeezing.

Literature [66] has shown a different approach by using the quantum Fisher information (QFI) to define metrologically useful entanglement,

$$\chi^2 \equiv \frac{N}{F_Q[\hat{\rho}_{inp}, \hat{J}_{\vec{n}}]} < 1, \tag{2.45}$$

where $F_Q[\hat{\rho}_{inp}, \hat{J}_{\vec{n}}] = 4(\Delta \hat{R})^2$ is the QFI [70, 71, 72] and $\vec{n}$ is an arbitrary direction. The Hermitian operator $\hat{R}$ is the solution of the equation $\left\{\hat{R}, \hat{\rho}_{inp}\right\} = i\left\{\hat{J}_{\vec{n}}, \hat{\rho}_{inp}\right\}$. The QFI is naturally related to the problem of phase estimation. Generally speaking, an interferometer is quantum mechanically described as a collective, linear, rotation of the input state by an angle θ: $\hat{\rho}(\theta) = e^{-i\theta \hat{J}_{\vec{n}}} \hat{\rho}_{inp} e^{-i\theta \hat{J}_{\vec{n}}}$. For an arbitrary interferometer and phase estimation strategy, the phase sensitivity is limited by a fundamental bound, the Quantum Cramer-Rao (QCR) [72], which only depends on the specific choice of the input state,

$$\Delta\theta_{QCR} = \frac{1}{\sqrt{F_Q[\hat{\rho}_{inp}, \hat{J}_{\vec{n}}]}} = \frac{\chi}{\sqrt{N}}. \tag{2.46}$$

A comparison with Eq. (2.46) reveals that Eq. (2.45) is not only a sufficient condition for particle-entanglement, as already discussed, but also a necessary and sufficient condition for sub-shot-noise phase estimation. $\chi < 1$ provides the class of entangled states which are useful for sub-shot-noise sensitivity.

Phase resolution limits for separable and entangled states We consider the phase estimation of different input states as separable states and entangled states [61] using the QFI. The QFI of any separable state of N qubits is upper bounded,

$$F_Q[\hat{\rho}_{sep}, \hat{J}_{\vec{n}}] \leq N, \tag{2.47}$$

therefore the maximum phase sensitivity achievable with separable states is,

$$\Delta\theta_{sep} = \frac{1}{\sqrt{N\nu}}. \tag{2.48}$$

where ν is the number of independent measurements. In Eq. (2.48) N and ν play the same role: repeating the phase estimation ν times with one particle has the same sensitivity bound as repeating the phase estimation 1 time with $N = \nu$ particles in a separable state.

As for a k-particle entangled state, when used as an input state of an interferometer, the QFI increases monotonically with k as $F_Q[\hat{\rho}_{k\ sep}, \hat{J}_{\vec{n}}] \leq Nk$. The maximum value of the QFI is obtained for genuine N-particle entangled states $k = N$ giving [66],

$$F_Q[\hat{\rho}, \hat{J}_{\vec{n}}] \leq N^2, \tag{2.49}$$

which defines the ultimate Heisenberg limit of phase sensitivity,

$$\Delta\theta_{\mathrm{HL}} = \frac{1}{N\sqrt{\nu}}. \tag{2.50}$$

This result is consistent with the derivation of HL in Eq. (2.41).

We conclude this section by summarizing the relations between squeezing, entanglement and sub shot-noise phase measurement. Useful entanglement, which can be quantified by the QFI (Eq. (2.45)), is a necessary and sufficient condition for sub shot-noise phase measurement. However, it is to be noted that spin squeezing is only a sufficient condition for entanglement yet not necessary, there are states that are not spin-squeezed and yet entangled and useful for quantum metrology, for example, the NOON state and the twin-Fock state (Dicke state), which will be presented in the next section.

2.4 Atom interferometer with non-classical states

In this section, using non-classical states in atom interferometers for quantum phase estimation is considered. We record that an AI is a device that converts the accumulated relative phase between the two modes of a collective spin state into the population difference between the two modes. The resolution of this phase estimation is limited by the standard quantum limit $\delta(\Delta\phi) = 1/\sqrt{N}$ for uncorrelated particles. Entanglement, or correlations between the atoms can surpass this limit. One of the most prominent candidate states for phase estimation beyond the SQL is the spin squeezed state.

In this section, the Ramsey interferometer and its application in quantum phase estimation is discussed. It is shown that the Mach-Zehnder interferometer

used in atom interferometry is conceptually equivalent to the Ramsey interferometer in terms of phase estimation. The Ramsey interferometer sequences with CSS and SSS are presented. The phase noise reduction of the SSS with respect to the CSS is analyzed.

2.4.1 Ramsey interferometer and quantum phase estimation

The Ramsey interferometer, or Ramsey spectroscopy is commonly used in the field of atomic clocks and frequency standards [28]. The mathematical representation of the Ramsey sequence in atom interferometry can be found in [73] and will be briefly reviewed in section 3.2. Here we analyze the Ramsey interferometer in a pictorial way on the Bloch sphere (as in Fig. 2.3) and explain the process of phase estimation.

The optical counterpart of a Ramsey interferometer is an optical Mach-Zehnder interferometer, which consists of two beamsplitters to split and recombine the laser beams. The atomic optics counterpart for beamsplitters are the $(\pi/2)$ pulses. In the Bloch sphere, the $(\pi/2)$ pulses rotate the Bloch vector by 90°.

The Ramsey interferometer sequence with CSS is depicted in Fig. 2.3 (a) with the Bloch sphere representation. It consists of four steps, as detailed in the following:

- The initial state is a CSS prepared in the ground state $|\downarrow\rangle$, which is easily available experimentally.
- The first $(\pi/2)$ pulse prepares the state into a superposition state with equal probability of $|\downarrow\rangle$ and $|\uparrow\rangle$, which corresponds to an unitary rotation of the collective spin state by 90° around the J_y axis.
- After a free evolution of time τ the state accumulates a relative phase $(\Delta\phi)$ between the two modes, which corresponds to a rotation of angle ϕ in the equatorial plane.
- A second $(\pi/2)$ pulse is then applied to transfer the relative phase ϕ into the angle θ by rotating the Bloch vector by 90° around the J_x axis. This method maps the relative phase between the two modes, which is not observable, into the population difference, which can be further detected by fluorescence or absorption detection.

It can be proven that the Mach-Zehnder interferometer which consists of a pair of $\pi/2$-π-$\pi/2$ pulses is conceptually equivalent to the Ramsey interferometer

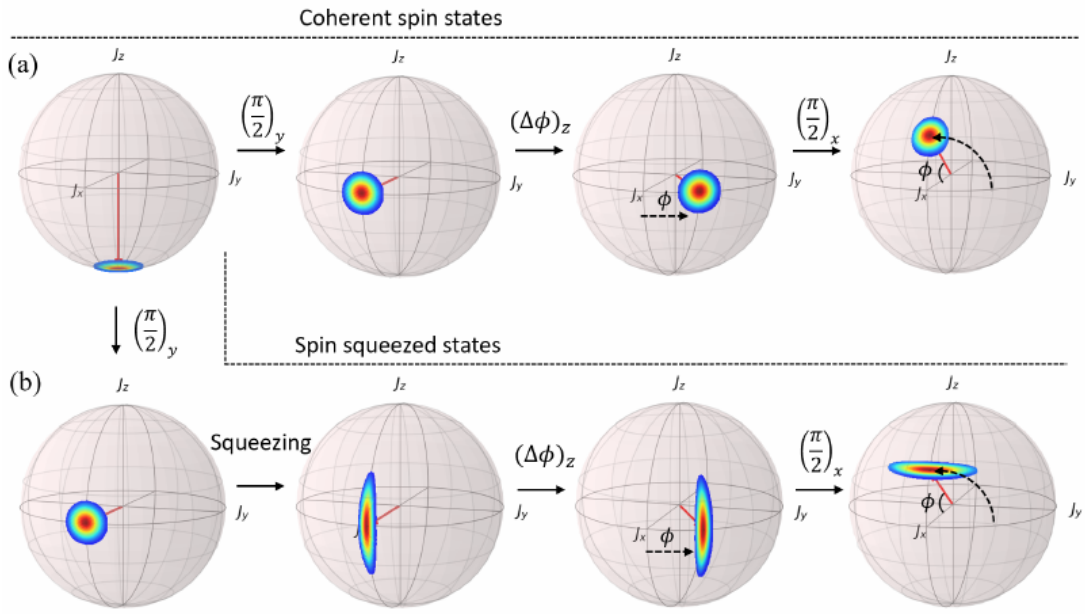

Figure 2.3: Ramsey interferometers with (a) coherent spin states and (b) spin squeezed states in the Bloch sphere representation. The uncertainty distributions according to the Husimi Q function are represented by the colorful disks. The rotation of the Bloch vector (red arrows) is stimulated by the $(\pi/2)_{x,y}$ pulses, with the subscript indicting the axis of rotation. During the free evolution of time τ the collective spin states accumulate a phase shift $\Delta\phi$, which corresponds to a rotation in the equatorial plane. The Ramsey interferometer converts the accumulated phase shift between the two states into the measurable population difference. This estimation of phase has a resolution of $\Delta\phi \sim 1/\sqrt{N}$ for the CSS (a), and can be surpassed by introducing spin squeezing into the atomic ensemble (b). Figure adapted from [58, 74].

in terms of phase estimation. The (π) pulse, which inverts the population of the $|\downarrow\rangle$ and $|\uparrow\rangle$ states, only contribute a relative phase between the two states and can be included in the total accumulated phase ϕ.

Fig. 2.3 (b) shows the Ramsey sequence with SSS. After preparing the CSS into the superposition state with the first $(\pi/2)$ pulse, squeezing is introduced and correlations between the atoms are created. This can be visualized as a squeezing in the uncertainty region of the Husimi Q function. In Fig. 2.3 (b), a phase-squeezed state is shown with reduced phase uncertainty and increased atom number uncertainty. After the phase accumulation and the second $(\pi/2)$ pulse, the collective spin state is rotated by 90° around the J_x axis thus the phase-squeezed state is converted into the number-squeezed state, of which the uncertainty in the atomic population is reduced. Finally, the detection of atomic number in the $|\downarrow\rangle$ and $|\uparrow\rangle$ states has a reduced uncertainty with respect to the

SQL. This signifies an improved sensitivity in the phase estimation.

2.4.2 Sensitivity of the Ramsey interferometer

The phase sensitivity of a Ramsey interferometer can be quantified by considering the population difference $J_z = (N_\uparrow - N_\downarrow)/2$ as a function of the accumulated relative phase ϕ, which is a sinusoidal wave called the Ramsey Fringe, as depicted in Fig. 2.4. The phase sensitivity to a small phase shift is defined as,

$$\Delta\phi = \frac{\Delta\hat{J}_z}{|\partial\langle\hat{J}_z\rangle/\partial\phi|}, \tag{2.51}$$

where $\Delta\hat{J}_z$ is the projection noise and $|\partial\langle\hat{J}_z\rangle/\partial\phi|$ is the slope of the Ramsey fringe. Based on the sensitivity function Eq. (2.51), it is obvious that two different ways can be used to improve the phase sensitivity of Ramsey interferometer. One can either reduce the projection noise $\Delta\hat{J}_z$ or increase the slope $|\partial\langle\hat{J}_z\rangle/\partial\phi|$ in order to increase the overall sensitivity. The increase of slope can be achieved in Schrödinger cat's like entanglement interferometers, which will be briefly introduced in subsection 2.4.3. In this thesis, we focus on the other method, which aims at reducing the projection noise by squeezing the noise distribution.

Figure 2.4 (a) shows the Ramsey fringe with the CSSs (red solid line) and the SSSs (blue dotted line), respectively. The shaded regions represent the rms fluctuations of the J_z measurement. The maximum sensitivity is achieved when $J_z = 0$ and at the largest slope, $|\partial\langle\hat{J}_z\rangle/\partial\phi|_{max} = \mathcal{V}N/2$, where $\mathcal{V}$ is the visibility which measures the mean spin length $\langle\mathbf{J}\rangle = \mathcal{V}N/2$. For CSSs, $\mathcal{V} = 1$ while for SSSs, $\mathcal{V} \leq 1$ due to the decoherence. Nevertheless, the overall sensitivity can be improved if the projection noise J_z can be reduced.

In Fig. 2.4 (b) an enlargement of the maximum sensitivity region is shown, where we assume that slopes for the CSSs and the SSSs are similar and $\simeq N/2$. The projection noise for CSSs is $\Delta J_{z,CSS} = \sqrt{N}/2$ at the shot-noise-limit, which yields a phase sensitivity of $\phi_{SQL} = 1/\sqrt{N}$, and therefore corresponds to the standard quantum limit. For SSSs the projection noise is reduced so that $\Delta J_z < \Delta J_{z,CSS}$, therefore the phase sensitivity overcomes the SQL with CSSs.

2.4.3 Useful states for quantum metrology

Apart from the SSS which can be used in Ramsey interferometry to surpass the SQL, there are other non-classical states which are important for sub-shot noise quantum metrology. Among them the NOON state and the Dicke state are most studied and will be discussed here.

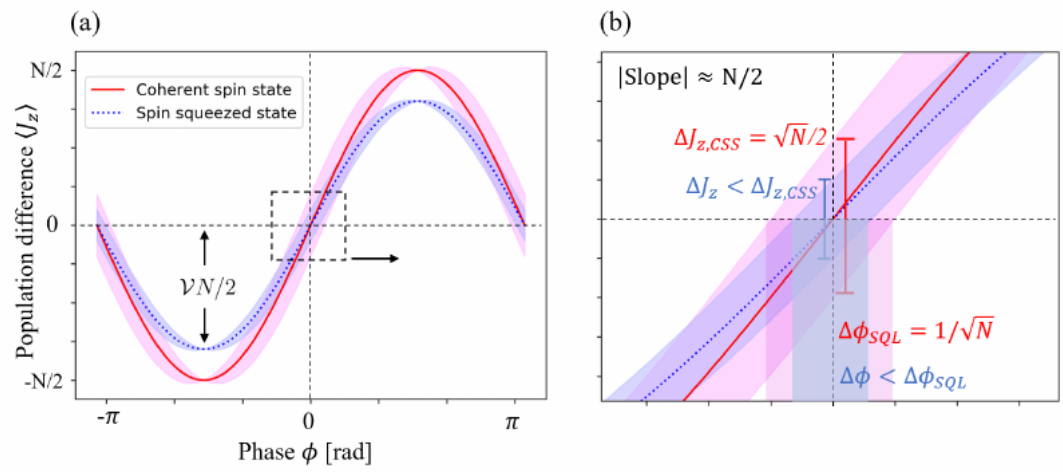

Figure 2.4: Phase sensitivity of Ramsey interferometer. (a) Population difference $J_z = (N_\uparrow - N_\downarrow)/2$ as a function of the accumulated relative phase ϕ for CSSs (red solid line) and SSSs (blue dotted line), respectively. Shaded regions show the uncertainty of phase estimation. The maximum sensitivity is achieved when $J_z = 0$ and at the largest slope of $\simeq N/2$. (b) shows the zoom in of the maximum sensitivity region where the projection noise for CSSs and SSSs are shown by the shaded areas. The CSSs can perform at best at the phase sensitivity of $\phi_{SQL} = 1/\sqrt{N}$, while employing the SSSs, it is possible to surpass the SQL. Figure adapted from [58, 74].

NOON states The NOON state is also called Schrödinger cat state in quantum metrology and the name originates from its form in the Fock states basis,

$$|NOON\rangle = \left(|N, O\rangle + e^{i\phi_N} |O, N\rangle\right)/\sqrt{2} \tag{2.52}$$

It can be seen as a coherent superposition of all atoms in state $|\uparrow\rangle$ and zero atoms in state $|\downarrow\rangle$ and vice versa. The Husimi Q function for the NOON state is written as,

$$Q(\theta, \phi) = \frac{2J+1}{8\pi}\left[\cos^{4J}\left(\frac{\theta}{2}\right) + \sin^{4J}\left(\frac{\theta}{2}\right) + 2\sin^{2J}\left(\frac{\theta}{2}\right)\cos^{2J}\left(\frac{\theta}{2}\right)\cos(2J\phi)\right]. \tag{2.53}$$

A plot of this function is presented in Fig. 2.5 (a) showing that the NOON state can be seen as an equal superposition of two coherent states.

The importance of this state stems from its large sensitivity to atomic phase variations. In spin representation the NOON state is the superposition of the two maximal Dicke states:

$$|NOON\rangle = \left(|J, -J\rangle + e^{i\phi_N} |J, J\rangle\right)/\sqrt{2}, \tag{2.54}$$

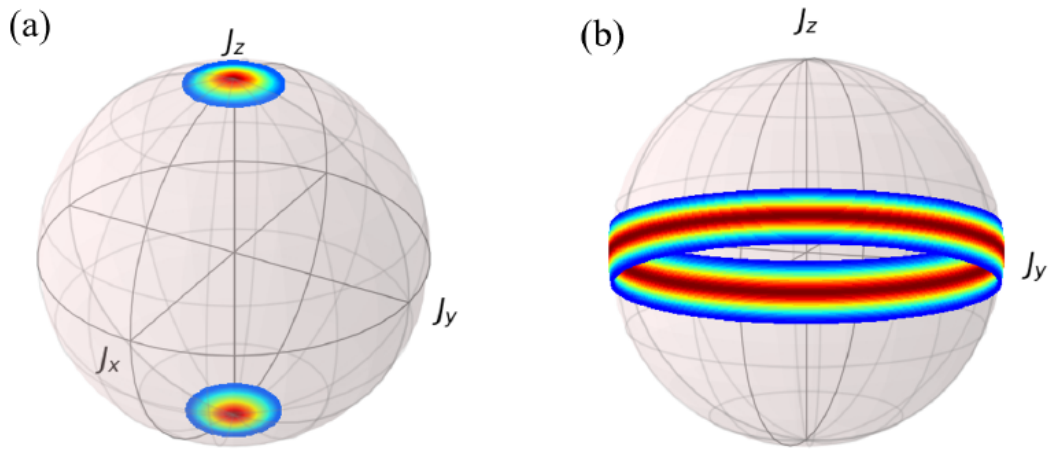

Figure 2.5: Husimi Q representation of NOON state and Dicke state. (a) The NOON state can be viewed as an equal superposition of two coherent spin states. (b) The Dicke state is also known as the twin Fock-state, which is represented by a ring in the Bloch sphere. Figure adapted from [52].

The increase of the signal slope for a NOON state is obvious since the phase acquired between the two components $\phi_N = N\phi$ is N times larger than for a coherent spin state [40, 75, 76]. Experimentally it is important to note that the readout of the interferometer cannot be realized by measuring $\langle \hat{J}_z \rangle$. The reason is the vanishing mean spin length $\langle \hat{J} \rangle$ of this state. It has been shown that the parity of the state is a useful experimental observable to make use of NOON states in interferometry and to reach the Heisenberg limit [77, 78].

Dicke states Another important example is that of the Dicke state $|J, m\rangle$ with Husimi Q function

$$Q(\theta, \phi) = \frac{2J+1}{4\pi} \begin{pmatrix} 2J \\ J+m \end{pmatrix} \cos^{2(J+m)}\left(\frac{\theta}{2}\right) \sin^{2(J-m)}\left(\frac{\theta}{2}\right). \tag{2.55}$$

Because the Dicke state is a state where the population between the two spin states is defined, the Husimi Q function is represented by a ring in the Bloch sphere (Fig. 2.5 (b)). An interferometric phase measurement with such a state would then proceed as follows. After preparation of the state $|J, 0\rangle$, also known as the twin-Fock state [79], a $\pi/2$-pulse rotates the state into a phase-sensitive state and after a precession, another $\pi/2$-pulse is applied as in a standard Ramsey interferometer. The result is a state with increased variance $(\Delta J_z)^2$ which is proportional to $(\Delta\phi)^2$. A measurement of the relative population variance therefore yields the phase measurement. It can be shown that for small $\Delta\phi$ the phase

resolution is [80],

$$\delta\Delta\phi = \frac{\sqrt{2}}{N} \ . \tag{2.56}$$

2.5 Generating spin squeezed states with QND measurements

It has been shown in the last section that SSSs can be used to surpass the SQL in quantum metrology, which is advantageous for quantum sensors for the potential to increase the phase sensitivity. In this section the main approaches for the generation of SSSs are reviewed. The major focus is put on spin squeezing induced by QND measurement, which is the method considered in this thesis. QND measurement can be performed either in free space through atom-light interactions, or with the aid of optical resonators to increase the optical depth. Both methods are analyzed and experimental achievements are reviewed. Finally, other methods to generate SSSs are also briefly introduced.

2.5.1 Quantum non-demolition measurement

The QND measurement is currently one of the most successful methods for producing large amounts of squeezing in atomic ensembles. It is based on the collective measurement of the atomic states, since this kind of measurement does not distinguish each individual atom, it prepares the atomic ensemble in an entangled state. There are some requirements for a quantum measurement to be of non-demolition type:

- (i) weak enough not to collapse the state into a certain J_z eigenvalue,
- (ii) strong enough to resolve J_z better than the SQL,
- (iii) does not resolve each spin.

(i) is important to maintain the phase coherence. If a state collapses to a specific J_z state, the uncertainty in the J_z direction is zero, but the usefulness of this spin state is zero, because the state wraps all around the sphere, and there remains no phase resolution. (ii) sets a technical requirement on how strong the measurement is. A squeezed spin state is generated only when the resolution of the measurement is larger than SQL. (iii) means that we should keep the contrast of the state through the measurement. In a typical situation of measuring the atom state with photons, the scattering of a photon into free space, which is not captured by a photon detector, cannot be avoided. This free space scattering picks a

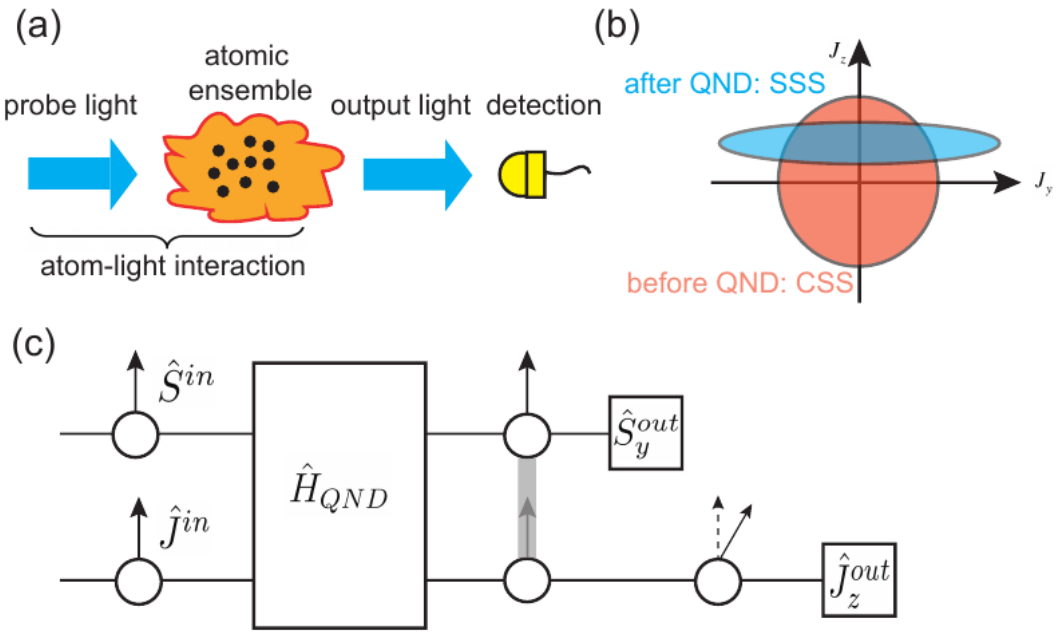

Figure 2.6: Spin squeezing by QND measurement. (a) Atom-light interaction. By detecting the output light one gains the information of the atomic state; (b) the initial CSS changes into SSS after the QND measurement, the orange circle and the blue ellipse show the uncertainty distributions; (c) QND protocol. The QND Hamiltonian $\hat{H}_{QND}$ preserves the atomic state, by resolving the light output state one gains information about the atomic state. The shaded region shows the atom-light entanglement. Figures adapted from [35, 81]

certain spin out of the coherent spin state, and the loss of contrast incorporated in the Wineland parameter occurs.

We first consider a general model for quantum measurement, as shown in Fig. 2.6, where a system (e.g. an atomic ensemble) and a meter (e.g. an probe light) are coupled through the interaction Hamiltonian $\hat{H}_{int}$ and become entangled. A projective measurement on the meter then gives information about the system. Usually this kind of measurement changes the state of the system, however, if we can find an observable $\hat{o}(t)$ which is a constant of motion, i.e.,

$$[\hat{o}(t), \hat{H}_{int}(t)] = 0, \tag{2.57}$$

then the state of the system can be preserved, as the name QND suggests.

A general QND Hamiltonian can be described by considering a far-off resonant dispersive interaction between the collective spin of an atomic ensemble and a two-mode light beam in free space [81, 82],

$$\hat{H}_{QND} = \hbar \mathcal{K} \hat{S}_z \hat{J}_z, \tag{2.58}$$

where $\mathcal{K} \propto (\sigma/A)\Gamma/\Delta$ denotes the coupling strength between the two systems, σ is the resonant photon scattering cross section of the probe transition, Γ is the spontaneous emission rate, A is the spatial cross section of the atomic ensemble illuminated by the probe, and Δ is the detuning of the light from resonance [83]. $\hat{\mathbf{J}} = \left\{\hat{J}_x, \hat{J}_y, \hat{J}_z\right\}$ is the atomic collective spin, $\hat{\mathbf{S}} = \left\{\hat{S}_x, \hat{S}_y, \hat{S}_z\right\}$ is the Stokes vector operator of the light, with components

$$\hat{S}_x = (\hat{a}_+^\dagger \hat{a}_- + \hat{a}_-^\dagger \hat{a}_+)/2 \tag{2.59a}$$

$$\hat{S}_y = (\hat{a}_+^\dagger \hat{a}_- - \hat{a}_-^\dagger \hat{a}_+)/2i \tag{2.59b}$$

$$\hat{S}_z = (\hat{a}_+^\dagger \hat{a}_+ - \hat{a}_-^\dagger \hat{a}_-)/2. \tag{2.59c}$$

The operators $\hat{a}_\pm$ can refer to two polarization modes in which case describes the paramagnetic Faraday rotation of light [84]; or two spatial modes of an optical Mach-Zehnder interferometer where atoms are placed in one arm and phase shift the light [85, 86].

The Hamiltonian satisfies the backaction evasion condition $[\hat{J}_z, \hat{H}_{QND}] = 0$ such that $\hat{J}_z$ is a constant of motion. Using the Heisenberg's equation of motion, we can construct the input-output relations

$$\hat{S}_x^{out} \approx \hat{S}_x^{in} - \mathcal{K}\hat{S}_y^{in}\hat{J}_z^{in}, \quad \hat{J}_x^{out} \approx \hat{J}_x^{in} - \mathcal{K}\hat{J}_y^{in}\hat{S}_z^{in} \tag{2.60a}$$

$$\hat{S}_y^{out} \approx \hat{S}_y^{in} + \mathcal{K}\hat{S}_x^{in}\hat{J}_z^{in}, \quad \hat{J}_y^{out} \approx \hat{J}_y^{in} + \mathcal{K}\hat{J}_y^{in}\hat{S}_z^{in} \tag{2.60b}$$

$$\hat{S}_z^{out} = \hat{S}_z^{in}, \qquad \hat{J}_z^{out} = \hat{J}_z^{in} \tag{2.60c}$$

A measurement of $\hat{S}_x^{out}$ or $\hat{S}_y^{out}$ thus realizes a QND measurement of $\hat{J}_z$ while preserving the system's quantum coherence.

2.5.2 QND measurements in free space

Taking the atomic and light pseudo-spin vectors to be aligned along the x-axis, we consider the fluctuations in the two orthogonal directions. To gain information about the atomic system we measure $\langle \hat{S}_y^{out} \rangle = y_s$, and conditioned on this outcome we get [83],

$$\langle \hat{J}_z^{out} \rangle|_{y_s} = \langle \hat{J}_z^{out} \rangle - \frac{\langle \hat{J}_z^{out} \hat{S}_y^{out} \rangle}{\langle (\hat{S}_y^{out})^2 \rangle} y_s \ , \tag{2.61a}$$

$$\mathrm{var}(\hat{J}_z^{out})|_{y_s} = \mathrm{var}(\hat{J}_z^{out}) - \frac{\langle \hat{J}_z^{out} \hat{S}_y^{out} \rangle^2}{\langle (\hat{S}_y^{out})^2 \rangle}. \tag{2.61b}$$

Here we have taken $\hat{J}_z$ and $\hat{S}_y$ to be Gaussian distributed random variables. This is valid as $\hat{S}_y^{in}$ and $\hat{J}_z^{in}$ are both Gaussian noise processes (shot noise and

projection noise), and that $\hat{H}_{QND}$ is linear. Taking the limit where $\hat{J}_y^{out}$ and $\hat{S}_y^{out}$ are uncorrelated we see that a measurement of $\hat{S}_y^{out}$ does not affect $\hat{J}_y^{out}$. From Eqs. (2.59) and (2.60) we find that [87],

$$\langle(\hat{S}_y^{out})^2\rangle = (1+\kappa^2)\frac{N_{ph}}{4}, \tag{2.62}$$

where $\kappa = \mathcal{K}N_{ph}N_{at}/4$ and N_{ph} and N_{at} are the number of photons and the number of atoms, respectively. Inserting this back to Eq. (2.61) gives,

$$\langle\hat{J}_z^{out}\rangle|_{y_s} = \langle\hat{J}_z^{in}\rangle - \frac{\kappa}{1+\kappa^2}\sqrt{\frac{N_{at}}{N_{ph}}}y_s \ , \tag{2.63a}$$

$$\mathrm{var}(\hat{J}_z^{out})|_{y_s} = \frac{1}{1+\kappa^2}\mathrm{var}(\hat{J}_z^{in}). \tag{2.63b}$$

This equation shows that the noise of $\hat{J}_z$ has been reduced by a factor $(1+\kappa^2)^{-1}$. As we are starting from a CSS which minimizes Heisenberg's uncertainty relation the variance $\mathrm{var}(\hat{J}_z^{out})$ is reduced below the SQL, i.e., the ensemble is in a SSS. The consequence can be visualized in Fig. 2.6 (b), where the noise distribution after the QND measurement is squeezed in one direction.

To quantify the amount of squeezing, we relate the coupling constant $\mathcal{K}$ to the resonant optical depth and use the Wineland criterion and find

$$\xi_R = \frac{1}{\exp(-\eta N_{ph})}\frac{1}{1+\alpha_0\eta N_{ph}/4}, \tag{2.64}$$

where α_0 is the on-resonance optical depth, and η is the number of scattering events per photon, such that $\exp(-\eta N_{ph})$ gives the coherence. From Eq. (2.64) it is clear that it is desirable to have a high optical depth and at the same time a low decoherence η. The photon number enters both in the loss of coherence (the more photons the worse) and in the noise reduction (the more photons the better). Therefore, the used photon number has to be carefully chosen to give enough information while at the same time not destroying the coherence.

The first experimental demonstration of metrological spin squeezing (reaching $\xi_R < 1$) via QND measurements in free space is reported in [42]. This experiment used 1.2×10^5 Cs atoms (with measured $\kappa^2 \simeq 3.2$ and optical depth $\alpha_0 \simeq 16$). Two equally intense and linearly polarized laser beams of different frequencies enter the arms of an optical Mach-Zehnder interferometer, see Fig. 2.7 (a). The beams off resonantly probe different atomic transitions and experience phase shifts proportional to the number of atoms in the probed levels [43]. The detection of the relative phase shift ϕ accumulated in the optical path performs a QND measurement of the relative population in the two atomic levels.

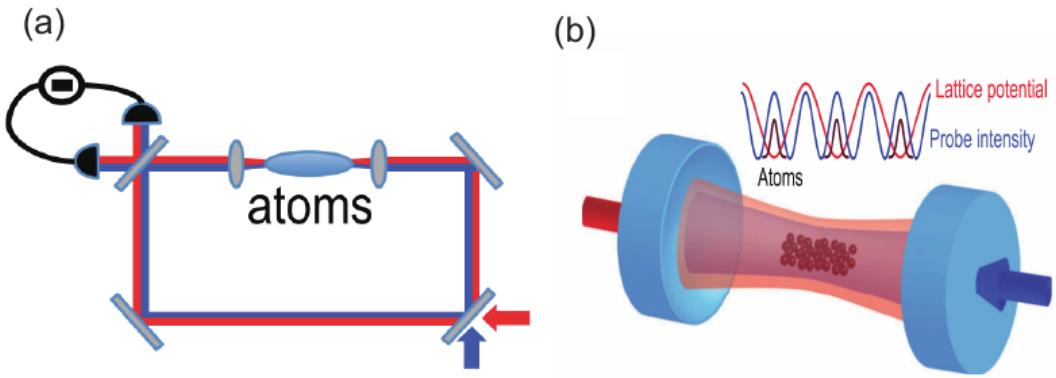

Figure 2.7: QND measurements in free space and with an optical cavity. (a) Free space QND measurement used in [42], the atoms are in one arm of an optical Mach-Zehnder interferometer, two laser beams of different frequency (blue and red arrows) probe the atomic phase shift and performs the QND measurement. (b) Cavity-aided QND measurement used in [45], uniform atom-light coupling is achieved using trapping and probe beams of commensurate frequencies. The cavity resonance is shifted in proportion to the relative population of two clock levels. The shift is measured from the transmission of a probe beam.

Spin squeezing is quantified by correlations between two consecutive QND measurements. One finds

$$\mathrm{Var}(\phi_2 - \zeta\phi_1) = \frac{1}{n} + \frac{\kappa^2}{1+\kappa^2}\frac{N}{4} \tag{2.65}$$

where ϕ_1 and ϕ_2 refer to the first and second phase shift detections, respectively, and the covariance

$$\zeta = \mathrm{Cov}(\phi_1,\ \phi_2)/\mathrm{Var}(\phi_1) = \frac{\kappa^2}{1+\kappa^2} \tag{2.66}$$

expresses the correlations between the two measurements. The results reveal a spin squeezing $\xi_R^2 = -3.4$ dB.

2.5.3 Cavity-aided QND measurements

The strength of the interaction between the light and the atomic ensemble is usually weak, but can be enhanced by placing the atoms inside an optical cavity. This method is very promising as the squeezing factor increases with the cavity finesse, which can be pushed to large values.

The essential features of dispersive atom-light interaction in a cavity are captured by a simplified model comprising N three-level atoms. Each atom has two

hyperfine levels $|a\rangle$ and $|b\rangle$ of energy difference $\hbar\omega$, and an excited state $|e\rangle$ with linewidth Γ (spontaneous decay rate into free space). The atoms are placed in an optical cavity with resonance frequency ω_c and linewidth κ_c, driven resonantly with a single-atom-single-photon effective intracavity Rabi frequency $2g$.

The detuning of the cavity from the $|a\rangle \rightarrow |e\rangle$ and $|b\rangle \rightarrow |e\rangle$ transitions is chosen of equal magnitude $\Delta = \pm\omega/2$. Assuming homogeneous interaction, low intracavity photon number ($n_c = \langle\hat{c}^\dagger\hat{c}\rangle \ll \Delta^2/g^2$), and large detuning ($\Delta \gg \kappa_c, \Gamma, \sqrt{N}g$), the coupling Hamiltonian is

$$\hat{H} = \hbar\omega_c\hat{c}^\dagger\hat{c} + \hbar\frac{2g^2}{\Delta}\hat{c}^\dagger\hat{c}\hat{J}_z + \hbar\omega\hat{J}_z, \tag{2.67}$$

where $\hat{c}$ and $\hat{c}^\dagger$ are cavity photon annihilation and creation operators..

The effect of the light on the atoms is an ac Stark shift of the transition frequency $\delta\omega = (2g^2/\Delta)n_c$ between $|a\rangle$ and $|b\rangle$. Atoms in $|a\rangle$ ($|b\rangle$) increase (decrease) the index of refraction seen by the probe light, so that the net effect is a shift of the cavity resonance by

$$\delta\omega_c = \frac{2g^2}{\Delta}\frac{N_a - N_b}{2} = \frac{2g^2}{\Delta}J_z, \tag{2.68}$$

where N_a and N_b are the numbers of the atoms in $|a\rangle$ and $|b\rangle$, respectively. This shift can be probed by injecting a laser into the cavity, providing a QND measurement of $\hat{J}_z$. The possible gain considering the decoherence associated with free-space scattering of the probe light is

$$\xi_R^2 = \frac{1 + NC(\Gamma/\omega)^2}{\sqrt{NC}}, \tag{2.69}$$

where $C = (2g)^2/(\kappa_c\Gamma)$ is the single-atom cavity cooperativity. C is the ratio between the number of photons scattered into the cavity mode and those scattered into free space and quantifies the optical depth of an atom with respect to the cavity mode [41]. Note that C depends on the cavity geometry and is proportional to the cavity finesse.

Spin squeezing via a cavity-based QND measurement was first demonstrated by [44] using magnetically insensitive clock states of ^{87}Rb atoms. This experiment reported a spin squeezing $\xi_R^2 = -1.45$ dB with respect to the standard quantum limit $(\Delta\theta_{SQL})^2 = 1/N_{eff}$, referring to $N_{eff} \simeq 0.66N$ uncorrelated atoms (N_{eff} accounts for spatial variation in the atom-light coupling due to the trapping lattice being incommensurate with the cavity mode used for probing, and $N = 5 \times 10^4$). This result is mainly limited by inhomogeneous dephasing due to the cavity locking light.

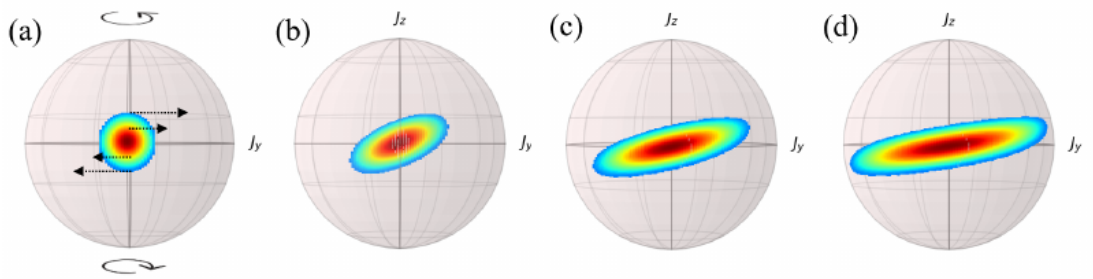

Figure 2.8: Spin squeezing with one-axis twisting Hamiltonian. (a) The OAT Hamiltonian twist the Bloch sphere around the z-axis, causing the noise distribution to shear. (b)-(d) are the Q representation of the spin squeezed states with different interaction strength. Figure adapted from [52].

[45] used a cavity of higher cooperativity and exploited probing and trapping beams of commensurate frequencies, achieving a uniform atom-light coupling; see Fig. 2.7 (b). This avoids the need for spin-echo techniques required for nonuniformly coupled systems. This experiment demonstrated 10.5 dB of improved phase sensitivity with respect to $(\Delta\theta_{SQL})^2 = 1/N$, with $N = 5 \times 10^5$ ^{87}Rb atoms, and a spin squeezing $\xi_R^2 = -18.5$ dB (-20.1 dB inferred). This represents the highest value in expected metrological spin squeezing and measured phase sensitivity gain to date.

2.5.4 Other methods to generate SSSs

Spin squeezing based on QND measurement is one of the most successful methods to using squeezing in quantum metrology. There are, however, other important approaches to generate metrological useful states. One important category is based on non-linear Hamiltonians, both through atomic collision in Bose-Einstein condensation (BEC) and through light-mediated interactions. In this subsection, those approaches are introduced and the main experimental achievements are presented.

Collisional interactions in BEC Kitagawa and Ueda proposed a method to generate spin squeezing with a non-linear Hamiltonian, also referred to as the one-axis twisting (OAT) Hamiltonian, written as

$$\hat{H}_{OAT} = \hbar\chi \hat{J}_z^2. \tag{2.70}$$

The OAT Hamiltonian can be realized in BEC through atom-atom collisional interactions.

To explain how squeezing is generated, consider the evolution of a CSS along $\hat{x}$ under this Hamiltonian. The Dicke states [59] $|J, m\rangle$ are eigenstates of the OAT Hamiltonian with eigenvalue χm^2, and evolves phase in time as $e^{-i\chi m^2 t}$. This implies the precession frequency of the state $|J, m\rangle$ scales linearly with m as $2\chi m$ in a rotating frame whose frequency is proportional to m. As the CSS is a (weighted) superposition of the Dicke states, the noise components of the CSS with larger m would precess faster than those with smaller m. Also, noise components with positive m would precess in the opposite sense compared to noise components with negative m. This process is depicted pictorially in Fig. 2.8 with the resulting noise distribution sheared such that noise in one direction is lower than the CSS projection noise. The shearing process can be viewed as arising from twisting the Bloch sphere about the z-axis, hence the name one-axis twisting. A small rotation can be performed to rotate the squeezed quadrature to lie along $\hat{y}$ or along $\hat{z}$.

Recent experiments employing this collision-induced OAT has produced $\xi_R^2 \sim -4$ to -8 dB of inferred squeezing after background subtraction in ensemble sizes of $N \sim 400$ to 2000 atoms [88, 89, 90]. It is in fact, not necessary to utilize BECs and anti-squeezing has been observed in the non-degenerate ^{87}Sr fermion optical lattice clock at JILA [91].

Cavity mediated interactions In contrast to the measurement-based scheme, off-resonant atom-light coupling can also be used to realize a light-mediated coherent interaction between distant atoms. When the light Stokes operator $\hat{S}_z$ is proportional to the atomic $\hat{J}_z$, the Hamiltonian $\hat{H} \propto \hat{S}_z \hat{J}_z$ describing atom light interaction (Eq. (2.58)) becomes $\hat{H} \propto \hat{J}_z^2$ [92, 93], corresponding to an effective one-axis twisting nonlinearity that generates unconditional spin squeezing [38]. In contrast to spin squeezing obtained from QND measurements, it deterministically produces known entangled states, independently from the detector performance. Furthermore, atom-cavity coupling can be easily switched on and off.

One-axis twisting by light-mediated interactions has been experimentally implemented in an optical cavity [94, 95], using an effective number $N_{eff} = 3 \times 10^4$ of ^{87}Rb atoms. The squeezed state is characterized via spin noise tomography and the contrast of Rabi oscillations. The results of [94] demonstrate a gain $\xi_R^2 = -4.6$ dB over $(\Delta\theta_{SQL})^2 = 1/N_{eff}$ ($\xi_{eff}^2 = -5.6$ dB over the sensitivity experimentally reached in the absence of entanglement). [95] used the squeezed states generated with this method to realize an atomic clock with short-time fractional frequency stability a factor 2.8 (corresponding to 4.5 dB) in variance below the SQL.

Recently, [47] reports near-unitary spin squeezing in ^{171}Yb with light mediated

OAT Hamiltonian in an asymmetric cavity [96]. The squeezing is induced between the two nuclear sublevels $|m = \pm 1/2\rangle$ of the electronic ground state $^1S_0$ of ^{171}Yb and is later transferred to the $^3P_0$ excited clock state, which demonstrates the first entanglement-enhanced optical atomic clock [48]. A metrological gain of $\xi_R^2 = -4.4^{+0.6}_{-0.4}$ dB over the SQL using a few hundreds ^{171}Yb atoms allows to reach a given stability 2.8 ± 0.3 times faster than the same clock operated at the SQL.

Interactions with squeezed light Spin-squeezed states can be also created by transferring quadrature squeezing of light to atomic spin squeezing [97, 83]. This effect can be understood from the Jaynes-Cummings model Hamiltonian

$$\hat{H}_{JC} = \hbar\Omega(\hat{c}\hat{J}_+ + \hat{c}^\dagger \hat{J}_-), \tag{2.71}$$

describing the interaction of non-decaying two-level atoms with a light mode.

Quantum state transfer from light to atoms was first experimentally demonstrated by [98] using an ensemble of 10^7 cold Cs atoms, following the theoretical proposal of [97]. This experiment used a V-level scheme consisting of three atomic hyperfine levels [98, 99]. The reduction of atomic spin noise below the projection noise of uncorrelated atoms is generated by the absorption of polarized coherent and squeezed vacuum light with opposite circular polarizations.

2.6 Conclusions

In this chapter, the theoretical background for quantum metrology with spin squeezed states is discussed. Any quantum interferometric measurement using an atomic ensemble is enclosed into the estimation of the accumulated phase of the atoms during the interrogation. The resolution of this phase is limited by the SQL for N uncorrelated atoms. This limit can be surpassed by introducing correlation or entanglement between the atoms, thus generating spin squeezed states.

Various methods for the generation of SSSs are reviewed and the main experimental achievements are cited. QND measurement in an optical cavity is one of the most successful methods for generating highly spin-squeezed states because of the large available optical depth and the non-destructibility. This method is considered in this thesis. The main purpose of this thesis is the construction and characterization of an optical ring cavity for QND measurement in order to generate spin squeezing in the momentum states of a Sr atom interferometer.

Chapter 3

Squeezing on momentum states in Sr atom interferometry

As described in chapter 2, spin squeezing can be used to surpass the SQL in quantum precision measurements. The aim of this thesis is to generate spin squeezing on the momentum states of a Sr atom interferometer. In this chapter, the basic properties of Sr and the two-stage cooling of Sr atoms in a magneto-optical trap (MOT) are introduced. Then the principle of atom interferometry is discussed. Different types of atom interferometers are presented and their respective phase shifts are calculated. Finally, the proposal for squeezing on the momentum states of Sr atom interferometer is reviewed and the potential squeezing and metrological gain are estimated.

3.1 Ultra-cold Sr atoms for precision measurement

3.1.1 Basic properties of Sr atoms

Strontium is an alkaline-earth atom with atomic number $Z = 38$. There are four stable isotopes of Sr in nature, among them three are bosons with zero nuclear spin while the only fermion ^{87}Sr has a nuclear spin $I = 9/2$. The nuclear spin and scattering properties of all four isotopes are summarized in Table. 3.1.

The bosonic ^{88}Sr isotope has the largest natural abundance. Due to the absence of orbital and spin angular momentum in electrons and the zero nuclear spin, the ground state of ^{88}Sr is a pure scalar state with zero magnetic moment. This property of ^{88}Sr makes its ground state extremely insensitive to spurious magnetic fields, which is advantageous in high-precision measurements since no

Table 3.1: Four stable isotopes of strontium and their properties on abundance [102], atomic mass [103], nuclear spin and scattering length [104, 105].

Isotope	Abundance (%)	Atomic mass (M)	Nuclear spin (I)	Scattering length (a_0)
^{88}Sr	82.58(1)	87.905612257(10)	0	−2.00(27)
^{87}Sr	7.00(1)	86.908877497(9)	9/2	97.37(7)
^{86}Sr	9.86(1)	85.909260731(9)	0	798(12)
^{84}Sr	0.56(1)	83.913425(3)	0	122.76(9)

magnetic shield is needed. The ^{88}Sr isotope has another special property of a small s-wave scattering length. This leads to weak cold collisions which maintains the long coherence time of atoms in an optical lattice [24, 100]. The drawback of this small scattering length is that evaporative cooling of ^{88}Sr is nearly impossible and the BEC of ^{88}Sr can be achieved only with sympathetic cooling [101].

Electronic properties Strontium, as well as all the alkaline-earth (like) atoms such as Be, Mg, Ca, Ba, Ra, Zn, Cd, Hg and Yb, has two valence electrons in the outer shell. Due to the different orientation of the two electron spins there are two series of levels: singlet states for anti-parallel spins and triplet states for parallel spins. The low level diagram of Sr is shown in Fig. 3.1, where each energy level is presented with Russell-Saunders notation [106] $^{2S+1}\mathrm{L}_J$, where S is the total spin of the two electrons (either 0 or 1), L is the orbital angular momentum of the electrons, and J is the total angular momentum of the state. The interesting transitions for cooling and trapping of Sr atoms, as well as that used in spin squeezing, are presented in Fig. 3.1. We describe in detail some of the transitions used in this work.

- Dipole transition $^1\mathrm{S}_0$-$^1\mathrm{P}_1$, corresponding to the laser wavelength of 461 nm, with a natural linewidth of 32 MHz. It is used for the first stage MOT laser cooling because it has a wide linewidth of 32 MHz. The strong, blue transition is also useful for Zeeman slowing since the fast scattering rate and relatively large per photon momentum give large deceleration.

- Intercombination transitions $^1\mathrm{S}_0$-$^3\mathrm{P}_J$. In the case of pure LS coupling, the three 5s5p^{3}P states are forbidden to decay to the ground state, so they are meta-stable. However the spin-orbit interaction provides a finite lifetime for the $^3\mathrm{P}_1$ state.

  $^1\mathrm{S}_0$-$^3\mathrm{P}_1$, corresponding to the laser wavelength of 689 nm, with a natural linewidth of 7.5 kHz. This narrow intercombination transition can be used

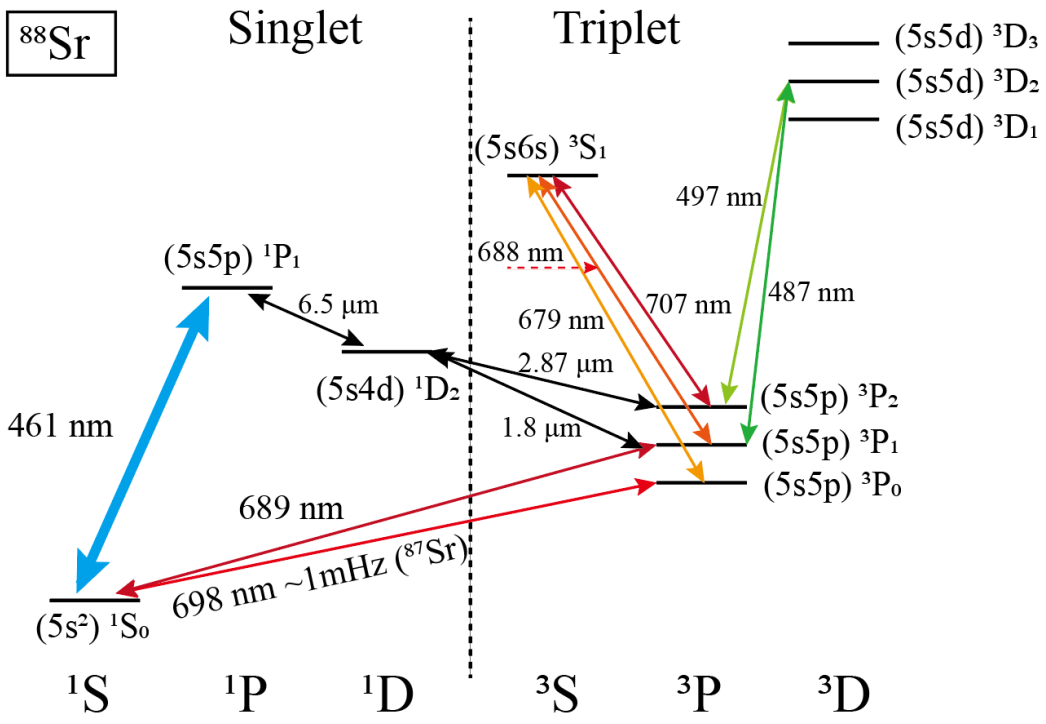

Figure 3.1: Strontium low-level diagram and transitions of interest for cooling, trapping and spin squeezing. The states are represented in the Russell-Sunders notation $^{2S+1}\mathrm{L}_J$ and are divided between singlet ($S = 0$) and triplet ($S = 1$) states. We indicate the valence electron configuration for each level and the wavelength corresponding to each transition.

for efficient and simple Doppler optical cooling down to the recoil temperature. This transition can also be used for high-efficiency multiphoton Bragg interactions. More details about atom interferometry using the intercombination transition with Sr atoms can be found in [27].

$^1\mathrm{S}_0$-$^3\mathrm{P}_0$ transition, also called the *clock transition*, corresponding to the laser wavelength of 698 nm. The ultranarrow $^1\mathrm{S}_0$-$^3\mathrm{P}_0$ transition is only present in the isotope with nuclear spin (^{87}Sr), and in the bosonic isotope it can be induced by a static magnetic field through mixing the $^3\mathrm{P}_0$ and $^3\mathrm{P}_1$ states [107].

- Repump transitions. During optical cooling of strontium on the broad $^1\mathrm{S}_0$-$^1\mathrm{P}_1$ transition, a small fraction of the atoms decay to the metastable $^3\mathrm{P}_2$ state through the $^1\mathrm{D}_2$ state thus reduce the lifetime of the cooled and trapped atoms. As a result, it is often necessary to repump the

atoms to the ground $^1S_0$ state. This can be achieved in a number of ways [108, 109, 110, 111].

One possibility is to repump the atoms from the $^3P_2$ state to the $^3P_1$ state through the 707 nm transition that connects to the excited state $5s6s\,^3S_1$ [112]. From the $^3P_1$ state the atoms decay back to the ground state. A fraction of the atoms excited to the $^3S_1$ state, however decays to the $^3P_0$ state and a second laser is then added, at 679 nm, resonant with the $^3P_0$-$^3S_1$ transition. From the $^3S_1$ state, the atoms decay back to $^3P_1$ state through the 688 nm transition.

Another option is repumping through the $5s5d\,^3D_2$ state with the 497 nm transition. Here a single laser is sufficient and the atoms are pumped to the $^3P_1$ state by decay on the 487 nm transition. All these transitions are dipole-allowed with a linewidth of a few MHz.

3.1.2 Two-stage MOT of Sr atoms

In order to perform atom interferometry experiments with strontium atoms, it is necessary to reduce the atomic kinetic energy to temperatures on the order of 1 μK, while working with reasonably large atom numbers. This result is achieved in a magneto-optical trap, through two successive cooling stages, operating on the broad $^1S_0$-$^1P_1$ transition and on the narrow $^1S_0$-$^3P_1$ transition. The goal of the first stage, the so-called blue MOT, is to collect a large number of atoms with a relatively large temperature. In the second stage, the red MOT, atoms from the blue MOT are further cooled and large densities are reached owing to the narrow linewidth of the red $^1S_0$-$^3P_1$ transition. A more detailed discussion about the laser cooling techniques of Sr can be found in [113, 28], here only a brief introduction is given.

First stage cooling and the blue MOT The first stage of laser cooling is performed on the broad $^1S_0$-$^1P_1$ transition, which is shown in Fig. 3.1. After exiting the oven, the atoms are slowed in a Zeeman slower with an optical power of 30 mW, a polarization of σ_+, and a detuning of approximately -317 MHz below the $^1S_0$-$^1P_1$ transition. Then, upon reaching the science chamber the atoms are collected in a MOT operating on the $^1S_0$-$^1P_1$ transition. Each MOT beam operates close to $s \simeq 1$ where $s = I/I_s$ (I is the laser intensity) indicates the saturation factor. The field gradient utilized for the $^1S_0$-$^1P_1$ MOT is $\simeq 50$ G/cm in the horizontal direction. The $^1S_0$-$^1P_1$ transition has a decay pathway to the metastable $^3P_2$ state, in order to maintain efficient MOT operation, the atoms in the $^3P_2$ state must be repumped by a separate repump laser. Two repump

schemes can be used, as already discussed before. The repumpers make a huge difference with a factor of $\simeq 20$ improvement in the observed fluorescence. Ultimately, the first-stage 461 nm MOT accumulates $\simeq 2 \times 10^7$ atoms in 2 s.

Second stage cooling and the red MOT In order to enable efficient transfer from the blue MOT into the red MOT, two distinct MOT phases of the red MOT are adopted. In the first phase, the red laser is modulated with a few MHz modulation depth. The modulation is chosen to provide good overlap with the Doppler profile of the atoms after being pre-cooled in the blue MOT, with a final temperature of a few mK. In the initial broadband phase of the red MOT, the magnetic field gradient is extinguished from the 50 G/cm employed in the blue MOT. Subsequently, the field is slowly ramped up to 0.6 G/cm in 200 ms for maintaining an adiabatic condition on the deceleration. The ramp compressed the MOT in all three spatial dimensions. When the field gradient reaches 0.6 G/cm, the broadband frequency modulation is switched off, and the laser is tuned closer to the atomic resonance. Then steeping into the final phase of the MOT cooling: the single frequency red MOT. After the broadband stage, the resonance is broadened by sending all the laser power to the atoms. Then the power is slowly decreased and the detuning is ramped down to approach the resonance. The transfer efficiency from the blue MOT is approximately 30%, resulting in a sample of atoms with μK temperatures.

3.2 Working principle of atom interferometry

This section describes the working principle of atom interferometry. We start with the general model of atom-light interaction where the atom is considered as a two-level system, the phenomenon of Rabi oscillation due to atomic excitation is discussed. Then the principle of a general Mach-Zehnder atom interferometer is analyzed and the phase determination is derived. Based on different transition schemes atom interferometers can be categorized into single-photon interferometer, two-photon Raman interferometer and multi-photon Bragg interferometer. The differences between those schemes are addressed and the corresponding phase shifts are calculated. For more information about atom interferometers, one may refer to [1, 114, 115, 116, 117].

3.2.1 Atom-light interaction and Rabi oscillations

We consider the simplest model of the interaction between a two-level atom and the electromagnetic field, as shown in Fig. 3.2 (a). Here the semi-classical treat-

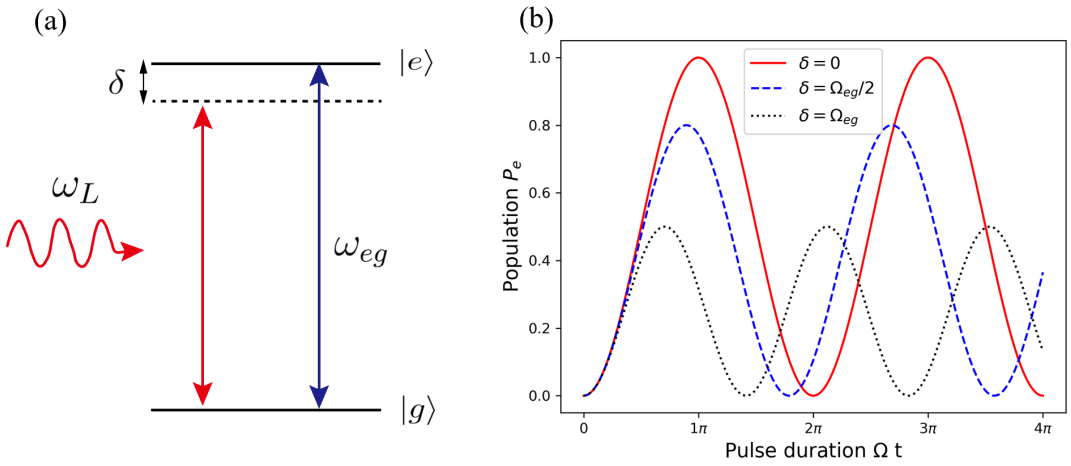

Figure 3.2: Atom-light interaction and Rabi oscillation. (a) Atom-light interaction. The atom is modeled as a two-level system with the ground and excited states ($|g\rangle$ and $|e\rangle$), respectively. A laser beam with a detuning δ to the atomic transition ω_{eg} interact with the atom and excite the atom between the two states. (b) Rabi oscillations with different detunings. Excited state population P_e as a function of the laser pulse duration Ωt for different laser detunings ($\delta = 0$, $\delta = \Omega_{eg}/2$ and $\delta = \Omega_{eg}$).

ment is used where the atom is quantized while the electromagnetic field is classical. The atom is modeled as a two-level system with the ground state $|g\rangle$ and excited state $|e\rangle$, the atomic wave function can be written as a superposition of the two eigenstates $|g\rangle$ and $|e\rangle$ as,

$$|\Psi(t)\rangle = c_g(t)e^{-i\omega_g t}|g\rangle + c_e(t)e^{-i\omega_e t}|e\rangle\,, \tag{3.1}$$

where ω_g, ω_e are the fast oscillating frequencies and $c_g(t)$, $c_e(t)$ are the slowly varying factors of the ground and excited states, respectively.

The electromagnetic field has a frequency ω_L, the detuning of the laser frequency ω_L to the atomic resonance frequency $\omega_{eg} = \omega_e - \omega_g$ is defined as $\delta = \omega_L - \omega_{eg}$, when the condition $\delta \ll \omega_{eg}$ is satisfied, the rotating wave approximation can be introduced and the light field can be expressed in the form:

$$E(t) = E_0\cos(k_L \cdot r - \omega_L t_0 + \phi_{L,0}) = \frac{E_0}{2}(e^{i(\phi_L - \omega_L t)} + e^{-i(\phi_L - \omega_L t)}), \tag{3.2}$$

where

$$\phi_L = k_L \cdot r - \omega_L t_0 + \phi_{L,0} \tag{3.3}$$

is the effective phase of the laser fields at the position r with a laser frequency of ω_L. t_0 is the initial time of the atom-light interaction.

The time-dependent Schrödinger equation for the atomic wave function $|\Psi(t)\rangle$ is

$$\hat{H}\,|\Psi(t)\rangle = i\hbar\frac{\partial\,|\Psi(t)\rangle}{\partial t}. \tag{3.4}$$

Considering the electric dipole interactions, the time-dependent Hamiltonian is composed of two parts,

$$\hat{H} = \hat{H}_a + \hat{H}_{int}, \tag{3.5}$$

where $\hat{H}_a = \hbar\omega_g\,|g\rangle\,\langle g| + \hbar\omega_e\,|e\rangle\,\langle e|$ describes the atomic internal energy, $\hat{H}_{int} = -\boldsymbol{d}\cdot\boldsymbol{E}(t)$ describes the interaction matrix element between the electronic dipole moment $\boldsymbol{d}$ for the atom and the electric field $\boldsymbol{E}(t)$. Here we define the on-resonance Rabi frequency Ω_{eg} and the general Rabi frequency Ω_R with a detuning δ ($\delta = \omega_L - \omega_{eg}$) as,

$$\Omega_{ge} = -\frac{\langle g|\,\boldsymbol{d}\cdot\boldsymbol{E}_0\,|e\rangle}{\hbar} = -\frac{\langle e|\,\boldsymbol{d}\cdot\boldsymbol{E}_0\,|g\rangle^*}{\hbar} = {\Omega_{eg}}^*, \tag{3.6}$$

$$\Omega_R = \sqrt{\Omega_{eg}^2 + \delta^2}. \tag{3.7}$$

By introducing the Hamiltonians (Eq. (3.5)) into the Schrödinger equation, one gets,

$$i\hbar\frac{dc_g(t)}{dt} = \frac{1}{2}c_e(t)\hbar\Omega_{eg}\left[e^{i(\phi_L-\omega_L t)} + e^{-i(\phi_L-\omega_L t)}\right]e^{-i\omega_{eg}t}, \tag{3.8a}$$

$$i\hbar\frac{dc_e(t)}{dt} = \frac{1}{2}c_g(t)\hbar\Omega_{eg}^*\left[e^{i(\phi_L-\omega_L t)} + e^{-i(\phi_L-\omega_L t)}\right]e^{i\omega_{eg}t}. \tag{3.8b}$$

The equations can be simplified by making the rotating wave approximation and neglecting the rapidly oscillating terms at frequency $\omega_L + \omega_{eg}$ as,

$$\frac{dc_g(t)}{dt} = -i\frac{\Omega_{eg}}{2}c_e(t)e^{i(\delta t-\phi_L)}, \tag{3.9a}$$

$$\frac{dc_e(t)}{dt} = -i\frac{\Omega_{eg}^*}{2}c_g(t)e^{i(\delta t-\phi_L)}. \tag{3.9b}$$

A solution to Eq. (3.9) after an interaction time τ is

$$\begin{aligned} c_g(t_0+\tau) = e^{i\frac{\delta\tau}{2}}\Bigg\{&\left[\cos\left(\frac{\Omega_R\tau}{2}\right) + i\cos\beta\sin\left(\frac{\Omega_R\tau}{2}\right)\right]c_g(t_0)\\ &+e^{i(\delta t_0-\phi_L)}\left[-i\sin\beta\sin\left(\frac{\Omega_R\tau}{2}\right)\right]c_e(t_0)\Bigg\}\end{aligned} \tag{3.10}$$

$$\begin{aligned} c_e(t_0+\tau) = e^{-i\frac{\delta\tau}{2}}\Bigg\{&e^{-i(\delta t_0-\phi_L)}\left[-i\sin\beta\sin\left(\frac{\Omega_R\tau}{2}\right)\right]c_g(t_0)\\ &+\left[\cos\left(\frac{\Omega_R\tau}{2}\right) - i\cos\beta\sin\left(\frac{\Omega_R\tau}{2}\right)\right]c_e(t_0)\Bigg\}\end{aligned} \tag{3.11}$$

or in the matrix form:

$$\begin{bmatrix} c_g(t_0+\tau) \\ c_e(t_0+\tau) \end{bmatrix} = \begin{bmatrix} e^{i\delta\tau/2} & 0 \\ 0 & e^{-i\delta\tau/2} \end{bmatrix} \cdot \begin{bmatrix} \cos\left(\frac{\Omega_R\tau}{2}\right) + i\cos\beta\sin\left(\frac{\Omega_R\tau}{2}\right) & -ie^{i(\delta t-\phi_L)}\sin\beta\sin\left(\frac{\Omega_R\tau}{2}\right) \\ -ie^{-i(\delta t-\phi_L)}\sin\beta\sin\left(\frac{\Omega_R\tau}{2}\right) & \cos\left(\frac{\Omega_R\tau}{2}\right) - i\cos\beta\sin\left(\frac{\Omega_R\tau}{2}\right) \end{bmatrix} \begin{bmatrix} c_g(t_0) \\ c_e(t_0) \end{bmatrix} \tag{3.12}$$

In those equations $\sin\beta = \frac{\Omega_{eg}}{\Omega_R}$, $\cos\beta = -\frac{\delta}{\Omega_R}$ $(0 \leq \beta \leq \pi)$. Suppose that the initial state of the atom is the ground state, i.e. $c_g(t_0) = 1$, $c_e(t_0) = 0$, then,

$$c_g(t) = \left[\cos\left(\frac{\Omega_R\tau}{2}\right) - i\frac{\delta}{\Omega_R}\sin\left(\frac{\Omega_R\tau}{2}\right)\right] e^{\delta\tau/2}, \tag{3.13a}$$

$$c_e(t) = -i\frac{\Omega_{eg}}{\Omega_R}\sin\left(\frac{\Omega_R}{2}\right) e^{-i(\delta\tau/2-\phi_L)}. \tag{3.13b}$$

Therefore, the probability to find the atom in the excited state is

$$P_e(\tau) = |c_e(\tau)|^2 = \left(\frac{\Omega_{eg}}{\Omega_R}\right)^2 \frac{1-\cos(\Omega_R\tau)}{2}. \tag{3.14}$$

Figure 3.2 (b) shows examples of Rabi oscillations for different detunings $\delta = 0$, $\delta = 0.5\ \Omega_{eg}$ and $\delta = \Omega_{eg}$, respectively. One can see that by increasing the detuning, the contrast of the flopping is decreased and the Rabi frequency is increased. There are two especially interesting times τ in terms of Eq. (3.14). Firstly, if $\Omega_R\tau = \pi/2$, the population is evenly distributed between $|g\rangle$ and $|e\rangle$, the light pulse corresponding to this time duration can therefore be used as a beamsplitter and is called $\pi/2$ pulse. The second interesting event occurs when $\Omega_R\tau = \pi$, where the population between two states is fully swapped. This can be used as a mirror pulse and is referred as π pulse, as population is reflected from one state to the other.

The discussion described above only focuses on the internal state. However, the internal and external degrees of freedom are coupled. The absorption and emission of a photon is correlated with a momentum change. If also the center-of-mass motion is included in the description, then there are two eigenstates $|g, p_0\rangle$ and $|e, p_0 + \hbar k\rangle$, corresponding to a ground state $|g\rangle$ with momentum of p_0 and an excited state $|e\rangle$ with an additional momentum $\hbar k$. The wave function can be described by

$$|\Psi(t)\rangle = c_g(t)e^{-i[\omega_g + p^2/(2m\hbar)]t}\,|g, p_0\rangle + c_e(t)e^{-i[\omega_e + (p+\hbar k)^2/(2m\hbar)]t}\,|e, p_0 + \hbar k\rangle\,. \tag{3.15}$$

The eigenenergies of the system become

$$E_{|g,p_0\rangle} = \hbar\omega_g + \frac{p_0^2}{2m}, \tag{3.16a}$$

$$E_{|e,p_0+\hbar k\rangle} = \hbar\omega_e + \frac{(p_0+\hbar k)^2}{2m}. \tag{3.16b}$$

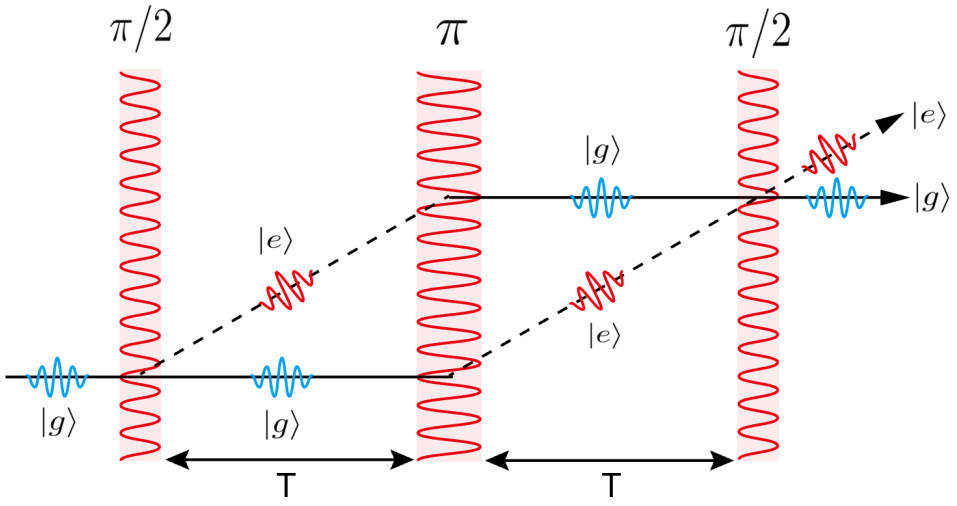

Figure 3.3: Mach-Zehnder type atom interferometer. A series of $\pi/2$, π and $\pi/2$ pulses are used to split, redirect and recombine the atomic wave packet. After the first $\pi/2$ pulse, the initial ground state $|g\rangle$ is prepared into a superposition state of $|g\rangle$ and $|e\rangle$ with equal population. The momentum state is also split therefore a π pulse is needed to redirect the two trajectories. Finally another $\pi/2$ pulse is applied to combine the two wave packets and produce interference.

A typical type of Mach-Zehnder atom interferometer is shown in Fig. 3.3. A series of $\pi/2$-π-$\pi/2$ pulses are used to split, redirect and recombine the atomic wave packet. After the first $\pi/2$ pulse, the initial ground state $|g\rangle$ is prepared into a superposition state of $|g\rangle$ and $|e\rangle$ with equal population. The momentum state is also split therefore a π pulse is needed to redirect the two atomic trajectories. Finally another $\pi/2$ pulse is applied to combine the two wave packets and interference occurs. The atoms through two different paths accumulate different phases, in the final state detection, the population of $|g\rangle$ and $|e\rangle$ depends on this accumulated phase. One can tune the laser phase of the second $\pi/2$ pulse in order to add a phase shift to the interferometer and scan the interference fringe.

3.2.2 Phase shift determination

Considering the atom center-of-mass motion during the interferometer, one can rewrite the system Hamiltonian Eq. (3.5) as [118, 119],

$$\hat{H}_{tot} = \hat{H}_a + \hat{H}_{int} + \hat{H}_{ext}, \tag{3.17}$$

where $\hat{H}_{ext} = \frac{p^2}{2m} + V_r$ is the Hamiltonian of the atomic external degrees of freedom.

According to Eq. (3.17), the total phase shift accumulated by an interferometer can be divided into three main contributions. Firstly, the differential laser phase $\Delta\phi_{int}$ is due to the interactions between lasers and atoms. Another source is the differential free evolution since the two arms follow their independent trajectories under the influence of a variety of forces, giving rise to the propagation phase $\Delta\phi_{prop}$. The third source is due to the imperfect overlap of the trajectories of the two arms at the final beamsplitter pulse $\Delta\phi_{sep}$. Therefore, the total interferometer shift is given by

$$\Delta\Phi = \Delta\phi_{int} + \Delta\phi_{prop} + \Delta\phi_{sep}. \tag{3.18}$$

The first term is the largest one and the main reason for high sensitivity and accuracy in atom interferometry. It originates from the interaction of the atomic wave packet with the interrogating light field and is the sum of the imprinted laser phases $\pm\phi(t_i)$ defined in Eq. (3.3) at each time t_i and position r at the beginning of each optical pulse. The sign of the phase at each pulse depends on whether the atom gains or loses momentum

$$\Delta\phi_{int} = \sum_u \pm\phi(t_i) - \sum_l \pm\phi(t_i), \tag{3.19}$$

where u and l represent the upper and lower arm, respectively. In a typical Mach-Zehnder configuration as analyzed in the last section, the phase shift is

$$\Delta\phi_{int} = \phi_1(t_1) - 2\phi_2(t_2) + \phi_3(t_3). \tag{3.20}$$

According to Eq. (3.3), suppose the initial time $t_0 = 0$, the separation time is T, then the laser phase for each pulse is

$$\phi_i(t_i) = k_L \cdot r(t_i) + \phi_i, \tag{3.21}$$

where $r(t_i) = v_0 t_i + g t_i^2/2$ follows the classical trajectory in the uniform gravitational potential with gravity acceleration g, ϕ_i is the phase reference of the ith pulse. Then the interaction phase can be simplified to

$$\Delta\phi_{int} = kgT^2 + (\phi_1 - 2\phi_2 + \phi_3). \tag{3.22}$$

The second contribution, the propagation phase, is given by taking the difference of the Lagrangian $\mathcal{L}$ integrated over the two interferometer arms along the trajectory with inclusion of the phase evolution due to the internal state energy E,

$$\Delta\phi_{prop} = \frac{1}{\hbar}\sum_u \int_{t_i}^{t_f} (\mathcal{L} - E)dt - \frac{1}{\hbar}\sum_l \int_{t_i}^{t_f} (\mathcal{L} - E)dt, \tag{3.23}$$

The last phase shift term is due to imperfect overlapping in position and velocity in a single output port from the two interferometer arms. This term includes any such mismatch and depends on the position difference between two arms at the final beamsplitter pulse, $\Delta \boldsymbol{x} = \boldsymbol{x}_u - \boldsymbol{x}_l$. The momentum in one of the two output ports of the final interferometer, averaged between the two arms, is $\bar{\boldsymbol{p}} = ([\nabla_{\dot{\boldsymbol{x}}} \mathcal{L}]_u + [\nabla_{\dot{\boldsymbol{x}}} \mathcal{L}]_l)/2$. The separation phase can be described by

$$\Delta\phi_{sep} = -\frac{1}{\hbar} \bar{\boldsymbol{p}} \cdot \Delta \boldsymbol{x}. \tag{3.24}$$

Due to rotations and gravity gradients, the classical trajectories characterizing the motion of the wave packets for the two branches of the interferometer do not close in space, an effect which increases significantly with the interferometer time. The relative displacement between the interfering wave packets in such open interferometers leads to a loss of contrast. The problem can be mitigated by small changes in the timing of the laser pulses which is very easy to implement [120] or by adjusting the wave vector of laser pulses [121]. The latter is also interesting for its opposite application as adopted in [27] to characterize the performance of a gradiometer when the phase shift introduced by the gravity gradient is too small to see an open ellipse where the interference fringes are plotted by on interferometer against with the other one.

3.2.3 Different types of atom interferometer

In the last subsection we have discussed the working principle of a typical Mach-Zehnder atom interferometer. The physics model is based on a two-level atom system with single-photon transition, the expressions of atom excitation and the accumulated phase during the interferometric process are presented. The single-photon interferometer, being the simplest model, is however inconvenient to realize due to the usually limited lifetime of the upper state. Only a few examples of single-photon interferometers have been demonstrated very recently using the clock transition [30, 31] or the intercombination transition [32] of Sr. The more popular scheme is the interferometer based on two-photon Raman transitions [2]. In recent years, multi-photon Bragg interferometers also attracted attention due to the benefit of large momentum transfer (LMT) [122]. The single-photon interferometer has been briefly discussed in section 1.2. In this subsection, the Raman and Bragg type atom interferometers will be discussed and their advantages will be presented.

Two-photon Raman interferometer The first implementations of atom interferometers with separated arms exploited two-photon Raman transitions [2].

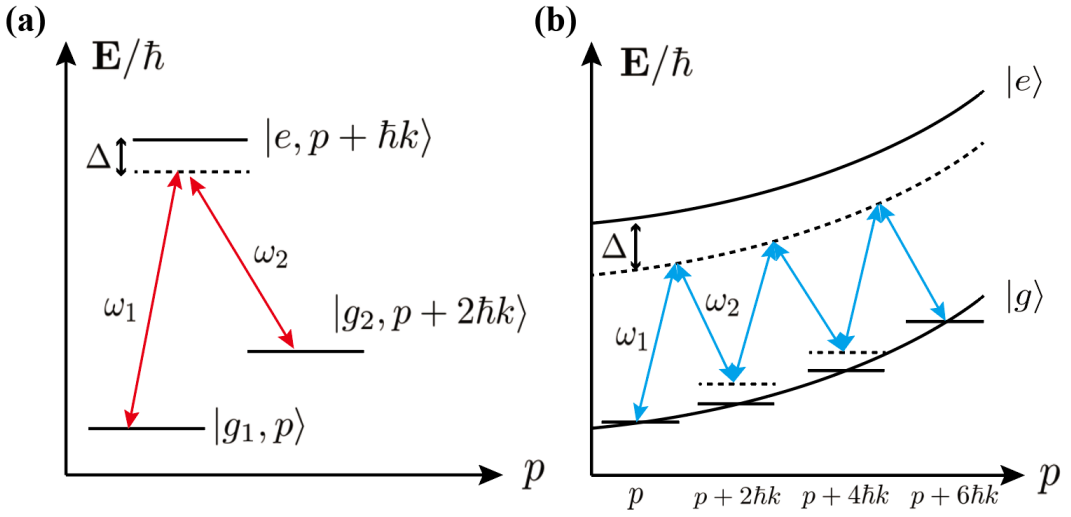

Figure 3.4: Different types of atom interferometer. (a) Two-photon Raman interferometer; (b) multi-photon Bragg interferometer.

A simplified level diagram for this case is shown in Fig. 3.4 (a).

The system that we consider is composed of two internal and stable ground states $|g_1\rangle$ and $|g_2\rangle$ and an optically excited state $|e\rangle$. The atomic system is illuminated by a couple of counterpropagating laser beams with frequencies ω_1 and ω_2. Because of the photon recoil, the combined internal and external states as $|\alpha, p\rangle$, where $\alpha = g_1, g_2, e$ are considered. Starting from a plane wave with momentum p and in the internal state g_1, $|g_1, p\rangle$, the field with frequency ω_1 and Rabi frequency Ω_1 couples to the excited state $|e, p + \hbar k\rangle$. Similarly, the counterpropagating field with frequency ω_2 and Rabi frequency Ω_2 couples the excited state to the ground $|g_2, p + 2\hbar k\rangle$ state. Both laser fields are detuned from the transition to the excited state and we define the detunings of the two fields from the excited states as $\Delta_1 = \omega_1 - \omega_{31}$ and $\Delta_2 = \omega_2 - \omega_{32}$, where ω_{31} and ω_{32} are the frequencies of the $|g_1, p\rangle$-$|e, p + \hbar k\rangle$ and $|g_2, p + 2\hbar k\rangle$-$|e, p + \hbar k\rangle$ transitions, respectively.

We first consider the Hamiltonian in the absence of the laser fields,

$$\hat{H}_a = \hbar\omega_1 |g_1, p\rangle \langle g_1, p| + \hbar\omega_2 |g_2, p + 2\hbar k\rangle \langle g_2, p + 2\hbar k| + \hbar\omega_3 |e, p + \hbar k\rangle \langle e, p + \hbar k| , \tag{3.25}$$

and transform the atomic state according to $|\psi\rangle = e^{-i\hat{H}_a t/\hbar} |\phi_{at}\rangle$. We then write the time-dependent Schrödinger equation for $|\phi_{at}\rangle = c_1 |g_1, p\rangle + c_2 |g_2, p + 2\hbar k\rangle +$

$c_3 |e, p + \hbar k\rangle$ as,

$$i\hbar \frac{dc_1}{dt} = \frac{\hbar\Omega_1}{2} e^{-i(\Delta_1 t + \phi_1)} c_3 \tag{3.26a}$$

$$i\hbar \frac{dc_2}{dt} = \frac{\hbar\Omega_2}{2} e^{-i(\Delta_2 t + \phi_2)} c_3 \tag{3.26b}$$

$$i\hbar \frac{dc_3}{dt} = \frac{\hbar\Omega_1}{2} e^{-i(\Delta_1 t + \phi_1)} c_1 + \frac{\hbar\Omega_2}{2} e^{-i(\Delta_2 t + \phi_2)} c_2, \tag{3.26c}$$

where ϕ_1 and ϕ_2 are the phases of the two laser fields. In the limit where the population of the excited state is kept small, $|\Delta_1|, |\Delta_2| \gg \Omega_1, \Omega_2, |\Delta_1 - \Delta_2|$, it is possible to adiabatically eliminate the excited state amplitude by integrating Eq. (3.26a) with constant c_1 and c_2 and substituting the result in equations Eq. (3.26b) and Eq. (3.26c). Then, by neglecting terms that oscillate at the detunings Δ_i, the system reduces to a soluble two-level problem,

$$i\hbar \frac{dc_1}{dt} = \hbar \frac{\Omega_1^2}{4\Delta} + \hbar \frac{\Omega_1 \Omega_2}{4\Delta} e^{i(\delta t + \phi_e)} c_2 \tag{3.27a}$$

$$i\hbar \frac{dc_2}{dt} = \hbar \frac{\Omega_2^2}{4\Delta} + \hbar \frac{\Omega_1 \Omega_2}{4\Delta} e^{i(\delta t + \phi_e)} c_1, \tag{3.27b}$$

where in the coefficients we neglected the difference between Δ_1 and Δ_2 by setting $\Delta_1 \simeq \Delta_2 \equiv \Delta$ and in the complex exponentials we set $\delta = \Delta_1 - \Delta_2$. The effective phase ϕ_e is defined as the difference $\phi_e = \phi_1 - \phi_2$.

If we only look at the second terms of the right-hand side of equations (3.27a) and (3.27b), these are the same as in the actual two-level system but with an effective (two-photon) Rabi frequency $\Omega_{eff} = \Omega_1 \Omega_2 / (2\Delta)$ and the system is driven by an effective laser with frequency $\omega_{eff} = \omega_1 - \omega_2$, effective wavevector $k_{eff} = 2k$ and effective phase $\phi_e = \phi_1 - \phi_2$. The first two terms, on the other hand, represent the light shift of the atomic levels. We note that when these are equal, they would merely change the energy offset and therefore not cause an effect. On the other hand, if these terms are different, they change the frequency difference between the two ground states. The light shift terms can cause several difficulties in precision measurements, especially if the intensity profile of the laser beams is considered. In this case, the resulting spatial dependence of the Rabi frequency can cause unwanted interferometer phase shifts.

It is possible to see that by a suitable unitary transformation, this system of equations can be mapped into the Hamiltonian (Eq. (3.5)) with detuning, generalized Rabi frequency and phase given by

$$\delta_e = \delta + \frac{\Omega_1^2}{4\Delta} - \frac{\Omega_2^2}{4\Delta} \tag{3.28a}$$

$$\Omega_R = \sqrt{\Omega_{eff} + \delta_e^2} \tag{3.28b}$$

$$\phi_e = \phi_1 - \phi_2 \tag{3.28c}$$

respectively. The phase shift of a Raman-based atom interferometer is written by adapting Eq. (3.22) with the replacements $k \to k_{eff}$ and $\phi \to \phi_e$:

$$\Phi = k_{eff} g T^2 + \phi_{e,1} - 2\phi_{e,2} + \phi_{e,3}. \tag{3.29}$$

Multi-photon Bragg interferometer Multi-photon transitions can be used for the implementation of atom interferometers where the two states differ by their momentum but have no internal excitation. These processes are generally identified as Bragg diffraction because of the analogy with the scattering of X-rays and neutrons off crystals [123]. In atomic Bragg diffraction, the optical lattice formed by two counterpropagating laser fields acts as the diffracting crystal planes and the atomic matter-waves act as the beam of X-rays. In the atom-photon interaction picture, Bragg diffraction is described in terms of combined cycles of absorption and stimulated emission resulting in the net transfer of pairs of photon momenta (Fig. 3.4 (b)). Atomic Bragg diffraction was first studied in [124]. The first experimental realization consisted in the diffraction of a collimated atomic beam [125] and, in a related experiment, up to sixth-order Bragg diffraction was observed on a beam of metastable neon atoms [126]. Later on, Bragg diffraction was implemented in laser-cooled atomic systems, transferring up to 102 photon recoils and inducing momentum state superpositions with a half-meter scale spatial separation between the wavepackets [122, 127, 128].

In order to describe atomic Bragg diffraction, we consider the same setup as for Raman transitions, with two counterpropagating laser fields with frequencies ω_1 and ω_2 and follow the same procedure. We write the wavefunction as a superposition of atomic states for the ground and excited states and with momentum differing by $\hbar k_{eff}$ (Fig. 3.4 (b)):

$$|\phi_{at}\rangle = \sum_n c_{g,n}(t)\,|g, p + n\hbar k_{eff}\rangle + \sum_n c_{e,n}(t)\,|e, p + n\hbar k_{eff} + \hbar k\rangle\,. \tag{3.30}$$

Similar to the Raman transitions, we can perform adiabatic elimination of the excited state by assuming that the detuning from the optical transitions is large compared to the single-photon Rabi frequencies and to the frequency difference between the two fields. The result is the system of coupled equations

$$i\hbar\frac{dc_{g,n}}{dt} = \hbar\left(\frac{\Omega_1^2}{4\Delta} + \frac{\Omega_2^2}{4\Delta}\right)c_{g,n} + \hbar\frac{\Omega_{eff}}{2}e^{i(\delta_n t+\phi_e)}c_{g,n+1} + \hbar\frac{\Omega_{eff}}{2}e^{-i(\delta_{n-1}t+\phi_e)}c_{g,n-1}, \tag{3.31}$$

where δ_n is the detuning from the transition $|g, n\rangle$-$|g, n+1\rangle$ which can be expressed in terms of the difference of kinetic energy of the two states as,

$$\delta_n = \omega_1 - \omega_2 - \left[\frac{(2n+1)\hbar k_e^2}{2m} + k_{eff} v\right]. \tag{3.32}$$

These results are similar to those for Raman transitions but there are some important differences. Indeed, because the transitions do not change the internal state, the frequency of the transition between two internal states is absent. For this reason Bragg diffraction is more robust against perturbations such as electromagnetic fields that can alter δ_n and therefore induce an undesired phase shift. This same immunity is reflected in the light shift terms which are the same for every state $|g, p + n\hbar k_{eff}\rangle$ as long as the conditions for adiabatic elimination hold [129]. Bragg diffraction therefore appears to have a number of advantages compared to two-photon Raman transitions.

The first advantage is the immunity to internal energy shifts. This immunity is valid in the framework of adiabatic elimination and as long as spatial internal energy gradients are small. This means that if the internal atomic energy is position-dependent, the resulting force acting on the atom might still cause undesired systematic effects. This is the case, for example, when magnetic gradients or laser intensity gradients are present during the interferometer. The second advantage is the large momentum transfer. The possibility in Bragg diffraction of transferring several pairs of photon momenta in a single light pulse, generally referred to as large momentum transfer, enhances the phase sensitivity by increasing the interferometer area. For a Mach-Zehnder interferometer, the phase shift is given by

$$\Phi_n = nk_{eff}gT^2 + n(\phi_1 - 2\phi_2 + \phi_3). \tag{3.33}$$

3.3 Bragg atom interferometer with spin squeezed states

In this section we present the proposal of using spin squeezed states in a Bragg atom interferometer. This proposal is based on the research work of Dr. Leonardo Salvi [51, 52]. The main objective of the current thesis is the experimental realization of this proposal.

3.3.1 Motivations

The Bragg atom interferometer based on bosonic ^{88}Sr atoms has been implemented both with the $^1S_0$-$^1P_1$ dipole transition [26] and the $^1S_0$-$^3P_1$ intercombination transition [27]. There are some advantages in using the Bragg diffraction in Sr atom interferometers. First, the ground state of ^{88}Sr has zero nuclear spin and is therefore immune to the stray magnetic fields when operated as an atom interferometer. This advantage is more pronounced with Bragg transitions since

only the motional state changes. Second, the large-momentum transfer due to high-order Bragg diffraction can significantly enhance the sensitivity of the quantum sensor.

The presence of narrow intercombination transitions in Sr also makes the atom well suited for squeezing experiments involving external degrees of freedom. The squeezing method relies on resolving the Doppler effect due to the different speed of the two momentum components. For dipole-allowed transitions, however, the Doppler splitting, of the order of 10-100 kHz, is hidden by the large linewidth on the order of 10 MHz. Probing on a dipole-allowed transition therefore can only provide information about the total atom number rather than about the population difference. The linewidth $\Gamma = 2\pi \times 7.5$ kHz of the intercombination transition at 689 nm of strontium is however small enough to perform as a probe that can resolve the Doppler splitting.

In this proposal, squeezing is introduced with quantum non-demolition measurements in an high-finesse optical ring cavity. It is shown that effective squeezing can be introduced in the momentum states with large Bragg diffraction orders. The scheme can be extended also to small Bragg diffraction orders and large atom number by inducing atomic transparency at the frequency of the probe field.

3.3.2 Experimental scheme

The proposed scheme is illustrated in Fig. 3.5, where two vertical counterpropagating laser beams B1 and B2 induce a momentum-state superposition between the states $|^1\mathrm{S}_0, p = 0\rangle$ and $|^1\mathrm{S}_0, p = 2n\hbar k_b\rangle$ by nth-order Bragg diffraction [122] on the dipole-allowed $^1\mathrm{S}_0$-$^1\mathrm{P}_1$ blue Sr transition at 461 nm. Here the atomic linear momentum is indicated by p, and the photon momentum is denoted by $\hbar k_b$. The duration of the Bragg diffraction pulses is set in order to couple the two momentum states only. This condition is typically met by pulse durations of the order of 10 μs [26].

We consider the squeezing of the atomic states by collective measurements of the relative population of the two momentum states through dispersive detection in a ring cavity (Fig. 3.5). This is achieved by probing for a time T_m on the red $^1\mathrm{S}_0$-$^3\mathrm{P}_1$ intercombination line of strontium at 689 nm using a laser beam, of angular frequency ω_r, incident onto the cavity. Probing is performed when the free-falling atoms cross the cavity mode volume.

In the following, measurements of the cavity output field $\hat{b}_{out}$ are considered, and the sensitivity to atom number fluctuations between momentum states is computed. As such measurements provide collective information about the ensemble without distinguishing between individual atoms, they project the ensem-

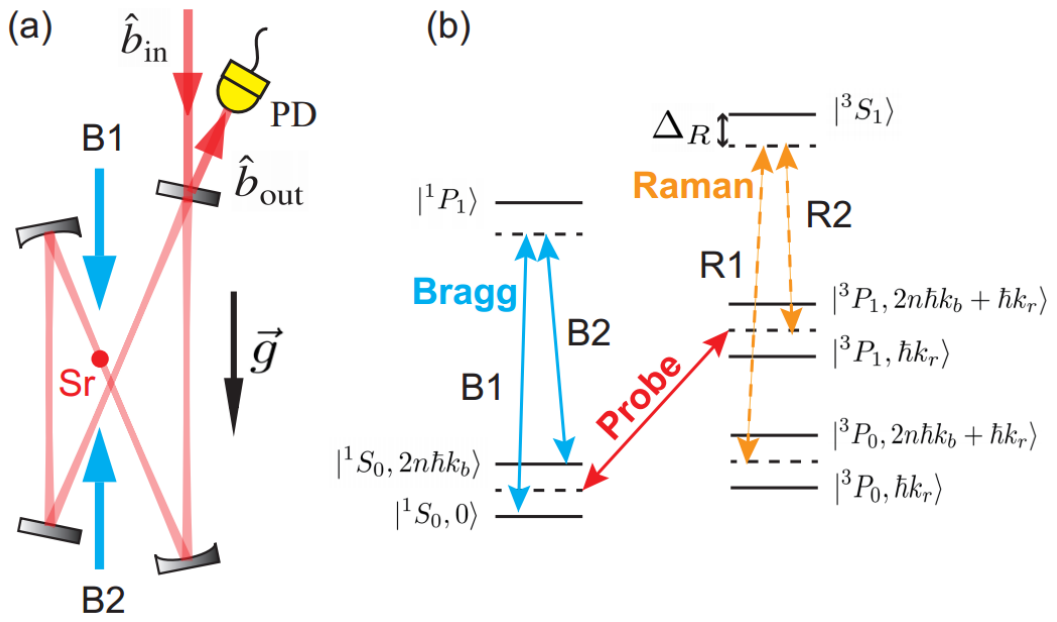

Figure 3.5: Squeezing on momentum states with Sr atoms. (a) Experimental scheme, an optical ring cavity is used for nondemolition probe of the atomic state, squeezing is induced by resolving the two momentum states prepared by two counter-propagating Bragg beams. (b) Level diagram and transitions related to Bragg pulse (blue arrows), squeezing probe (red arrow) and EIT coupling (orange arrows). Figure adapted from [51].

ble into a collective state which corresponds to the measurement outcome [44]. This process can produce conditionally squeezed atomic momentum states that can be implemented in atom interferometers with significant metrological gain.

In this proposal, it is shown than with large Bragg diffraction orders ($n > 5$), substantial metrological gain can be achieved. However, for small n, the optical transitions are not sufficiently resolved in frequency space compared to the atomic linewidth, which prevents operating in the dispersive regime of atom-light interaction and leads to substantial absorption and squeezing reduction. This condition can be relaxed with the technique called electromagnetically induced transparency (EIT) [130, 131], which couples the decaying $^3\text{P}_1$ state to the metastable state $^3\text{P}_0$ with a much longer lifetime (Fig. 3.5 (b)). With this technique it is possible to enhance the signal-to-noise ratio of momentum-state population collective measurements also at small Bragg diffraction orders n, while keeping the collective cooperativity $N\eta$, and thus the squeezing, large.

An atom interferometry scheme including the squeezed source proposed here is the following (Fig. 3.6): strontium atoms are cooled and trapped at the cavity

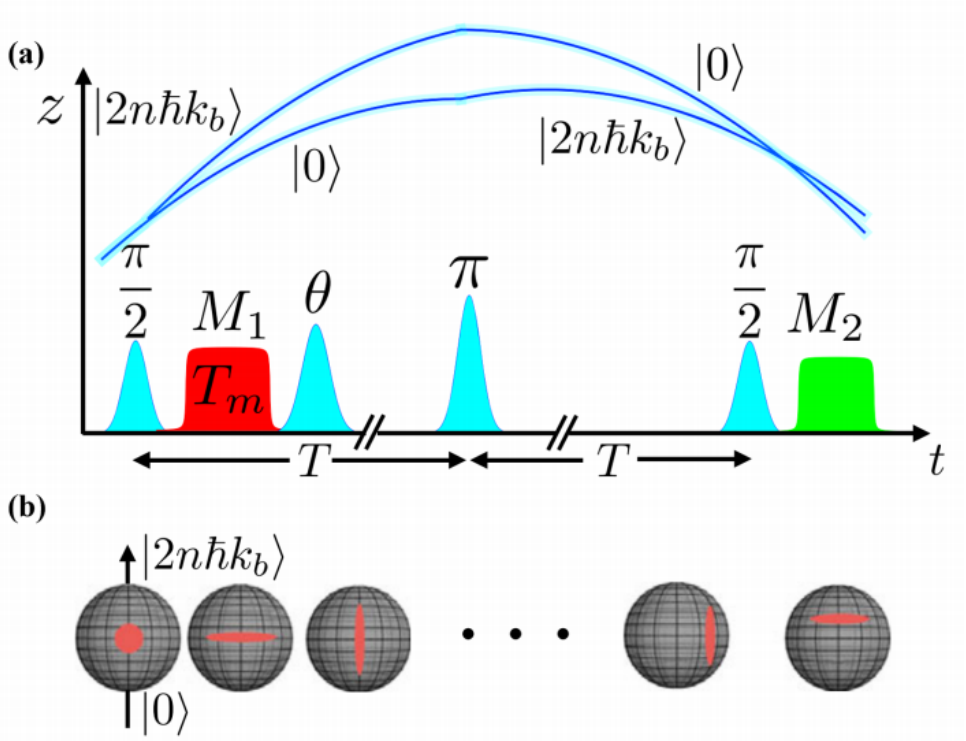

Figure 3.6: Squeezing sequence and state evolution. (a) Trajectory of atomic wave packet and the squeezing sequence, a standard Mach-Zehnder interferometer sequence is applied. After the first $\pi/2$ pulse, squeezing measurement (M1) is performed through the ring cavity for a duration of 200 μs, then the spin orientation is rotated through the x-axis by 90° and transfers the number squeezing to phase squeezing. After state evolution and phase accumulation, a final measurement (M2) detects the atomic state with the fluorescence method. (b) Bloch sphere representation of the state evolution, each sphere corresponds to the atomic state in the same position of (a). Figure adapted from [51].

mode waist close to the center of the optical cavity, then a momentum superposition is created by a Bragg $\pi/2$ pulse, and immediately after that, the squeezing measurement of the relative population is performed (M1). At this stage, the atomic ensemble is projected into a state with reduced relative population uncertainty. The state on the Bloch sphere is then transformed into a phase-sensitive state by applying a Bragg $\pi/2$ pulse with a phase shift of 90° with respect to the first pulse. Following this preparation stage, the π and $\pi/2$ laser pulses complete the Mach-Zehnder interferometer sequence. Finally, a final state measurement (M2) is performed using the fluorescence detection.

3.3.3 Metrological gain and squeezing

We quantify the attainable metrological gain ξ_m by the ratio between the contrast squared $\mathcal{C}^2$ and the population variance $(2\Delta J_z)^2$ normalized to the atom shot noise variance $2J$ [64]:

$$\xi_m = \frac{J}{2(\Delta J_z)^2}\mathcal{C}^2. \tag{3.34}$$

The squeezing pre-measurement of J_z can be achieved by arranging a situation where the atom-light interaction is dispersive and the two momentum states are associated with opposite variations of the index of refraction and shift the cavity resonance frequency in opposite directions. When the cavity resonance frequency ω_c is tuned halfway between the two optical transitions, atoms in the two momentum states produce opposite shifts of the cavity resonance frequency that can be detected via the phase shift $\Delta\phi_{ph}$ of the light reflected from the cavity,

$$\Delta\phi_{ph} = \frac{4\frac{\kappa_{in}}{\kappa}J_z\eta\mathcal{L}_d(\delta\omega_r)}{\left[2\frac{\kappa_{in}}{\kappa} - 1 - N\eta\mathcal{L}_a(\delta\omega_r)\right]\left[1 + N\eta\mathcal{L}_a(\delta\omega_r)\right]}, \tag{3.35}$$

i.e., the population difference can be detected via the phase shift of the light emerging from the cavity. Here $\mathcal{L}_d(\Delta) = -2\Gamma\Delta/(\Gamma^2+4\Delta^2)$ and $\mathcal{L}_a(\Delta) = \Gamma^2/(\Gamma^2+4\Delta^2)$ are the atomic dispersion and absorption profiles, respectively. The single-atom cooperativity is indicated as $\eta = 4g^2/(\Gamma\kappa)$, where $2g$ is the vacuum Rabi frequency, κ is the cavity mode linewidth, and κ_{in} is the contribution to κ due to the input mirror transmission. The light phase measurement can be performed, for example, through the Pound-Drever-Hall technique. If the detector operates at the photon shot noise level, the variance of the population difference between the two momentum states, normalized to the variance $2J$ of the atom shot noise, is given by [51],

$$\frac{2(\Delta J_z)^2}{J} = \frac{\mathcal{L}_a(\delta\omega_r)\left[1 + N\eta\mathcal{L}_a(\delta\omega_r)\right]^2}{4N\eta\epsilon_d n_{sc}\left[\mathcal{L}_d(\delta\omega_r)\right]^2}, \tag{3.36}$$

where ϵ_d is the detection efficiency [51], and we have expressed the measurement strength in terms of the average number n_{sc} of photons scattered per atom into free space, since the latter process constitutes the main, and fundamental, limitation to the attainable squeezing [43].

After the scattering of one photon by one atom, the momentum superposition is destroyed, and the associated recoil causes the trajectory to deviate from the vertical direction. The resulting losses cause a random imbalance $2(\Delta J_z)_{sc}$ of the populations in the two momentum states. Assuming that each atom scatters at most one photon, the population variance increase is $(2\Delta J_z)^2_{sc} = 2Jn_{sc}$. By accounting for free space scattering, we can then compute the optimum metrological

gain, which is attained for

$$n_{sc} = \sqrt{\frac{\mathcal{L}_a(\delta\omega_r)\left[1 + N\eta\mathcal{L}_a(\delta\omega_r)\right]^2}{4N\eta\epsilon_d\left[\mathcal{L}_d(\delta\omega_r)\right]^2}}. \tag{3.37}$$

Finally, we put some realistic parameters and estimate the potential squeezing with the proposed measurement scheme. We consider an optical cavity where one of the foci has a waist $w_0 = 150$ μm, at the position where the atoms cross the cavity mode volume. With a cavity finesse $\mathcal{F} = 10^5$ and at the wavelength $\lambda = 689$ nm, we get a single-atom cooperativity $\eta = 3\mathcal{F}\lambda^2/(2\pi^3 w_0^2) \simeq 0.1$ [41]. We then consider $N \simeq 10^5$ atoms occupying a volume with a linear size of about 30 μm. In this case, a collective cooperativity $N\eta \simeq 10^4$ is achievable. The maximum possible Bragg diffraction order with our method is set by the condition that the transit time of the wave packets corresponding to the two momentum states through the cavity beam waist is larger than the time duration of the collective measurement. Because the atoms are crossing the cavity beam vertically, the effective mode waist is $w_0/\sin\alpha$. We therefore estimate the maximum Bragg diffraction order as $n_{max} = Mw_0/(10\hbar k_b T_m \sin\alpha)$, where T_m is the measurement time duration. With $\alpha \simeq 0.4$ rad and $T_m \simeq 200$ μs, we get $n_{max} = 10$. However, the maximum Bragg order can be made considerably larger by a suitable design of the cavity geometry, where w_0 is made larger and α is made smaller.

The measurement time is set by the requirement that the number of photons scattered into free space be sufficient to provide the optimum metrological gain. To resume, by considering a collective cooperativity $N\eta = 10^4$, first-order diffraction $n = 1$, a Raman coupling strength $\Omega_{eff} = 2\pi \times 400$ kHz, a measurement time $T_m = 200$ μs, and a detection efficiency $\epsilon_d = 1$, we conclude that the optimum number of photons scattered into free space per atom is $n_{sc} = 5 \times 10^{-3}$, corresponding to the excited-state population $P_{ext} = n_{sc}/(\Gamma T_m) = 5 \times 10^{-4}$. In this case it is possible to achieve a metrological gain of 20 dB.

3.4 Conclusions

This chapter presents a proposal for squeezing on the momentum states in Sr atom interferometry. The basic properties and two-stage cooling of Sr are introduced and the working principle of atom interferometry is discussed. Different types of atom interferometer are studied and the corresponding phase shifts are determined. A novel proposal for squeezing on the momentum states of Sr atom interferometers is presented and the metrological gain and squeezing are estimated.

Chapter 4

Construction of an optical ring cavity for QND measurement

This chapter is dedicated to the construction of the optical ring cavity, which is the core element in the generation of spin squeezed states. Spin squeezing based on the cavity-enhanced measurement has been realized in a few groups with Rb [132, 45] and Yb [47, 48] atoms. Different cavity geometries such as the Fabry-Pérot cavity [133] and the asymmetric cavity [96] have been proposed and demonstrated, further details about the cavity building can be found in [134]. Indeed, the crafts of optical cavity construction by itself is already an active field, especially in the community of optical lattice clocks, where ultra-stable cavities are built to provide a stable frequency reference for clock lasers [135, 136].

The main difficulty in building an optical cavity lies on the dilemma that, on the one hand, the cavity geometry needs to be tunable to find the optimized alignment, ie., the designated mirror positions, angles and maximum laser-cavity coupling, etc. On the other hand, the cavity geometry needs to be stable and robust to maintain a fixed cavity length, which is directly related to the frequency stability of an oscillator. The *tunability* and the *stability* are the two ends of a balance scale. This dilemma is alleviated in the case of two-mirror cavities, where we can fix one mirror on the one end of a cylindrical cavity spacer and tune the other one in the other end, while monitoring the cavity transmission. Generally, epoxy is used to glue the cavity mirrors on a spacer. In some cases with super-polished surfaces on the cavity mirrors and spacers, optical contact is used to fix the cavity mirrors with the spacer by creating a layer of molecule bonds between the surfaces [137, 138], therefore better stability can be attained.

In this thesis, the construction of an optical ring cavity with four mirrors is considered, which has far more complexity and degrees of freedom. In this chapter, we first take an overview of the optical ring cavity under consideration and

discuss the alignment and assembly procedures. Then a series of original designs of cavity components are presented, which are essential in the manipulation and assembly of the cavity. Then the laser-cavity mode matching is discussed and the usage of different epoxies to glue different cavity components is presented in detail. Finally, a cavity prototype is constructed and assembled which can be used for performance characterization and finally serve as a transfer cavity for laser locking. The contents presented in this chapter can be a tutorial guide for the construction of an optical ring cavity or similar multi-mirror cavities.

4.1 Cavity design considerations

Optical cavities can either consist of two mirrors facing each other (a Fabry-Pérot cavity) or more than two mirrors forming a traveling wave (ring cavity) or standing wave resonator [133]. They are one of the fundamental building blocks of many laser interferometers, including LIGO-Virgo and LISA, and provide a platform where atom-light interaction effects can be enhanced. The theory of a Fabry-Pérot cavity has already been investigated intensively and a more general description can be found in [139, 133]. Here we investigate some of the most important properties of an optical ring cavity, which is the main concern of this thesis.

4.1.1 General description of an optical cavity

Cavity geometry In this thesis an optical ring cavity geometry composed of four mirrors is considered. We start from the simplest model where only the fundamental mode of the cavity is considered and use the general ABCD matrix treatment [139] for the analysis.

The ray transfer matrix or the ABCD matrix describes the beam propagation in an optical system. In the paraxial approximation, it describes the transformation from the input beam with position x_1 and slope x_1' to the output beam with quantities x_2 and x_2',

$$\begin{pmatrix} x_2 \\ x_2' \end{pmatrix} = \begin{pmatrix} A & B \\ C & D \end{pmatrix} \begin{pmatrix} x_1 \\ x_1' \end{pmatrix} \tag{4.1}$$

with the ray transfer matrix of the optical system

$$\mathbf{H} = \begin{pmatrix} A & B \\ C & D \end{pmatrix}. \tag{4.2}$$

For a ray propagating through multiple optical systems, the collective effect can be enclosed in one single ABCD matrix given by the product of each individual

matrix.

For the laser beam circulating in an optical ring cavity, we first define the sagittal plane which is orthogonal to the cavity plane and the tangential plane which is parallel to the cavity plane. The ABCD matrix for a beam propagating freely through a distance d is

$$\mathcal{M}_f(d) = \begin{pmatrix} 1 & d \\ 0 & 1 \end{pmatrix}. \tag{4.3}$$

The ABCD matrix for a beam at reflection from a mirror with a radius of curvature R_m and angle of incidence θ in the tangential plane $\mathcal{M}_t(R_m, \theta)$ and sagittal plane $\mathcal{M}_s(R_m, \theta)$ are

$$\mathcal{M}_t(R_m, \theta) = \begin{pmatrix} 1 & 0 \\ -\frac{2}{R_m \cos\theta} & 1 \end{pmatrix}, \tag{4.4}$$

and

$$\mathcal{M}_s(R_m, \theta) = \begin{pmatrix} 1 & 0 \\ -\frac{2\cos\theta}{R_m} & 1 \end{pmatrix}, \tag{4.5}$$

respectively.

Cavity stability condition The field envelope of a Gaussian beam is supposed to follow the Gaussian function,

$$U = \frac{A_0}{q} \exp\left(-i\frac{\pi r^2}{\lambda q}\right), \tag{4.6}$$

where A_0 is the amplitude, λ is the wavelength, r is the radial distance from the center axis of the beam. The complex q parameter is a very useful parameter which can fully characterize the beam at a certain point with the beam waist w ($1/e^2$ radius) and the radius of phase front curvature R as

$$\frac{1}{q} = \frac{1}{R} - i\frac{\lambda}{\pi w^2}. \tag{4.7}$$

As the beam is circulating in the cavity, here the cavity can be considered as an optical system with a round trip matrix

$$\mathbf{H}_{cavity} = \begin{pmatrix} A & B \\ C & D \end{pmatrix}. \tag{4.8}$$

Suppose q_{in} and q_{out} as the beam parameters in the input and output planes of the cavity, following the ABCD law we have

$$q_{out} = \frac{Aq_{in} + B}{Cq_{in} + D}. \tag{4.9}$$

For the cavity to be stable, the q parameter should fulfill the self-consistency condition, which means that the q parameter should regain its value after a round-trip in the cavity. Therefore we can rewrite Eq. (4.9) as

$$Cq^2 + (D - A)q - B = 0. \tag{4.10}$$

For the q parameter to be self-consistent, the solution of q should have an imaginary part, which leads to

$$(D - A)^2 + 4BC < 0. \tag{4.11}$$

Since the ABCD matrix has an unitary determinant $AD - BC = 1$, Eq. (4.11) leads to the cavity stability condition

$$|A + D| < 2. \tag{4.12}$$

4.1.2 Optical ring cavity properties

As for the optical ring cavity model we have established in this chapter, the collective matrix in the tangential plane and sagittal plane are

$$\mathcal{M}_t = \mathcal{M}_t^{(1)}\mathcal{M}_f^{(1)}\mathcal{M}_t^{(2)}\mathcal{M}_f^{(2)}\mathcal{M}_t^{(3)}\mathcal{M}_f^{(3)}\mathcal{M}_t^{(4)}\mathcal{M}_f^{(4)}, \tag{4.13}$$

and

$$\mathcal{M}_s = \mathcal{M}_s^{(1)}\mathcal{M}_f^{(1)}\mathcal{M}_s^{(2)}\mathcal{M}_f^{(2)}\mathcal{M}_s^{(3)}\mathcal{M}_f^{(3)}\mathcal{M}_s^{(4)}\mathcal{M}_f^{(4)}, \tag{4.14}$$

respectively. In those expressions $\mathcal{M}_t^{(i)}$ and $\mathcal{M}_s^{(i)}$ are the mirror reflection matrix for the ith mirror in the tangential plane and the sagittal plane, respectively, $\mathcal{M}_f^{(i)}$ is the free space propagation of the ith path ($L_1 \sim L_4$) in the cavity. With the ABCD matrix of the cavity at hand, we can consider the cavity geometry which fulfills the stability condition (Eq. 4.12).

As for the optical ring cavity used in this work, we consider a setup with two curved and two flat mirrors that produce a mode with two foci, one with a large waist and the other with a smaller waist, as shown in Fig. 4.1 (a). We considered a geometry where the two curved mirrors have a radius of curvature of $R = 50$ mm, the length of the first vertical arm is $L_1 = 55$ mm and the second is $L_3 = 44$ mm long. The angle of incidence on the cavity mirrors is set to be $\theta = 0.2$ rad (11.5°).

Beam size propagation In order to characterize the beam size propagation inside the cavity, the beam waist on the four paths ($L_1 \sim L_4$) should be considered separately. As an example, if we consider a point P in L_3 with a distance d from

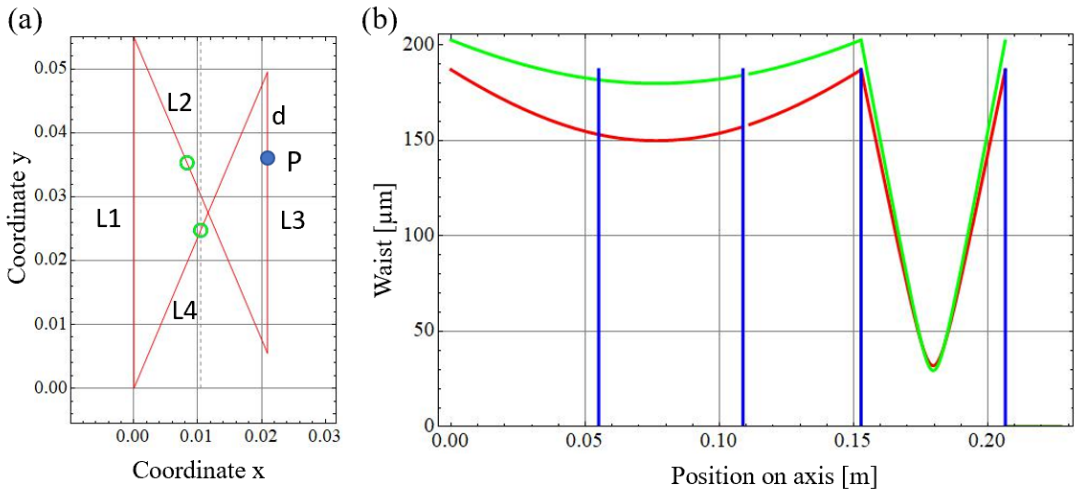

Figure 4.1: Ring cavity schematic and beam size propagation. (a) Computed cavity geometry. The numbers on the plot label the arms of the ring cavity and the green circles identify the waist positions. The upper waist (in arm 2) is the largest whereas the lower (arm 4) is the smallest. The dashed line indicates the midpoint, where the atomic trajectories are likely to be. (b) Evolution of the cavity waist along the optical axis. Red line: waist on the tangential plane. Green line: waist on the sagittal plane. Blue vertical lines: mirror positions. Figure adapted form [52].

mirror 4, following the beam propagation in the cavity, the round-trip ABCD matrix can be written as,

$$\mathcal{M}_{t,s} = \mathcal{M}_f^d \mathcal{M}_{t,s}^{(4)} \mathcal{M}_f^{(4)} \mathcal{M}_{t,s}^{(1)} \mathcal{M}_f^{(1)} \mathcal{M}_{t,s}^{(2)} \mathcal{M}_f^{(2)} \mathcal{M}_{t,s}^{(3)} \mathcal{M}_f^{(L_3-d)}. \tag{4.15}$$

Then the beam waist at point P can be calculated as,

$$w^2 = \frac{2\lambda}{\pi} \frac{|B|}{\sqrt{4(AD-BC)-(A+D)^2}}, \tag{4.16}$$

where $AD - BC = 1$. By changing the position of the point and considering different ABCD matrices when P is located in different paths, the beam size propagation inside the cavity can be calculated, as shown in Fig. 4.1 (b), where the red and green lines shows the waists on the tangential and the sagittal plane, respectively.

Basic properties of a ring cavity The cavity resonance occurs when the cavity round trip length is an integer multiple of the laser wavelength. Thus we should be able to detune the cavity either by moving a mirror, or by changing the laser frequency. The distance in frequency between two resonance peaks

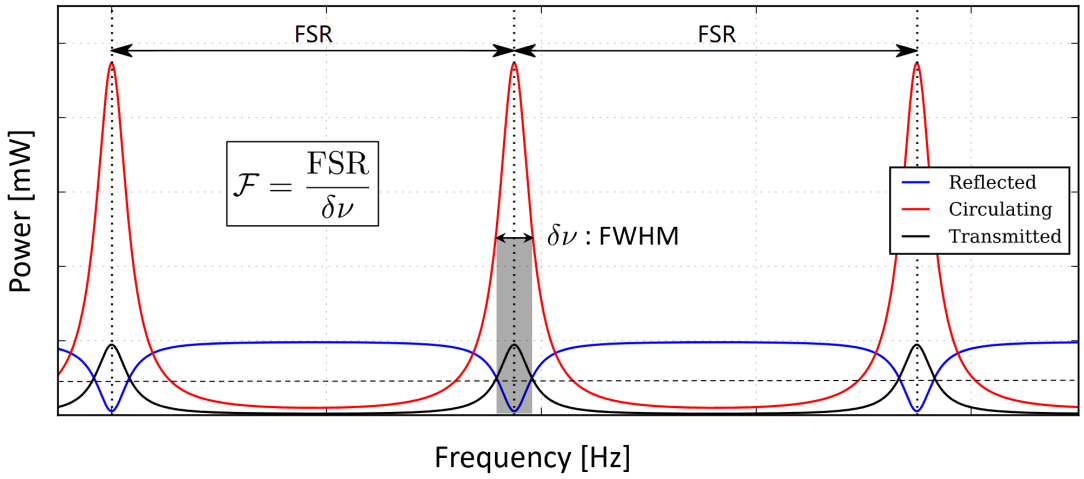

Figure 4.2: Basic properties of an optical cavity. Cavity transmission, reflection and intra-cavity power as a function of frequency detuning from cavity resonance. The distance in frequency between two resonance peaks is called the FSR. The FWHM of the transmission peak is called the cavity linewidth ($\delta\nu$). The finesse of the cavity is defined as $\mathcal{F} = \mathrm{FSR}/(\delta\nu)$.

is defined as the free spectral range (FSR) of a cavity. The FSR is often an important property of a cavity since it tells how well separated the resonance peaks are.

For an optical ring cavity, the laser propagating inside the cavity forms a traveling wave, therefore the FSR is,

$$\mathrm{FSR} = \frac{c}{L_1 + L_2 + L_3 + L_4}, \tag{4.17}$$

where c is the speed of light, $\sum L_i$ is the cavity round-trip length.

The finesse of an optical cavity is defined as its FSR divided by the linewidth of its resonances. It is fully determined by the cavity losses and is independent of the cavity length. For ring cavity with four mirrors, the finesse can be expressed as,

$$\mathcal{F} = \frac{\pi\sqrt{R_1 R_2 R_3 R_4}}{1 - r_1 r_2 r_3 r_4}, \tag{4.18}$$

where r_i and R_i are the reflection amplitude and power ratio of each mirror and $r_i = \sqrt{R_i}$.

Finally, the linewidth of a cavity is commonly defined as the Full Width at Half Maximum (FWHM) of the resonance peak and can be evaluated through,

$$\delta\nu = \frac{\mathrm{FSR}}{\mathcal{F}}. \tag{4.19}$$

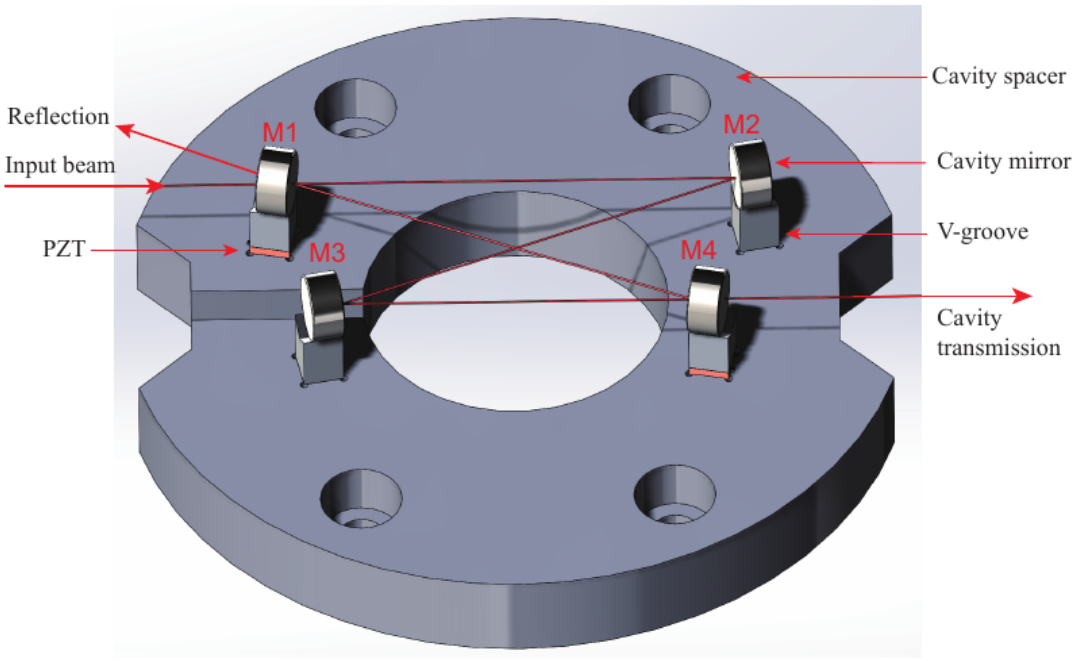

Figure 4.3: Ring cavity schematic. The ring-shaped cavity spacer can be fixed on a CF 100 flange with four PEEK plastic pillars. The four cavity mirrors are supported by four V-shaped grooves, forming the butterfly shape ring resonator. The V-grooves under M1 and M4 are supported by shear-force PZTs which is used for cavity length modulation.

Figure 4.2 plots the cavity transmission, reflection and intra-cavity circulating power as a function of the frequency detuning from cavity resonance. The definitions of cavity FSR, linewidth and finesse and their relationships are also shown.

4.1.3 Optical ring cavity for spin squeezing

The cavity geometry design has been discussed in the last subsection. Here we consider the cavity schematic which can be assembled into the vacuum chamber and is capable for performing cavity QED experiments.

The ring cavity schematic is illustrated in Fig. 4.3. Here we denote the four mirrors as M1, M2, M3 and M4 as shown in the figure. The cavity mirrors are manufactured and coated by *Fivenine Optics*. M1 and M4 are plane mirrors, while M2 and M3 are curved mirrors with a radius of curvature (ROC) of 50 mm, corresponding to a focal length of 25 mm. The mirror diameter is 7.75 mm and the thickness is 4 mm, the small size of the mirror guarantees sufficient optical access for the experiment. The mirror reflection surfaces are super-polished and

are coated to have different transmission rate with lasers at 689 nm, 461 nm and 813 nm wavelength, which correspond to the probe beam, Bragg beam and lattice beam in the Sr spin squeezing experiment. Table 4.1 lists the basic properties of the cavity mirrors, transmissions are expressed in parts per million (ppm). The mirror transmission surfaces are AR (anti-reflection) coated in order to avoid the etalon effects inside the substrates.

Table 4.1: Cavity mirror basic properties. Mirror transmissions are expressed in ppm, data acquired from the specs sheet of the company.

Mirror	ROC (mm)	T_i 689 (ppm)	T_i 461 (ppm)	T_i 813 (ppm)
M1	$+\infty$	240(5)	9990(100)	950(10)
M2	50	0.5(2)	800(10)	75(5)
M3	50	0.5(2)	800(10)	75(5
M4	$+\infty$	7(1)	9000(100)	970(10)

The four cavity mirrors are positioned on the ring spacer with the designated geometry. The mirrors are connected with the cavity spacer with four V-shaped supports. The support is a V-shaped groove where the angle of the V is 120°, the cross section of the support body is a square with side lengths of 5 mm. The V-grooves that hold M1 and M4 are based on two piezoelectric actuators (PZT, Noliac NAC2402-H2.3) with size of $(5 \times 5 \times 2.3$ mm). When the voltage is applied on the two electrodes of the PZT, it undergoes a shear movement, which can be used for fine tuning and fast modulation of the cavity length. All the connections between the mirrors, V-grooves, PZTs and the cavity spacer are performed with high-vacuum compatible epoxies, the usage of the epoxy is detailed in section 4.5.

4.2 Ring-cavity alignment and assembly procedures

In this section we describe the procedures for cavity alignment and assembly. We follow the steps listed here with more details illustrated in the following sections. The ring cavity and the corresponding optics are all set in an independent breadboard (600×300 mm) which is fixed on an optical table. The breadboard can be moved around without changing the alignment of the optics, which enables us to flip the breadboard upside-down and mount it on a vertical translation stage (elevator). With the reversed breadboard mounted on the elevator we can epoxy the four cavity mirrors on the cavity spacer, at the same time maintaining the cavity

geometry and alignment. These procedures provide our optimum compromise to the dilemma of the *tunability* and the *stability*.

- **Cavity mirror holder design.** Design and manufacture a kind of mirror holder which has the freedom for alignment both in the horizontal and vertical directions, the access for epoxying the mirror on a cavity spacer, and the ability to be released after the mirrors are glued without changing the cavity alignment. See subsection 4.3.1.

- Fix the mirrors on the mirror holder, check the angle of the mirror surface plane and preset it to be vertical. Locate the center of the mirrors which are fixed on the mirror holder and mark the height of the mirror center.

- **Laser setup.** Set the laser beam with optimized mode-matching with the cavity. This includes the measurement of the laser beam size in the propagation direction from the fiber output, the calculation and simulation of the laser-cavity mode-matching, and choose lenses with appropriate focal length and relative distances. After setting up the laser beam size, align the beam height to coincide with that of the mirror center.

- Design on a paper the optical paths that the cavity beams should follow, mark the corresponding positions of the mirrors and the mirror holders. Align the paper path with the incident beam of the cavity laser and paste the paper on the breadboard.

- Put the four cavity mirrors which are now mounted on the cavity holders one by one on the corresponding positions indicated by the path paper. After putting each one, check that the transmission of M1 and the reflections of the remaining mirrors follow the beam path and that the height of the beam is always correct.

- Set the other optics after the cavity transmission, including a $\lambda/2$ waveplate, a PBS, a camera and a fast photodetector at the transmission and reflection of the PBS, respectively.

- **Cavity alignment.** Align the cavity with the mirror holders, optimize the alignment to reach the highest ratio between the TEM00 mode and all the other higher-order modes. Check that the cavity beams follow the designed paths regularly.

- Loose the cavity breadboard from the optical table, flip it upside-down and mount it on a vertically translation stage (elevator), check and re-optimize

the cavity alignment. Test the robustness of the cavity alignment against the translation movement of the elevator.

- **Prototype cavity spacer.** Design and manufacture a prototype cavity spacer which is made of a stainless steel block ($70 \times 50 \times 30$ mm). Mark the cavity beam paths and the corresponding positions of the PZTs and the V-grooves on the top surface of the block with a cutter. Pre-bake the block at 200 ℃ for 3 hours to remove the water inside the material.

- **Test epoxies.** Test different epoxies which will be used to glue the cavity components, including the electric-conductive epoxy (EPO-TEK, H20E, curing condition: 150 ℃ for 1 hour from the specs sheet), the thermally conductive epoxy (EPO-TEK, H77, curing condition: 150 ℃ for 1 hour from the specs sheet) and the Torrseal epoxy (curing condition: 25 ℃ for 24 hours from the specs sheet). See section 4.5.

- **Heating preparation.** Wind the prototype cavity spacer with a heating tape and cover with aluminum foils for heating, insert thermistors for temperature monitoring . Fix the spacer on a small breadboard (300×300 mm) with pillars and clamps, move the cavity spacer under the elevator, align the cavity mirrors with the marked positions of the PZT and the V-grooves on the spacer. Then fix the small breadboard on the optical table, note that the breadboard is fixed on the optical table through four bars and pillars to reduce the heat sinking to the large table.

- **Epoxying of components** Glue the PZTs at their positions with H20E epoxy, make sure that the two electrodes of the PZT are not shorted. Check that the PZTs are healthy by measuring the resistance and capacitance and the varying voltage when they are mechanically solicited.

- Glue the four V-grooves at their positions, follow the steps in section 4.5.2.

- Glue the cavity mirrors to the V-grooves with Torrseal epoxy. Follow the steps as the gluing of the V-grooves, except that the curing condition of the Torrseal epoxy does not require heating.

4.3 Cavity components design

4.3.1 Cavity mirror holder design

The cavity mirrors have a diameter of 7.75 mm and a thickness of 4 mm. Due to the small size, the manipulation of the mirror is challenging. The necessity for

gluing them on the cavity spacer also pose some requirements for the geometric structure of the mirror holder. Commercial mirror mounts and holders cannot fulfill the requirements since they wrap the whole mirror side, leaving no access for the epoxy. A homemade mirror holder which is capable for holding and aligning the cavity mirrors is therefore designed and manufactured. To start, we list the requirements for this home-made mirror holder design:

- It should have the freedom for alignment both in the horizontal and vertical directions.
- It can hold the mirror in a way that allows the mirror to be glued on a V-groove, and the V-groove glued on a spacer.
- It should be capable for holding the mirror tightly and be able to release the mirror freely after the epoxy is cured without changing the cavity alignment.
- The size of the mirror holders should be small enough to avoid conflicting with each other since the distance between the mirrors are small (21 mm, 44 mm and 55 mm).

With those considerations in mind, we designed a kind of mirror holder which is composed of three parts, a home-made mirror mount, a base plate for clamping and a commercial rotary stage. As shown in Fig. 4.4, the top part is a base plate which holds the other parts and can be clamped on a breadboard with standard clamps. The middle one is a commercial rotary stage (Edmund Optics, ID:2399) which enables 360 ° coarse adjustment and 17 ° fine adjustment. The top and middle parts are locked with three 2 mm screws.

The bottom part is the core of this mirror holder design. Generally, it is a U shaped aluminum part, on the front plane there is a half cylinder cut with 8 mm diameter to hold the mirror, on both side planes there are two 3 mm screw holes for inserting plastic screws to lock the mirror, the top small arc is left for the access of tweezers when transferring the cavity mirrors. On the back plane there is a structure where a commercial fine-tuning screw-barrel couple can be inserted (Thorlabs NO.F25USA1 and F25US075, see Fig. 4.4 for details). This structure enables the tuning of vertical angles of the mirrors with a resolution of 1 μm. When combined with the rotary stage, tuning the mirror both in the vertical and horizontal directions is possible. To ensure the passage of light beams both in the transmission and reflection, the through hole in the back plane is made expansive, as a 120° cone. The stability of this mirror holder is tested by reflecting one laser beam from the mirror and monitoring the beam position in a 2 meter distance. The mirror holder has proved robust enough for our application.

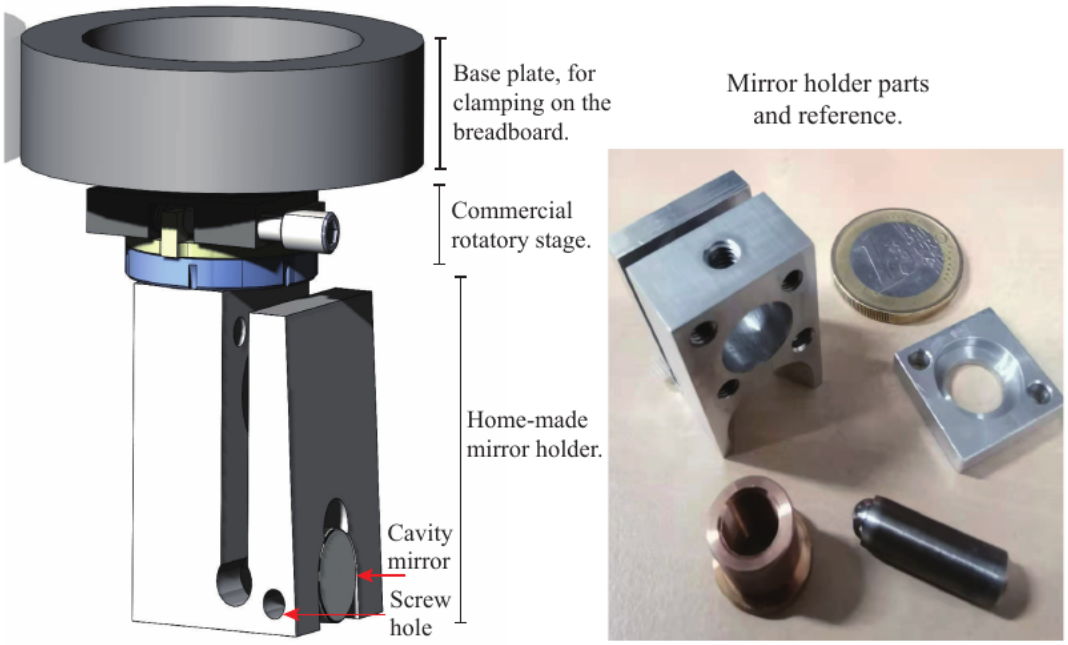

Figure 4.4: Cavity mirror holder design. The mirror holder is composed of three parts. From top to bottom: Base plate, which is used for clamping on the breadboard and connecting the remaining parts with three screws. Commercial rotary stage, which enables a fine tuning of rotary angle of 17 °. Homemade mirror holder, which can grab and release the cavity mirror without changing alignment, the screw barrel on the back enables a fine tuning of the vertical angle of the mirror (see the right pictures for details). The combination of the rotary angle and vertical angle freedom makes the tuning of the cavity mirror possible.

4.3.2 Cavity prototype design

The building of the optical ring-cavity is the core of the spin-squeezing experiment, and it is experimentally challenging. In order to gain experience from the gluing activities and characterize the cavity alignment under a simpler condition, a cavity prototype is built with the same gluing procedure as the real experimental cavity, but without time-consuming baking and vacuum-pumping processes. Indeed, this cavity prototype is not just a prototype, but can be used as a transfer cavity to bridge the frequency gap between the lattice laser (813 nm) and the red laser (689 nm), where the latter is locked to a high-finesse Fabry-Pérot cavity and to the atomic absorption line, thus attaining frequency stability both in the short and the long term.

As a fast try and prove, we made the cavity prototype as simple as possible. The cavity prototype is composed of a cavity spacer and a box. The spacer

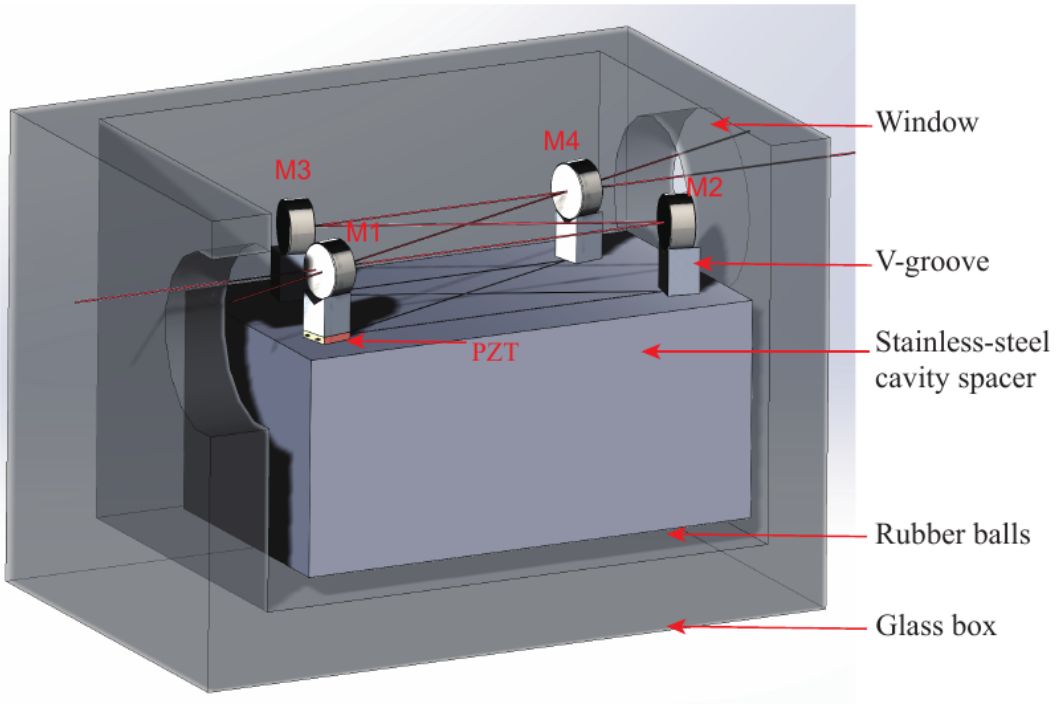

Figure 4.5: Section view of the cavity prototype design. The cavity spacer is made of a stainless steel block, which holds the four cavity mirrors in a ring shape. The spacer is laid on a plexiglass cavity box with four rubber balls, which can suppress the vibration from the optical table. The cavity box has two wedged windows to allow for the incidence, reflection and transmission of the cavity beam. The cavity prototype can be put in a clean nitrogen flowing environment in order to avoid dust contamination of the cavity mirrors.

is chosen as a stainless-steel block for its stiffness and comparatively low thermal expansion ratio. Of course there are some other ultra-low expansion (ULE) materials like Invar, which are better candidates for the cavity spacer, but here stainless-steel is chosen mainly due to its availability and since we have the PZT, the cavity length can be tuned at will.

The top surface of the cavity block (spacer) is super-polished and marked with the cavity beam paths and the corresponding positions of the PZT and the V-grooves. The mark is done with a cutter following a paper covering the block with printed beam paths. The bottom plane of the block contains three M4 screw holes, which are used to connect with three 5 cm-high pillars to fix the position while gluing the V-grooves and the mirrors. The stainless steel block is cleaned with acetone and baked at 200 ℃ for 3 hours after manufacturing. This process can remove the dust in the surface and the water inside the material.

Once the cavity prototype spacer is ready, one can glue the PZT and the four V-grooves on the top surface. The process of gluing and the characteristic of different epoxies are detailed in section 4.5. After the cavity mirrors are also glued, the cavity prototype is ready.

The cavity length is sensitive to the temperature fluctuation of the cavity spacer and to the air flow which can cause fluctuations in the index of refraction of air. Therefore, it is appropriate to temperature stabilize the cavity spacer and put the cavity inside the vacuum environment. However, in our case, as a fast try and prove, a prototype cavity is designed without the consideration of vacuum pumping but is kept inside a cavity box which can provide a clean and safe environment for the cavity mirrors. The cavity box is made from plexiglass, with two wedged windows which allow for the incident, reflection and transmission beam accesses for the cavity. There is also a feed-through BNC connector for the connections of PZT cables. The assembly of the cavity prototype with cavity spacer inside the box is illustrated in Fig 4.5.

4.4 Laser setup and mode-matching

In order to couple the laser beam into an optical cavity with high efficiency, it is necessary to match the mode of the Gaussian beam and the cavity fundamental mode. This process is usually referred to as mode-matching. On the one hand, the cavity modes are determined once the cavity geometry is fixed, usually the fundamental mode is Gaussian and has the largest power coupling efficiency. On the other hand, the laser mode is also Gaussian and usually has certain divergence, this divergence can be determined by measuring the beam size at different positions. The purpose of mode-matching is to find a pair of lenses to shape the laser mode to match the cavity mode.

4.4.1 Laser beam propagation

The laser beam that we use for coupling into the cavity is the output of a fiber-EOM (Jenoptik PM705), the fiber output is through an integrated collimation lens. The beam radius varies along the propagation direction according to [140]

$$w(z) = w_0\sqrt{1 + (\frac{x - x_f}{z_R})^2}, \tag{4.20}$$

where x_f is the position of the beam focus, $z_R = \frac{\pi w_0^2 n}{\lambda}$ is the Rayleigh range. By measuring the beam waist along the propagation direction, we can fit the data to derive the beam waist w_0 and the focus position x_f.

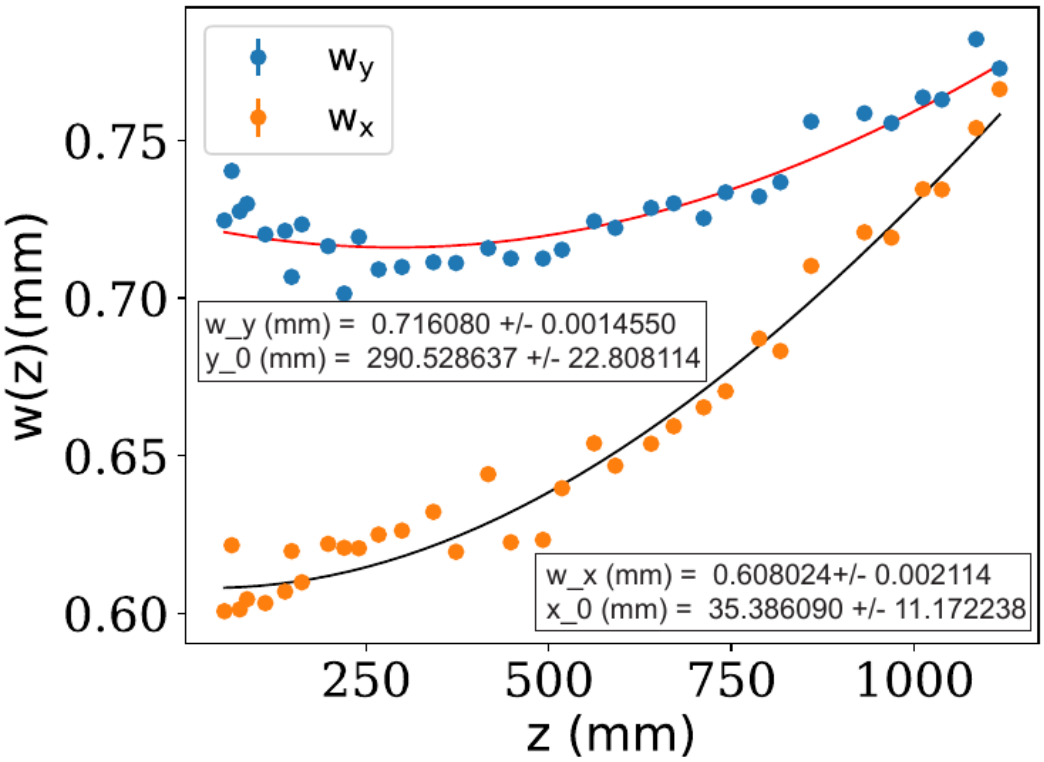

Figure 4.6: Laser beam waist measurement. The laser beam waist from the output of the fiber-EOM is measured with a CCD camera at different distances, the w_x and w_y are the beam size in the horizontal and vertical directions, respectively. The two lines are the fit of the data according to Eq. (4.20), which yields the focused beam size of $w_x \simeq 0.608$ mm and $w_y \simeq 0.716$ mm, respectively.

We use the CCD camera to measure the laser beam spot at various distances along the propagation direction. The image is fitted with the Gaussian function,

$$y = y_0 + A \exp\left\{-2\left(\frac{x - x_0}{w_z}\right)^2\right\}, \tag{4.21}$$

which yields the beam size w_z. The beam size in the horizontal and vertical directions as a function of distance is plotted in Fig. 4.6 as the orange and the blue dots, respectively. The two lines are the fit of the data according to Eq. (4.20), which yields the beam size of $w_x \simeq 0.608$ mm and $w_y \simeq 0.716$ mm. The waist at the focus is chosen as the geometric mean, which is $w_0 \simeq 0.660$ mm. The cavity mode is calculated based on ABCD matrix. From Fig. 4.1 it is shown that the target beam waist of the cavity should be 0.159 mm.

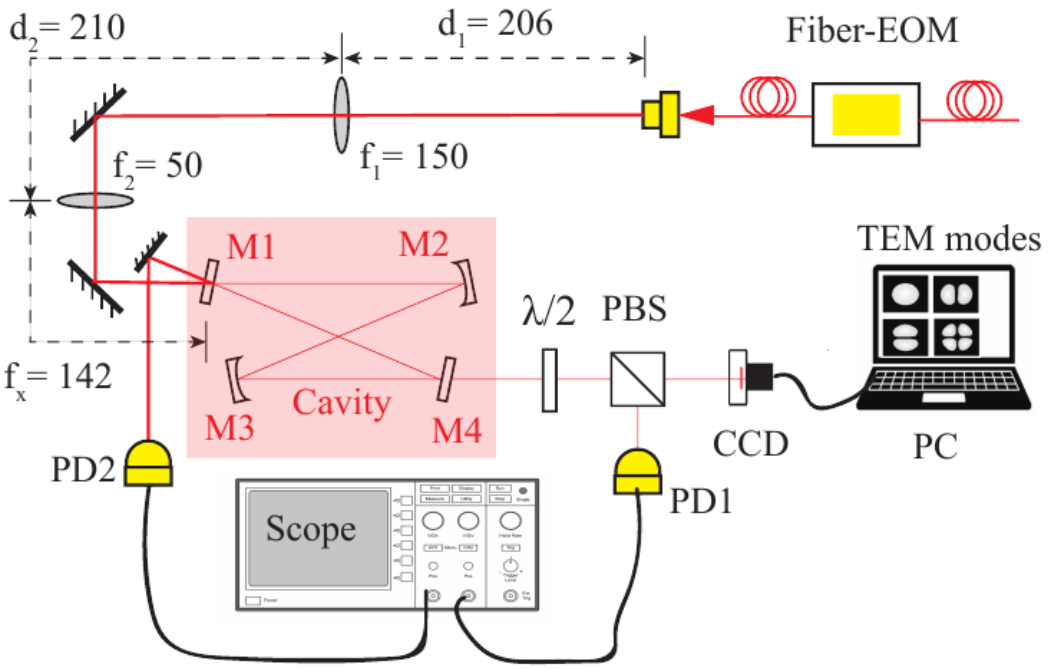

Figure 4.7: Laser setup for mode-matching. The laser cavity mode-matching is realized with a pair of lenses, positioned at the calculated distances. The laser beam provides a reference for cavity building and alignment. The CCD camera is used to monitor the cavity transmission modes, the two PDs are used to detect the transmission and reflection power, providing an indication for laser-cavity coupling efficiency.

4.4.2 Laser cavity mode-matching

When the initial beam waist (laser mode) and the target waist (cavity mode) are known, we need to find a pair of lenses to perform the mode-matching. We choose two lenses with focal lengths of $f_1 = 150$ mm and $f_2 = 50$ mm, respectively. Other combinations of lenses may also do the job, here we choose those due to their availability and convenience. We run a simulation based on the ray transfer matrix to minimize the difference between shaped laser waist and the target waist at the focus position, which yields the optimized distances d_1, d_2 and f_x, as shown in Fig. 4.7.

When the mode-matching parameters are determined, we place the lenses at the calculated positions and use the CCD camera to measure the beam size propagation after shaping. With the same analysis presented in the last subsection, we can confirm if the shaped beam has the right properties as we expect. Results confirmed that the shaped beam has a waist of 0.168 mm, which matches the target cavity waist of 0.159 mm.

4.4.3 Cavity alignment

When the laser setup is ready, we could put the four cavity mirrors one by one at the designated positions. However, the resonance condition of the optical cavity puts stringent requirements on the cavity alignment, also we want to build the cavity as close to the designed one as possible. This means that every angle, every distance should be kept exactly the same as the calculation. In order to facilitate the cavity alignment procedure, we consider the following steps.

Pre-check the mirror verticality and center The cavity mirrors are mounted on the homemade mirror holders with two plastic screws, as shown in Fig. 4.4. In order to reduce the degrees of freedom in the ring cavity alignment, we fix the vertical degree of freedom by setting all the mirrors vertically. This can be achieved by setting a horizontal collimated beam on the optical table, incident on the cavity mirror with 0° incidence angle so the reflection goes back. By tuning the micro screw at the back of the mirror holder, the reflection beam superimposes with the incidence beam, this confirms the verticality of the mirror with high precision. For curved mirrors M2 and M3, the laser beam is incident on the back facet which is plane.

It is practical to make sure that the laser beam hits the center of the cavity mirrors while circulating inside the cavity. In order to do this, we pre-check the height of the cavity mirrors and locate the mirror center. This can be done by illuminating a large size collimated beam on the mirror and project the image of the mirror on a CCD camera. Then by putting an iris mounted on a 3D translation stage before the cavity mirror, we can locate the center of the mirror on the camera. Then we can determine the mirror height by recording the iris center height. Finally, we mark the beam height on a paper pasted on a vertical bar, which could be a simple and good tool for checking the laser height during the cavity alignment.

Cavity path indicator The cavity beam should follow the designed geometry strictly. In order to provide a reference for the beam alignment, a cavity path indicator is made by printing on a paper the ring cavity path and the positions and angle orientations of each mirror holder. We print the paper with $1:1$ scale and paste it on the optical breadboard at the right position. While aligning each mirror, we should make sure that the transmissions and reflections of each mirror follow the path indicator.

Positioning of M1 The positioning of the first cavity mirror (M1) is crucial due to the fact that the following three mirrors would change accordingly. To

precisely position the M1, we need to pre-define a schematic where the incident, transmitted and reflected light beams strictly follow. We should also consider the fact that the 4 mm thick mirror substrate, with an index of refraction of $n = 1.455$ for fused silica, may shift the laser beam by 250 μm in transmission and 500 μm in the reflection, with the condition that the angle of incidence is 11.5°(0.2 rad).

Detection setup After the four mirrors are well positioned and fixed, we setup a detection system as shown in Fig. 4.7. In the cavity transmission, the half-waveplate and the PBS split the transmitted light into two and are detected by a CCD camera and a photodiode PD1, respectively. The cavity reflection is detected by PD2. When the laser is scanning, PD1 can detect the transmission peak while PD2 detects the reflection dip.

Since we have already preset the verticality of all cavity mirrors, the vertical alignment of the cavity should be well defined and can be checked through the cavity transmission modes in the CCD camera. In addition, the horizontal degree of freedom can be adjusted by tuning the rotary stage of the mirror holder. The optimization of the cavity alignment can be achieved when TEM00 mode appears and that the highest power in PD1 is obtained, which indicates the highest laser-cavity coupling efficiency. During the cavity alignment, one should always check that the cavity beams are following the path indicator and that the beams are hitting the center of each mirror.

4.5 Epoxying of cavity components

In the last section we align a cavity on a breadboard with four independent mirrors mounted on four mirror holders. The cavity geometry is as what we designed and the laser-cavity coupling is optimized, which leads to the maximum power in the fundamental cavity mode. The next step is to glue the four mirrors on a single cavity spacer, while keeping the cavity geometry unchanged. Additionally, mirror 1 should be supported on a PZT in order to tune the cavity length. The gluing work is fulfilled by epoxies.

In this section, we characterize different epoxies which are used for gluing cavity components. We present the electrically conductive epoxy (H20E), the thermally conductive epoxy (H77) and the Torrseal epoxy. Those epoxies are used in different situations and have different curing condition, however, they are all high-vacuum compatible and typically have a total mass loss of 0.2% or less at a temperature of 200 ℃ [134].

4.5.1 Characterization of different epoxies

Table 4.2: Epoxies used for gluing cavity components. Three types of epoxies used for gluing different cavity components are presented, with their characteristics, mixing ratio and curing conditions. Note that the curing of H20E and H77 requires 2 hours heating to become fully solid instead of what presented in the specs sheet. Abbreviations: P: PZT; S: spacer; V: V groove; H: heater.

Epoxy	Character	Mixing ratio	Curing condition	Interface
H20E	E-conductive	1:1	150 ℃ 2 hours	P-S, V-P, V-S
H77	T-conductive	100:15	150 ℃ 2 hours	H-S
Torrseal	Mirror protective	2.5:1	25 ℃ 24 hours	M-V

Table 4.2 summarizes all the epoxies used in our experiments and their corresponding characteristics. The interface indicates that the epoxy can be used to glue the two components. The schematic view of using different epoxy for different cavity components are depicted in Fig. 4.8.

Electrically conductive epoxy H20E The electrically conductive epoxy (H20E) is used to glue the PZT and the V-grooves to the cavity spacer and the V-grooves to the PZT, or more generally, the metal-to-metal contact. The epoxy is composed of two ingredients, part A and part B. Following the prescription, we mix part A and B with 1 : 1 ratio in a plastic tube with a 2 mm diameter needle. As a preliminary test of the epoxy characteristic and the curing condition, we glued a small piece of aluminum plate onto the surface of an aluminum block. We wound heating tapes on the aluminum block for heating and used a K-typed thermistor to monitor the temperature. After a few tries, we found that the super-polishing of the contacting faces and the pressing during curing process are necessary for a solid curing. We heat the aluminum block at 150 ℃ for 2 hours and the curing is very robust.

Then we start the gluing of the PZT and the four V-grooves. As discussed before, mirror M1 is positioned on a shearing-force piezo, which is used for modulating the cavity length. The PZT has two electrodes (V_+) and (GND), where (GND) is shorted with the PZT surface and thus to the cavity spacer. The applied voltage on the PZT electrodes can reach $\simeq 300$ V, thus it is of great importance to avoid shorting the two electrodes during the gluing process since the epoxy is electrically conductive.

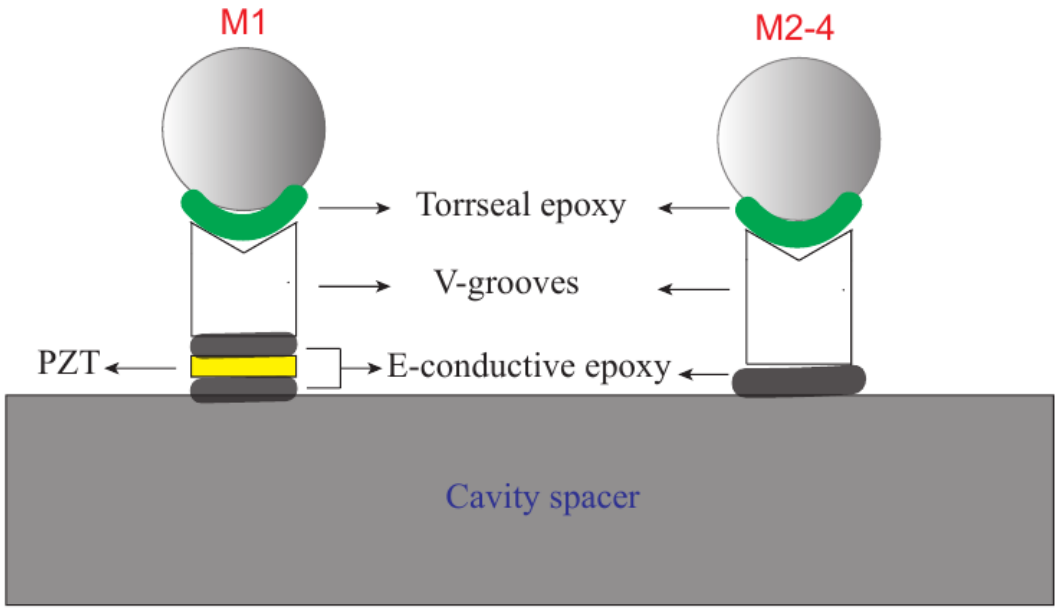

Figure 4.8: Schematic view of epoxying different cavity components. The choice of epoxy depends largely on the material to be glued. The E-conductive epoxy is used in the case of metal to metal contact, eg. V-groove, PZT and cavity spacer, while the Torrseal epoxy is applied when glass or ceramic is involved, like the cavity mirrors. T-conductive epoxy is used in the case that efficient heat transfer is required, for example, the glue of heaters.

Thermally conductive epoxy H77 The thermally conductive epoxy (H77) also has two components part A and B, part A is black while part B is amber. This epoxy is thermally conductive and electrically insulating which can be used for gluing the heaters to the cavity spacer. The curing condition for the H77 is 150 ℃ for 2 hours and it is tested in the same way as the H20E. The heaters are kapton insulated round metal foils with a diameter of 12.7 mm (from *Allectra* company), they can provide temperature control of the cavity spacer. In the case that the PZT range is not enough for cavity length tuning, the heaters can provide additional tuning of the cavity length.

After mixing the two parts A and B with a ratio of 100 : 15, the haters can be glued on the surface of the cavity spacer with the epoxy. The heaters should be pressed with a bar and the temperature of the spacer should be kept around 150 ℃ for 2 hours for curing.

Torrseal epoxy The Torrseal epoxy is used to glue the mirrors to the V-grooves. The choice of Torrseal epoxy in gluing the mirrors is motivated by the

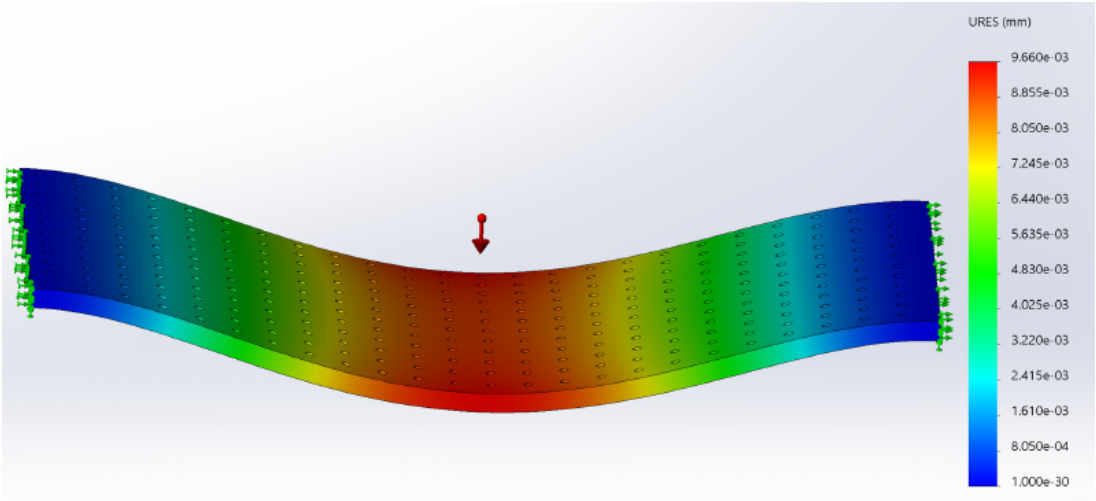

Figure 4.9: Bending simulation of the inverting breadboard. The simulation is performed using Solidworks simulation by fixing the two edge sides of a breadboard and gravity is applied as the only simulating force. The simulation result shows a maximum displacement of $\simeq 10$ μm.

fact that the curing of Torrseal does not require high temperature. In the case of H20E and H77, both require 150 ℃ curing condition and the baking of the cavity spacer. It is possible that the baking of the cavity mirror at high temperature can break the mirror, or at least damage the super-polished high-reflectivity surfaces, due to the uncontrolled thermal gradients as well as the fact that we have all sorts of optics around when the mirrors are close to the spacer. Therefore baking should be avoided when we glue the mirrors.

The Torrseal epoxy is a good option for gluing the mirrors since it can cure at room temperature (25℃) after 24 hours. It has two components which should be mixed at the ratio of 2.5 : 1 in volume before the application. In a test of the Torrseal epoxy we glue a fused-silica lens vertically on the surface of an aluminum block. The epoxy is cured after 6 hours at room temperature and became robust overnight.

4.5.2 Epoxying of cavity components

The epoxying process is facilitated by a vertical translation stage (elevator) shown in Fig. 4.10. The elevator can be fixed on the optical table with two base plates, an optical breadboard can be fixed on the top layer and the height of the breadboard can be tuned through the adjusting screws. We preset the breadboard to be horizontal and rotate the two adjusting screws simultaneously and with the same speed, this ensures that the translation of the breadboard is vertical.

The epoxying work requires precision to make sure that every components is glued at the designed position. It also requires caution since cavity mirrors are delicate so any dust or nonuniform heat distribution may damage the mirror surface. Finally, it requires patience since if one of the components is wrong, we need to break the glue and do everything again. To proceed with the epoxying of the V-grooves and the cavity mirrors in a way that fulfills those requirements, we follow the steps as described here.

- **Invert the cavity breadboard.** Flip the cavity breadboard, fix it on the elevator, check the horizontality of the breadboard. Re-optimize the cavity alignment. Since the breadboard has a limited stiffness, the effect of gravity may induce a bending of the breadboard, which induces a change in the cavity length and cavity alignment. In order to estimate how much this bending effect could be, a simulation is performed using Solidworks simulation by fixing the two edge sides of a breadboard and applying gravity as the only simulating force. The simulation result is shown in Fig. 4.9, giving a maximum displacement of $\simeq 10$ μm. By flipping the cavity breadboard, we observed a vertical misalignment from the cavity transmission modes. After optimization of the alignment, we re-found the fundamental mode, which is robust against the translation of the elevator.

- **Prepare the cavity spacer.** Wrap the cavity spacer with heating tapes and aluminum foils, fix the spacer on an independent breadboard, which is held by four pillars. The purpose of doing this is to reduce the heat dissipation to the optical table. During the heating, another small breadboard covered with aluminum foils will be put between the spacer and the cavity to avoid the heat transfer to cavity mirrors. The mirrors are protected by flowing clean nitrogen continuously.

- **Glue the V-grooves.** Use the cavity mirrors on the elevator to find the positions of the V-grooves on the spacer, then go up with the elevator, mark the positions of the V-grooves, place the E-conductive epoxy. Then place the V-grooves using a bar which can grab the V-grooves from the side, fix the bar on the optical table. Then go down with the elevator, verify that the positioning of the V-grooves is correct, go up with the elevator. Finally, do the heat isolation as described before, heat the spacer to 150 ℃ for 2 hours. After the E-conductive epoxy is cured, use the cavity mirrors to check the V-groove positions again.

- **Setup the monitoring optics.** Using the 497 nm green laser available in our lab, setup a monitoring system for each cavity mirror. Go down with

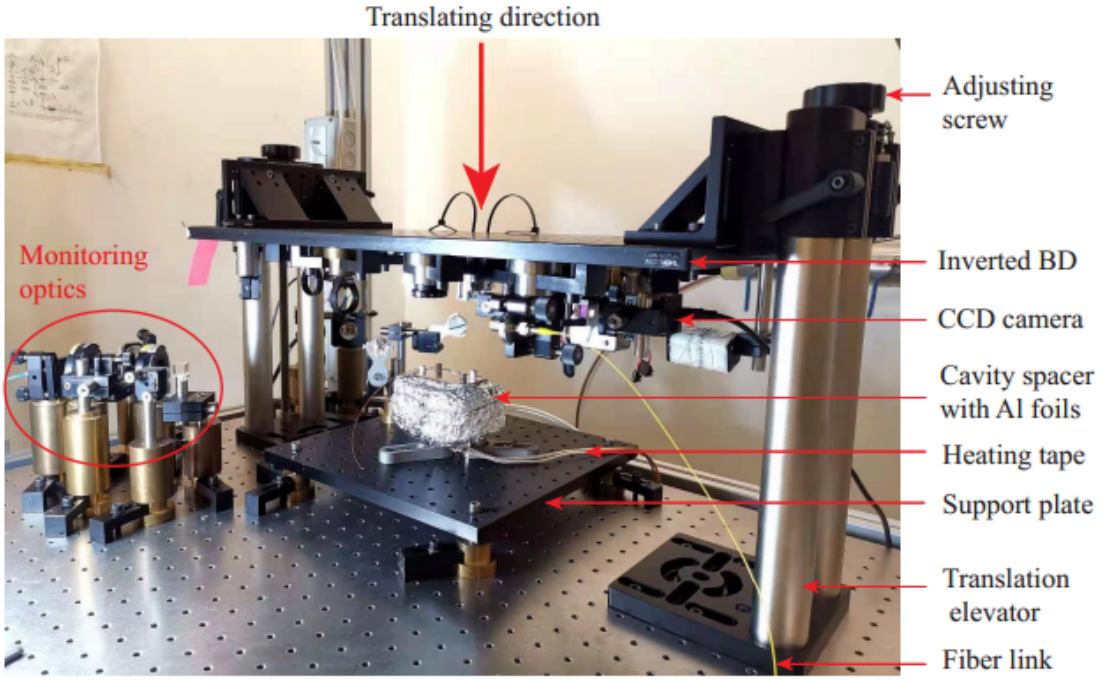

Figure 4.10: Epoxying of cavity components. The vertical translation stage (elevator) holds the inverted breadboard and can translate in the vertical direction by tuning the adjusting screws. The four-mirror cavity and the corresponding optics and the detection system are all mounted on the breadboard. The cavity spacer is put under the breadboard, wrapped with heating tapes and aluminum foils for heating, the small board which holds the cavity spacer is fixed on four pillars to reduce heat sinking to the optical table. The monitoring optics are arranged to send a laser beam to each mirror independently, the reflections are monitored during the curing of the Torrseal epoxy.

the elevator until the cavity mirrors approach close to the V-grooves but do not contact, direct the green laser beams on each cavity mirror and monitor the reflections. Then go up with the elevator, put the Torrseal epoxy on the V-grooves, go down with the elevator until the mirrors reach the Torrseal epoxy. Check the mirror reflections and monitor them until the end of the curing. This extra monitoring system proves to be useful since if the cavity misaligns during the movement or curing, we can distinguish immediately which mirror has moved from the reflection signals.

- **Removal of the mirror holders** After the Torrseal epoxy is cured and the cavity is still aligned, we can say that the epoxying is successful. The final step is to remove the two plastic screws that fix each cavity mirror to the mirror holder, and separate the cavity from the elevator. This removal procedure should be carefully done because any hit-force applied to the

mirrors can possibly break the Torrseal epoxy or misalign the cavity. Since the access to reach some of the plastics screws is limited, we developed a tool which resembles a screw driver but has a longer handle and thinner diameter to loose the screws. In fact, when we remove the screws, we observed a slight misalignment of the cavity mode but the epoxies are still robust. After all the screws are released, we went up with the elevator breadboard and remove the surrounding optics. Finally, the cavity is there.

As a fast confirmation that the cavity is not misaligned, we flipped the optical breadboard again and use the mode-matching setup to test the cavity alignment. This time, we align the cavity by tuning the input beam, with some effort we can see the TEM00 mode, which confirms that the cavity alignment is still good.

4.6 Cavity prototype assembly

4.6.1 Cavity prototype assembly

After the epoxying of the PZT, V-grooves and the cavity mirrors on the cavity spacer is done, we assemble this cavity inside a plexiglass box as a prototype cavity. This prototype cavity is used, first for the characterization of the cavity performance, second for the test of the cavity noise cancellation scheme and finally as a transfer cavity to bridge the 689 nm laser stability to the 813 nm lattice laser.

The assembled prototype cavity is shown in Fig. 4.11. We made a box from the plexiglass according to the geometry of the cavity spacer. The two side walls of the box are both with a one-inch hole, where two wedged windows are glued through the standard lens holder. The red lines in Fig. 4.11 show the incident, reflected, transmitted and circulating cavity beams. Inside the box lies the cavity spacer, which is on four pieces of rubber balls for vibration isolation. The four cavity mirrors are glued on four V-grooves, the V-groove which holds M1 is based on a PZT. The two electrodes of the PZT are connected to a BNC connector, which can be used for cavity length modulation. An extra hole is left near the bottom of the box, where a tube can be inserted to flow clean nitrogen. The whole cavity box is then fixed on the optical table by two clamps, in this way the vibration of the optical table will be damped before transmitting to the cavity.

4.6.2 Cavity mirror cleaning

The cavity mirrors are delicate optics and the surfaces are super-polished. Any damage or dust on the mirror surface may increase the scattering of light and degrade the cavity finesse. Therefore the cavity is assembled in a plexiglass box

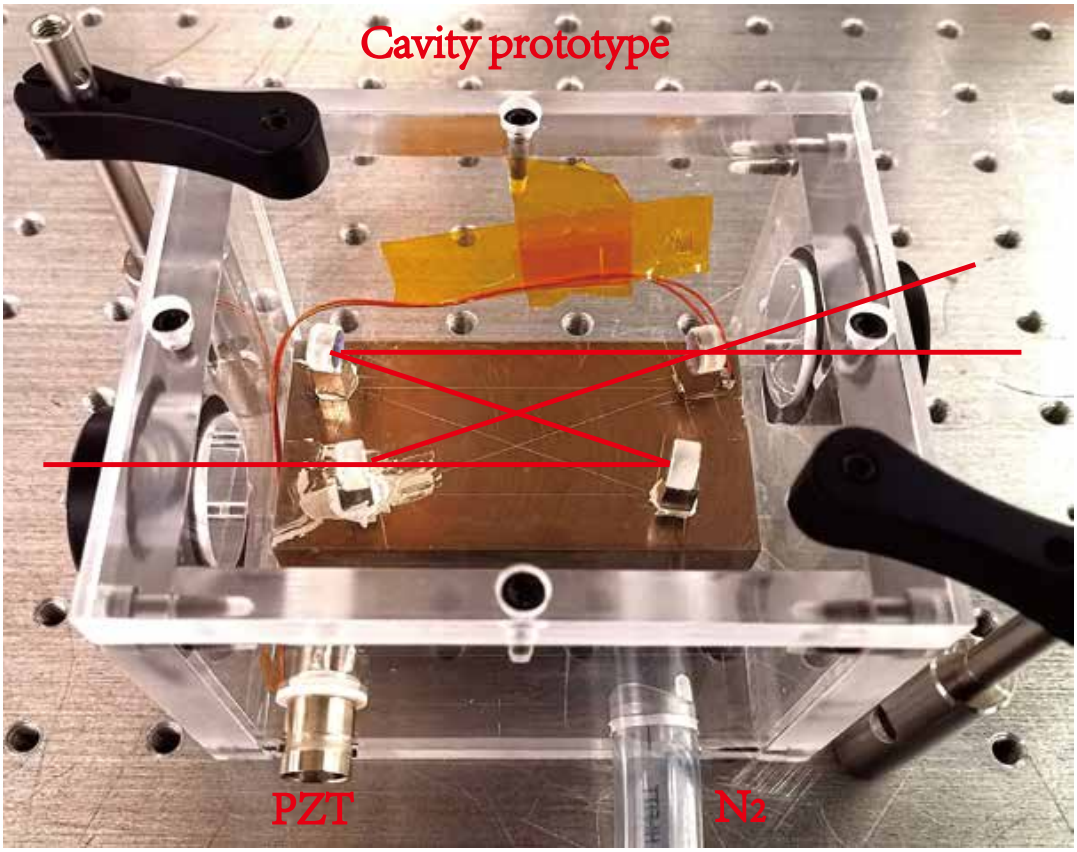

Figure 4.11: Prototype ring cavity. The ring cavity is assembled inside a plexiglass box with two wedged windows, the spacer lies on four rubber balls for vibration isolation. The two electrodes of the PZT are connected to a BNC connector, an extra hole is left for flowing in clean nitrogen. The plexiglass box is fixed on the optical table with two clamps.

and kept in the clean nitrogen flowing environment to avoid the dusts in the air. However, during the process of epoxying in the ambient air, it is unavoidable that the mirror surfaces will be contaminated, mainly by the dusts. When it happens, we need to clean the mirrors with great caution.

Following the suggestions from the *Fivenine optics* company, in order to clean the mirrors, we should first blow away the dusts on the mirror surfaces with flowing nitrogen. Then we use acetone to remove the remaining dusts, after acetone we use methanol to clean the remaining acetone. With this procedure we can clean most of the dusts on the mirror surface. It is appreciable that every time after cleaning, a sizeable finesse improvement can be obtained.

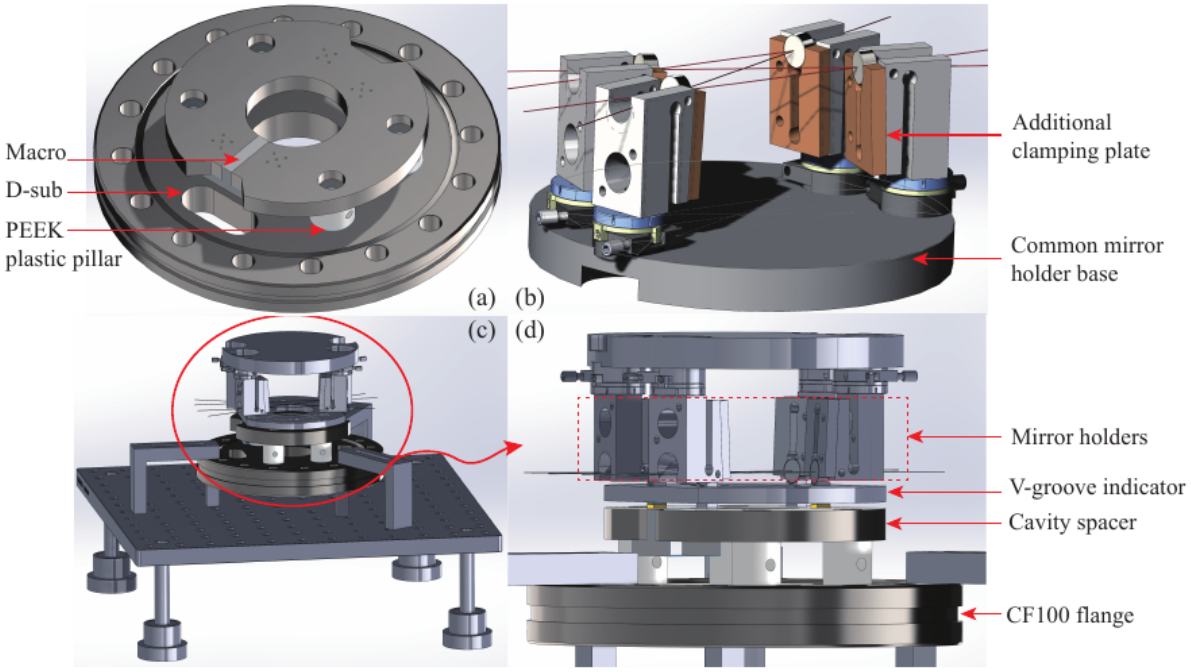

Figure 4.12: New cavity design and the improved cavity alignment tools. (a) Optical ring cavity spacer to be assembled into the vacuum chamber. (b) Improved cavity alignment tools, an additional clamping plate is added into the original cavity mirror holder (see Fig. 4.4) to facilitate the mirror holding, a common baseplate with fixed positions corresponding to the four mirror holders helps align the cavity in the initial stage. (c) Schematic for gluing the cavity mirrors with the new tools, details in the red circle is expanded in (d). (d) Cavity mirror gluing with the new tools, a circular baseplate with four rectangular holes corresponding to the positions of four V-grooves is used as an indicator for V-grooves.

4.7 Improvements and progress

There are some difficulties in the construction of the cavity prototype where the corresponding designs can be improved to facilitate the building of the in-vacuum squeezing cavity (see Fig. 4.12). Here I list the main difficulties that we met during the construction and discuss some improvements in the design.

- The mirror holder design. In the original design (see Fig. 4.4), the cavity mirror is fixed on the holder with two plastic screws from both sides. The fixing with screws exerts a non-even force on the mirror which tends to rotate the mirror. Also after epoxying the cavity mirrors it is difficult to remove the plastic screws due to the constrains of the space (see subsection 4.5.2).

An improved design of the mirror holder is presented in Fig. 4.12 (b), where an additional plate is fixed on the original holder which can clamp the cavity mirror with the curved face by exerting a force between the two halves through a screw. Also in this case one can release the mirrors from the external side of the cavity therefore the space constrain is relaxed.

- Common baseplate design. The original idea is to use four independent mirror holders for each mirror. At the initial stage of cavity alignment, a path indicator is used by printing on a paper the corresponding positions of the mirror holder baseplates and the laser paths. This procedure involves the degree of freedom of four baseplates. Although it is helpful to prove that our cavity alignment procedure is applicable, once it is proved, the freedom of movement of four baseplates can be reduced to only one.

  Indeed, in the new design (see Fig. 4.12), a common baseplate with four fixed positions is used instead of four independent baseplates. This new design reduces the degree of freedom, therefore facilitates the cavity alignment and improves the overall stability of the cavity.

- V-groove indicator. In the cavity prototype (see subsection 4.3.2), the positioning of four V-grooves on the cavity spacer is indicated by marking on the spacer with a cutter, which is not precise. Also during the epoxying of the V-grooves with the H20E epoxy, the curing requires pressing which may displace the positions of V-grooves.

  In order to avoid those problems, a V-groove indicator is designed, which is a circular plate with four rectangular holes corresponding to the positions of four V-grooves. This indicator can be a reference when the V-grooves are positioned, also it prevents any movement of the V-grooves during the epoxying.

The construction of the in-vacuum squeezing cavity is illustrated in Fig. 4.12. The ring-shaped cavity spacer is fixed on the CF 100 flange with four PEEK plastic pillars (Fig. 4.12 (a)). The ring of the spacer is interrupted by inserting a piece of electrically insulating material called Macor, which can significantly suppress the Eddy currents in the material when variable magnetic fields are applied during the laser cooling of Sr. The electronic connections, including those for piezo electrodes, temperature sensors and heaters, are all assembled in a D-sub vacuum feedthrough with kapton-foil cables.

The schematic for epoxying the cavity mirrors with the new tools on the squeezing cavity spacer is shown in Fig. 4.12 (c), where the details in the red

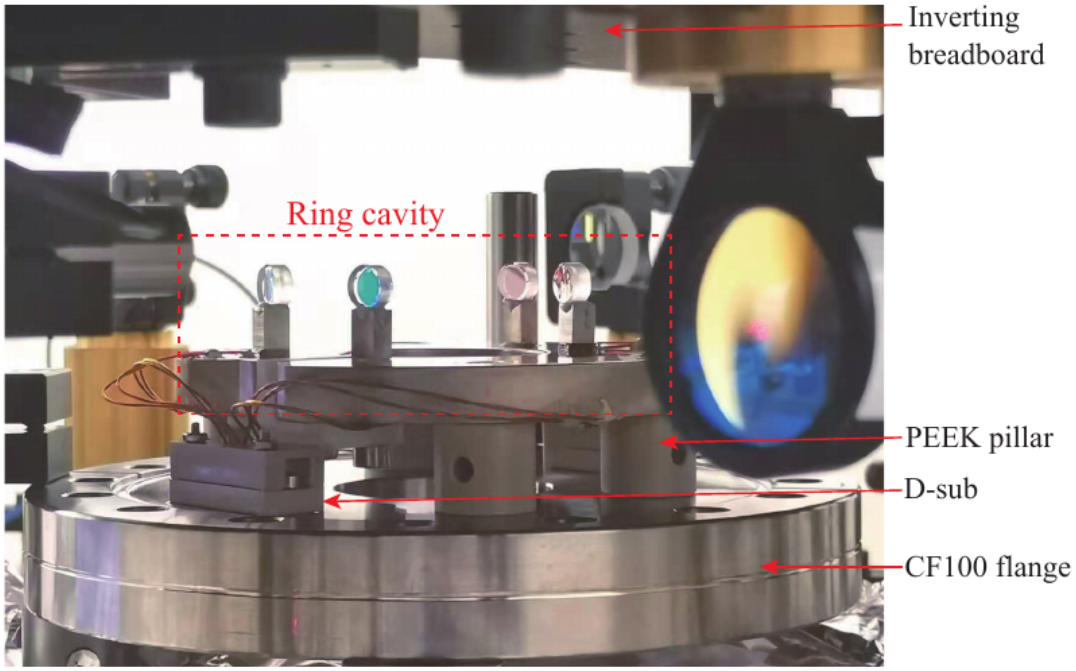

Figure 4.13: Real cavity construction. By the time I finish this thesis, a real cavity is constructed using the improved design and alignment tools, which can be assembled into the vacuum chamber and used for spin squeezing experiments.

circle are expanded in (d). The procedures are similar to subsection 4.5.2 but with the new tools the construction will be easier and more robust.

By the time I finish this thesis, a real ring cavity is constructed using the improved design and alignment tools, which can be assembled into the vacuum chamber through the CF 100 flange (see Fig. 4.13). The construction procedure is simplified thanks to the newly-designed V-groove indicator, since once the relative position of the V-groove indicator and the cavity mirrors is confirmed, we can heat the flange to cure the H20E epoxy independently, without affecting the cavity mirrors. With the help of those improvements, the construction of the new cavity takes only three weeks. In the future, this ring cavity will be assembled into a vacuum chamber, where low-temperature baking ($\leq$ 110 ℃) and vacuum pumping will be conducted.

4.8 Conclusions

In this chapter, a complete construction procedure of an optical ring cavity is presented. We aim at resolving the dilemma of the *tunability* and the *stability* in the construction of an optical cavity. A novel cavity mirror holder is designed

and tested which has the tuning freedom both from the horizontal and the vertical directions, and is able to be removed after epoxying the mirrors without changing the cavity alignment. Different types of epoxies are characterized and the procedures and considerations in conducting the epoxying are described in detail. Finally, a cavity prototype is constructed and assembled inside a plexiglass cavity box. This cavity prototype is characterized and used for demonstrating a cavity noise cancellation scheme in chapter 6. The improvements of the design based on the limitations we met are discussed and the progress of the real cavity building is reported. The methods and considerations presented in this chapter provides first-hand experiences for the construction of a general-purpose optical cavity in physics laboratories.

Chapter 5

Apparatus for atom cooling and squeezing detection

In this chapter we present the apparatus for the spin-squeezing experiment, except for the optical ring cavity which has already been discussed in chapter 4.

In section 5.1, the vacuum system for preparing a Sr MOT is presented, with the main focus on the novel science chamber and the MOT coils. Then in section 5.2, the laser systems for cooling and trapping Sr atoms and squeezing probe are discussed, a homemade optical shutter is also presented. Finally in section 5.3, a detection system is designed and characterizeed specifically for the purpose of weak light detection for cavity phase shift measurement, which features a low-noise and high gain.

5.1 Vacuum system

In this section the vacuum system used for laser cooling and trapping of Sr atoms and for the squeezing probe is discussed. The vacuum system used in this work is based on an existing apparatus which has already been described elsewhere [114]. In order to adapt it for our scientific purpose, we have kept the atomic oven and Zeeman slower while updated the science chamber and MOT coils. The ion pumps and some mechanical parts are also updated. The optical accesses for two stage MOT and squeezing cavity are also presented together with the corresponding vacuum parts.

5.1.1 Vacuum system overview

A top view of the updated vacuum system is shown in Fig. 5.1. We follow the trace of the Sr atoms inside the vacuum system from the source in the atomic

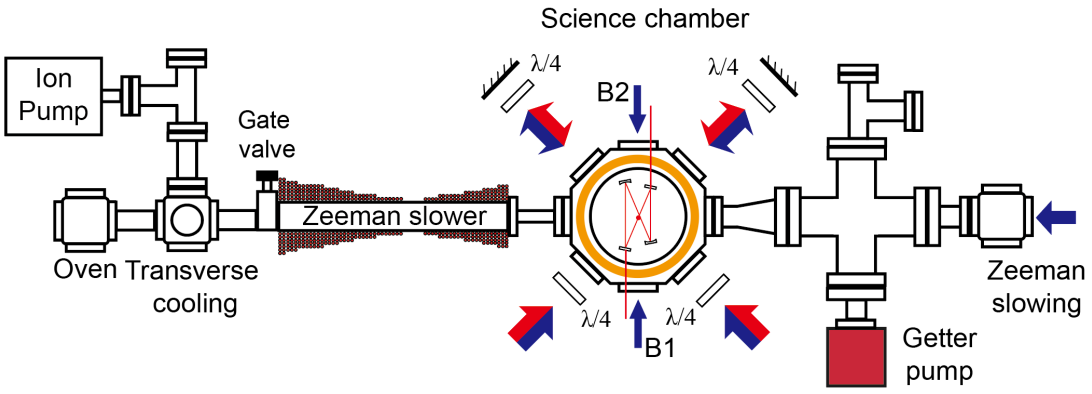

Figure 5.1: Schematic overview of the vacuum system. A collimated atomic beam is produced in the Sr oven and is slowed by the counterpropagating Zeeman slowing beam in combination with the Zeeman slower coils. The atoms are cooled and trapped at the center of the science chamber, where three pairs of orthogonal counterpropagating MOT beams (blue for 461 nm and red for 689 nm) and a pair of anti-Helmholtz coils generate the condition for magneto-optical trap. The optical ring cavity which is fixed on one of the flanges of the science chamber provides non-demolition measurement of the trapped atoms and induce spin-squeezing. The blue Bragg beams in the vertical direction are used for atom interferometry.

oven to the MOT in the science chamber.

The atomic source is provided by a compact in-vacuum oven [141] containing about 5 g of solid strontium (99.99% purity). The oven is operated at the temperature of 430 ℃ with a power consumption of 15 W. The atomic beam is collimated by a collimation tube filled with 120 stainless-steel capillaries with internal diameters of 100 μm.

After the oven, a transverse cooling cube is connected. The cube can be used for the transverse cooling of the atomic beam, which further reduces the transverse expansion of the atomic beam. In reality this cube can also be used for the spectroscopy purpose for locking of blue lasers on the $^1S_0$-$^1P_1$ transition. After the transverse cooling cube a gate valve is connected which can close the atomic beam when not needed.

The Zeeman slower consists of a tube with length $L = 30$ cm, around which two tapered coils are wound. The magnetic profile produced by the solenoid allows the compensation of the Doppler shift during the slowing [142]. In practice the solenoid is divided into two parts, with opposing independent current control in order to arbitrary set the input capture velocity and the output velocity for best loading of the MOT. The Zeeman slower can reduce the velocity of the atoms from $\simeq 430$ m/s at the oven to $\simeq 50$ m/s at the end of the Zeeman slower. Then

the atoms enter the science chamber and are further cooled and trapped by the magneto-optical trap. The science chamber and the MOT coils will be discussed in detail in the next subsection.

In order to maintain the high-vacuum condition, after the preliminary pumping stage, one 55 L/s ion pump (Agilent Technologies StarCell) and one getter pump (Saes Getters, Nextorr D 500-5) are used for the oven side and the science chamber side, respectively. The ion pump is attached to a cube connected to the oven, providing a residual pressure of about 10^{-8} mbar. The getter pump is an extremely compact pump able to absorb gases very effectively. It consists of a getter cartridge and a diode ion pump where the two parts are connected by a CF 63 flange. The getter cartridge can remove gases at room temperature without any need for electric power after the activation is carried out (500 ℃ for 1 hour). This configuration maintains a pressure of about $10^{-9} \sim 10^{-10}$ mbar level in the science chamber with low power consumption.

5.1.2 Science chamber and MOT coils

The science chamber is where the magneto-optical trap of the Sr atoms and the atom-light interaction in the cavity happens. In this subsection we describe the structure of the science chamber and the corresponding optical accesses. The novel MOT coils with efficient internal water cooling are also presented.

Science chamber The science chamber is based on a stainless-steel octagon chamber shown in Fig. 5.2. It has eight CF 40 viewports, of which six are used for windows and the remaining two are used for the connection to other vacuum parts. The front and back sides are CF 100 viewports. On the front side a CF 100 windows is fixed while on the back side a CF 40 window is attached on a CF 100 flange. On the inner side of the CF 100 flange the experimental cavity is fixed.

The optical accesses for the science chamber are also shown in Fig. 5.2. The three blue beams orthogonal to each other are the MOT beams, which are combinations of the 461 nm and 689 nm laser beams for the blue and red MOTs, respectively. The two oblique beams are shone from the edge of the windows instead of the center to avoid conflicting with the experimental cavity mirrors. The two vertical thin red beams are the cavity beams for non-demolition measurement, the reflections of the incident beam are redirected by angled mirrors glued on the cavity spacer to exit from the CF 100 window. The vertical thick green beam is the Bragg beam for atom interferometry. Other beams which are not shown in the figure are the repump beams, detection beams for fluorescence

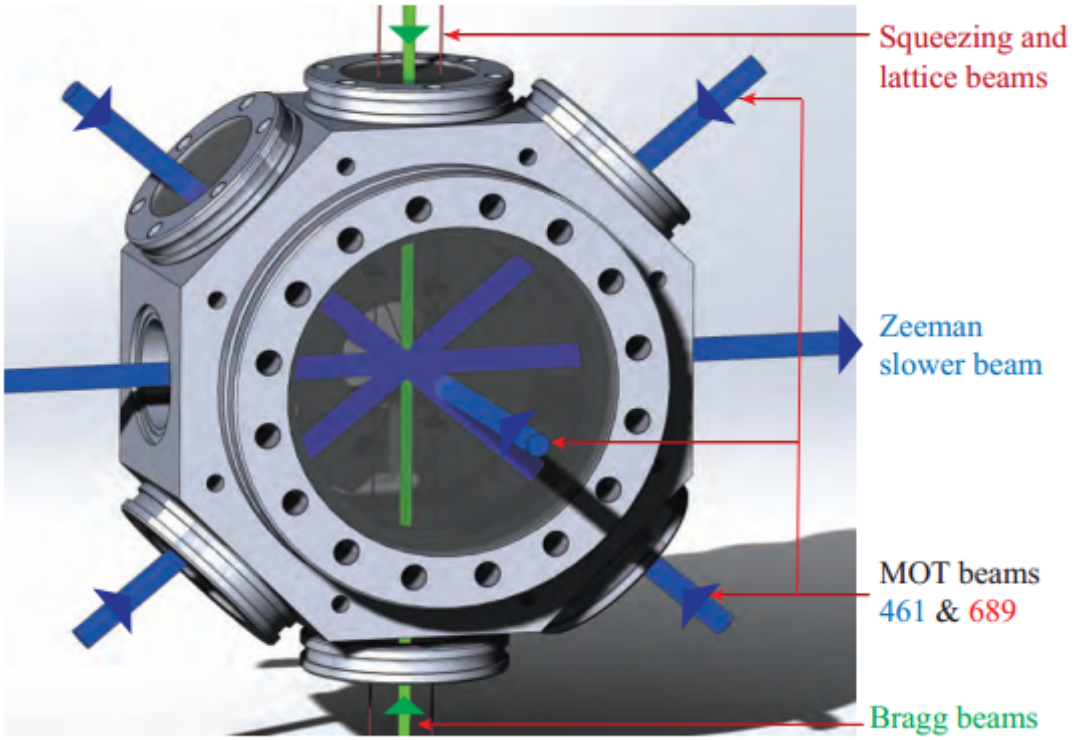

Figure 5.2: Science chamber and the optical accesses. The science chamber is an octagon chamber with six viewports for CF 40 windows and 2 viewports for vacuum parts connection. The front side is a CF 100 window and the back side is a CF 40 window fixed on a CF 100 flange. On the inner side of the CF 100 flange the experimental cavity is fixed. The optical accesses for the Zeeman slower beam, two-stage MOT beams, Bragg beams and the squeezing and lattices beams coupled into the ring cavity are shown. Other beams which are not shown in the figure are the repump beams, detection beams for fluorescence and image and EIT beams.

detection and absorption imaging and EIT beams.

MOT coils In order to generate the magnetic field and gradient required for the Sr MOT, we updated a pair of MOT coils so that it is compatible with our science chamber. Since in our case the MOT coils are put outside of the science chamber, the distance between the MOT coils and the center of the science chamber is large ($\simeq$ 7 cm). Therefore the current needed for generating the desired magnetic gradient is comparatively high ($\simeq$ 75 A) which leads to the undesired heating. In order to solve those problems, we choose a kind of coils made with a hollow core copper wire which enables efficient water cooling [143].

The MOT coils are customer ordered from Scanditronix company, a sketch of the MOT coils in anti-Helmholtz configuration is shown in Fig. 5.3. The copper

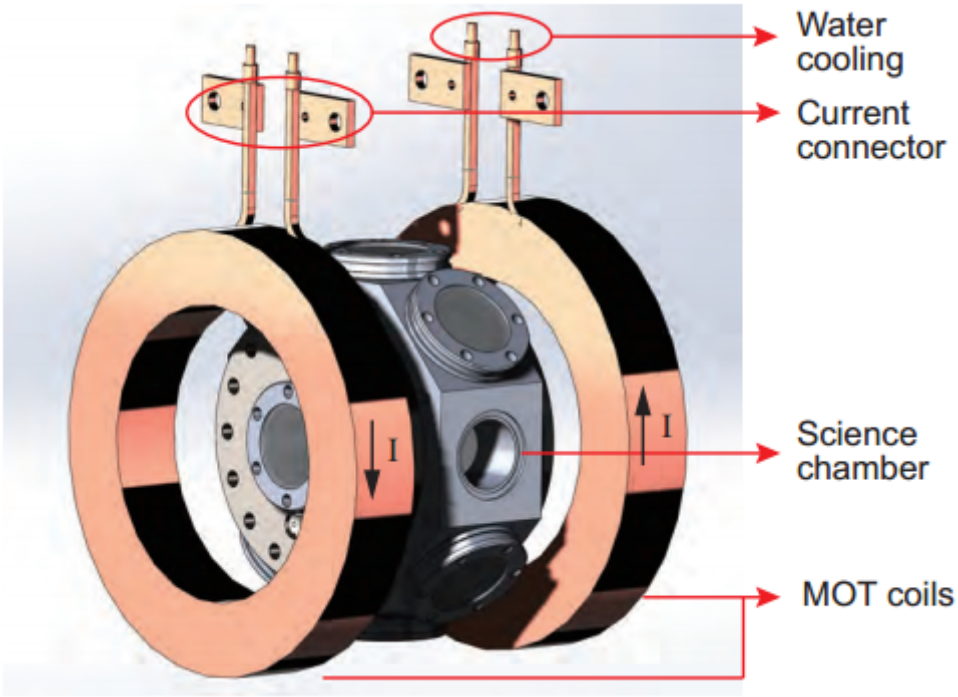

Figure 5.3: MOT coils schematic. Two MOT coils in anti-Helmholtz configuration provide the desired magnetic fields and gradients in the center of the science chamber. Internal water cooling is used to reduce the heat generated by the high operation current. The two flag connectors are used for current connections.

wire has a cross section of square with a dimension of 5 mm, the cross section for the hollow core has a diameter of 4 mm. The coils are wound with the number of both the axial and radial layers of 8, the inner and outer diameters of the MOT coils are 160 mm and 240 mm, respectively. At the two ends of the MOT coils, there are input and output water connectors for flowing water. Additionally, two copper flags are soldered near the water connectors to serve as general power supply connectors. A thermistor is attached to one of the copper flags to monitor the temperature.

The water cooling is provided by a chiller which has a power of 300 W in fully function mode. The fast switching of the magnetic fields can be achieved by using an IGBT in series with a DC current supply [143]. The current flowing through the coil can be stabilized by servo control of the gate voltage of the IGBT, a reference current servo schematic can be found in [144]. Overall, a switching time less than 1 ms can be achieved.

5.2 Laser system

In this section we discuss the laser systems used for the two-stage cooling and trapping of Sr atoms. This involves the 461 nm blue laser for the Zeeman slowing and blue MOT, the 689 nm red laser for the red MOT and the probe beam in the cavity, the 497 nm repump laser for recycling atoms from the metastable $^3P_2$ state. We also present the 813 nm lattice laser used to trap the atoms in an optical lattice circulating inside the cavity. Finally, we present a home-made optical shutter, which is used for switching on and off the laser beam for sequence control. Table 5.1 summarizes the main laser systems used in the experiment, except for the EIT laser system whose design still needs to be finalized.

Table 5.1: Laser systems for Sr cooling and squeezing

Lasers	λ (nm)	Transition	Function	Laser type
Red	689	$^1S_0$-$^3P_1$	Red MOT, squeezing probe	Master ECDL (HL6738MG) Slave, TA (EYP-TPA-0690)
Blue	461	$^1S_0$-$^1P_1$	Blue MOT, blue Bragg	Master ECDL (NDBA116T) Slave (NBD4916E)
Repump	497	$^3D_2$-$^3P_2$	Repumping	Infrared ECDL(EYP-RWE-1060) Frequency doubling
Lattice	813	-	Optical lattice	ECDL (EYE-RWE-0840)
EITs	679 688	$^3S_1$-$^3P_0$ $^3S_1$-$^3P_1$	EIT	ECDLs

5.2.1 Red laser

The 689 nm red laser system is used for laser cooling and squeezing and details can be found in [145]. Here we rearrange the laser system for the spin squeezing experiment, typically for the second stage cooling of Sr atoms and for the probing beam in the optical ring cavity inside the vacuum chamber.

The schematic of the red laser system is illustrated in Fig. 5.4. The red master is an ECDL locked to a high finesse Fabry-Pérot cavity and is stabilized to the spectroscopy signal obtained in a heat-pipe. Here we report the update and improvement of the red laser system, where we have optimized the mode-matching between the laser beam and the high-finesse cavity with a couple of lenses, implemented a master-slave configuration and use the slave laser to inject a tapered amplifier (TA). With this improvement we can get more laser coupling

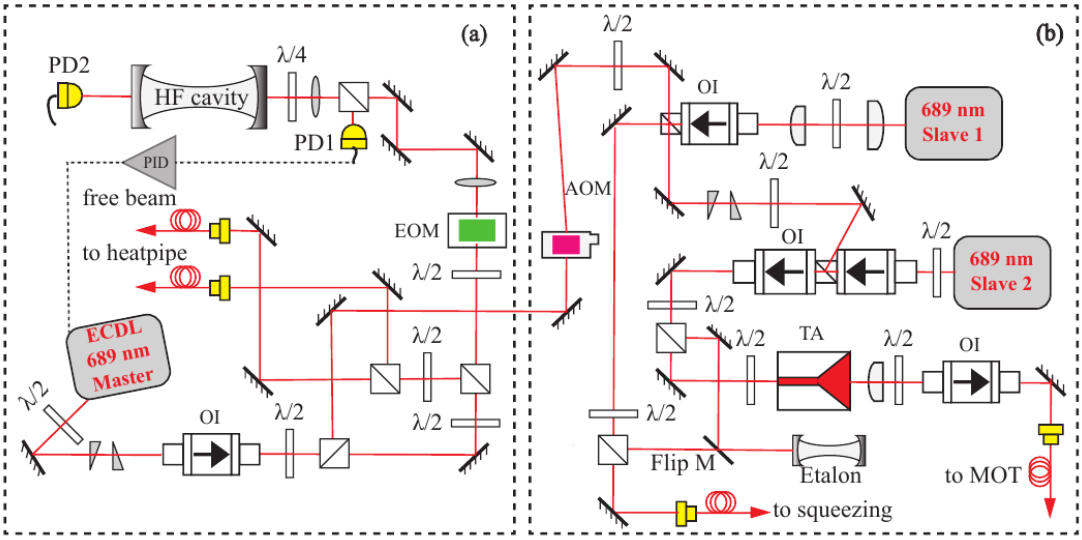

Figure 5.4: Optimized red laser system. (a) Red master and the cavity locking. The red master is an ECDL with an output power $\simeq$ 20 mW, a beam with power around 100 μW is phase modulated at 12 MHz with the EOM and is sent to the high-finesse ($\mathcal{F} \simeq 8860$) cavity for PDH locking. One beam of 5 mW is used for injection locking two slave laser, the other two beams are coupled to fibers and used for spectroscopy and future locking to an ULE cavity. (b) Power amplification. Two slave lasers are injected by the beam from the red master, both the outputs are split with a small portion ($\simeq$ 2 mW) to the etalon for injection checking, a flip mirror is used to switch between the two beams. Slave 1 is used for sending the light to another building via a 200 meters PM fiber, while Slave 2 is boosted by injecting a tapered amplifier. After power amplification, a total power of 180 mW is available.

efficiency to the high-finesse cavity and higher laser power. The improved red laser system can provide 180 mW power output with a narrowed FWHM linewidth of 20 Hz for a 100 μs averaging time, which is sufficient for the second stage cooling of Sr atoms and for the spin squeezing probing beam.

Mode-matching improvement

We first measure the finesse of the F-P cavity with the cavity ring-down method. The transmission of the cavity is monitored by a fast photodetector, when the laser is resonant with the cavity and the input beam is turned off abruptly, the photodetector records the decay of power inside the cavity. An exponential decay fit of the data gives a time constant $\tau \simeq 0.9596$ μs, corresponding to a cavity finesse of $\mathcal{F} = 8860$. Compared to the value from [145], it proves that after 12 years of function, the cavity finesse did not degrade.

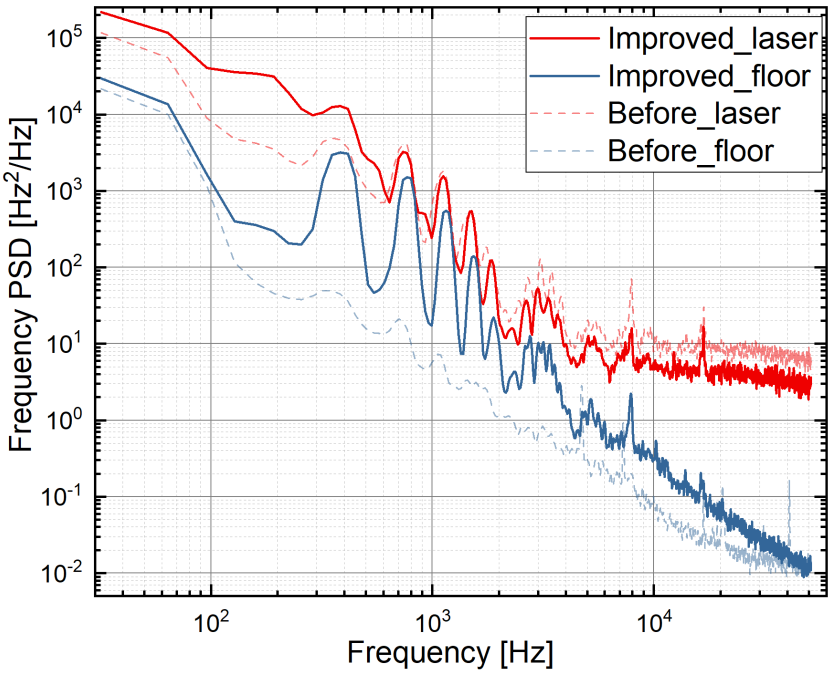

Figure 5.5: Frequency PSD of the high finesse F-P cavity. The frequency noise is measured before (dotted line) and after (solid line) the mode-matching improvement. The blue lines are the noise floors when the laser is out of lock, the red lines are laser noise PSD when the laser is locked to the high-finesse cavity.

We then optimize the laser-cavity mode matching. The laser beam size in the propagation direction is measured and the optimized lens position is determined. The alignment of the cavity is optimized through maximizing the transmission power in the TEM00 mode. The standard PDH method is used to lock to cavity, the frequency noise of the cavity is evaluated by sending the PDH error signal to a low frequency spectrum analyzer (FFT, Agilent 35670). Figure 5.5 shows the frequency noise of the cavity before and after the mode-matching improvement, the dotted lines are the noise floors when the laser is off-resonance with the cavity. The plot shows that the frequency noise of the error signal is on the level of 7 Hz^2/Hz, which corresponds to a laser linewidth of about 20 Hz.

Laser power amplification

In order to get higher available laser power, we adopt the master-slave injection setup to inject two single mode slave lasers (Slave 1 and Slave 2). Slave 1 provides a power of about 40 mW and is kept as a free beam for future use. Slave 2 provides a power of about 36 mW and is used to inject a tapered amplifier (TA). The TA

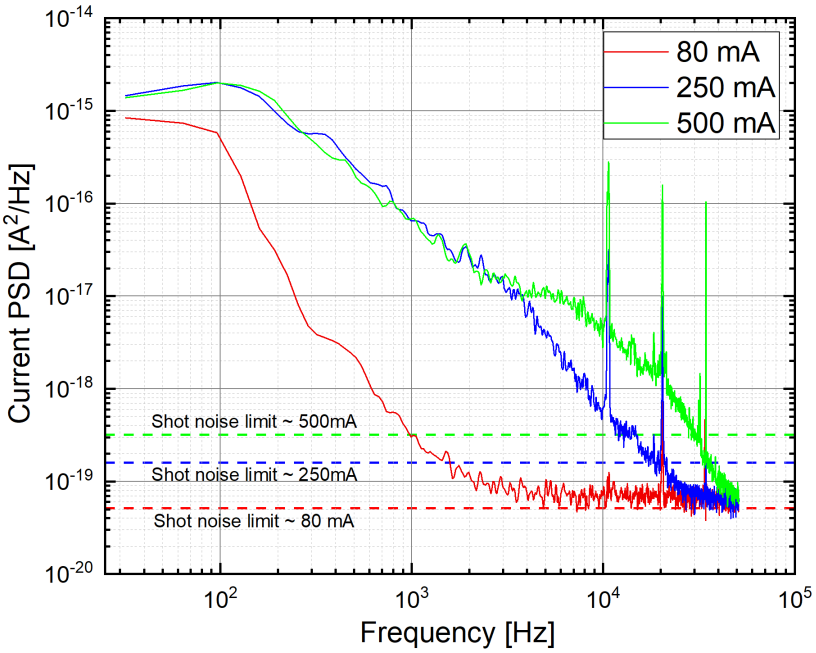

Figure 5.6: TA current supply noise performance. The curves show the TA current noise PSD measured at different operating current (80 mA, 250 mA and 500 mA, respectively). Dashed lines show the calculated electron shot noise at the corresponding current level. The TA current noise is close to the shot noise limit at an operating current of 250 mA.

can work at a current up to 1 A with a maximum output power of 180 mW.

A low-noise current supply is built to drive the TA with a maximum operation current of 3 A. Since the noise requirement for the red laser is high, any active sources like the current supply can add extra electronic noise which induces power fluctuations. Therefore we characterize the noise performance of the TA current supply and compare it to the current shot noise limit, of which the one-sided power spectrum density (PSD) is

$$\mathcal{S}_i(f) = 2eI \ , \tag{5.1}$$

where $e = 1.602 \times 10^{-19}$ is the electron charge and I is the current.

We apply the current supply output on a 50 Ω resistor and monitor the voltage PSD on the resistor with an FFT. The voltage PSD is then converted to the current PSD and the result is shown in Fig. 5.6. From the plot one can see that the current supply is current shot noise limited already at a operation current of 250 mA. For our typical application where $\geq$ 500 mA is used, the current supply is current shot noise limited.

The spatial mode of the TA is elliptical with a horizontal to vertical ratio of 3 : 1. This ratio matches the spatial mode of Slave 2, so no shaping lens or prism pair is used between the Slave 2 and the TA. The coupling efficiency of the TA is largely dependent on the polarization of the injection light, the polarization should be tuned with a half wave-plate to optimize the TA output when the operation current changes. The output of the TA is also elliptical, therefore a cylindrical lens is used to attain a 1:1 aspect ratio, making a circular mode and couple to a high power PM fiber. With an injection power of 25 mW, the TA output can reach 180 mW at the operation current of 700 mA. From the specification sheet of the TA chip, it can hold a maximum current of 1 A, however, for the consideration of longer lifetime, we always operate the TA below 700 mA. It is also noted that these TAs are observed (not only by us) to degrade over time quite significantly.

5.2.2 Blue laser

The blue laser at 461 nm is used for the Zeeman slowing and for the first stage cooling of Sr atoms. Due to the large scattering rate of the $^1S_0$-$^1P_1$ transition $\Gamma = 2\pi \times 32$ MHz, the requirement for the laser intensity is high. Generally a total laser power of larger than 100 mW is needed.

Traditionally, second-harmonic generation (SHG) with doubling crystals are used to frequency double the 922 nm infrared light to produce 461 nm blue light. Different crystals like $KNbO_3$ [146], BIBO [147] and periodically poled $KTiOPO_4$ (PPKTP) [148] are used in a butterfly cavity configuration. With the SHG method, an output power close to 1 W is available. However, this scheme involves a 922 nm ECDL, a TA, a frequency doubling crystal and a ring cavity, which is expensive and cumbersome to operate. The stability of the laser intensity largely depends on the stability of the cavity, which is not easily controllable. The large size of the system also limits the application of transportable Sr clocks or atom interferometers.

Recently, thanks to advances in semiconductor technology, lasers emitting in the 450-460 nm spectral region have become available [149]. We use one such laser diode from Nichia to build an ECDL at the wavelength of 460.8 nm with an output power of about 20 mW. By injection locking of two other laser diodes, a total power of 150 mW is available, which is sufficient for the Sr cooling experiment. Most recently, the blue laser diode with an output power $\simeq$ 500 mW has become commercially available and can be used as a slave laser by injection locking [150]. The combination of this ECDL master and the high power slave can provide more than 500 mW blue laser power with fairly good single mode operation. This will

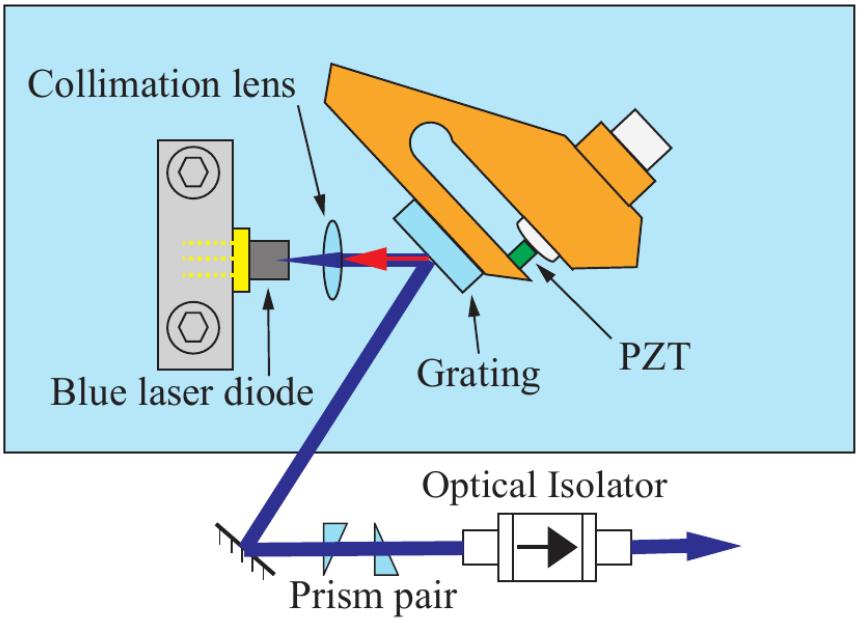

Figure 5.7: Blue ECDL in Littrow configuration. A collimation lens is used to collimate the beam. The first order diffraction of the grating (red arrow) is fed back to the laser diode while the specular reflection (blue beam) is the output. The PZT is used to fine tune the angle, which determines the frequency of the ECDL output.

facilitate the Sr cooling and trapping experiments.

In this subsection the construction and characterization of a blue ECDL with Nichia NDBA116T laser diode is discussed. The configuration of the ECDL and the procedure for external cavity alignment is described in detail. Finally, the characterization of the blue laser is presented.

Blue ECDL construction

The blue ECDL in the Littrow configuration is shown in Fig. 5.7. The blue ECDL is composed of a laser diode (LD, Nichia NDBA116T), a collimation lens (Thorlabs C230 TMD-A), a holographic grating (Thorlabs GH13-24V) and a piezoelectric transducer (PZT, AE0203D08F), which are all commercial parts, the rest of the system which are mechanical parts are manufactured by the Mechanical Workshop of LENS. The grating has a resolution of 2400 grooves/mm and the direction of the grooves is in parallel with the polarization of the laser. The first order diffraction is fed back to the laser diode to form an external cavity, while the specular reflection is the output of the laser. The PZT is fixed between a screw and the front plate to adjust the angle of the grating, this enables a coarse tuning of the angle through the screw and a fine tuning through the PZT. Changing the

angle of the grating can be used to select the frequency of the external cavity, therefore a frequency modulation can be applied through the PZT. The output of the ECDL has a dimension of 2 mm (1 mm) in the horizontal (vertical) direction, a prism pair is used after the laser output to shape the beam as a Gaussian beam. Finally, an optical isolator is used to extinguish the light from the optical feedback, which may lead to a damage to the laser diode.

The procedure of building the blue ECDL is as follows.

- **External cavity alignment.** We fix the laser diode on a specific holder and power it with a current supply. When the current reaches $\simeq$ 30 mA the spontaneous emission from the LD can be observed, using this spontaneous emission we align the collimation lens in order to make the beam collimated. Then we put the grating which is already glued on a flexible part, we tune the angle orientation of the grating in order to send the first order diffraction back to the LD. A homemade optical spectrum analyzer is used to monitor the output spectrum to distinguish the single-mode pattern due to the external cavity resonance. We increase the LD current and optimize the external cavity alignment until the lasing is observed.

- **Current modulation at threshold.** A current modulation circuit is built in order to apply external modulation on the LD current [151]. We set the current at the lasing threshold and apply a triangle wave modulation. We optimize the external cavity alignment by tuning the positions and angles of the collimation lens and the grating, in order to reduce the LD lasing threshold.

- **Gluing of collimation lens.** Finally, when the external cavity alignment is optimized, we fix the flexible parts that hold the grating, and glue the collimation lens on the baseplate. The collimation lens is fixed on a small aluminum piece ($20 \times 2 \times 10$ mm) which is held by a stable 3D translation stage. We found that the curing of the glue will exert a force on the collimation lens, and the external cavity is very sensitive to misalignment. During the curing of the glue, we apply the current modulation and monitor the threshold of the ECDL. We found a drift of the threshold and tuned the position of the collimation lens in order to keep the cavity alignment. After four hours of curing, the glue is fixed but we wait 24 hours before unmounting the stage used to align the collimation lens. Finally, the collimation lens is glued and the ECDL is constructed.

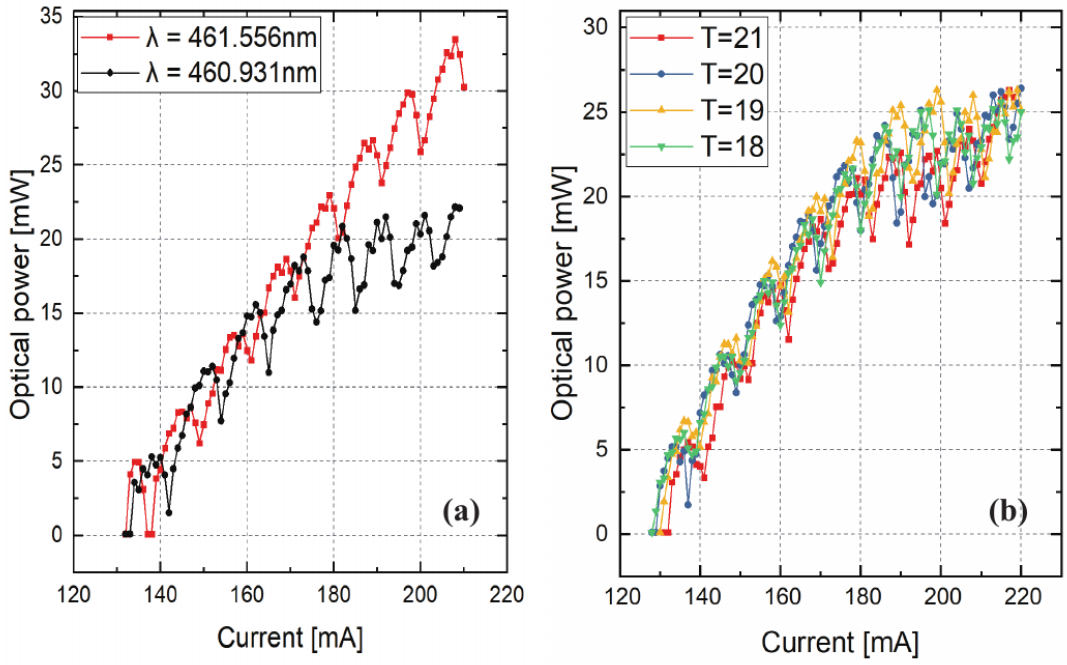

Figure 5.8: Performance characterization of the blue ECDL. (a) Power-current plot with different wavelength. At the target wavelength of $\simeq$ 460.8 nm, an output power of 20 mW is available with a current of 180 mA. (b) Power-current plot at different temperatures. An optimal temperature of 19 ℃ is used for the optimal output power.

Performance characterization

We characterize the blue ECDL performance after it is constructed. We observed a current threshold for lasing $\simeq$ 134 mA with the external cavity, the output power can be tuned to the maximum of $\simeq$ 23 mW at the current of $\simeq$ 210 mA and wavelength close to 460.9 nm. However, in order to keep a longer lifetime of the blue LD, we operate the laser around 180 mA, where 20 mW power is available. From the specification sheet, we know that the LD is selected from a patch with a centered wavelength of 461 nm. We can tune the angle of the grating and monitor the wavelength of the laser beam with a wavemeter. We measured two power-current traces at the wavelength around 461.5 nm and 460.9 nm, respectively, as shown in Fig. 5.8 (a). In our aimed wavelength of 460.862 nm, which corresponds to the $^1S_0$-$^1P_1$ dipole transition of Sr, we obtain a maximum power of $\simeq$ 20 mW.

We tune the laser frequency close to 460.86 nm and test the performance with temperature variations. The temperature sensing and control of the ECDL is achieved with a thermistor and a Peltier device put under the aluminum base-plate. We measure the power-current trace with different temperatures as shown

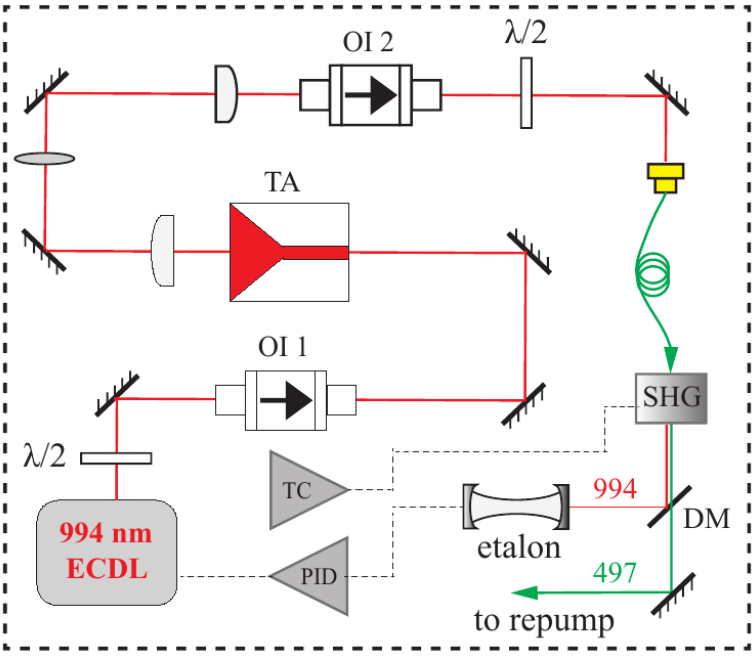

Figure 5.9: Schematic view of the repump laser. The 994 nm ECDL in Littrow configuration serves as a master and injects a TA for power amplification. A SHG module consisting a frequency doubling crystal converts the 994 nm laser to 497 nm green laser. The frequency stabilization of the master laser is achieved by locking the 994 nm laser to a F-P etalon. Abbreviations: TC, temperature control; DM: dichroic mirror.

in Fig. 5.8 (b). The temperature control can also be used to fine tune the laser wavelength. Finally, we keep the temperature of the ECDL at 19 ℃.

5.2.3 Repump laser

As has been discussed already in Section 2.1, there are two commonly used repumping schemes in the Sr Blue MOT. The first scheme is to use two repump lasers at 707 nm and 679 nm corresponding to the transitions of $^3S_1$-$^3P_2$ and $^3S_1$-$^3P_0$, while the second scheme involves only one laser at 497 nm, corresponding to the transition of $^3D_2$-$^3P_2$. The advantage of the second scheme is obvious, we need only one laser instead of two. However, due to the limitation of diode laser technology, the green laser diode at 497 nm has been made commercially available only recently. A first demonstration of the green ECDL working as the repump laser for Sr cooling is achieved by [152]. Here in our lab, we use the 497 nm repumping scheme with frequency doubling of a 994 nm infrared ECDL [145].

The schematic of the repump laser system is shown in Fig. 5.9. In brief, a

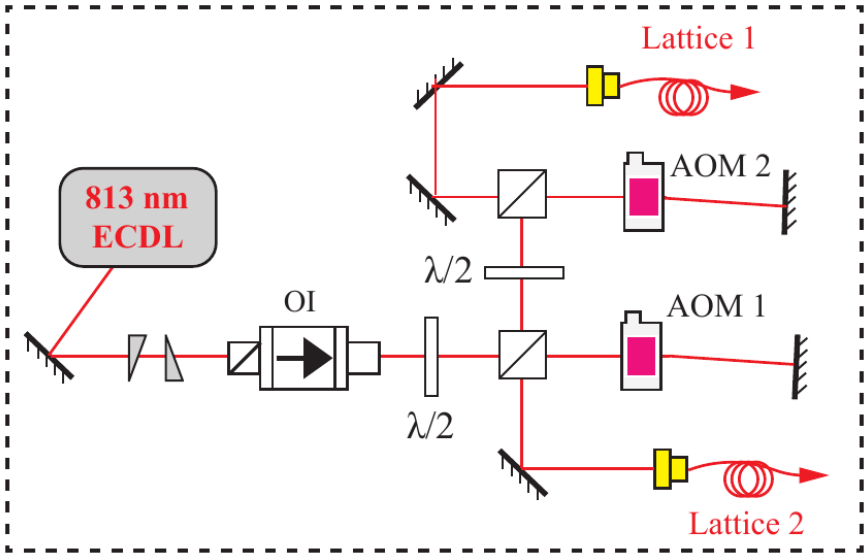

Figure 5.10: Schematic view of the lattice laser. The output of the 813 nm ECDL is split into two and are independently modulated by two AOMs in double-pass configuration. The two lattice beams in counter-propagating configuration forms the optical lattice inside the optical ring cavity.

994 nm ECDL in Littrow configuration provides a output power of about 22 mW, of which about 18 mW is injected to a TA. The TA gives an output power of $\simeq$ 450 mW at the operation current of 3.4 A. The output of the TA then injects a fiber coupled SHG module with a frequency doubling crystal inside, which provides the 497 nm output. The output of the SHG module is a combination of 497 nm laser and some remaining 994 nm laser, which are split with a dichroic mirror. The transmission (497 nm) is coupled to a fiber and sent to the MOT, while the reflection (994 nm) is sent to a F-P cavity for stabilizing the frequency of the master ECDL. This system can deliver more than 20 mW of green light, which is sufficient for our purposes.

5.2.4 Lattice laser

The lattice laser at 813 nm forms the optical lattice which can confine the cold atoms in its potential. In our case, two lattice lasers in counter-propagating configuration are coupled to the optical ring cavity from M1 and M4, respectively, as shown in Fig. 5.10. In this configuration, the atoms are confined in the lattice potential and the non-demolition probe can be performed homogeneously.

The 813 nm lattice laser is based on an ECDL similar to the blue laser. A total output power of about 80 mW at the operation current of 160 mA is achieved.

The laser output is split into two parts that are independently modulated with two AOMs in double-pass configuration. The outputs are coupled to optical fibers and are sent to the optical ring cavity in counter-propagating configuration, the frequency modulation on the two beams through the two AOMs can provide an acceleration to the cold atoms confined in the lattice.

5.2.5 Optical shutter

In our laser system, all the laser beams should be controlled with a certain sequence in accordance with the atom cooling and trapping procedure. This is usually achieved by AOMs, which have a fast response speed. However, AOMs cannot extinct the laser beam totally and the leaked light may introduce some perturbations to the atoms. It is a common practice to put an optical shutter before or after the AOM to block the light when needed. In some cases where only the switching of the laser beam is needed, an optical shutter can even replace an AOM.

Commercially available optical shutters are often expensive, bulky and noisy, while in typical laser cooling experiments usually tens of optical shutters are needed. In this subsection, we present a low-budget solution with homemade optical shutters which is proposed by [153] and has been adapted to fit our experiment. To build the optical shutter, we need a 3D-printed shutter body and blade, a DC motor and several simple electronic devices for the motor driving circuit. The optical shutter presented here is easy to assemble and robust for operation. We measured the activation delay and the jitter of the device with a focused laser beam. The results show that the jitter is within 100 μs in a running time duration of more than 4 hours, which fulfills the demand of our experiments.

Assembly

We take a reference from [153] where the design of the 3D-print file can be found in the supplementary materials. We redesigned the shutter body to fit our experimental conditions. Typically, the shutter body is glued on a baseplate instead of being fixed on a bar, therefore the base of the body is made flat. In addition, only one aperture instead of two is left for light beam going through. Finally, the front face of the shutter blade is covered with a piece of aluminum foil to avoid over heating due to lasers. The shutter body and blade are printed with a 3D printer from INFN mechanical workshop. The 3D design of the shutter and the assembled one are shown in Fig. 5.11 (a) and (b), respectively.

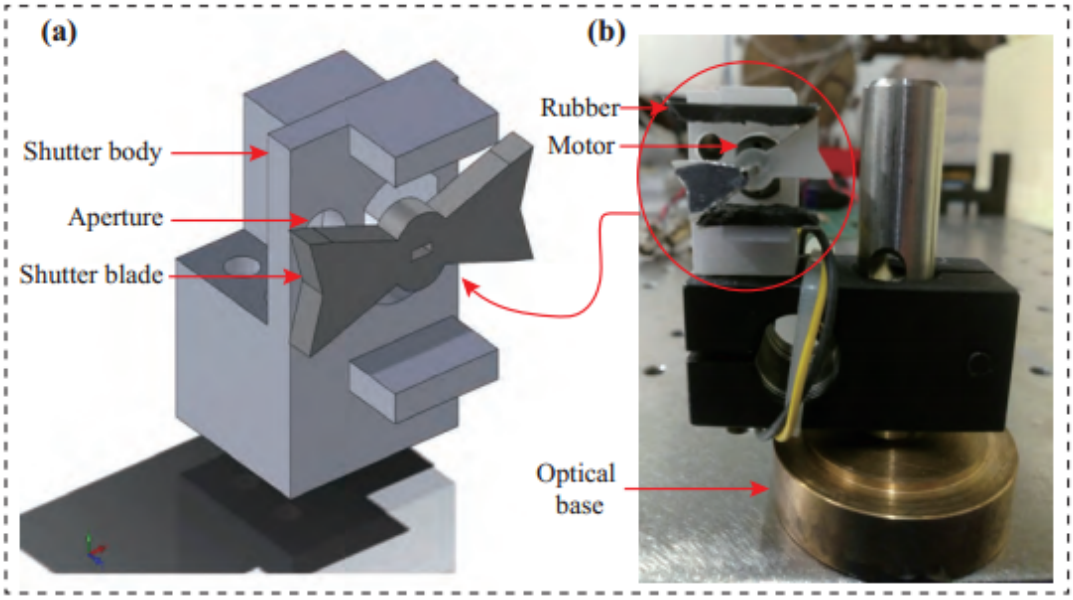

Figure 5.11: Optical shutter schematic. (a) Solidworks design of the shutter body and the blade; (b) assembled shutter glued on a baseplate with a pillar. The blade can be rotated by a DC motor and will be stopped by the two rubbers, the motor is controlled by a TTL signal, which can apply a sequence to turn on and off the aperture.

An DC motor is inserted inside the shutter body and can rotate the shutter blade according to the TTL signal applied on it. The shutter blade will be stopped by two pieces of rubber on the either side of the rotating direction to block the aperture or not, realizing the switching on and off of the laser beam. The electronic components and the schematic of the driving circuit for the motor are all available from [153].

Performance characterization

We characterize the performance of the optical shutter by measuring the activation delay both in a short term ($\simeq$ 3 minutes) and a long term ($\simeq$ 4 hours) time periods. The long term stability represents the jitter of the device, which is the main characterization in optical experiments.

We align a focused laser beam with two lenses and put the shutter aperture at the focus. A photodetector is put on the transmission of the shutter and the output is sent to an oscilloscope. We apply a TTL signal through the DC motor driver and send the same TTL to the oscilloscope. By setting the oscilloscope in the measurement mode of the time delay at rising edges between the TTL signal and the PD signal, the activation delay of the shutter is acquired. Figure. 5.12

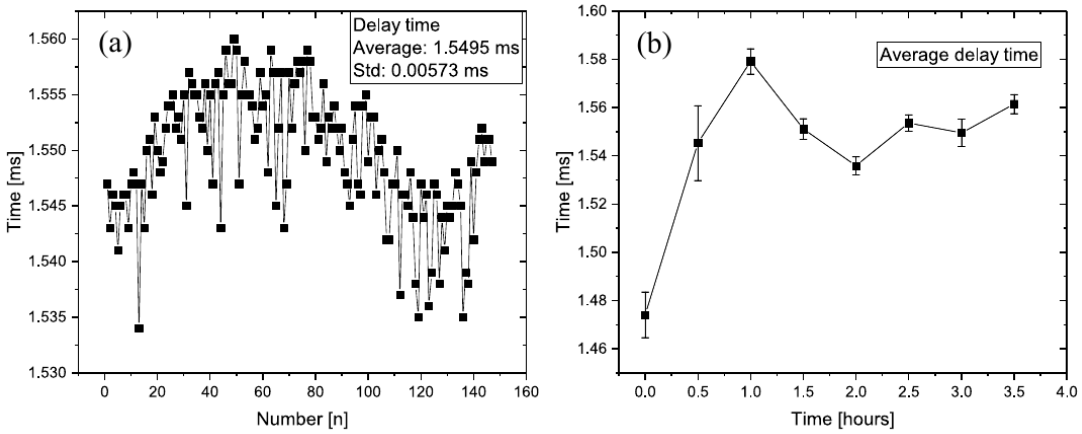

Figure 5.12: Optical shutter delay time and jitter measurement. (a) Activation delay in a time period of 3 minutes, each point is a record from the oscilloscope time delay reading. (b) Long-term measurement for 4 hours, each point is an average of 20 points.

(a) and (b) show the activation delay in a measurement period of 3 minutes and 4 hours, respectively, where in Fig. 5.12 (b) each point is an average of 20 measurements. From Fig. 5.12 (b) we estimate the jitter is within 100 μs in a time duration of 4 hours, which fulfills the typical requirement of $\simeq$ 1 ms in laser cooling experiments.

5.3 Detection system

It is essential to have a good detection system in any atom-optical related experiments to retrieve the information embedded in the light which interacts with the atoms. Usually there are two aspects that need to be considered when we choose or design a detection system: the signal to noise ratio (SNR) and the bandwidth [154].

Semiconductor photodiodes are widely used for the detection of light in the visible and near-infrared region due to the high quantum efficiency. The simplest photodetector (PD) is composed of a photodiode and a resistor, which converts the photo current into the output voltage with a trans-impedance gain of the resistance R. However, in this case the bandwidth is limited when a high gain R is adopted since the bandwidth is defined as $f_{-3dB} \simeq 1/(2\pi RC_j)$, where C_j is the p-n junction capacitance. It is therefore more practical to use the operational amplifier based transimpedance amplifiers (TIAs) to increase the bandwidth while keeping a high gain. The TIAs are active amplifiers therefore they also introduce some extra noise which needs to be addressed.

In this section, the requirements for the photo detection in our system are analyzed and the appropriate TIAs have been chosen. Later the TIA noise sources are specified and the total TIA noise is calculated based on the data sheets. The PD schematic is designed using the Eagle software and the PCB board is produced for the assembly of the PD circuit. Finally, when the PD is built, the bandwidth and the noise performance are characterized.

5.3.1 Detection requirements

In the cavity-aided spin squeezing experiments, a general PDH method [155] is used for cavity locking and the non-demolition measurement for spin squeezing. The atom-induced cavity resonance phase shift is retrieved from the PDH error signal, this shift is usually small and covered by the cavity noise. We propose a cavity noise-reduced phase shift measurement scheme in chapter 6 which can cancel the cavity length fluctuations as the common mode noise. It is therefore important to have a detection system which is low-noise and high-gain and is capable of detecting the phase modulated light in the PDH method.

Here we analyze the requirements for the detection system set by the squeezing experiment.

- **Low noise**. The noise for the detection system can be categorized into two parts, the photon shot noise (PSN) which is from the incident light, and the technical noise which originates from the dark current of the photodiode, TIA noise and circuit noise, etc.. The best situation would be that the PD is photon shot noise limited, which means that the PSN dominates over all the other technical noise sources.

- **High gain**. The transmission power of the cavity is usually very low, which gives a photo induced current of $I \simeq s \cdot P = 10$ nA, where $s \simeq 0.5$ (A/W) is the photo sensitivity of semiconductor photodiodes, P is the incident power. It is therefore necessary to have a high transimpedance gain to convert the photo current to voltage output. We expect for a transimpedance gain of $G \simeq 100$ kΩ which leads to an output voltage of 1 mV.

- **Bandwidth**. With the PDH method, the laser locked to the cavity is phase modulated at 10.5 MHz by an electro-optic modulator (EOM). It sets the minimum bandwidth of the PD and we expect a bandwidth of around 20 MHz. Note that we cannot set the bandwidth as high as possible since it will degrade the gain. Therefore it is always necessary to find a compromise between bandwidth and gain in designing a photodetector.

With all those requirements in mind, we choose the right photodiode and TIA. The Hamamatsu PIN photodiode S-5821-01 has a high quantum efficiency of $\eta_{PIN} \simeq 0.8$ and a photo sensitivity of $s = 0.47$ (A/W) in the wavelength close to ($650 \sim 700$ nm), which is a good choice. For the TIA, we considered two kinds of low-noise TIAs OPA 657 and OPA 847ID. In the following, we start with the calculation of the TIA noise.

5.3.2 Noise calculation of TIA

In order to characterize the noise spectrum of the TIA, we first establish the noise model, identify the noise sources, segment them into different categories and compute the rms noise of each category independently. Finally, we combine them by root-sum-squares to get the total noise [156, 157].

The noise model of TIA with a photodiode is depicted in Fig. 5.13. We assume an ideal op-amp as the noise is separated as voltage noise source V_A and current noise source I_A. The equivalent circuit of the photodiode is shown in the dashed rectangle in Fig. 5.13, where the dark current noise is modeled as I_d, $R_1 \simeq 10^8\ \Omega$ is a typical resistance for small geometry PIN photodiodes. The capacitance C_1 can be modeled as the sum over the photodiode internal capacitance C_d, the TIA differential capacitance C_{diff} and the TIA common-mode capacitance C_{cm} as

$$C_1 = C_d + C_{diff} + C_{cm}. \tag{5.2}$$

The value of $C_F \simeq 1$ pF is what would be expected from the stray capacitance with moderately careful layout. The thermal noise due to the large feedback resistor R_F is modeled as V_R.

The open loop gain of the circuit is

$$A(\omega) = \frac{A_{OL}\omega_A}{i\omega + \omega_A} = \frac{A_{OL}{\omega_A}^2}{\omega^2 + {\omega_A}^2} - i\frac{A_{OL}\omega_A\omega}{\omega^2 + {\omega_A}^2}, \tag{5.3}$$

where $A_{OL} = 3.2 \times 10^3$ for OPA 657, $\omega_A = 2\pi \times 500$ kHz is the cut-off frequency, where the amplification of the op-amp decrease by 3 dB. We also define

$$\frac{1}{\beta} = 1 + \frac{R_F(1 + i\omega R_1 C_1)}{R_1(1 + i\omega R_F C_F)}, \tag{5.4}$$

where β is the feedback factor. It is the amount of output voltage feedback to the input of the op-amp.

We calculate the total noise PSD by multiplying each noise contribution with their corresponding transfer functions and combine them by quadrature sum in the output port.

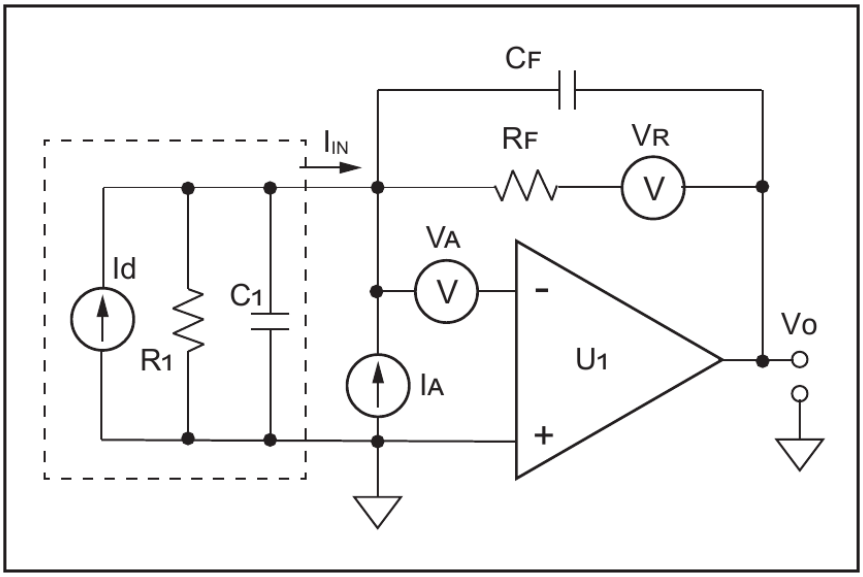

Figure 5.13: Noise model of the TIA for the photodiode application. The op-amp is assumed to be ideal while the noise sources are modeled as voltage noise V_A and current noise I_A. The equivalent circuit of the photodiode is shown in the dashed rectangle, which shows the dark current noise source I_d and equivalent R_1 and C_1. The thermal noise source of the large feedback resistor is modeled as V_R. Figure adapted from [156].

- **Voltage noise** The amplifier's internal voltage noise is modeled as V_A and the value can be found in the data sheet. The voltage noise contribution in the output PSD is

$$\mathcal{S}_{V_A} = |\frac{1}{\beta}\frac{A(\omega)}{1+\frac{1}{A(\omega)\beta}}|^2 \; {V_A}^2. \tag{5.5}$$

- **Current noise** The current noise contribution of the TIA in the output PSD is

$$\mathcal{S}_{I_A} = |A(\omega)\frac{R_F}{1+i\omega R_F C_F}\frac{1}{\frac{1}{\beta}+A(\omega)}|^2 \; {I_A}^2. \tag{5.6}$$

- **Dark current shot noise** The photo diode has a dark current which means that even with no light incident on the photo diode, there is a biased current I_d. The contribution of the dark current amplified by the TIA presented in the output is

$$\mathcal{S}_{I_d} = |A(\omega)\frac{R_F}{1+i\omega R_F C_F}\frac{1}{\frac{1}{\beta}+A(\omega)}|^2 \; {I_d}^2. \tag{5.7}$$

- **Johnson noise** The large feedback resistor R_F has a thermal noise which is also called Johnson noise. It can be modeled as the thermal noise source

$V_R = \sqrt{4KTR_FB}$, where $K = 1.38 \times 10^{-23}$ is the Boltzmann constant, T is the absolute temperature in Kelvin, B is the effective noise bandwidth. The contribution of the Johnson noise in the output is

$$\mathcal{S}_{V_R} = |\frac{A(\omega)}{R_F[\frac{1}{R_1} + i\omega C_1 + (\frac{1}{R_F} + i\omega C_F)(A(\omega)+1)]}|^2 \ {V_R}^2. \tag{5.8}$$

Finally the total noise is the root-sum-square of all above

$$\mathcal{S}_{total} = \mathcal{S}_{V_A} + \mathcal{S}_{I_A} + \mathcal{S}_{I_d} + \mathcal{S}_{V_R}. \tag{5.9}$$

We consider a photodetector based on the Hamamatsu S-5821-01 photodiode and OPA 657 transimpedance amplifier. From the datasheets we evaluate the values of $V_A \simeq 4.8$ nV/$\sqrt{\text{Hz}}$, $I_A \simeq 1.3$ fA/$\sqrt{\text{Hz}}$, and $I_d \simeq 35$ nA/$\sqrt{\text{Hz}}$. We calculate the noise contributions as analyzed above and the result is plotted in Fig. 5.14

From the calculation we can see that in the low frequency range the Johnson noise is dominating while at high frequency the voltage noise becomes dominant. In the whole spectrum the noise level is close to 100 nV/$\sqrt{\text{Hz}}$, which corresponds to a noise equivalent power (NEP) of 47 nW/$\sqrt{\text{Hz}}$. With those considerations in mind, we can start designing the photodetector circuit.

5.3.3 Photodetector design

The photodetector is based on a Hamamatsu photodiode S-5821-01 and a transimpedance amplifier OPA 657. The photodiode works in the reverse-biased mode and the TIA gives a transimpedance gain of 100 kΩ. The simplified schematic of the PD is shown in Fig. 5.15 (b). When light is incident on the photodiode, it generates a photo current, which is then amplified by the TIA with a gain of 100 kΩ. The output voltage is terminated with a 50 Ω resistor.

We use software *Eagle* to design the circuit on a printed circuit board (PCB) with surface-mount components (SMD). Using SMD components can further suppress the technical noise and increase the response speed, therefore alleviating the bandwidth limitation. We use two 12 V batteries as power supplies as they are extremely low noise compared to the DC power supplies. In order to supply the TIA, two ±5 V voltage regulators are used to convert the ±12 V to ±5 V. The biased voltage for the photodiode is provided by the −12 V battery. The PD schematic and the PD board on *Eagle* design are shown in Fig. 5.15 (a) and (c), respectively. The PCB board is commercially manufactured and the SMD components are soldered in the lab. Finally the PD circuit is assembled in an aluminum box in order to shield the ambient electromagnetic fields and the output of the PD is transported via a BNC connector.

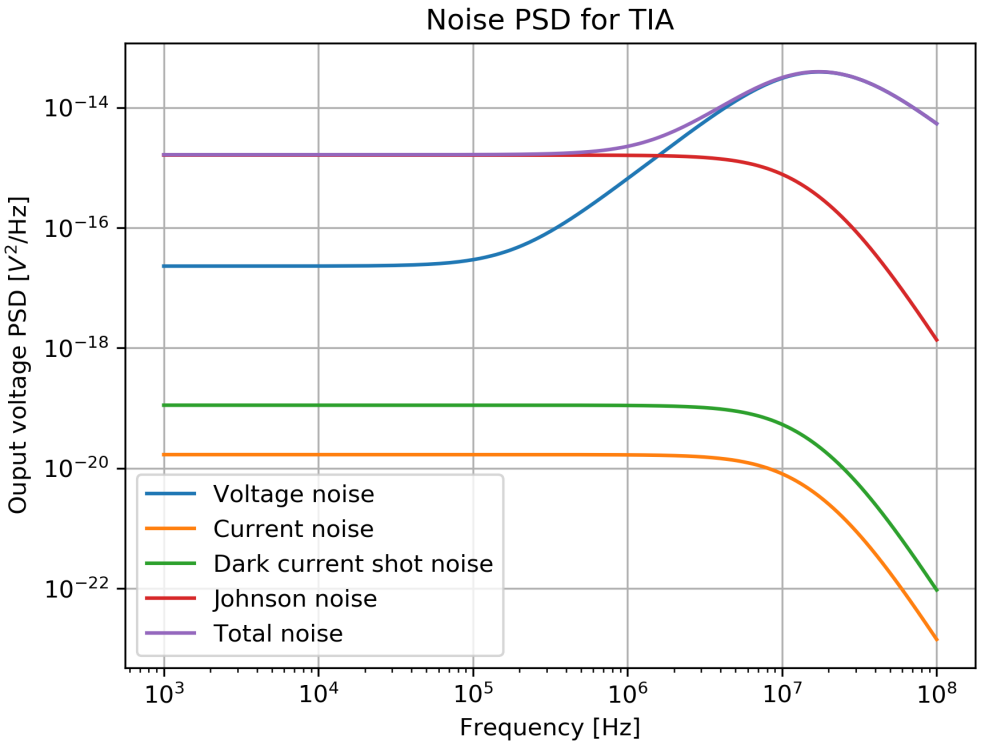

Figure 5.14: Calculation of the TIA (OPA 657) noise PSD. Presented here are the contributions from the TIA voltage noise, TIA the current noise, the photodiode dark current shot noise and the Johnson noise. The total noise is the root-sum-squares of all these noise sources.

5.3.4 Photodetector characterization

We characterize the PD performance with light sources and compare the results with the calculated values. The two main aspects that are interesting are the bandwidth and the noise performance.

Bandwidth measurement

The bandwidth of the PD is evaluated by measuring the beatnote of two laser beams. The frequency of the beatnote can be tuned with two AOMs which control the two beams independently. The output of the PD is therefore a sinusoid wave and is monitored by an oscilloscope, while the frequency of the beat note is tuned from 1 Hz to 20 MHz. We record the peak-to-peak voltage of the sinusoid signal as a function of the beatnote frequency, the result is plotted in Fig. 5.16. The red line shows a polynomial fit of the data, which yields a bandwidth of

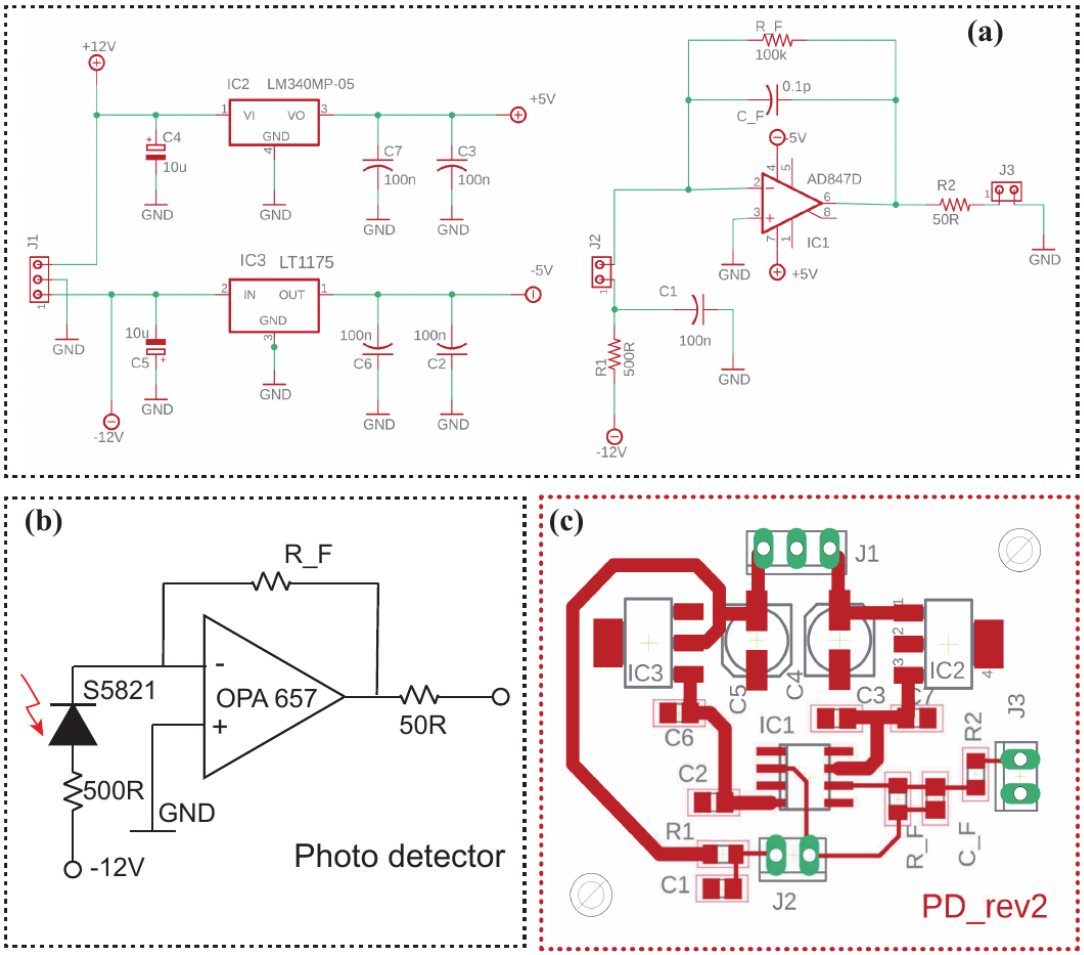

Figure 5.15: Photodetector design. (a) PCB schematic, the ±12 V battery supplies are converted to ±5 V via two voltage regulators, in the feedback network $R_F = 100$ kΩ while $C_F = 0.1$ pF is provided by the stray capacitance of the TIA. (b) Simplified schematic of the PD, the photodiode works in the reverse-biased mode, the output of the PD is terminated with a 50 Ω resistor. (c) PCB board, the board has a size of 40 × 40 mm with all surface-mount components, the board can be assembled in an aluminum box to shield the ambient electromagnetic fields.

$f_{-3dB} = 10.5$ MHz.

Noise measurement with thermal light

We characterize the PD noise by illuminating the photodiode with thermal light, which is assumed to be photon shot noise limited [154]. The output voltage of the PD is $V = R_F P s$, where $R_F = 100$ kΩ is the transimpedance gain, P is the incident thermal light power, $s = 0.47$ A/W is the photon sensitivity of

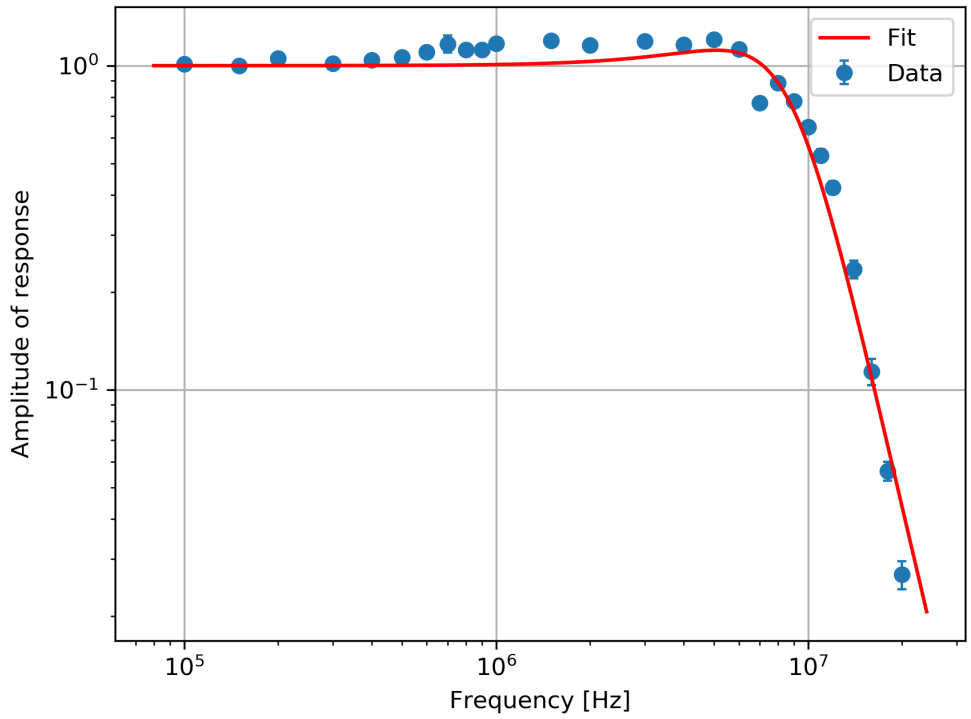

Figure 5.16: Photodetector bandwidth measurement. Blue dots are the peak-to-peak voltage of the beat signal normalized to the maximum, error bars shows the error of five measurements. Red line shows the polynomial fit of the data, which yields a −3 dB bandwidth of 10.5 MHz.

the S5821-01 photodiode with respect to the light close to 689 nm. Due to the uneven photon sensitivity of the PD in the thermal light spectrum, the measured PSD is a factor of 2 lower than the real PSD at 689 nm, this is corrected in the spectrum. We can therefore record the output voltage and convert it into light power. The photodetector noise is measured with a spectrum analyzer with a resolution bandwidth of 100 kHz, the converted voltage PSDs with different thermal light power as well as the background noise floor are shown in Fig. 5.17, in a frequency range from 500 kHz to 20 MHz.

We compare the photodetector noise with the photon shot noise (PSN) at the wavelength of $\lambda = 689$ nm. The PSD of the PSN is white and can be calculated as,

$$\mathcal{S}_V^{psn}(f) = 2h\nu P {R_F}^2 s^2, \tag{5.10}$$

where h is Plank's constant and $\nu = c/\lambda$ is the laser frequency, c is the speed of light in vacuum. The result is shown as the dashed lines in Fig. 5.17 where

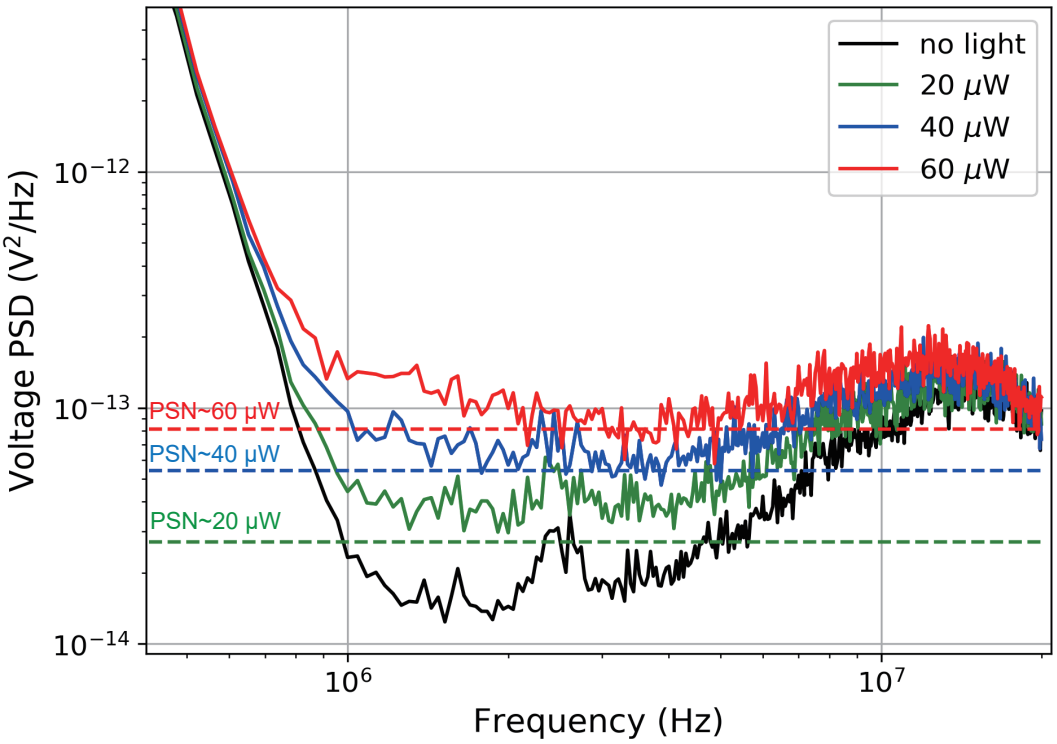

Figure 5.17: Photodetector noise measured with incident thermal light at different power levels (60 μW, 40 μW, 20 μW) and the background noise floor without light (top to bottom). The PSDs of PSN at different power levels are indicated by the dashed lines.

different colors represent different laser power levels.

From the spectrum we can see that around the modulation frequency of $\simeq$ 10.5 MHz, the PD noise is close to the PSN limit at the power of 40 μW, which is typical for our measurement condition. This means that the PSN of the light is equal to or larger than the electronic noise of the PD. This response was measured also for the laser light and shows no significant difference at the modulation frequency compared to the thermal light.

5.4 Summary

In summary, this chapter presents the experimental apparatus for preparing the Sr MOT and for the squeezing detection. The vacuum system is based on an upgraded version of the Sr apparatus where the science chamber and the MOT coils are novel. The main laser systems are constructed for laser cooling of Sr

atoms in a MOT and for performing squeezing probe in an optical cavity. The detection system is designed specifically for the purpose of weak light detection for cavity phase shift measurement, which is characterized to be high gain and low noise. Finally the power required to reach the shot noise is probably too large for certain schemes and that we will consider similar circuits with avalanche photodiodes (APDs) and multi-pixel photon counters (MPPCs).

Chapter 6

A new method of cavity noise cancellation for differential phase measurement and spin squeezing

In this chapter a series of experiments are described that were performed on the optical ring cavity which has been built and presented in chapter 4. It is demonstrated that by using two laser beams with a frequency gap of one FSR which are simultaneously resonant with the cavity, the cavity length fluctuations become common-mode to the two PDH error signals and can therefore be canceled. Furthermore, we simulate an atom-induced cavity phase shift by shifting the frequency of one of the two circulating laser beams and demonstrate an improved sensitivity to the cavity phase shift with the noise cancellation scheme [53].

6.1 Motivation

One of the main limitations in monitoring a quantum system lies in the destruction of the quantum states when a measurement is performed. In recent years, non-destructive measurements of quantum systems have been proposed [81, 158, 159] and demonstrated [43, 160], and have found applications in the fields of quantum simulation [161] and quantum metrology [61, 45]. They have stimulated a new generation of quantum sensors including atomic clocks [28, 95] and atom interferometers [1, 162], which utilize the so-called spin-squeezed states [35, 37] that are capable of surpassing the standard quantum limit [36] given by the number of the atoms involved [38, 64]. Such non-destructive measurements also assist in the realization of non-classical states of macroscopic systems [163, 164] which can be used to probe quantum gravity effects [165]. They also help pave the way

for searches of new physics beyond the standard model [166, 167].

In a quantum system the value of a given variable can often be enclosed into a phase shift of light interacting with the observed system [35]. It is often possible to arrange a situation where this phase shift is large for light only in a given frequency range [168]. Moreover, multiple interactions with the system as in an optical cavity [169], can amplify this phase shift, reaching a metrological gain given by the collective cooperativity [41] $N\eta$, where N is the number of atoms and η is the single-atom cooperativity, which is proportional to the finesse of the cavity. However, there are many noise sources that can prevent a precise phase shift measurement with an optical cavity. Yet it is possible to arrange a differential measurement scheme, where the phase shift for the probe mode is large while for another reference mode it is negligible, allowing the common-mode cavity noise to be canceled. Cavity noise cancellation in a Fabry-Pérot cavity has been demonstrated by probing two adjacent [170] or far-detuned [44] cavity modes simultaneously with a single phase-modulated light [49, 50], or with a laser locked to the cavity at twice the atomic transition wavelength and is frequency-doubled for probing [45].

In this chapter, we report a phase shift measurement scheme with reduced cavity-length-induced phase noise using an optical ring cavity and two counter-propagating beams that function as probe and reference with a frequency difference of one cavity free spectral range. The proposed scheme has several advantages over the general noise cancellation scheme in a Fabry-Pérot cavity with single phase-modulated light [44, 170, 45, 49, 50]. First, the ring cavity geometry allows for the manipulation [171] and probing [51] of atomic momentum states as well as their internal states. Second, the scheme where two independent beams are simultaneously resonant with the cavity is very flexible in practical applications, which enables independent phase modulation of the two beams. In addition, if the two lasers used are sufficiently stable individually, then they can be separated by an arbitrary frequency difference, extending the range of cavity modes that can be used for the reference measurement beyond the range of beat-note measurements [172] or the phase modulation bandwidth. Finally, the technique presented here could be used in addition to any of the existing techniques, treating the error signal of a frequency lock as the reference signal for additional suppression of cavity noise beyond the locking bandwidth.

The proposed system demonstrates close to 30 dB reduction in the cavity length fluctuations down to the noise floor in a frequency range up to half the cavity linewidth ($\delta\nu/2 \simeq 30$ kHz). We further apply this measurement scheme in a simulated spin-squeezing experiment [51] where a cavity phase shift measurement is performed with a 200 μs averaging time. We demonstrate an improvement in

phase sensitivity by a factor of 40 with a phase resolution of 0.7 mrad. With this improved phase resolution, the scheme removes one important barrier against attaining highly spin-squeezed states.

6.2 Theoretical model for cavity noise cancellation

Even though the proposed cavity noise-reduced phase shift measurement scheme can be used in general quantum systems, here we focus on a particular application in a spin squeezing experiment [51], where an optical ring cavity is used for the non-destructive measurement of the atomic momentum states (see Fig. 6.1). In this proposal 20 dB squeezing is estimated considering only the atom shot noise versus the scattering into free space. In reality, the effect of cavity length fluctuations is not considered and might present a major obstacle. These cavity length fluctuations may originate from acoustic and sub-acoustic pressure changes, resonances of piezoelectric transducers used to tune the cavity length, etc. Taking into account the phase shift $\delta\phi$ induced by cavity length fluctuations, we express the cavity overall phase shift in the presence of the atoms as,

$$\delta\Phi = 2\Phi_1 J_z + \delta\phi. \tag{6.1}$$

Under the assumptions that the detuning from atomic resonance Δ_e is larger than the linewidth Γ of the optical transition, and that the coupling from the $|\uparrow\rangle$ to the $|e\rangle$ can be neglected (whether because of selection rules or because the detuning Δ_e is much smaller than the ground-state splitting), $\Phi_1 = \eta\Gamma/(2\Delta_e)$ [44] (see supplementary materials, Sec. IV), where η is the single-atom cooperativity and $J_z = (N_\uparrow - N_\downarrow)/2$ is the atom number difference between two sublevels of the ground state (Fig. 6.1 (b)). At the atom shot noise limit, J_z follows a Gaussian distribution with a standard deviation of $\sqrt{N}/2$.

We denote the atom-induced cavity phase shift as the *signal* and the cavity-length-fluctuations-induced phase shift as *noise* and compute the signal-to-noise ratio (SNR) as,

$$\mathrm{SNR} = \frac{(2\Phi_1 \frac{\sqrt{N}}{2})^2}{\langle(\delta\phi)^2\rangle}, \tag{6.2}$$

where the numerator is taken at the atom shot noise limit $J_z = \sqrt{N}/2$ and $\langle\rangle$ denotes the expectation value. In order to resolve the atom-induced phase shift and achieve 20 dB squeezing, it is essential to suppress the cavity-length-fluctuations-induced phase noise down to a level 20 dB lower than the atom-induced phase shift.

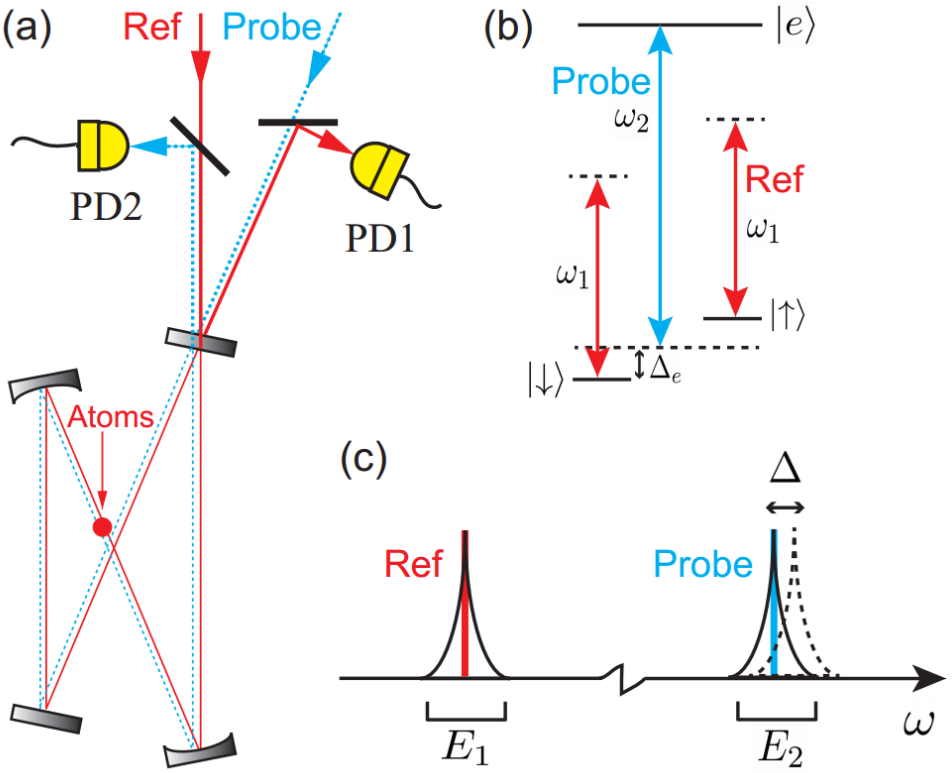

Figure 6.1: (a) Non-destructive phase shift measurement with reduced noise due to cavity length fluctuations. Laser cooled atoms (red circle) interact with the fundamental mode of an optical ring cavity and induce a shift Δ of the cavity resonance frequency. Two beams (Ref and Probe) are coupled to the cavity in counter-propagating directions and the reflections are collected by two photodetectors (PD1 and PD2). (b) Simplified level diagram of the reference and probe beams with respect to the atomic transitions. The probe is close to the atomic resonance while the reference is far detuned. (c) Two beams are resonant with two modes of the cavity therefore the PDH error signals display common cavity-length fluctuations. In the differential scheme the atom-induced phase shift Δ can be resolved while the common-mode cavity noise can be suppressed.

The proposed noise-reduced phase shift measurement scheme is illustrated in Fig. 6.1, where we consider two laser beams (Ref and Probe) with frequencies ω_1 and ω_2 that are resonant with two modes of an optical cavity at frequencies ω_{c1} and ω_{c2}, respectively. The resulting Pound-Drever-Hall (PDH) error signals [155], E_1 and E_2, in the limit where the cavity resonance frequency fluctuations are small compared to the cavity linewidth, are proportional to the detunings $\delta_{c1} = \omega_1 - \omega_{c1}$ and $\delta_{c2} = \omega_2 - \omega_{c2}$. If the laser noise can be neglected, then δ_{c1} and δ_{c2} are proportional thus making it possible to consider a single detuning δ_c and a

combination of E_1 and E_2 that is immune to cavity length fluctuations. Taking into account additional, uncorrelated noise contributions to the error signals, δE_1 and δE_2, whose minimum variance is set by photon shot noise fluctuations, the two error signals can be expressed as,

$$E_1(t) = A_1 R_1(t) * \delta_c(t) + \delta E_1(t), \tag{6.3}$$

$$E_2(t) = A_2(R_2(t) * \delta_c(t) - \Delta) + \delta E_2(t), \tag{6.4}$$

where A_1 and A_2 are constants representing the amplitude of the signal. In these expressions we have introduced the convolution with the response functions $R_1(t)$ and $R_2(t)$ which can arise from, e.g., electronic filtering, time delays or the response of the optical cavity. In this model, a constant shift Δ of the mode at frequency ω_{c2} is also introduced, as illustrated in Fig. 6.1 (c). This can be caused, for example, by the presence of a state-dependent index of refraction introduced by an atomic ensemble, as shown in Eq. (6.1). While temporal variations of Δ can be considered, here we assume that these are slow compared to the averaging time scale. It is the main purpose of the proposed noise cancellation method to find a function E of the error signals E_1, E_2 that maximizes the sensitivity to the shift Δ. To this end, we define the sensitivity error function S as,

$$S^2 = \frac{\mathrm{Var}(E)}{\left(\frac{\partial\langle E\rangle}{\partial\Delta}\big|_{\Delta=0}\right)^2}, \tag{6.5}$$

where Var denotes the variance.

It is instructive to first consider the trivial situation where $\delta E_1 = \delta E_2 = 0$ and $R_1 = R_2$. In this case one can see that S^2 is minimized and vanishes for a linear combination $E = E_1 + \alpha E_2$ with $\alpha = -A_1/A_2$. If now the condition $\delta E_1 = \delta E_2 = 0$ is relaxed, but the noise floor fluctuations remain small, i.e. $\langle \delta E_i^2 \rangle \ll A_i^2 \langle \delta_c^2 \rangle$, and $R_1 = R_2$, it is still possible to consider the linear combination $E = E_1 + \alpha E_2$. In this limit, one can show that minimizing S^2 is equivalent to minimizing,

$$\mathrm{Var}(E) = \mathrm{Var}(E_1) + \alpha^2 \mathrm{Var}(E_2) + 2\alpha \mathrm{Cov}(E_1, E_2), \tag{6.6}$$

where Cov denotes the covariance. The minimum variance is attained when $\alpha = -\mathrm{Cov}(E_1, E_2)/\mathrm{Var}(E_2)$ and the resulting sensitivity error is,

$$(S^2)_{\min} = \frac{\langle \delta E_1^2 \rangle}{A_1^2} + \frac{\langle \delta E_2^2 \rangle}{A_2^2}, \tag{6.7}$$

which is the sum of the noise floor contributions from the two error signals in frequency units.

We finally consider the case where the response functions R_i differ. While determining the individual functions may not be experimentally straightforward, it is possible to measure the ratio of their Fourier transforms, i.e., the ratio of the transfer functions $\tilde{R} = \tilde{R}_1/\tilde{R}_2$. Such a measurement can be performed, for example, by modulating the cavity length or the laser frequencies at a known frequency and then measuring the amplitude ratio and relative phase of the two error signals. Alternatively, in the presence of broadband cavity noise, as is our case, $\tilde{R}$ is determined by averaging the ratio of the Fourier transforms $\tilde{E}_1/\tilde{E}_2$, calculated from the (noisy) error signals. Once $\tilde{R}$ is determined, the noise cancellation can be applied to E_1 and the inverse transform of $\tilde{R}\tilde{E}_2 = A_2\tilde{R}_1\tilde{\delta}_c + \tilde{R}\widetilde{\delta E}_2$. These two signals now share the same frequency response to cavity length fluctuations.

Finally, if $\tilde{R}$ differs from unity and one wishes to determine the residual cavity noise due to imperfect cancellation, it is first necessary to realize that the value of α determined as $-\mathrm{Cov}(E_1, E_2)/\mathrm{Var}(E_2)$ differs from the value $-A_1/A_2$ by a factor $\mathcal{I} = \int_0^\infty |\tilde{R}(\nu)| \cos(\phi_R(\nu)) \mathcal{S}_{\delta_c}^{(0)}(\nu) d\nu / \int_0^\infty \mathcal{S}_{\delta_c}^{(0)}(\nu) d\nu$, where $\tilde{R} = |\tilde{R}| e^{i\phi_R}$ and $\mathcal{S}_{\delta_c}^{(0)} = |\tilde{R}_2|^2 \mathcal{S}_{\delta_c}$ is the spectral density of cavity frequency fluctuations multiplied by the amplitude of $\tilde{R}_2$. In this case, the residual cavity noise can be computed as,

$$\delta S_E = A_1^2(|\tilde{R}|^2 + \mathcal{I}^2 - 2\mathcal{I}|\tilde{R}| \cos\phi_R) S_{\delta_c}^{(0)}. \tag{6.8}$$

6.3 Optical ring cavity characterization

In this section, a series of measurements are performed to characterize the optical ring cavity prototype, including the cavity mirror transmissions, cavity FSR, linewidth and finesse. Methods for the measurement are presented and the data is analyzed, giving the results in accordance with the designed cavity properties.

6.3.1 Cavity mirror transmission

The first measurement is the cavity mirror transmission ratio. The purpose of this measurement is to evaluate the total loss of the cavity, which is directly related to the scattering and absorption of light on the cavity mirrors .

Let us review the definition of the cavity finesse for a four-mirror ring cavity, which can be written as

$$\mathcal{F} = \frac{\pi\sqrt{R_1 R_2 R_3 R_4}}{1 - r_1 r_2 r_3 r_4}, \tag{6.9}$$

where r_i and R_i are the reflection amplitude and power ratio and $r_i = \sqrt{R_1}$. For

high-reflectivity mirrors, $\sqrt{R_1R_2R_3R_4} \simeq 1$, and due to the energy conservation,

$$r_i = \sqrt{1 - T_i - L_i} \simeq 1 - \frac{1}{2}(T_i + L_i), \tag{6.10}$$

where the second part of the equation is obtained by the Taylor expansion and by omitting the high-order components. Therefore the cavity finesse can be approximated as,

$$\mathcal{F} = \frac{\pi}{1 - r_1r_2r_3r_4} = \frac{2\pi}{\sum_{i=1}^{4}(T_i + L_i)}. \tag{6.11}$$

In this case, if the finesse $\mathcal{F}$ and the total transmission ratio $\sum_{i=1}^{4} T_i$ are measured, the total loss of the cavity $\sum_{i=1}^{4} L_i$ can be estimated.

Here we perform the measurement of the mirror transmission ratios for each mirror (M1-M4) and at different wavelengths (689 nm, 461 nm and 813 nm), which are also specified in the datasheet from the manufacturing company (see Table 4.1). Note that for each wavelength we measured the transmission ratio for light both with the horizontal and the vertical polarizations. This is motivated by the fact that the laser beams are incident on the mirrors with an angle of 11.5° and in that case the fused silica substrates are polarization sensitive.

The measurement of the mirror transmission ratio is quite straightforward. A laser beam is shone onto the mirror surface with the right incidence angle, a half waveplate and a PBS are used to check the polarization. Then the input power P_{in} and the output power P_{out} are measured with Thorlabs power meter and the transmission ratio is $T_i = P_{out}/P_{in}$. For 461 nm and 813 nm lasers, the measurement is simple because the transmission ratio is high so that a comparatively higher signal-to-noise ratio is available. However, for low transmission wavelengths like 689 nm red lasers, and especially for curved mirrors M2 and M3, of which the transmission is lower than 1 part-per-million (ppm), the ambient light or the laser light scattered from the mirror substrates can have a significant influence.

A simple setup is considered to address this problem. At the output of the mirror, two irises separated by a black tube are put to block the ambient and scattered light, a CCD camera is put at the end of the second iris to detect the transmission spot. When we checked from the camera that the transmission beam is detected and that the ambient and scattered light are blocked, we use the Thorlabs power meter in the non-filtering condition to measure the transmission power. This method proves to be very useful for weak transmission power detection, however, for M2 and M3 with 689 nm laser, the transmission is too low and we can only provide an upper bound to the transmission ratio. Table 6.1 presents all the measured transmission ratios in ppm for four cavity mirrors at different wavelengths and for both polarizations.

Table 6.1: Mirror transmission ratio in ppm, for each wavelength the measurement is performed both with the horizontal and vertical polarizations. For M2 and M3 the transmission power at 689 nm is too weak and we can only provide an estimated upper bound to the transmission ratio.

Mirrors	689 nm		461 nm		813 nm	
	Horizontal	Vertical	Horizontal	Vertical	Horizontal	Vertical
M1	303.8(4)	219.6(4)	10993(4)	9573(8)	1926(6)	1396(5)
M2	< 0.2	< 0.2	904(9)	652(5)	266(2)	183(8)
M3	< 0.2	< 0.2	1032(3)	851(9)	258(8)	171(7)
M4	8.8(1)	6.6(1)	10258(9)	9372(9)	1246(3)	1012(6)

6.3.2 Cavity free spectral range

For an optical ring cavity, the free spectral range is defined according to Eq. (4.17). As a first estimation of the cavity FSR, one can measure the cavity length by summing the four light paths inside the cavity, which gives:

$$L_{total} = L_1 + L_2 + L_3 + L_4 = 55 + 44 + 54 + 54 = 207 \text{ mm}. \tag{6.12}$$

with an uncertainty of ± 1 mm. Since the cavity is in air (or nitrogen) environment, one should also consider the index of refraction of the air $n_{air} = 1.0003 \pm 0.0001$, so the total cavity length in air is $L_{air} = L_{total} \times n_{air} = 207 \pm 2$ mm. Therefore one can estimate the FSR as,

$$\text{FSR}_{est} = \frac{c}{L_{air}} \simeq 1.449 \text{ GHz}. \tag{6.13}$$

A more precise measurement of FSR can be implemented by measuring the transmission peaks of the cavity with phase-modulated light. Here a fiber-EOM is used for phase modulating the incident laser beam. When the laser frequency is tuned close to the cavity resonance and the cavity length is scanning with PZT, in the transmission a carrier and two sidebands can be recorded on the oscilloscope. When the modulation frequency of the fiber-EOM equals to one FSR, the two sidebands should merge with the carrier. For each modulation frequency, we record the temporal difference between the sideband and the carrier by fitting the trace with multi-peak Lorentzian function, as shown in Fig. 6.2. Since the detuning of the modulation frequency to the FSR is proportional to the temporal difference of the sideband and the carrier, by fitting the data with function $y = a \times |x - b|$, one can derive the FSR as the fitting result of b, as shown in Fig. 6.3. Therefore, the measured FSR is,

$$\text{FSR}_{mea} = 1.43136 \pm 0.00003 \text{ GHz}. \tag{6.14}$$

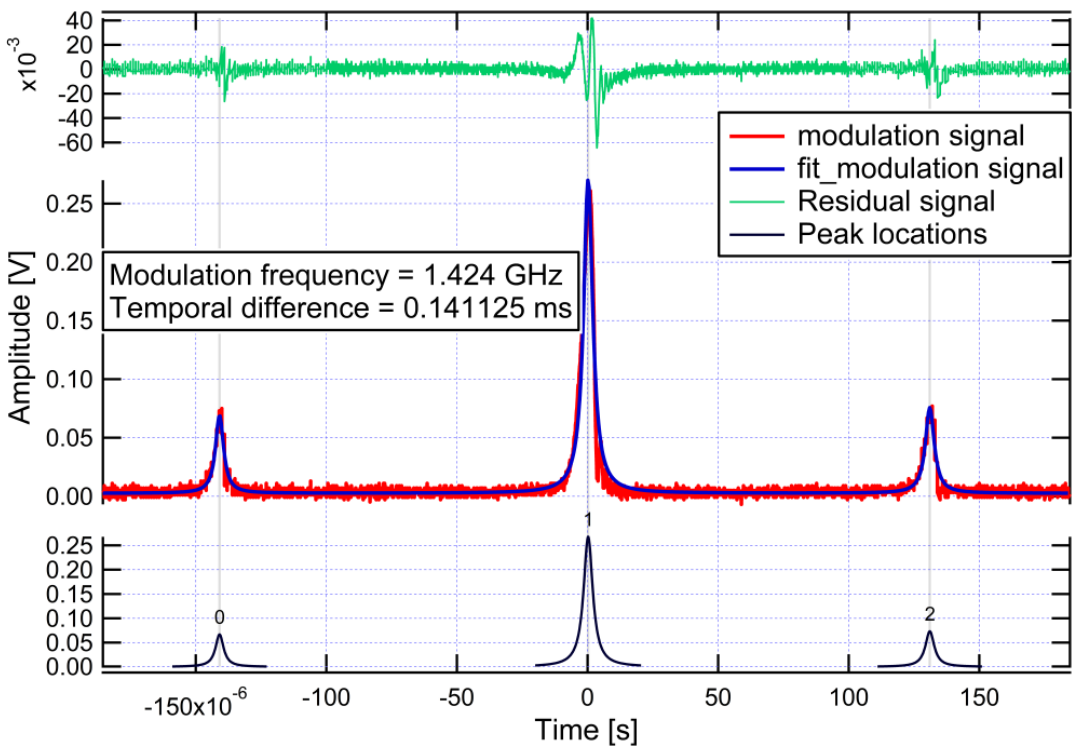

Figure 6.2: Cavity transmission signal with fiber-EOM modulation frequency at 1.424 GHz. The temporal difference between the carrier and the side-band is proportional to the difference between the modulation frequency and the cavity FSR. The transmission signal (red) is fitted with a multi-peak fitting function specifying Lorentzian peak shapes (blue). The positions of three peaks (black) are shown in the lower panel, the fit residuals (green) are shown in the upper panel. The temporal difference between peak 0 and peak 1 is 0.141125 ms.

6.3.3 Cavity linewidth and cavity finesse

The cavity ringdown measurement is a precise method to evaluate the cavity photon lifetime and the cavity linewidth. When the laser is on resonance with the cavity, the photons inside the cavity will be reflected by the cavity mirrors for multiple times which is close to the order of the cavity finesse, therefore the intensity of the light inside the cavity is also amplified. When the incident light is switched off, the photon number inside the cavity will not disappear immediately but decay from the cavity mirrors exponentially. If we consider the laser power transmitted from the cavity as a function of time, we have

$$A(t) = A_0 e^{-t/\tau} \ , \tag{6.15}$$

where A_0 is the initial laser power and τ is the photon lifetime of the cavity.

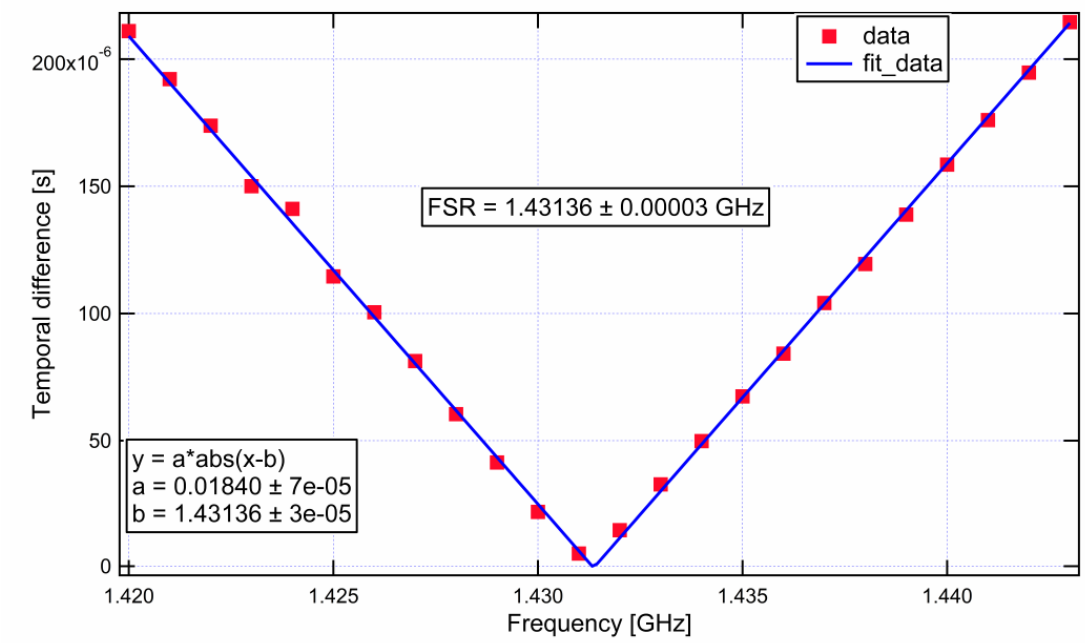

Figure 6.3: Free spectral range measurement data and fitting curve. The data is the temporal difference between peak 0 and peak 1 at different modulation frequency. When the modulation frequency equals to one FSR, the two sidebands merge with the carrier, thus the temporal difference is zero. The data is fitted with function $y = a \times |x - b|$, where $b = (1.43136 \pm 0.00003)$ GHz is the cavity FSR.

For the measurement of the cavity decay, we need to keep the laser resonant with the cavity and switch off the incident laser quickly. This is achieved by applying a TTL signal on the RF of the double-pass AOM, whose response time $\tau_{AOM} \simeq 100$ ns. On the cavity transmission, a fast photodiode with a response time $\tau_{PD} < 100$ ns records the cavity photon decay. Generally, $\tau_{AOM}, \tau_{PD} \ll \tau$ so the measurement will not be limited by the response speed of the AOM or the photodiode. Figure 6.4 shows the cavity decay signal with an exponential decay fit, the fit gives a time constant $\tau \simeq 2.7557 \times 10^{-6} s$. We have acquired 100 such cavity decay signals, the average value of the photon lifetime inside the cavity is,

$$\bar{\tau} = (2.763 \pm 0.003) \times 10^{-6} \text{ s}. \tag{6.16}$$

With the measured $\bar{\tau}$ one can estimate the cavity linewidth according to,

$$\delta\nu = \frac{1}{2\pi\bar{\tau}} = 57.6(1) \text{ kHz} . \tag{6.17}$$

One can perform another independent cavity linewidth measurement using the setup in Fig. 6.6 by locking one beam to the cavity while scanning the frequency

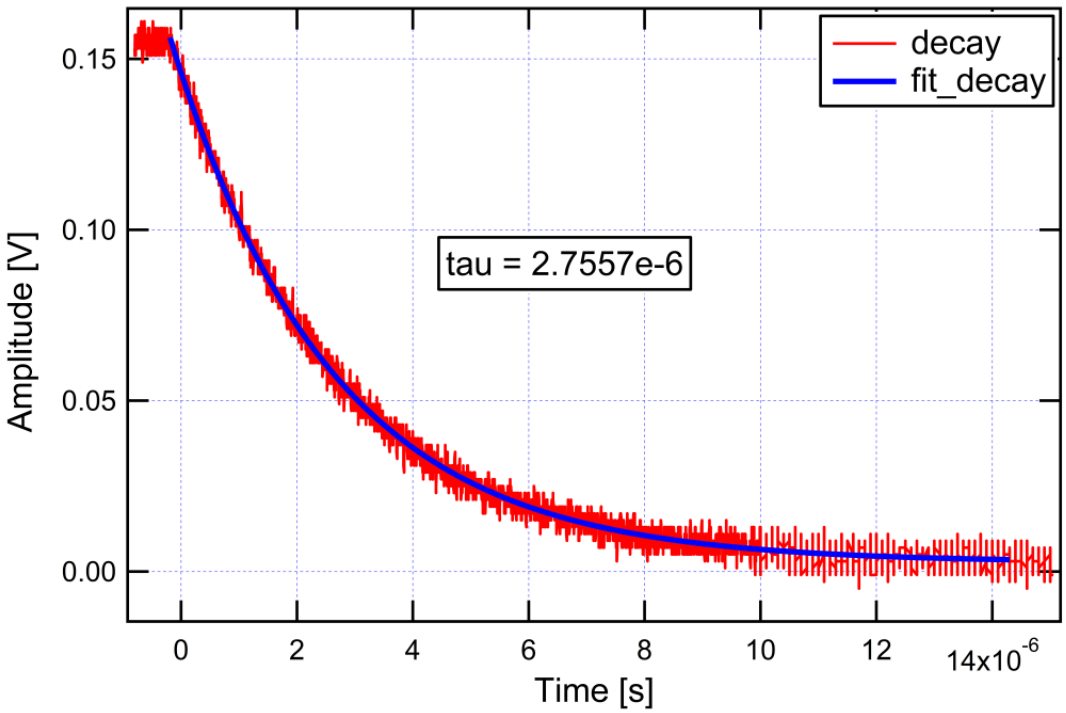

Figure 6.4: Cavity photon decay signal and the fitting curve with exponential decay function. The laser incident onto the cavity is tuned close to the resonance with the cavity. The double-pass AOM which is used to shift the laser frequency is modulated with a TTL signal which turns on and off the laser beam. When the laser is on resonance with the cavity and then immediately switched off, the number of photons remained in the cavity will decay through the cavity mirrors. The red plot is the cavity photon decay in the transmission, the blue curve is the exponential decay fit of the data, the time constant τ of the fit is the lifetime of the photon in the cavity. We have acquired 100 photon decay signals, the average value of the photon lifetime is $\bar{\tau} = (2.763 \pm 0.003) \times 10^{-6}$ s.

of another beam. The cavity output power of the scanning beam as a function of the scanning frequency follows the Lorentzian lineshape, therefore a fit of the data yields the FWHM of the Lorenzian lineshape, which is the linewidth of the cavity (see Fig. 6.5). This measurement gives $\delta\nu = 63.6(5)$ kHz, which agrees with the photon decay measurement.

With the cavity FSR and the cavity linewidth measured, one can estimate the cavity finesse according to,

$$\mathcal{F} = \frac{\mathrm{FSR}}{\delta\nu} = 2.40(2) \times 10^4. \tag{6.18}$$

Note that all those measurement are performed with 689 nm laser and with

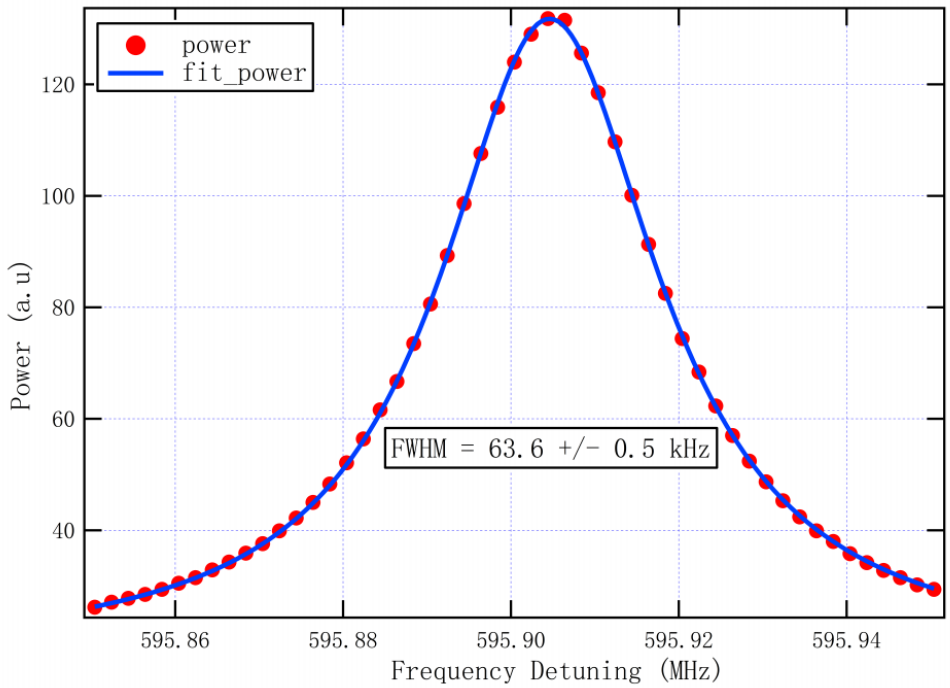

Figure 6.5: Cavity linewidth measurement by locking one beam to the cavity while scanning the frequency of another beam. Red circles are the measured cavity output power with respect to the scanning beam, blue curve is the Lorentzian fit of the data, which yields a cavity linewidth (FWHM) $\delta\nu = 63.6(5)$ kHz.

the vertical polarization, in this condition the highest finesse can be obtained. Finally, the total cavity loss can be estimated with Eq. 6.11 as

$$\sum_{i=1}^{4} L_i = \frac{2\pi}{\mathcal{F}} - \sum_{i=1}^{4} T_i = 34.8(5) \text{ ppm}, \tag{6.19}$$

where $\sum_{i=1}^{4} T_i = 226.6(4)$ is the total transmission ratio measured with 689 nm at the vertical polarization.

In summary, a full characterization of the cavity prototype is performed. In Table 6.2 the main cavity characteristics are summarized. The mirror ROC and the mirror transmission are given in the sequence of (M1-M4) with respect to the cavity schematic of Fig. 6.6. The mirror transmission ratio, linewidth and finesse are all specified with laser wavelength of 689 nm, which is also used in the following sections.

Table 6.2: Relevant cavity parameters with respect to the laser wavelength at 689 nm.

Parameter	Symbol	Value	Units
Mirror ROC	ROC_i	$+\infty, 50, 50, +\infty$	mm
Mirror transmission	T_i	$219.6(4), < 0.2, < 0.2, 6.6(1)$	ppm
Free spectral range	FSR	1.43136(3)	GHz
Linewidth	$\delta\nu$	57.6(1)	kHz
Finesse	$\mathcal{F}$	$2.40(2) \times 10^4$	–
Total loss	$\sum L_i$	34.8(5)	ppm

6.4 Cavity noise cancellation setup

The core of the experimental setup is a bow-tie optical ring cavity with four high-reflectivity mirrors, shown in Fig. 6.6. The cavity mirrors are glued onto four V-shaped grooves, the V-groove that holds mirror 1 (M1 in Fig. 6.6) is placed on a shear-force PZT in order to tune the cavity length. The whole cavity is assembled inside a plexiglass box and is supported on sorbothane rubber balls for vibration isolation. Additionally, we can flow clean nitrogen through the box in order to reduce dust contamination.

The experimental setup for cavity noise cancellation and phase shift measurement is also illustrated in Fig. 6.6 and it is divided in two parts: (i) preparation of the two optical beams; (ii) measurement and detection setup using the cavity. The two parts of the setup are placed on two independent breadboards, BD1 and BD2. While BD1 is fixed on the optical table, BD2 is placed on four pieces of sorbothane rubber for vibration isolation. The input laser light is frequency stabilized by locking to a high-finesse Fabry-Pérot cavity ($\mathcal{F}' \simeq 8600$), reaching a 20 Hz laser linewidth [145] and is transported to BD1. The input beam is split into two parts with a frequency difference of one FSR by two acousto-optic modulators (AOM) in double-pass configuration. AOM1 is a high-frequency AOM (Brimrose) which shifts the frequency of the beam by -1.21 GHz, while AOM2 introduces a frequency shift of +220 MHz. The two beams are then phase modulated independently with two EOMs at 10.5 MHz and are transported to BD2 via two optical fibers. We refer to the two beams after the optical fibers as Ref and Probe, as shown in Fig. 6.6 and corresponding to the beams in Fig. 6.1. On BD2, the two beams are independently mode-matched to the optical cavity. Optical isolators are used to couple two s-polarized beams to the optical cavity and detect the corresponding reflections from the back of the cavity incoupling mirror. The reflected beams emerging from the side ports of the optical isolators are detected via two homemade photodetectors (PD1 and PD2) in order to derive

the two error signals using the PDH method.

PD1 and PD2 are low-noise and high-gain photodetectors with a bandwidth of 20 MHz, optimized for this application (see section 5.3). The output of the PDs are band-pass filtered at 10.5 MHz and are sent directly to a mixer (Minicircuits ZAD-1-1+) with no need for extra amplification. A single two-channel signal generator is used to produce the local oscillator (LO) and modulation (MOD) signals required for both PDH signals. The two output channels are both split and sent to the independent mixers and phase modulators, respectively. The output of the two mixers, which are the PDH error signals, are filtered by a second-order anti-aliasing low-pass filter (LPF) with a cut-off frequency of $f_0 = 80$ kHz and a low-frequency gain of 10. This amplification reduces the relative contribution of the quantization noise of the analog-to-digital converter (ADC). Finally, cavity locking is achieved by acting on the PZT under M1 using a standard PI controller with error signal E_1. Due to the limitation on the PZT response speed, the low frequency ($\lesssim 100$ Hz) noise is largely compensated by cavity locking, while the high frequency ($\gtrsim 100$ Hz) noise remains and can be further suppressed by our noise cancellation scheme.

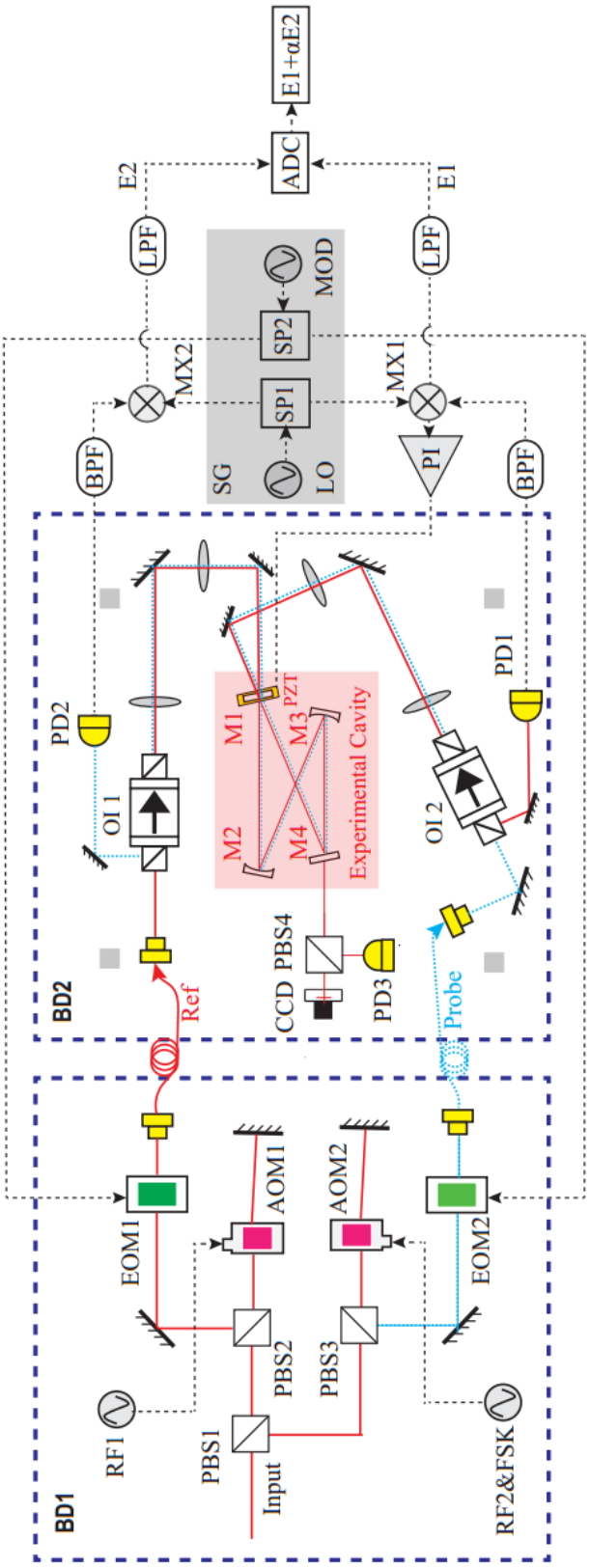

Figure 6.6: Experimental setup. BD1: two AOMs induce a frequency difference FSR = 1.43 GHz between the two beams, indicated by the red and blue lines. AOM2 is driven by RF2, to which the FSK modulation can be applied. Two EOMs are driven at 10.5 MHz from the same source but with tunable relative phase and amplitude. BD2: cavity, mode-matching optics and detection system. See text. Abbreviations: BD, breadboard; PBS, polarizing beamsplitter; AOM, acousto-optic modulator; EOM, electro-optic modulator; RF, radio frequency; FSK, frequency shift key; OI, optical isolator; PD, photodetector; CCD, charge-coupled device; SG. signal generator; LO, local oscillator; MOD, phase modulation; SP, splitter; MX, mixer; PI, proportional-integral controller; BPF, band-pass filter; LPF, low-pass filter; ADC, analog-to-digital converter; M, mirror; E, error signal.

6.5 Experimental results

In this section the results for the cancellation of the cavity length fluctuations are presented. With the proposed scheme the cavity length fluctuations can be canceled down to a level close to the noise floor, which is set by other noise sources. The contributions from various noise sources to the noise floor are also estimated.

6.5.1 Noise cancellation performance

In the following, the experimental sequence for data acquisition and the analysis are described. We set the laser power of Ref and Probe (in Fig. 6.6) to be 40 μW at the reflection which is detected by PD1 and PD2. When the cavity is scanning, the error signals E_1 and E_2 exhibit a typical dispersive shape with a peak-to-peak voltage of $V_{pp} \simeq 2.45$ V. When the cavity is locked with the PI controller acting on the PZT under M1, E_1 and E_2 show strong correlations since they both represent the cavity length fluctuations, as shown in Fig. 6.7. The error signals are acquired by a digital oscilloscope for 10 ms with a sampling rate of 10 MHz. In order to analyze the data in the frequency domain, we compute the Fast Fourier Transform (FFT) and estimate the voltage power spectral density $\mathcal{S}_V(f)$ in a frequency range from 100 Hz to half the sampling rate, i.e., 5 MHz. The spectral density of frequency fluctuations can then be expressed as,

$$\mathcal{S}_\nu(f) = \left(\frac{\delta\nu}{V_{pp}}\right)^2 \mathcal{S}_V(f) \ , \tag{6.20}$$

where $\delta\nu = 57.6(1)$ kHz is the cavity linewidth.

The result of cavity noise cancellation is shown in Fig. 6.8. The red trace 1 shows the original frequency fluctuations of E_1, while the green trace 2 shows the dramatically reduced frequency fluctuations of the combined error signal $E = E_1 + \alpha E_2$, where $\alpha = -\mathrm{Cov}(E_1, E_2)/\mathrm{Var}(E_2)$. The orange trace 3 shows the noise floor corresponding to Eq. (6.7) and is obtained when the two laser beams are out of the cavity resonance. Figure 6.8 shows that the original cavity noise patterns are frequency-dependent. In the low-frequency range (100 Hz to 1 kHz), it follows a $1/f$ behavior indicating that flicker noise is dominating. In the mid-frequency range (1 kHz to 10 kHz), oscillations due to mechanical structures are dominating. For the cavity-aided phase shift measurement, we are interested in a bandwidth close to half the cavity linewidth ($\delta\nu/2 \simeq 30$ kHz). It is demonstrated that with our cavity noise cancellation scheme, within this frequency range the cavity noise can be reduced by more than 30 dB, close to the noise floor. At higher frequencies, up to 100 kHz, the cancellation scheme is still able to reach

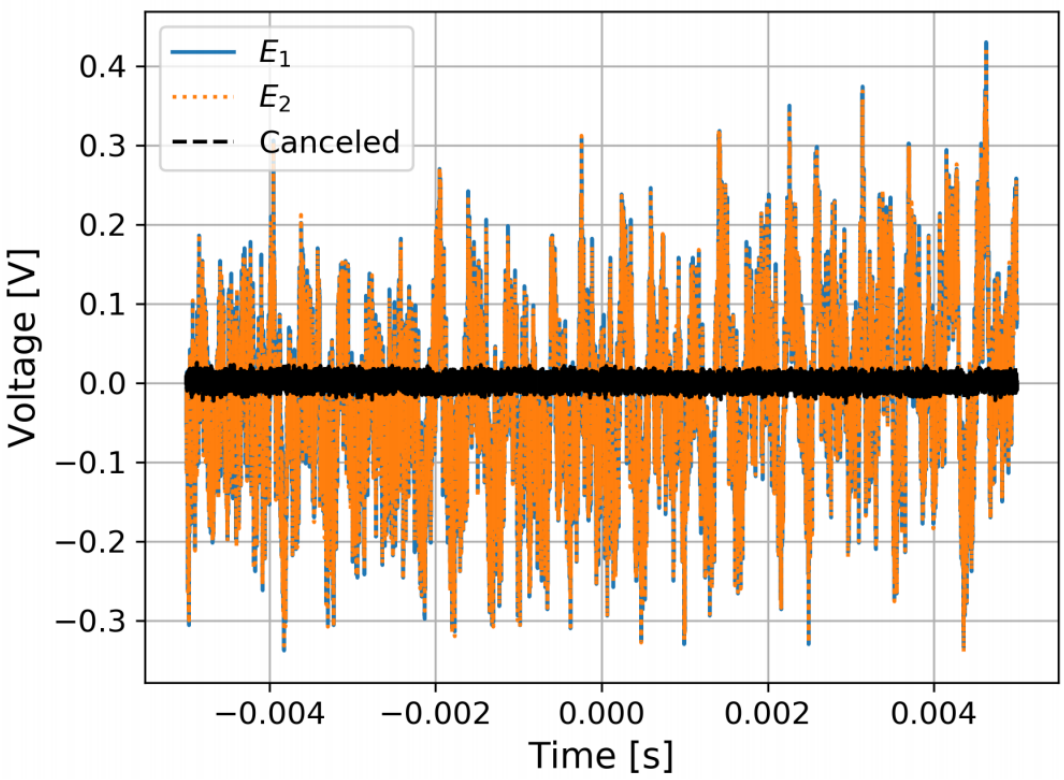

Figure 6.7: Time domain error signals and noise cancellation. The blue solid lines and the orange dotted lines represent the error signals E_1 and E_2, respectively, which show strong correlations. The black dashed line shows the canceled signal, which has significantly reduced noise fluctuations compared to the non-canceled ones.

the noise floor, but the reduction is lessened due to the original cavity noise being strongly filtered.

6.5.2 Noise sources analysis

In the following we analyze the noise sources in our system and estimate their contributions to the noise floor. We investigate the effects from the laser intensity noise, the residual amplitude modulation (RAM) of the EOMs, the phase noise due to the fiber transportation, the different frequency responses of the two channels and the quantization noise in the ADC. The noise analysis of the PD has already been discussed in subsection 5.3.4.

Laser intensity noise It is known that the PDH error signal is first-order immune to laser intensity fluctuations [155]. In our system, however, the cavity is locked on one beam while the other beam can be tuned. If there is a mismatch

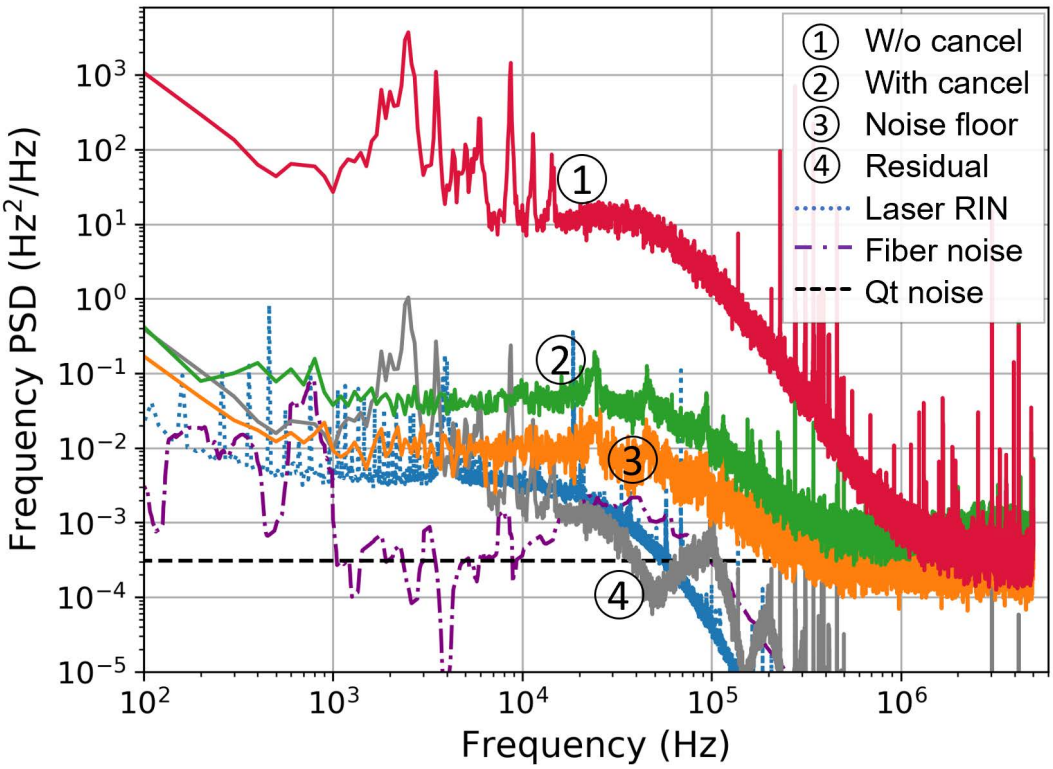

Figure 6.8: Cavity noise cancellation results. Traces 1 and 2 (red and green solid traces) show the frequency PSD of the error signals before and after the noise cancellation, showing about 30 dB noise reduction in a frequency range up to half the cavity linewidth ($\delta\nu/2 \simeq 30$ kHz). The noise of the canceled error signal is close to the noise floor (orange solid trace 3) determined when the laser is off-resonance with the cavity. Also shown are the residual noise due to the difference in the frequency response of the two channels (grey solid trace 4), the laser relative intensity noise (blue dotted trace), the quantization noise (black dashed trace) due to ADC and the fiber phase noise (purple dashdot trace).

between the laser frequency and the cavity resonance, then the laser intensity fluctuations may give a noise contribution in the PDH error signal. We cannot say a priori how large this frequency mismatch is, but we can estimate an upper limit to it. We observed that the amplitudes of the time domain error signals are within 1/5 of the V_{pp}, therefore we choose the upper limit of frequency mismatch as 1/5 of the cavity linewidth $\delta\nu$. With this hypothesis we can estimate the maximum contribution of the laser intensity noise to the PDH error signal.

In order to measure the relative intensity noise (RIN), we illuminate the laser beam on PD1 and record the output for 10 s with an oscilloscope. We compute the PSD of this trace $\mathcal{S}_V^{rin}(f)$ and normalize it to the mean PD output voltage

V_{PD}. Note that in the PDH method, the laser is filtered by the cavity and the error signals are filtered by a second-order LPF at the cut-off frequency of $f_0 = 80$ kHz. Therefore, in order to compare the RIN with the noise floor in Fig. 6.8, the computed $\mathcal{S}_V^{rin}(f)$ should be corrected by the amplitude of the transfer function of the cavity, $|H_{cav}|^2 = [1 + (2f/\delta\nu)^2]^{-1}$, and that of the LPF, $|H_{LPF}|^4 = [1 + (f/f_0)^2]^{-2}$. Finally, the upper-limit contribution of the laser RIN to the PDH error signal in frequency PSD is,

$$\mathcal{S}_\nu^{rin}(f) = \left(\frac{\delta\nu}{5}\right)^2 \frac{\mathcal{S}_V^{rin}(f)}{V_{PD}^2} \cdot |H_{cav}|^2 \cdot |H_{LPF}|^4. \tag{6.21}$$

The result is shown as the dotted blue line in Fig. 6.8, which has the largest contribution to the noise floor in a frequency range from 100 Hz to 10 kHz.

Residual amplitude modulation (RAM) The residual amplitude modulation arises from the imperfections in laser phase modulation when an EOM is used. It has been studied extensively and has confirmed contributions from the etalon effect [173], the misalignment of light from the principal axis of the crystal [174] and temperature variations, etc. Methods to actively cancel the RAM have also been demonstrated with a reduction down to the thermal noise level [175]. In order to estimate an upper limit of the noise contribution from the RAM, we record the PDH error signals for 10 s when the laser is out of resonance with the cavity and compute the frequency PSD in a range from 100 mHz to 5 kHz. The results show that the noise contribution from the RAM of both the two EOMs are below 10^{-1} Hz^2/Hz at 10 Hz. At this level the RAM would not have an effect on the cavity noise cancellation since we are concerned about a frequency range where the contributions from the RAM are negligible. Indeed no active cancellation of the RAM is needed in our experiment.

Fiber phase noise As shown in Fig. 6.6, two 2-meter fibers are used for light transmission and mode-cleaning. Due to the pressure and temperature variations, the fiber transmission can introduce phase noise on the light, which can cause a phase shift in the cavity for the two beams and degrade the noise cancellation. To evaluate the differential phase noise introduced by the fiber transmission, we combined the two transmitted beams and measured the phase noise of the beatnote. A fast photodetector is used to detect the 1.43 GHz beatnote and the output is sent to a phase noise analyzer (R&S FSWP). Since the phase PSD $\mathcal{S}_\phi^{fiber}(f)$ is related to the frequency PSD by a factor of f^2, we can compute the frequency PSD due to the fiber phase noise as,

$$\mathcal{S}_\nu^{fiber}(f) = f^2 \mathcal{S}_\phi^{fiber}(f) \cdot |H_{cav}|^2 \cdot |H_{LPF}|^4, \tag{6.22}$$

where the transfer functions of the cavity response and the second-order LPF are considered. The result is plotted as the purple dashdot trace in Fig. 6.8, which is well below the noise floor and has a negligible effect on the cavity noise cancellation.

Frequency response difference between the two channels The difference in the frequency response of the two channels E_1, E_2 to cavity-length fluctuations may degrade the noise cancellation. However, as discussed in section 6.2, this difference can be compensated if it is a dominating noise source. Different responses can originate from different polarizations of the two beams, accumulated phase shifts from electronics and optics, etc. We minimize this difference by using laser beams with the same polarization and cables with the same length for the RF signals. In order to measure the ratio $\tilde{R} = \tilde{R}_1/\tilde{R}_2$ of transfer functions for the two channels, we acquire 100 traces of E_1 and E_2 on resonance for 10 s with a sampling rate of 1 MHz. For each trace we compute the phase and amplitude of the ratio between the FFTs of the two channels and average over all the traces. We establish that the relative phase between the two channels is less than about 1° in the relevant frequency range (see Fig. 6.9). We computed the residual cavity noise contribution by evaluating Eq. (6.8) and the result is shown as the grey solid trace 4 in Fig. 6.8, thus showing that compensation of $\tilde{R}$ is unnecessary at the current level.

Quantization noise Quantization noise is introduced in the process of analog-to-digital conversion. In our data acquisition system, a digital oscilloscope (Tek MDO3014) is used to acquire the error signal data for 10 ms with a sampling frequency of $f_s = 10$ MHz. The 8-bit oscilloscope has a vertical resolution of $2^8 - 1 = 255$ and is set for a vertical full scale of FS = 1 V. As a result, the least-significant-bit is LSB = FS/$(2^8 - 1)$ = 3.9 mV and the one-sided voltage PSD is $\mathcal{S}_V^{qt}(f) = \mathrm{LSB}^2/(6f_s)$. We compute the frequency PSD contribution due to quantization noise in the combined error signal E as,

$$\mathcal{S}_\nu^{qt}(f) = \mathcal{S}_V^{qt}(f) \left(\frac{\delta\nu}{V_{pp}}\right)^2 (1+\alpha^2) = 3.08 \times 10^{-4}\ \mathrm{Hz}^2/\mathrm{Hz}, \tag{6.23}$$

where $\alpha = 1$ is used as an approximation. The quantization noise is plotted as the dashed black trace in Fig. 6.8, it is clear that the quantization noise becomes dominant in the noise floor only in a frequency range higher than 100 kHz, which is beyond the cavity response and the effect can be neglected.

In summary, taking into account the PD noise analysis presented in Fig. 5.17, we conclude that for the current setup, the main contributions to the noise floor

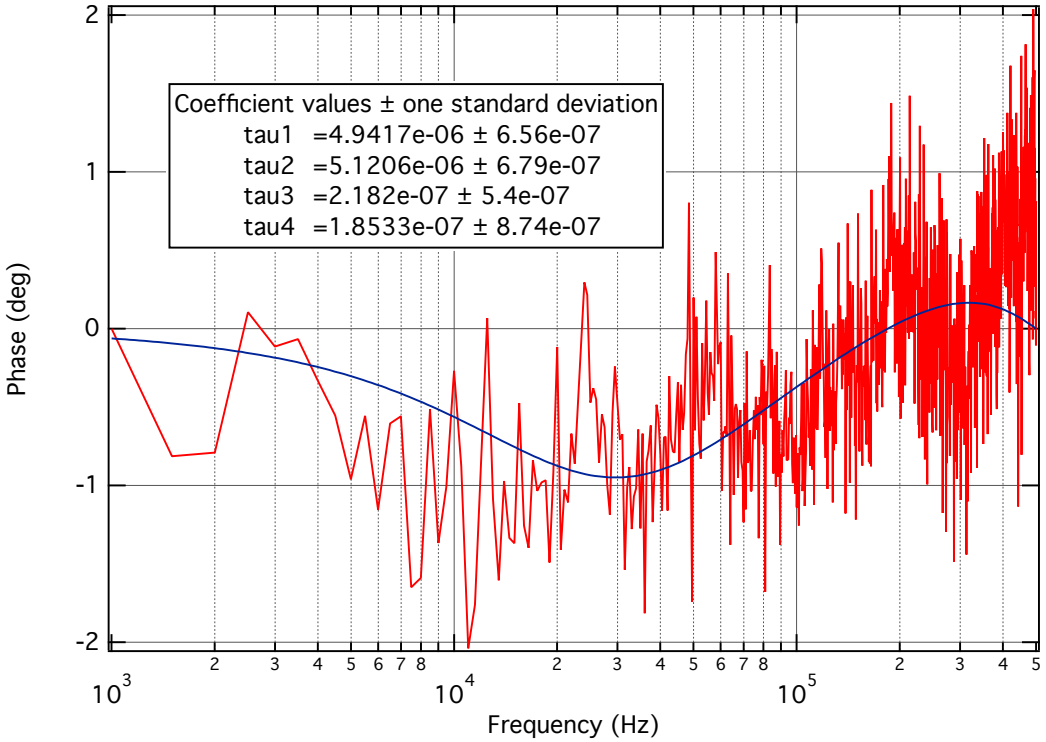

Figure 6.9: Estimation of the relative phase between the two channels. Red solid trace is the relative phase between the two channels, data is acquired by computing the FFTs of the traces of two channels and average over 100 traces. The blue curve is the fit with a double ratio of low-pass filter transfer functions, showing that the relative phase between the two channels is below 1° in the relative frequency range.

come from the detection circuitry and the laser RIN, while the other noise sources and the effect due to different response between the two channels have negligible contributions. The current noise performance is still far above the shot noise limit which is set by the probe power, however, it is possible to further reduce the noise floor by adopting low-noise detection systems and by actively stabilizing the laser power, and the noise cancellation scheme should still work.

6.6 Application: measuring a cavity phase shift

6.6.1 Experimental procedure

The cavity noise cancellation method provides a powerful tool for the precise measurement of a phase shift of the light circulating inside the cavity. We apply this scheme on a simulated squeezing measurement [51], where we mimic the

atom-induced cavity shift Δ in Eq. (6.4) by shifting the frequency of the Probe beam in Fig. 6.6. This frequency shift can be introduced through the frequency shift key (FSK) modulation on the RF source of AOM2. Therefore, the Probe beam will be detuned from the cavity resonance by the amount of the FSK. We apply an FSK modulation of 2 kHz and record the time domain traces of the error signal E_2 and compute the combined error signal E, as shown in Fig. 6.10. The black trace shows the trigger of the FSK modulation, where the data before the trigger are used for determining the value of α in Eq. (6.6) and the same value is applied on the whole dataset for noise cancellation.

As for a squeezing measurement, a typical probe time $T_m = 200$ μs is used and a differential scheme is adopted. In our scenario, we simulate the squeezing measurement by extracting 200 μs data segments from both the non-shifted and shifted regions (P1 and P2 in Fig. 6.10) with a delay time of 1 ms. We calculate the difference in the average of the two time series as $\delta P = \overline{P2} - \overline{P1}$ for both E_2 and E. For ten acquisitions with the same FSK frequency shift, the standard deviation in δP for E is reduced by a factor of 25 when compared to that of E_2, as shown by the error bars in Fig. 6.11.

6.6.2 Performance analysis

For a more precise estimation of the measurement sensitivity to laser frequency (phase) shift, a series of FSK modulations from 20 Hz to 2 kHz is performed. Figure 6.11 shows the δP values of E (red circles) and E_2 (blue squares) as a function of the FSK modulation frequency, with error bars signifying the standard deviation of ten acquisitions. We quantify the sensitivity to laser frequency shift with Eq. (6.5) by computing the frequency sensitivity $S = \sigma/a$, where $\sigma = \sqrt{\frac{n-1}{kn-1}\sum_{i=1}^{k}\sigma_i^2}$ is the weighted standard deviation of the error bars σ_i, $k = 37$ is the number of FSK frequencies, $n = 10$ is the number of acquisitions for each frequency and a is the slope of the linear fit of δP as a function of the FSK modulation frequency. For E_2 and E we compute the frequency sensitivity as $S_{E_2} = 801$ Hz and $S_E = 20$ Hz, respectively, which can be converted into cavity phase resolution through $\delta\phi = S/(\delta\nu/2)$ as $\delta\phi_{E_2} = 28$ mrad and $\delta\phi_E = 0.7$ mrad, signifying an improvement in phase sensitivity by a factor of 40. In order to prove the consistency of the frequency sensitivity measurements made with the FSK (Fig. 6.11) and the measured frequency PSDs (Fig. 6.8), we evaluate the frequency sensitivity from the measured frequency PSDs, using the transfer function for the difference between averages of a time series (see Appendix A). This yields a phase resolution of $\delta\phi_{E_1} = 24$ mrad and $\delta\phi'_E = 0.5$ mrad, consistent with the results from the FSK measurement.

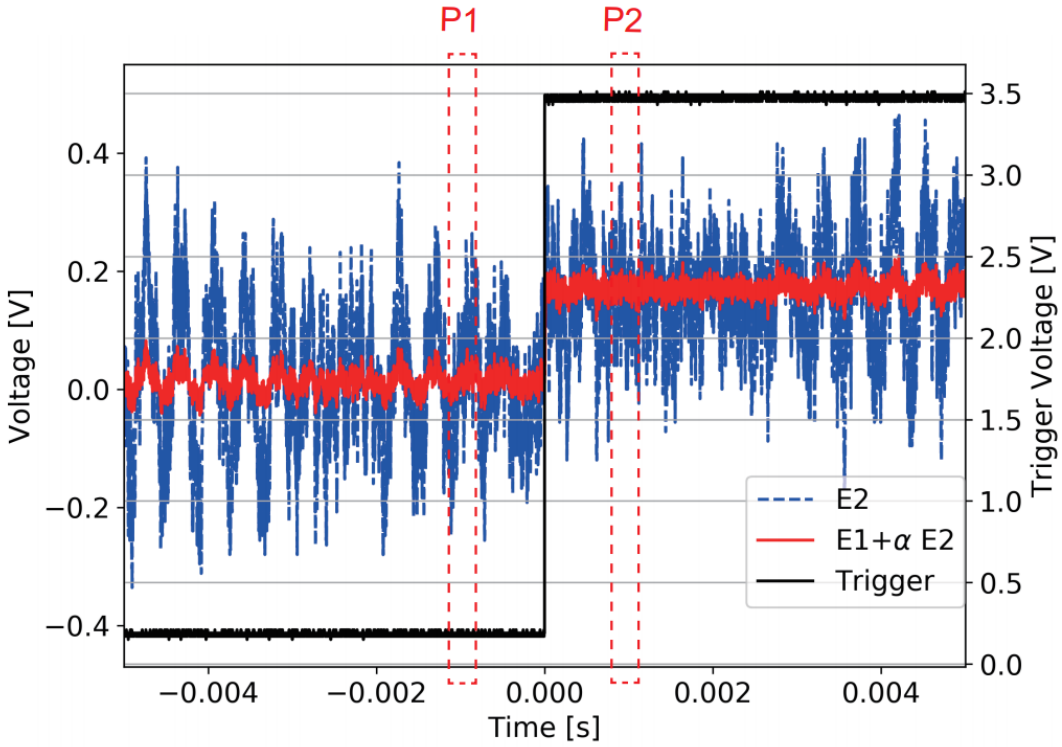

Figure 6.10: FSK modulation with 2 kHz laser frequency shift. The black trace is the trigger of the FSK, P1 and P2 are $T_m = 200$ μs long probes with a delay time of 1 ms, representing the measurement sequence of a typical squeezing experiment.

We can therefore use Eq. (6.2) to estimate the SNR (in dB) of the atom shot noise versus the cavity noise. For realistic experimental parameters [51], where $\eta \simeq 0.025$, $\Gamma \simeq 2\pi \times 7.5$ kHz is the linewidth of the $^1S_0$-$^3P_1$ transition of Sr, $\Delta_e \simeq 2\pi \times 2.8$ MHz is the effective detuning from atomic resonance with electromagnetically induced transparency (EIT) [51] and $N \simeq 1 \times 10^5$ atoms are involved, we estimate the atom-induced phase shift as $2\Phi_1 \frac{\sqrt{N}}{2} \simeq 10.7$ mrad. Therefore the SNRs with and without the noise cancellation are $\mathrm{SNR}_w = 24$ dB and $\mathrm{SNR}_{w/o} = -8$ dB, respectively. In the proposal paper [51], 20 dB squeezing is estimated by considering only the atom shot noise versus the scattering into free space, the cancellation of the cavity noise to a level 24 dB lower than the atom shot noise makes the conclusion of this proposal solid, as the cavity noise would no longer play a dominant role. If instead the cancellation method were not applied, our current level of cavity-length fluctuations would completely mask the atomic signal.

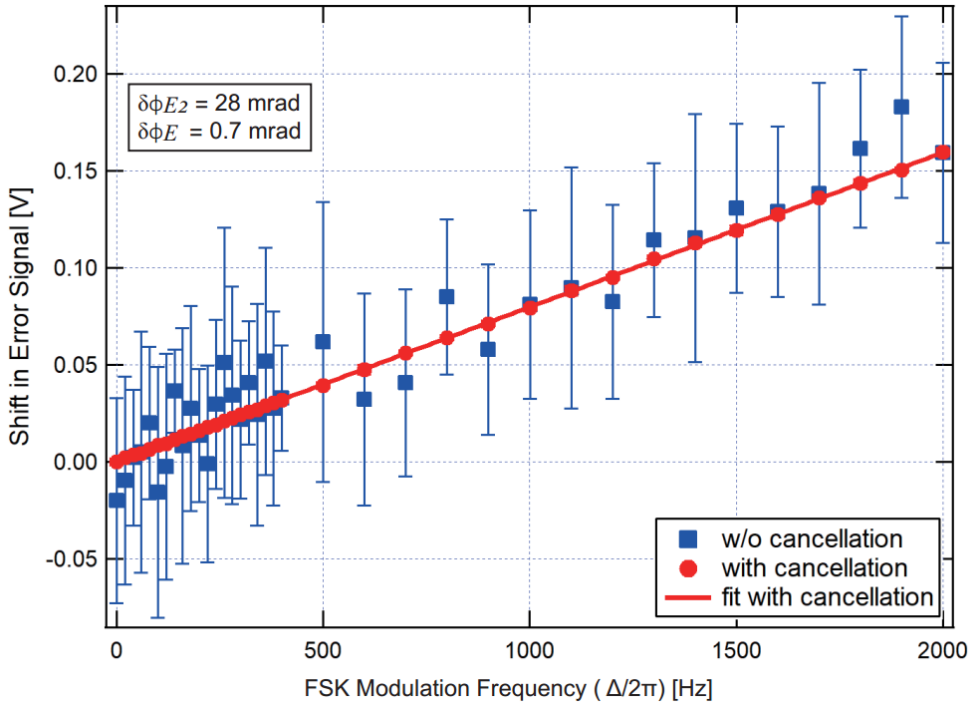

Figure 6.11: FSK modulation and sensitivity to laser frequency shift. A series of frequency shifts ranging from 20 Hz to 2 kHz is applied, each with ten acquisitions. The blue squares and red circles show the value of δP for E_2 and E, respectively, error bars represent the standard deviation of 10 acquisitions. The red line is a linear fit of the red circle data. Inset shows the calculated phase resolutions of E_2 and E, respectively.

6.7 Conclusions and prospects

In conclusion, we have demonstrated for the first time a phase shift measurement with pronounced immunity to cavity-length fluctuations using an optical ring cavity and two separate beams. We have achieved more than 30 dB reduction in the cavity noise due to length fluctuations, close to the limit of the measured noise floor. We have applied this phase shift measurement scheme in a simulated spin squeezing experiment where we mimic the atom-induced cavity phase shift by changing the frequency of one of the two circulating laser beams. An improvement in phase sensitivity by a factor of 40 with a phase resolution of 0.7 mrad is achieved. With this method, squeezing up to 20 dB would not be limited by cavity-length fluctuations.

This method is also applicable to two laser beams with largely different wavelengths as long as their frequency noise is negligible compared to the cavity res-

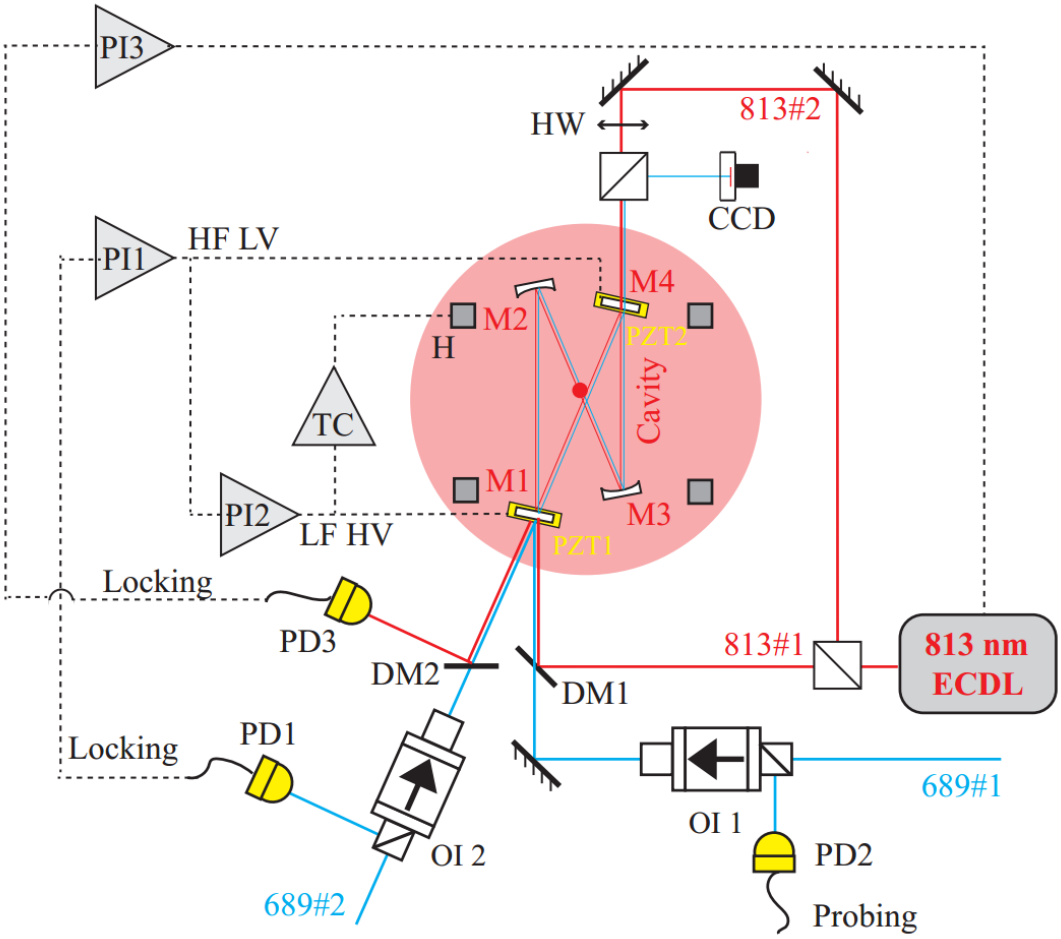

Figure 6.12: Experimental design of dual-color cavity noise cancellation. The squeezing cavity has two PZTs under M1 and M4 respectively and four heaters (H) for long-range and versatile cavity length tuning. Two 689 nm laser beams are coupled into the cavity for locking and probing purposes, the same as in Fig. 6.6. In addition, two 813 nm laser beams are coupled into the cavity from M1 and M4, respectively, to form a one dimensional optical lattice. Two shortpass dichroic mirrors (DM) are used to couple and split the lasers with different frequencies. In this scenario, one can derive the two PDH error signals for 689 nm and 813 nm lasers and explore the cancellation of the common mode cavity length fluctuations.

onance frequency fluctuations. This condition can be met by using the current cavity prototype as a transfer cavity to bridge the frequency stability of two lasers with largely different wavelengths, in our case, the 689 nm laser for squeezing and the 813 nm laser for optical lattice. The 689 nm red laser is further stabilized to a high-finesse F-P cavity (induced laser linewidth $\simeq$ 20 Hz), therefore in this condition both laser frequency noise are negligible compared to the cavity resonance

frequency fluctuations.

Another squeezing cavity will be built and assembled into the vacuum chamber and can be used to demonstrate the noise cancellation in a dual-color cavity scheme, as illustrated in Fig. 6.12. The squeezing cavity has two PZTs under M1 and M4 respectively and four heaters (H) for coarse cavity length tuning. Two 689 nm laser beams are coupled into the cavity for locking and probing purposes, the same as in Fig. 6.6. In addition, two 813 nm laser beams are coupled into the cavity from M1 and M4, respectively, to form a one-dimensional optical lattice. Two shortpass dichroic mirrors (DM) are used to couple and split the lasers with different frequencies. In this scenario, one can derive the two PDH error signals for 689 nm and 813 nm lasers and explore the cancellation of the common mode cavity length fluctuations.

In the future, we will apply this method to quantum non-destructive measurements for the generation of spin-squeezed states in atom interferometers. This method can find direct application to the cancellation of the effect of cavity length fluctuations in a cavity-aided non-destructive probe of Bloch oscillations [176] and Rabi oscillations [177]. More generally, it can assist in the non-destructive monitoring of quantum systems and find applications in the field of quantum simulation and quantum metrology.

Chapter 7

Conclusions and prospects

In this thesis, we have studied the cavity-enhanced measurement for the generation of spin squeezed states in Sr atom interferometry. It has been proposed that by resolving the Doppler effect due to momentum state superposition via cavity-enhanced nondestructive measurement, we can prepare the spin squeezed states for Bragg atom interferometers which can surpass the standard quantum limit for phase estimation. However, one major obstacle that we are going to meet is the cavity length fluctuations, which will mask the atomic signal. A method to cancel the cavity length fluctuations in measuring the atom-induced phase shift is therefore proposed and we have demonstrated close to 30 dB reduction of cavity noise down to the noise floor.

The core of the whole thesis is an optical ring cavity, which is designed for generating spin squeezed states. We dedicate a whole chapter to describe in detail the procedure for cavity alignment and construction. Innovative tools for cavity holding and manipulation are designed and implemented. Various epoxies are tested and the curing conditions are specified for gluing different cavity components. This chapter provides a tutorial for the construction of optical cavities in general.

We also demonstrate a method to cancel the cavity length fluctuations in measuring a phase shift, which removes a major barrier in attaining highly spin-squeezed states. Two independent laser beams which can potentially have largely different wavelengths are simultaneously resonant with the optical ring cavity, demonstrating noise correlations in the PDH error signals. In the differential scheme the common-mode cavity noise can be canceled, therefore higher sensitivity to phase shift can be achieved. In our setup, close to 30 dB noise reduction is demonstrated down to the noise floor, with the main limitation from the PD noise and the laser intensity noise.

We further apply the demonstrated noise-reduced measurement scheme in a

simulated squeezing experiment, where we mimic the atom-induced cavity phase shift by shifting the frequency of one of the two circulating beams. The noise cancellation scheme demonstrates an improvement by a factor of 40 in phase sensitivity with a phase resolution of 0.7 mrad. With this improvement we estimate that the cavity noise will no longer play an important role in spin squeezing measurement. While if the noise cancellation is not applied, the cavity noise will completely mask the atomic signals.

The demonstrated cavity noise cancellation scheme has a broader application in monitoring a general quantum system, where the signal is enclosed onto the light phase shift and can be enlarged by optical cavities. It can find direct applications to the cancellation of the effect of cavity length fluctuations in cavity-aided non-destructive probe of Bloch oscillations and Rabi oscillations. More generally, it can assist the non-destructive monitoring of quantum systems and find applications in the field of quantum simulation and quantum metrology.

As we are making progress in the lab, a new optical ring cavity is constructed and assembled inside the vacuum chamber. In the future, we will use this cavity to interact with laser-cooled atoms and measure the atom induced phase shift. The collective measurement of the atomic momentum state can induce spin squeezing in the atomic ensembles. Atom interferometers that utilize this spin squeezed state can achieve better phase resolution, even surpassing the standard quantum limit.

Appendix A

Transfer function for the difference between averages of a time series

We consider the time series of N points $x(n)$ for $n = 0, \cdots, N-1$. The difference between averages of the time series can be expressed as

$$\Delta S = \frac{1}{n_a} \sum_{n=0}^{n_a-1} x(n) - \frac{1}{n_a} \sum_{n=n_a+n_d-2}^{2n_a+n_d-3} x(n) \ , \tag{A.1}$$

where the two terms correspond to averages over n_a points, spaced by a delay of n_d points.

The corresponding response function is given by

$$R(n) = \frac{1}{n_a} \times \begin{cases} 1 & \text{if} \quad 0 \leq n \leq n_a - 1 \\ -1 & \text{if} \quad n_a + n_d - 2 \leq n \leq 2n_a + n_d - 3 \\ 0 & \text{otherwise} \end{cases} \tag{A.2}$$

and the discrete Fourier transform (i.e. the transfer function) reads

$$\tilde{R}(k) = \sum_{n=0}^{N-1} R(n) \exp\left(-2\pi i \frac{nk}{N}\right) . \tag{A.3}$$

This can be computed by using the identity

$$\sum_{n=0}^{m} q^n = \frac{1 - q^{m+1}}{1 - q} \tag{A.4}$$

so that

$$\begin{aligned}\tilde{R}(k) &= \frac{1}{n_a}\left[\sum_{n=0}^{n_a-1}\exp\left(-2\pi i\frac{nk}{N}\right) - \sum_{n=n_a+n_d-2}^{2n_a+n_d-3}\exp\left(-2\pi i\frac{nk}{N}\right)\right] \\ &= \frac{1}{n_a}\left[\sum_{n=0}^{n_a-1}\exp\left(-2\pi i\frac{nk}{N}\right) - \sum_{n=0}^{2n_a+n_d-3}\exp\left(-2\pi i\frac{nk}{N}\right) + \sum_{n=0}^{n_a+n_d-3}\exp\left(-2\pi i\frac{nk}{N}\right)\right] \\ &= \frac{1}{n_a}\frac{1+\exp\left[-2\pi i\frac{(an_a+n_d-2)k}{N}\right] - \exp\left(-2\pi i\frac{n_a k}{N}\right) - \exp\left[-2\pi i\frac{(n_a+n_d-2)k}{N}\right]}{1-\exp\left(-2\pi i\frac{k}{N}\right)}.\end{aligned} \tag{A.5}$$

Note that this expression is not valid for $k = 0$, where both the numerator and the deminominator vanish. In this case we recall that $e^y = 1 + y + o(y)$ and we find $\lim_{k\to 0}\tilde{R}(k) = 0$ so that we can take $\tilde{R}(0) = 0$. This agrees with intuition in the sense that in the difference of two averages one does not expect significant contributions from the low-frequency part of the spectrum.

Finally, the expected variance of ΔS, given the numerical PSD of x, $S_x(k)$ for $k = 0, \cdots, N-1$, is

$$\mathrm{Var}(\Delta S) = \sum_{k=0}^{N-1}|\tilde{R}(k)|^2 S_x(k)\Delta\mu, \tag{A.6}$$

where $\Delta\mu = 1/T$ is the frequency spacing and T the acquisition time corresponding to N points. Note that here the full numerical spectrum should be accounted for. If only half of the spectrum is known, one can still use Eq.(A.6) but multiply the result by 2 given the symmetry of S_x and $\tilde{R}$ around half the sampling rate.

Appendix B

Publications

This research activity has led to publications in international journals and conferences. These are summarized below.

International Journals

1. **E. Wang**, G. Verma, J. N. Tinsley, N. Poli and L, Salvi. "Method for the differential measurement of phase shifts induced by atoms in an optical ring cavity", *Physical Review A*, 103,022609(2021). [DOI:10.1103/PhysRevA.103.022609]

2. L. Hu, **E. Wang**, L, Salvi, J. N. Tinsley, G. M. Tino and N. Poli. "Sr atom interferometry with the optical clock transition as a gravimeter and a gravity gradiometer", *Classical and Quantum Gravity*, 37(1),014001, 2019. [DOI: 10.1088/1361-6382/ab4d18]

3. G. Rosi, A. Viceré, L. Cacciapuoti, G. D'Amico, L. Hu, M. Jain, N. Poli, L. Salvi, F. Sorrentino, **E. Wang** and G. M. Tino. "Detecting gravitational waves with atomic sensors", *IL NUOVO CIMENTO*, 100(130), 41, 2018. [DOI: 10.1393/ncc/i2018-18130-8]

International Conferences and Workshops

1. L. Hu, L, Salvi, **E. Wang**, G. M. Tino and N. Poli. "Characterization of the gravity gradiometer based on the Sr optical clock transition", in *European Frequency and Time Forum (EFTF)*, 2018.

2. L. Salvi, L. Cacciapuoti, G. D'Amico, L. Hu, M. Jain, N. Poli, G. Rosi, **E. Wang** and G. M. Tino. "Testing gravity with atomic quantum sensors on ground and in space", in *Quantum Technologies*, 2018.

Bibliography

[1] G. M. Tino and M. A. Kasevich, *Atom interferometry*, vol. 188. IOS Press, 2014.

[2] M. A. Kasevich and S. Chu, "Atomic interferometry using stimulated Raman transitions," *Physical Review Letters*, vol. 67, no. 2, p. 181, 1991.

[3] G. M. Tino, "Testing gravity with cold atom interferometry: Results and prospects," *arXiv preprint arXiv:2009.01484*, 2020.

[4] A. Peters, K. Y. Chung, and S. Chu, "Measurement of gravitational acceleration by dropping atoms," *Nature (London)*, vol. 400, no. 6747, pp. 849–852, 1999.

[5] Z.-K. Hu, B.-L. Sun, X.-C. Duan, M.-K. Zhou, L.-L. Chen, S. Zhan, Q.-Z. Zhang, and J. Luo, "Demonstration of an ultrahigh-sensitivity atom-interferometry absolute gravimeter," *Physical Review A*, vol. 88, no. 4, p. 043610, 2013.

[6] J. M. Mcguirk, G. Foster, J. Fixler, M. Snadden, and M. A. Kasevich, "Sensitive absolute-gravity gradiometry using atom interferometry," *Physical Review A*, vol. 65, no. 3, p. 033608, 2002.

[7] F. Sorrentino, Q. Bodart, L. Cacciapuoti, Y.-H. Lien, M. Prevedelli, G. Rosi, L. Salvi, and G. M. Tino, "Sensitivity limits of a Raman atom interferometer as a gravity gradiometer," *Physical Review A*, vol. 89, no. 2, p. 023607, 2014.

[8] G. Rosi, L. Cacciapuoti, F. Sorrentino, M. Menchetti, M. Prevedelli, and G. M. Tino, "Measurement of the gravity-field curvature by atom interferometry," *Physical Review Letters*, vol. 114, no. 1, p. 013001, 2015.

[9] T. Gustavson, P. Bouyer, and M. A. Kasevich, "Precision rotation measurements with an atom interferometer gyroscope," *Physical Review Letters*, vol. 78, no. 11, p. 2046, 1997.

[10] F. Riehle, T. Kisters, A. Witte, J. Helmcke, and C. J. Bordé, "Optical Ramsey spectroscopy in a rotating frame: Sagnac effect in a matter-wave interferometer," *Physical Review Letters*, vol. 67, no. 2, p. 177, 1991.

[11] G. Rosi, F. Sorrentino, L. Cacciapuoti, M. Prevedelli, and G. M. Tino, "Precision measurement of the Newtonian gravitational constant using cold atoms," *Nature*, vol. 510, no. 7506, pp. 518–521, 2014.

[12] M. Prevedelli, L. Cacciapuoti, G. Rosi, F. Sorrentino, and G. M. Tino, "Measuring the Newtonian constant of gravitation G with an atomic interferometer," *Philosophical Transactions of the Royal Society A: Mathematical, Physical and Engineering Sciences*, vol. 372, no. 2026, p. 20140030, 2014.

[13] J. B. Fixler, G. Foster, J. McGuirk, and M. A. Kasevich, "Atom interferometer measurement of the Newtonian constant of gravity," *Science*, vol. 315, no. 5808, pp. 74–77, 2007.

[14] A. Wicht, J. M. Hensley, E. Sarajlic, and S. Chu, "A preliminary measurement of the fine structure constant based on atom interferometry," *Physica Scripta*, vol. 2002, no. T102, p. 82, 2002.

[15] R. H. Parker, C. Yu, W. Zhong, B. Estey, and H. Müller, "Measurement of the fine-structure constant as a test of the standard model," *Science*, vol. 360, no. 6385, pp. 191–195, 2018.

[16] M. G. Tarallo, T. Mazzoni, N. Poli, D. Sutyrin, X. Zhang, and G. M. Tino, "Test of Einstein equivalence principle for 0-spin and half-integer-spin atoms: search for spin-gravity coupling effects," *Physical Review Letters*, vol. 113, no. 2, p. 023005, 2014.

[17] S. Fray, C. A. Diez, T. W. Hänsch, and M. Weitz, "Atomic interferometer with amplitude gratings of light and its applications to atom based tests of the equivalence principle," *Physical Review Letters*, vol. 93, no. 24, p. 240404, 2004.

[18] D. Schlippert, J. Hartwig, H. Albers, L. L. Richardson, C. Schubert, A. Roura, W. P. Schleich, W. Ertmer, and E. M. Rasel, "Quantum test of the universality of free fall," *Physical Review Letters*, vol. 112, no. 20, p. 203002, 2014.

[19] L. Zhou, S. Long, B. Tang, X. Chen, F. Gao, W. Peng, W. Duan, J. Zhong, Z. Xiong, J. Wang, *et al.*, "Test of equivalence principle at 10^{-8} level by a dual-species double-diffraction Raman atom interferometer," *Physical Review Letters*, vol. 115, no. 1, p. 013004, 2015.

[20] G. M. Tino and F. Vetrano, "Is it possible to detect gravitational waves with atom interferometers?," *Classical and Quantum Gravity*, vol. 24, no. 9, 2007.

[21] A. Arvanitaki, P. W. Graham, J. M. Hogan, S. Rajendran, and K. Van Tilburg, "Search for light scalar dark matter with atomic gravitational wave detectors," *Physical Review D*, vol. 97, no. 7, p. 075020, 2018.

[22] N. Poli, M. Schioppo, S. Vogt, U. Sterr, C. Lisdat, G. M. Tino, *et al.*, "A transportable strontium optical lattice clock," *Applied Physics B*, vol. 117, no. 4, pp. 1107–1116, 2014.

[23] F. Sorrentino, K. Bongs, P. Bouyer, L. Cacciapuoti, M. De Angelis, H. Dittus, W. Ertmer, A. Giorgini, J. Hartwig, M. Hauth, *et al.*, "A compact atom interferometer for future space missions," *Microgravity Science and Technology*, vol. 22, no. 4, pp. 551–561, 2010.

[24] G. Ferrari, N. Poli, F. Sorrentino, and G. M. Tino, "Long-lived Bloch oscillations with bosonic Sr atoms and application to gravity measurement at the micrometer scale," *Physical Review Letters*, vol. 97, no. 6, p. 060402, 2006.

[25] X. Zhang, R. P. del Aguila, T. Mazzoni, N. Poli, and G. M. Tino, "Trapped-atom interferometer with ultracold Sr atoms," *Physical Review A*, vol. 94, no. 4, p. 043608, 2016.

[26] T. Mazzoni, X. Zhang, R. Del Aguila, L. Salvi, N. Poli, and G. M. Tino, "Large-momentum-transfer Bragg interferometer with strontium atoms," *Physical Review A*, vol. 92, no. 5, p. 053619, 2015.

[27] R. P. del Aguila, T. Mazzoni, L. Hu, L. Salvi, G. M. Tino, and N. Poli, "Bragg gravity-gradiometer using the $^1S_0$-$^3P_1$ intercombination transition of ^{88}Sr," *New Journal of Physics*, vol. 20, no. 4, p. 043002, 2018.

[28] A. D. Ludlow, M. M. Boyd, J. Ye, E. Peik, and P. O. Schmidt, "Optical atomic clocks," *Reviews of Modern Physics*, vol. 87, no. 2, p. 637, 2015.

[29] M. Takamoto, I. Ushijima, N. Ohmae, T. Yahagi, K. Kokado, H. Shinkai, and H. Katori, "Test of general relativity by a pair of transportable optical lattice clocks," *Nature Photonics*, pp. 1–5, 2020.

[30] L. Hu, N. Poli, L. Salvi, and G. M. Tino, "Atom interferometry with the Sr optical clock transition," *Physical Review Letters*, vol. 119, no. 26, p. 263601, 2017.

[31] L. Hu, E. Wang, L. Salvi, J. N. Tinsley, G. M. Tino, and N. Poli, "Sr atom interferometry with the optical clock transition as a gravimeter and a gravity gradiometer," *Classical and Quantum Gravity*, vol. 37, no. 1, p. 014001, 2019.

[32] J. Rudolph, T. Wilkason, M. Nantel, H. Swan, C. M. Holland, Y. Jiang, B. E. Garber, S. P. Carman, J. M. Hogan, *et al.*, "Large momentum transfer clock atom interferometry on the 689 nm intercombination line of strontium," *Physical Review Letters*, vol. 124, no. 8, p. 083604, 2020.

[33] S. Dimopoulos, P. W. Graham, J. M. Hogan, M. A. Kasevich, and S. Rajendran, "Atomic gravitational wave interferometric sensor," *Physical Review D*, vol. 78, no. 12, p. 122002, 2008.

[34] N. Yu and M. Tinto, "Gravitational wave detection with single-laser atom interferometers," *General Relativity and Gravitation*, vol. 43, no. 7, pp. 1943–1952, 2011.

[35] L. Pezzè, A. Smerzi, M. K. Oberthaler, R. Schmied, and P. Treutlein, "Quantum metrology with nonclassical states of atomic ensembles," *Reviews of Modern Physics*, vol. 90, no. 3, p. 035005, 2018.

[36] W. M. Itano, J. C. Bergquist, J. J. Bollinger, J. Gilligan, D. J. Heinzen, F. Moore, M. Raizen, and D. J. Wineland, "Quantum projection noise: Population fluctuations in two-level systems," *Physical Review A*, vol. 47, no. 5, p. 3554, 1993.

[37] J. Ma, X. Wang, C.-P. Sun, and F. Nori, "Quantum spin squeezing," *Physics Reports*, vol. 509, no. 2-3, pp. 89–165, 2011.

[38] M. Kitagawa and M. Ueda, "Squeezed spin states," *Physical Review A*, vol. 47, no. 6, p. 5138, 1993.

[39] D. J. Wineland, J. J. Bollinger, W. M. Itano, F. Moore, and D. J. Heinzen, "Spin squeezing and reduced quantum noise in spectroscopy," *Physical Review A*, vol. 46, no. 11, p. R6797, 1992.

[40] V. Giovannetti, S. Lloyd, and L. Maccone, "Quantum-enhanced measurements: beating the standard quantum limit," *Science*, vol. 306, no. 5700, pp. 1330–1336, 2004.

[41] H. Tanji-Suzuki, I. D. Leroux, M. H. Schleier-Smith, M. Cetina, A. T. Grier, J. Simon, and V. Vuletić, "Interaction between atomic ensembles and optical resonators: classical description," in *Advances in atomic, molecular, and optical physics*, vol. 60, pp. 201–237, Elsevier, 2011.

[42] J. Appel, P. J. Windpassinger, D. Oblak, U. B. Hoff, N. Kjærgaard, and E. S. Polzik, "Mesoscopic atomic entanglement for precision measurements beyond the standard quantum limit," *Proceedings of the National Academy of Sciences*, vol. 106, no. 27, pp. 10960–10965, 2009.

[43] M. Saffman, D. Oblak, J. Appel, and E. S. Polzik, "Spin squeezing of atomic ensembles by multicolor quantum nondemolition measurements," *Physical Review A*, vol. 79, no. 2, p. 023831, 2009.

[44] M. H. Schleier-Smith, I. D. Leroux, and V. Vuletić, "States of an ensemble of two-level atoms with reduced quantum uncertainty," *Physical Review Letters*, vol. 104, no. 7, p. 073604, 2010.

[45] O. Hosten, N. J. Engelsen, R. Krishnakumar, and M. A. Kasevich, "Measurement noise 100 times lower than the quantum-projection limit using entangled atoms," *Nature*, vol. 529, no. 7587, p. 505, 2016.

[46] Z. Chen, J. G. Bohnet, J. M. Weiner, K. C. Cox, and J. K. Thompson, "Cavity-aided nondemolition measurements for atom counting and spin squeezing," *Physical Review A*, vol. 89, no. 4, p. 043837, 2014.

[47] B. Braverman, A. Kawasaki, E. Pedrozo-Peñafiel, S. Colombo, C. Shu, Z. Li, E. Mendez, M. Yamoah, L. Salvi, D. Akamatsu, *et al.*, "Near-unitary spin squeezing in Yb 171," *Physical Review Letters*, vol. 122, no. 22, p. 223203, 2019.

[48] E. Pedrozo-Peñfiel, S. Colombo, C. Shu, A. F. Adiyatullin, Z. Li, E. Mendez, B. Braverman, A. Kawasaki, D. Akamatsu, Y. Xiao, *et al.*, "Entanglement-enhanced optical atomic clock," *arXiv preprint arXiv:2006.07501*, 2020.

[49] G. Vallet, E. Bookjans, U. Eismann, S. Bilicki, R. Le Targat, and J. Lodewyck, "A noise-immune cavity-assisted non-destructive detection for an optical lattice clock in the quantum regime," *New Journal of Physics*, vol. 19, no. 8, p. 083002, 2017.

[50] R. Hobson, W. Bowden, A. Vianello, I. R. Hill, and P. Gill, "Cavity-enhanced non-destructive detection of atoms for an optical lattice clock," *Optics Express*, vol. 27, no. 26, pp. 37099–37110, 2019.

[51] L. Salvi, N. Poli, V. Vuletić, and G. M. Tino, "Squeezing on momentum states for atom interferometry," *Physical Review Letters*, vol. 120, no. 3, p. 033601, 2018.

[52] L. Salvi, *Towards atom interferometry beyond the Standard Quantum Limit with strontium atoms*. PhD thesis, University of Florence, Florence, 2017.

[53] E. Wang, G. Verma, J. N. Tinsley, N. Poli, and L. Salvi, "Method for the differential measurement of phase shifts induced by atoms in an optical ring cavity," *Physical Review A*, vol. 103, no. 2, p. 022609, 2021.

[54] P. W. Graham, J. M. Hogan, M. A. Kasevich, and S. Rajendran, "New method for gravitational wave detection with atomic sensors," *Physical Review Letters*, vol. 110, no. 17, p. 171102, 2013.

[55] M. Hohensee, S.-Y. Lan, R. Houtz, C. Chan, B. Estey, G. Kim, P.-C. Kuan, and H. Müller, "Sources and technology for an atomic gravitational wave interferometric sensor," *General Relativity and Gravitation*, vol. 43, no. 7, pp. 1905–1930, 2011.

[56] S. Dimopoulos, P. W. Graham, J. M. Hogan, M. A. Kasevich, and S. Rajendran, "Gravitational wave detection with atom interferometry," *Physics Letters B*, vol. 678, no. 1, pp. 37–40, 2009.

[57] W. Chaibi, R. Geiger, B. Canuel, A. Bertoldi, A. Landragin, and P. Bouyer, "Low frequency gravitational wave detection with ground-based atom interferometer arrays," *Physical Review D*, vol. 93, no. 2, p. 021101, 2016.

[58] C. Gross, "Spin squeezing, entanglement and quantum metrology with Bose-Einstein condensates," *Journal of Physics B: Atomic, Molecular and Optical Physics*, vol. 45, no. 10, p. 103001, 2012.

[59] R. H. Dicke, "Coherence in spontaneous radiation processes," *Physical Review*, vol. 93, no. 1, p. 99, 1954.

[60] L. Mandel and E. Wolf, *Optical coherence and quantum optics*. Cambridge university press, 1995.

[61] V. Giovannetti, S. Lloyd, and L. Maccone, "Quantum metrology," *Physical Review Letters*, vol. 96, no. 1, p. 010401, 2006.

[62] C. Lee, "Q representation of the atomic coherent states and the origin of fluctuations in superfluorescence," *Physical Review A*, vol. 30, no. 6, p. 3308, 1984.

[63] F. Arecchi, E. Courtens, R. Gilmore, and H. Thomas, "Atomic coherent states in quantum optics," *Physical Review A*, vol. 6, no. 6, p. 2211, 1972.

[64] D. J. Wineland, J. J. Bollinger, W. M. Itano, and D. J. Heinzen, "Squeezed atomic states and projection noise in spectroscopy," *Physical Review A*, vol. 50, no. 1, p. 67, 1994.

[65] X. Wang and B. C. Sanders, "Relations between bosonic quadrature squeezing and atomic spin squeezing," *Physical Review A*, vol. 68, no. 3, p. 033821, 2003.

[66] L. Pezzé and A. Smerzi, "Entanglement, nonlinear dynamics, and the Heisenberg limit," *Physical Review Letters*, vol. 102, no. 10, p. 100401, 2009.

[67] O. Gühne, G. Tóth, and H. J. Briegel, "Multipartite entanglement in spin chains," *New Journal of Physics*, vol. 7, no. 1, p. 229, 2005.

[68] A. S. Sørensen and K. Mølmer, "Entanglement and extreme spin squeezing," *Physical Review Letters*, vol. 86, no. 20, p. 4431, 2001.

[69] A. Sørensen, L.-M. Duan, J. I. Cirac, and P. Zoller, "Many-particle entanglement with Bose-Einstein condensates," *Nature*, vol. 409, no. 6816, pp. 63–66, 2001.

[70] S. L. Braunstein and C. M. Caves, "Statistical distance and the geometry of quantum states," *Physical Review Letters*, vol. 72, no. 22, p. 3439, 1994.

[71] W. K. Wootters, "Statistical distance and Hilbert space," *Physical Review D*, vol. 23, no. 2, p. 357, 1981.

[72] C. W. Helstrom and C. W. Helstrom, *Quantum detection and estimation theory*, vol. 3. Academic press New York, 1976.

[73] M. Inguscio and L. Fallani, *Atomic physics: precise measurements and ultracold matter*. OUP Oxford, 2013.

[74] Z. Chen, *Breaking Quantum Limits with Collective Cavity-QED: Generation of Spin Squeezed States via Quantum Non-Demolition Measurements*. PhD thesis, University of Colorado at Boulder, 2013.

[75] P. Bouyer and M. A. Kasevich, "Heisenberg-limited spectroscopy with degenerate Bose-Einstein gases," *Physical Review A*, vol. 56, no. 2, p. R1083, 1997.

[76] J. P. Dowling, "Correlated input-port, matter-wave interferometer: Quantum-noise limits to the atom-laser gyroscope," *Physical Review A*, vol. 57, no. 6, p. 4736, 1998.

[77] D. Leibfried, M. D. Barrett, T. Schaetz, J. Britton, J. Chiaverini, W. M. Itano, J. D. Jost, C. Langer, and D. J. Wineland, "Toward Heisenberg-limited spectroscopy with multiparticle entangled states," *Science*, vol. 304, no. 5676, pp. 1476–1478, 2004.

[78] J. J. Bollinger, W. M. Itano, D. J. Wineland, and D. J. Heinzen, "Optimal frequency measurements with maximally correlated states," *Physical Review A*, vol. 54, no. 6, p. R4649, 1996.

[79] M. Holland and K. Burnett, "Interferometric detection of optical phase shifts at the Heisenberg limit," *Physical Review Letters*, vol. 71, no. 9, p. 1355, 1993.

[80] T. Kim, O. Pfister, M. J. Holland, J. Noh, and J. L. Hall, "Influence of decorrelation on Heisenberg-limited interferometry with quantum correlated photons," *Physical Review A*, vol. 57, no. 5, p. 4004, 1998.

[81] A. Kuzmich, N. Bigelow, and L. Mandel, "Atomic quantum non-demolition measurements and squeezing," *EPL (Europhysics Letters)*, vol. 42, no. 5, p. 481, 1998.

[82] Y. Takahashi, K. Honda, N. Tanaka, K. Toyoda, K. Ishikawa, and T. Yabuzaki, "Quantum nondemolition measurement of spin via the paramagnetic Faraday rotation," *Physical Review A*, vol. 60, no. 6, p. 4974, 1999.

[83] K. Hammerer, A. S. Sørensen, and E. S. Polzik, "Quantum interface between light and atomic ensembles," *Reviews of Modern Physics*, vol. 82, no. 2, p. 1041, 2010.

[84] K. Hammerer, K. Mølmer, E. S. Polzik, and J. I. Cirac, "Light-matter quantum interface," *Physical Review A*, vol. 70, no. 4, p. 044304, 2004.

[85] D. Oblak, P. G. Petrov, C. L. G. Alzar, W. Tittel, A. K. Vershovski, J. K. Mikkelsen, J. L. Sørensen, and E. S. Polzik, "Quantum-noise-limited interferometric measurement of atomic noise: Towards spin squeezing on the Cs clock transition," *Physical Review A*, vol. 71, no. 4, p. 043807, 2005.

[86] S. Chaudhury, G. A. Smith, K. Schulz, and P. S. Jessen, "Continuous nondemolition measurement of the Cs clock transition pseudospin," *Physical Review Letters*, vol. 96, no. 4, p. 043001, 2006.

[87] S. L. Christensen, *Generation of Exotic Quantum States of a Cold Atomic Ensemble*. PhD thesis, The Niels Bohr Institute, Faculty of Science, University of Copenhagen, 2014.

[88] C. Gross, T. Zibold, E. Nicklas, J. Esteve, and M. K. Oberthaler, "Nonlinear atom interferometer surpasses classical precision limit," *Nature*, vol. 464, no. 7292, pp. 1165–1169, 2010.

[89] C. F. Ockeloen, R. Schmied, M. F. Riedel, and P. Treutlein, "Quantum metrology with a scanning probe atom interferometer," *Physical Review Letters*, vol. 111, no. 14, p. 143001, 2013.

[90] T. Berrada, S. van Frank, R. Bücker, T. Schumm, J.-F. Schaff, and J. Schmiedmayer, "Integrated Mach-Zehnder interferometer for Bose-Einstein condensates," *Nature communications*, vol. 4, no. 1, pp. 1–8, 2013.

[91] M. Martin, M. Bishof, M. Swallows, X. Zhang, C. Benko, J. Von-Stecher, A. Gorshkov, A. Rey, and J. Ye, "A quantum many-body spin system in an optical lattice clock," *Science*, vol. 341, no. 6146, pp. 632–636, 2013.

[92] G. S. Agarwal, R. Puri, and R. Singh, "Atomic Schrödinger cat states," *Physical Review A*, vol. 56, no. 3, p. 2249, 1997.

[93] J. Zhang, K. Peng, and S. L. Braunstein, "Backaction-induced spin-squeezed states in a detuned quantum-nondemolition measurement," *Physical Review A*, vol. 68, no. 3, p. 035802, 2003.

[94] I. D. Leroux, M. H. Schleier-Smith, and V. Vuletić, "Implementation of cavity squeezing of a collective atomic spin," *Physical Review Letters*, vol. 104, no. 7, p. 073602, 2010.

[95] I. D. Leroux, M. H. Schleier-Smith, and V. Vuletić, "Orientation-dependent entanglement lifetime in a squeezed atomic clock," *Physical Review Letters*, vol. 104, no. 25, p. 250801, 2010.

[96] A. Kawasaki, B. Braverman, E. Pedrozo-Peñafiel, C. Shu, S. Colombo, Z. Li, Ö. Özel, W. Chen, L. Salvi, A. Heinz, *et al.*, "Geometrically asymmetric optical cavity for strong atom-photon coupling," *Physical Review A*, vol. 99, no. 1, p. 013437, 2019.

[97] A. Kuzmich, K. Mølmer, and E. Polzik, "Spin squeezing in an ensemble of atoms illuminated with squeezed light," *Physical Review Letters*, vol. 79, no. 24, p. 4782, 1997.

[98] J. Hald, J. Sørensen, C. Schori, and E. Polzik, "Spin squeezed atoms: a macroscopic entangled ensemble created by light," *Physical Review Letters*, vol. 83, no. 7, p. 1319, 1999.

[99] J. Hald, J. Sørensen, C. Schori, and E. Polzik, "Entanglement transfer from light to atoms," *Journal of Modern Optics*, vol. 47, no. 14-15, pp. 2599–2614, 2000.

[100] N. Poli, F.-Y. Wang, M. Tarallo, A. Alberti, M. Prevedelli, and G. M. Tino, "Precision measurement of gravity with cold atoms in an optical lattice and comparison with a classical gravimeter," *Physical Review Letters*, vol. 106, no. 3, p. 038501, 2011.

[101] P. G. Mickelson, Y. M. De Escobar, M. Yan, B. DeSalvo, and T. C. Killian, "Bose-Einstein condensation of Sr 88 through sympathetic cooling with Sr 87," *Physical Review A*, vol. 81, no. 5, p. 051601, 2010.

[102] D. R. Lide, *CRC handbook of chemistry and physics*, vol. 85. CRC press, 2004.

[103] R. Rana, M. Höcker, and E. G. Myers, "Atomic masses of strontium and ytterbium," *Physical Review A*, vol. 86, no. 5, p. 050502, 2012.

[104] Y. M. De Escobar, P. Mickelson, P. Pellegrini, S. Nagel, A. Traverso, M. Yan, R. Côté, and T. Killian, "Two-photon photoassociative spectroscopy of ultracold Sr 88," *Physical Review A*, vol. 78, no. 6, p. 062708, 2008.

[105] A. Stein, H. Knöckel, and E. Tiemann, "The $^1S + {}^1S$ asymptote of Sr_2 studied by Fourier-transform spectroscopy," *The European Physical Journal D*, vol. 57, no. 2, pp. 171–177, 2010.

[106] G. Woodgate, "Elementary atomic structure, clarendon," 1980.

[107] A. Taichenachev, V. Yudin, C. Oates, C. Hoyt, Z. Barber, and L. Hollberg, "Magnetic field-induced spectroscopy of forbidden optical transitions with application to lattice-based optical atomic clocks," *Physical Review Letters*, vol. 96, no. 8, p. 083001, 2006.

[108] N. Poli, R. Drullinger, G. Ferrari, J. Léonard, F. Sorrentino, and G. M. Tino, "Cooling and trapping of ultracold strontium isotopic mixtures," *Physical Review A*, vol. 71, no. 6, p. 061403, 2005.

[109] S. Stellmer and F. Schreck, "Reservoir spectroscopy of $5s5p^3P_2$ - $5snd^3D_{1,2,3}$ transitions in strontium," *Physical Review A*, vol. 90, no. 2, p. 022512, 2014.

[110] F. Hu, I. Nosske, L. Couturier, C. Tan, C. Qiao, P. Chen, Y. Jiang, B. Zhu, and M. Weidemüller, "Analyzing a single-laser repumping scheme for efficient loading of a strontium magneto-optical trap," *Physical Review A*, vol. 99, no. 3, p. 033422, 2019.

[111] S. Zhang, P. Ramchurn, M. Menchetti, Q. Ubaid, J. Jones, K. Bongs, and Y. Singh, "Novel repumping on $^3P_0$-$^3D_1$ for Sr magneto-optical trap and Landé g factor measurement of $^3D_1$," *Journal of Physics B: Atomic, Molecular and Optical Physics*, vol. 53, no. 23, p. 235301, 2020.

[112] T. H. Loftus, T. Ido, M. M. Boyd, A. D. Ludlow, and J. Ye, "Narrow line cooling and momentum-space crystals," *Physical Review A*, vol. 70, no. 6, p. 063413, 2004.

[113] N. Poli, C. Oates, P. Gill, and G. M. Tino, "Optical atomic clocks," *La rivista del Nuovo Cimento*, vol. 36, pp. 555–624, 2013.

[114] T. Mazzoni, *Atom interferometry with fermionic and bosnic isotopes of strontium for precision gravity measurements and test of equivalence principle*. PhD thesis, University of Florence, Florence, 2015.

[115] B. V. Estey, *Precision Measurement in Atom Interferometry Using Bragg Diffraction*. PhD thesis, UC Berkeley, 2016.

[116] J. Hogan, *Towards precision tests of general relativity using an atom interferometer*. PhD thesis, Stanford University, 2010.

[117] S. M. Dickerson, *Long-time atom interferometry for precision tests of fundamental physics*. PhD thesis, Stanford University, 2014.

[118] J. M. Hogan, D. Johnson, and M. A. Kasevich, "Light-pulse atom interferometry," *arXiv preprint arXiv:0806.3261*, 2008.

[119] A. Peters, K. Y. Chung, and S. Chu, "High-precision gravity measurements using atom interferometry," *Metrologia*, vol. 38, no. 1, p. 25, 2001.

[120] A. Roura, W. Zeller, and W. P. Schleich, "Overcoming loss of contrast in atom interferometry due to gravity gradients," *New Journal of Physics*, vol. 16, no. 12, p. 123012, 2014.

[121] A. Roura, "Circumventing Heisenberg's uncertainty principle in atom interferometry tests of the equivalence principle," *Physical Review Letters*, vol. 118, no. 16, p. 160401, 2017.

[122] H. Müller, S.-w. Chiow, Q. Long, S. Herrmann, and S. Chu, "Atom interferometry with up to 24-photon-momentum-transfer beam splitters," *Physical Review Letters*, vol. 100, no. 18, p. 180405, 2008.

[123] W. H. Bragg and W. L. Bragg, "The reflection of X-rays by crystals," *Proceedings of the Royal Society of London. Series A, Containing Papers of a Mathematical and Physical Character*, vol. 88, no. 605, pp. 428–438, 1913.

[124] V. Chebotayev, B. Y. Dubetsky, A. Kasantsev, and V. Yakovlev, "Interference of atoms in separated optical fields," *JOSA B*, vol. 2, no. 11, pp. 1791–1798, 1985.

[125] P. J. Martin, B. G. Oldaker, A. H. Miklich, and D. E. Pritchard, "Bragg scattering of atoms from a standing light wave," *Physical Review Letters*, vol. 60, no. 6, p. 515, 1988.

[126] D. M. Giltner, R. W. McGowan, and S. A. Lee, "Theoretical and experimental study of the Bragg scattering of atoms from a standing light wave," *Physical Review A*, vol. 52, no. 5, p. 3966, 1995.

[127] T. Kovachy, P. Asenbaum, C. Overstreet, C. Donnelly, S. Dickerson, A. Sugarbaker, J. Hogan, and M. A. Kasevich, "Quantum superposition at the half-metre scale," *Nature*, vol. 528, no. 7583, pp. 530–533, 2015.

[128] S.-w. Chiow, T. Kovachy, H.-C. Chien, and M. A. Kasevich, "102 $\hbar$k large area atom interferometers," *Physical Review Letters*, vol. 107, no. 13, p. 130403, 2011.

[129] E. Giese, A. Friedrich, S. Abend, E. M. Rasel, and W. P. Schleich, "Light shifts in atomic Bragg diffraction," *Physical Review A*, vol. 94, no. 6, p. 063619, 2016.

[130] S. E. Harris, G. Yin, A. Kasapi, M. Jain, and Z. Luo, "Electromagnetically induced transparency," in *Coherence and Quantum Optics VII*, pp. 295–304, Springer, 1996.

[131] H. Wu, J. Gea-Banacloche, and M. Xiao, "Observation of intracavity electromagnetically induced transparency and polariton resonances in a Doppler-broadened medium," *Physical Review Letters*, vol. 100, no. 17, p. 173602, 2008.

[132] M. H. Schleier-Smith, I. D. Leroux, and V. Vuletić, "Squeezing the collective spin of a dilute atomic ensemble by cavity feedback," *Physical Review A*, vol. 81, no. 2, p. 021804, 2010.

[133] M. D. Álvarez, *Optical cavities for optical atomic clocks, atom interferometry and gravitational-wave detection*. Springer, 2019.

[134] B. Braverman, *Cavity Quantum Electrodynamics with Ensembles of Ytterbium-171*. PhD thesis, Massachusetts Institute of Technology, Cambridge, MA, 2 2018.

[135] T. Kessler, C. Hagemann, C. Grebing, T. Legero, U. Sterr, F. Riehle, M. Martin, L. Chen, and J. Ye, "A sub-40-mHz-linewidth laser based on a silicon single-crystal optical cavity," *Nature Photonics*, vol. 6, no. 10, pp. 687–692, 2012.

[136] J. M. Robinson, E. Oelker, W. R. Milner, W. Zhang, T. Legero, D. G. Matei, F. Riehle, U. Sterr, and J. Ye, "Crystalline optical cavity at 4 K with thermal-noise-limited instability and ultralow drift," *Optica*, vol. 6, no. 2, pp. 240–243, 2019.

[137] M. G. Tarallo, *Development of a strontium optical lattice clock*. PhD thesis, University of Florence, Florence, 2009.

[138] A. Heinz, J. Trautmann, N. Šantić, A. Park, I. Bloch, and S. Blatt, "Crossed optical cavities with large mode diameters," *arXiv preprint arXiv:2011.01616*, 2020.

[139] H. Kogelnik and T. Li, "Laser beams and resonators," *Applied Optics*, vol. 5, no. 10, pp. 1550–1567, 1966.

[140] A. E. Siegman, *Lasers*. University Science Books, 1986.

[141] M. Schioppo, N. Poli, M. Prevedelli, S. Falke, C. Lisdat, U. Sterr, and G. M. Tino, "A compact and efficient strontium oven for laser-cooling experiments," *Review of Scientific Instruments*, vol. 83, no. 10, p. 103101, 2012.

[142] M. Schioppo, *Development of a transportable strontium optical clock*. PhD thesis, University of Florence, Florence, 2010.

[143] E. Neri, *Mass imbalanced Fermi mixtures with 2- and 3-body resonant interactions*. PhD thesis, University of Florence, Florence, 2018.

[144] S. L. Campbell, *A Fermi-degenerate three-dimensional optical lattice clock*. PhD thesis, University of Colorado at Boulder, 2017.

[145] N. Poli, G. Ferrari, M. Prevedelli, F. Sorrentino, R. Drullinger, and G. M. Tino, "Laser sources for precision spectroscopy on atomic strontium," *Spectrochimica Acta Part A: Molecular and Biomolecular Spectroscopy*, vol. 63, no. 5, pp. 981–986, 2006.

[146] E. Polzik and H. Kimble, "Frequency doubling with $KNbO_3$ in an external cavity," *Optics Letters*, vol. 16, no. 18, pp. 1400–1402, 1991.

[147] L. S. Cruz and F. C. Cruz, "External power-enhancement cavity versus intracavity frequency doubling of Ti: sapphire lasers using BIBO," *Optics Express*, vol. 15, no. 19, pp. 11913–11921, 2007.

[148] R. Le Targat, J.-J. Zondy, and P. Lemonde, "75%-efficiency blue generation from an intracavity PPKTP frequency doubler," *Optics Communications*, vol. 247, no. 4-6, pp. 471–481, 2005.

[149] Y. Shimada, Y. Chida, N. Ohtsubo, T. Aoki, M. Takeuchi, T. Kuga, and Y. Torii, "A simplified 461-nm laser system using blue laser diodes and a hollow cathode lamp for laser cooling of Sr," *Review of Scientific Instruments*, vol. 84, no. 6, p. 063101, 2013.

[150] V. Schkolnik, J. R. Williams, and N. Yu, "Generating 500 mW for laser cooling of strontium atoms by injection locking a high power laser diode," *arXiv preprint arXiv:2004.11732*, 2020.

[151] M. Barbiero, *Novel techniques for a Strontium Optical Lattice Clock*. PhD thesis, Politecnico di Torino, Torino, 2019.

[152] V. Schkolnik, O. Fartmann, and M. Krutzik, "An extended-cavity diode laser at 497 nm for laser cooling and trapping of neutral strontium," *Laser Physics*, vol. 29, no. 3, p. 035802, 2019.

[153] G. H. Zhang, B. Braverman, A. Kawasaki, and V. Vuletić, "Note: Fast compact laser shutter using a direct current motor and three-dimensional printing," *Review of Scientific Instruments*, vol. 86, no. 12, p. 126105, 2015.

[154] N. D. Oppong, "Towards a degenerate Fermi gas of strontium-87 in a 3D optical lattice," *Masters, JILA, CU Boulder/NIST and ETH Zurich*, 2015.

[155] E. D. Black, "An introduction to Pound-Drever-Hall laser frequency stabilization," *American Journal of Physics*, vol. 69, no. 1, pp. 79–87, 2001.

[156] B. Brown, "Noise analysis of FET transimpedance amplifiers," *Texas Instrum. Dallas, TX, USA, Tech. Rep.[Online]. Available: http://www. ti. com/lit/an/sboa060/sboa060. pdf*, 1994.

[157] M. Chiarotti, "Development and analysis of an optical detection system for the generation of non-classical atomic states." Bachelor thesis, University of Florence, 2018.

[158] A. Kuzmich, L. Mandel, and N. Bigelow, "Generation of spin squeezing via continuous quantum nondemolition measurement," *Physical Review Letters*, vol. 85, no. 8, p. 1594, 2000.

[159] M. O. Scully and M. S. Zubairy, "Quantum optics," 1999.

[160] K. C. Cox, G. P. Greve, J. M. Weiner, and J. K. Thompson, "Deterministic squeezed states with collective measurements and feedback," *Physical Review Letters*, vol. 116, no. 9, p. 093602, 2016.

[161] I. M. Georgescu, S. Ashhab, and F. Nori, "Quantum simulation," *Reviews of Modern Physics*, vol. 86, no. 1, p. 153, 2014.

[162] K. C. Cox, G. P. Greve, B. Wu, and J. K. Thompson, "Spatially homogeneous entanglement for matter-wave interferometry created with time-averaged measurements," *Physical Review A*, vol. 94, no. 6, p. 061601, 2016.

[163] M. Aspelmeyer, T. J. Kippenberg, and F. Marquardt, "Cavity optomechanics," *Reviews of Modern Physics*, vol. 86, no. 4, p. 1391, 2014.

[164] A. Chowdhury, P. Vezio, M. Bonaldi, A. Borrielli, F. Marino, B. Morana, G. Prodi, P. Sarro, E. Serra, and F. Marin, "Quantum signature of a squeezed mechanical oscillator," *Physical Review Letters*, vol. 124, no. 2, p. 023601, 2020.

[165] M. Bonaldi, A. Borrielli, A. Chowdhury, G. Di Giuseppe, W. Li, N. Malossi, F. Marino, B. Morana, R. Natali, P. Piergentili, *et al.*, "Probing quantum gravity effects with quantum mechanical oscillators," *arXiv preprint arXiv:2004.14371*, 2020.

[166] G. Rosi, G. D'Amico, L. Cacciapuoti, F. Sorrentino, M. Prevedelli, M. Zych, Č. Brukner, and G. M. Tino, "Quantum test of the equivalence principle for atoms in coherent superposition of internal energy states," *Nature communications*, vol. 8, p. 15529, 2017.

[167] I. Obata, T. Fujita, and Y. Michimura, "Optical ring cavity search for axion dark matter," *Physical Review Letters*, vol. 121, no. 16, p. 161301, 2018.

[168] I. D. Leroux, M. H. Schleier-Smith, H. Zhang, and V. Vuletić, "Unitary cavity spin squeezing by quantum erasure," *Physical Review A*, vol. 85, no. 1, p. 013803, 2012.

[169] A. S. Sørensen and K. Mølmer, "Probabilistic generation of entanglement in optical cavities," *Physical Review Letters*, vol. 90, no. 12, p. 127903, 2003.

[170] Z. Chen, J. G. Bohnet, S. R. Sankar, J. Dai, and J. K. Thompson, "Conditional spin squeezing of a large ensemble via the vacuum Rabi splitting," *Physical Review Letters*, vol. 106, no. 13, p. 133601, 2011.

[171] H. Ling, H. Pu, L. Baksmaty, and N. Bigelow, "Theory of a collective atomic recoil laser," *Physical Review A*, vol. 63, no. 5, p. 053810, 2001.

[172] Y.-F. Chen, Y.-C. Liu, Z.-H. Tsai, S.-H. Wang, and A. Y. Ite, "Beat-note interferometer for direct phase measurement of photonic information," *Physical Review A*, vol. 72, no. 3, p. 033812, 2005.

[173] E. A. Whittaker, M. Gehrtz, and G. C. Bjorklund, "Residual amplitude modulation in laser electro-optic phase modulation," *JOSA B*, vol. 2, no. 8, pp. 1320–1326, 1985.

[174] N. Wong and J. L. Hall, "Servo control of amplitude modulation in frequency-modulation spectroscopy: demonstration of shot-noise-limited detection," *JOSA B*, vol. 2, no. 9, pp. 1527–1533, 1985.

[175] W. Zhang, M. Martin, C. Benko, J. Hall, J. Ye, C. Hagemann, T. Legero, U. Sterr, F. Riehle, G. Cole, *et al.*, "Reduction of residual amplitude modulation to 1×10^{-6} for frequency modulation and laser stabilization," *Optics Letters*, vol. 39, no. 7, pp. 1980–1983, 2014.

[176] B. Peden, D. Meiser, M. L. Chiofalo, and M. Holland, "Nondestructive cavity QED probe of Bloch oscillations in a gas of ultracold atoms," *Physical Review A*, vol. 80, no. 4, p. 043803, 2009.

[177] P. J. Windpassinger, D. Oblak, P. Petrov, M. Kubasik, M. Saffman, C. G. Alzar, J. Appel, J. H. Müller, N. Kjærgaard, and E. S. Polzik, "Nondestructive probing of Rabi oscillations on the cesium clock transition near the standard quantum limit," *Physical Review Letters*, vol. 100, no. 10, p. 103601, 2008.